Contents

Plenary Talks

Proceedings of the International School-seminar
"New Physics and Quantum Chromodynamics at external Conditions", pp. 5 − 8,
3-6 May 2009, Dnipropetrovsk, Ukraine

RADIATIVE CORRECTIONS TO MUON AND B QUARK DECAY WIDTHS

A. Ali[1,a], E. A. Kuraev[2,b], Yu. M. Bystritskiy[2,c],

[1]DESY, D-22603 Hamburg, Germany [2]Joint Institute for Nuclear Research, Dubna, Russia

QED radiative correction to muon width is calculated in leading and next-to leading approximations using the factorization hypothesis. QED and QCD radiative corrections are calculated for $b \to c l \nu_l$ quark decay. The QCD correction in c-quark jet averaged experimental set-up is finite at zero c-quark mass and have the same order as the QED correction in leading logarithmical approximations.

1 Introduction

B-meson factories are the laboratories to study the b quark nature. Another possibility is provided by such an equipment as collider LHC.

The estimation of counting rated of top-antitop production at LHC is one pair per second permits to obtain a rather good statistics for top-quark production to study it's decay channels and the subsequent b quark decay.

Keeping in mind large b-quark mass M compared with c-quark mass, as well as muon mass large compared with electron mass, the problem of radiative corrections arises to be relevant.

Really the logarithms of mass ratios

$$L_e = \ln\left(\frac{M_b^2}{m_e^2}\right) \approx 18.07, \qquad L_c = \ln\left(\frac{M_b^2}{m_c^2}\right) \approx 2.4, \qquad L_\mu = \ln\left(\frac{M_\mu^2}{m_e^2}\right) \approx 10.7, \tag{1}$$

are large and typical radiative corrections contribution in leading logarithmical approximation (LLA), i.e. keeping the terms proportional to

$$\frac{\alpha}{\pi} L_{e\mu} \sim 1, \qquad \frac{\alpha_s}{\pi} L_c \sim 1, \tag{2}$$

will be of order of several percents.

Below we consider leptonic channel of b-quark decay associated with the c-quark production. There are two types of radiative corrections: QCD corrections arise from gluon exchange between c and b quarks, QED corrections mainly associated of emission of photons from light charged particles. Considering the emission of real gluons by quarks (this corresponds to gluon jet production) we can not restrict our investigation by elastic case only. In experiments the averaged of gluon jets accompanying c-quarks can be measured. In this experimental set-up the energy distributions will not suffer of "mass singularities" (i.e. in the limit $M_c \to 0$), which is the consequence of Kinoshita-Lee-Nauenberg theorem [1, 2]. The cancellation of this singularities was shown in explicit calculations in frames of one loop QCD calculations by [3, 4]. The result of their calculations was taken into account by the so called QCD K-factor. This is important because this K-factor can be rather large, comparable with QED LLA contributions.

It is the motivation of this paper to consider the radiative corrections.

We consider only leptonic channel of b-quark decay, namely $b \to cW^+ \to c(l^+\bar{\nu}_l)$.

As a first step we reproduce the known results for muon decay [5, 6, 7, 8, 9] and generalize it to all orders of perturbation theory (see Section 2). We as well consider the polarized muon decay case. The radiative corrections to decay channels $\tau \to l\nu_l\nu_\tau$ (where $l = e^-, \mu$) can be written in a standard way by Structure Function (SF) approach [10].

We note that the intermediate state of W^+ contribution and H^+ in intermediate state leads to different chiral states of final leptons, thus the relevant amplitudes do not interfere.

2 The muon decay

As we know the electron energy spectrum in $\mu \to e\bar{\nu}_e\nu_\mu$ decay in Born approximation is given by the following formula [11]:

$$\frac{d\Gamma_B}{dx} = 6\Gamma_\mu \left[2x^2\left(1-x\right) - \frac{4}{9}\rho x^2\left(3-4x\right)\right], \tag{3}$$

e-mail: [a]ali@mail.desy.de, [b]kuraev@theor.jinr.ru, [c]bystr@theor.jinr.ru

where $x = 2E_e/m_\mu$ is the energy fraction of final electron and ρ is the well-known Michel parameter [12] and Γ is the total decay width:

$$\Gamma_\mu = \frac{G_F^2 m_\mu^5}{192\pi^3}. \tag{4}$$

Using the Structure Function (SF) approach [10] (based on factorization hypotheses [15]) we can immediately write out the formulae for this spectrum with radiative corrections taking into account all orders of large logarithms contribution:

$$\frac{d\Gamma_{RC}}{dx} = \int\limits_x^1 \frac{dy}{y} D\left(\frac{x}{y}, \beta\right) \frac{d\Gamma_B}{dy} \left(1 + \frac{\alpha}{2\pi} K(y)\right), \qquad \beta_\mu = \frac{\alpha}{2\pi}(L_\mu - 1), \tag{5}$$

where $\frac{\Gamma_B}{dx}$ is the electron spectrum in Born approximation (3) which is considered as hard subprocess. $D(x, \beta)$ is the so-called structure function, which describes the process of virtual and real photon emission in leading logarithmical approximation and have the form [10]:

$$D(x, \beta) = \delta(1 - x) + \beta P^{(1)}(x) + \frac{1}{2!}\beta^2 P^{(2)}(x) + \cdots \tag{6}$$

The quantities $P^{(1)}(x)$ is the evolution equation kernel which is defined by the following relation:

$$P^{(1)}(x) = \left(\frac{1+x^2}{1-x}\right)_+ = \lim_{\Delta\to 0}\left[\frac{1+x^2}{1-x}\theta(1 - x - \Delta) + \left(2\ln(\Delta) + \frac{3}{2}\right)\delta(1-x)\right]; \tag{7}$$

$$P^{(n)}(x) = \int\limits_x^1 \frac{dy}{y} P^{(1)}(y) P^{(n-1)}\left(\frac{x}{y}\right), \qquad n = 2, 3, \cdots$$

The structure function $D(x, \beta)$ defined in that way automatically satisfies the condition of Kinoshita-Lee-Nauenberg (KLN) theorem [1, 2] of mass singularities cancellation in the total decay width:

$$\int\limits_0^1 dx D(x, \beta) = 1. \tag{8}$$

There is also a smoothed form for structure function $D(x, \beta)$:

$$D(x, \beta) = 2\beta(1 - z)^{2\beta - 1}\left(1 + \frac{3}{2}\beta\right) - \beta(1 + z) + O\left(\beta^2\right), \tag{9}$$

which sums radiative corrections in all orders of perturbation theory which enhanced by "big logarithm" factor L_μ and is more convenient for numerical evaluation.

The quantity $K(x)$ in (5) is the so-called K-factor which takes into account the contributions of radiative corrections which are not enhanced by big logarithms and have rather complicated form (see [5] or [16], §147). We note that contrary to singular behavior ($\sim \ln(1 - x)$) of $K(x)$ in the limit when $x \to 1$ the quantity

$$\int\limits_x^1 \frac{dy}{y} D\left(\frac{x}{y}, \beta\right) K(y) \tag{10}$$

have a finite limit at $x \to 1$ [9].

Thus applying general form of corrected spectrum (5) we obtain the following form of electron energy spectrum in first order of big logarithms (leading logarithmical approximation (LLA)):

$$\frac{1}{6\Gamma}\frac{d\Gamma}{dx} = 2x^2\left[1 - x - \frac{2}{9}\rho(3 - 4x)\right] + \frac{\alpha L}{2\pi}\left[4F_1(x) - \frac{8}{9}\rho F_2(x)\right], \tag{11}$$

where functions $F_{1,2}(x)$ are the results of structure function application to Born electron spectrum:

$$F_1(x) = \int\limits_x^1 \frac{dy}{y} y^2 (1 - y) P^{(1)}\left(\frac{x}{y}\right) = 2x^2(1 - x)\ln\left(\frac{1-x}{x}\right) + \frac{1}{6}(1 - x)\left(1 + 4x - 8x^2\right), \tag{12}$$

$$F_2(x) = \int\limits_x^1 \frac{dy}{y} y^2 (3 - 4y) P^{(1)}\left(\frac{x}{y}\right) 2x^2(3 - 4x)\ln\left(\frac{1-x}{x}\right) + \frac{16}{3}x^3 - 8x^2 + x + \frac{1}{6}, \tag{13}$$

and satisfy the following property:

$$\int\limits_0^1 dx F_{1,2}\left(x\right)=0, \tag{14}$$

which is the specific form of general KLN theorem [1, 2].

In conclusion of this section we give give the distribution for the case of polarized muon decay with RC of lowest order LLA (here we put $\rho = 3/4$):

$$\frac{d\Gamma}{\Gamma dx d\cos\theta}\left(\mu\to e\nu_\mu\bar{\nu}_e\right) = x^2\left[3-2x-P_\mu(1-2x)\cos\theta\right]+\frac{\alpha L}{2\pi}\left[F_3(x)-P_\mu\cos\theta F_4(x)\right], \tag{15}$$

with P_μ, θ- the degree of muon polarization and the angle between muon polarization vector and the electron momentum (rest frame of muon implied). The functions

$$F_3=2\left(6F_1-F_2\right),\qquad F_4=2\left(-2F_1+F_2\right), \tag{16}$$

have a form:

$$\begin{aligned}F_3(x) &= 4x^2\left(3-2x\right)\ln\frac{1-x}{x}+\frac{5}{3}+4x-8x^2+\frac{16}{3}x^3,\\ F_4(x) &= 4x^2\left(1-2x\right)\ln\frac{1-x}{x}-\frac{1}{6}-4x^2+8x^3.\end{aligned}$$

3 The decay $b\to c(e^+\bar{\nu}_e)$ in Born approximation

Let us consider the decay

$$b\left(p_b\right)\to c\left(p_c\right)+e^+\left(p_e\right)+\bar{\nu}_e\left(p_\nu\right) \tag{17}$$

within Standard Model (SM). Matrix element of this process in Born approximation has the form:

$$M_B^{b\to ce^+\bar{\nu}_e}=i\frac{g^2V_{bc}}{4\sqrt{2}}\frac{1}{q^2-M_W^2}\left(g_{\mu\nu}-\frac{q_\mu q_\nu}{M_W^2}\right)\left[\bar{u}_c\left(p_c\right)\gamma^\mu\left(1-\gamma_5\right)u_b\left(p_b\right)\right]\left[\bar{u}_e\left(p_e\right)\gamma^\nu\left(1-\gamma_5\right)u_{\nu_e}\left(p_\nu\right)\right], \tag{18}$$

where $g^2=\frac{4\pi\alpha}{\sin^2\theta_W}=8\pi M_W^2G_F/\sqrt{2}$ is the electroweak interaction constant and V_{bc} is the element of Cabib-boKobayashiMaskawa matrix of quark mixing. We note that the contribution of second term in brackets are proportional to electron mass due to conservation of lepton current and can be omitted. The matrix element square summed over spin states than reads:

$$\sum_{\text{spins}}\left|M_B^{b\to ce^+\bar{\nu}_e}\right|^2=\left(\frac{g^2V_{bc}}{4\sqrt{2}\left(q^2-M_W^2\right)}\right)^2 2^8\left(p_bp_\nu\right)\left(p_cp_e\right). \tag{19}$$

Let us introduce the following notation for kinematical values:

$$x_c=\frac{2E_c}{M_b},\quad x_e=\frac{2E_e}{M_b},\quad x_\nu=\frac{2E_\nu}{M_b},\quad \xi=\frac{M_b^2}{M_W^2},\quad \eta=\frac{M_c^2}{M_b^2},$$

where E_c, E_e and E_ν are the energies of c-quark, positron and neutrino in the b-quark rest frame.

Thus using the standard formulae for double spectra of b-quark decay $b\to ce^+\bar{\nu}_e$ we obtain

$$\frac{d\Gamma_B^{b\to ce^+\bar{\nu}_e}}{dx_cdx_e} = 12\Gamma_B^b\left(2-x_e-x_c\right)\left(x_e+x_c-1\right), \tag{20}$$

Γ_B^b is the total width of $b\to ce^+\bar{\nu}_e$ decay:

$$\Gamma_B^b = \frac{G_F^2M_b^5V_{bc}^2}{192\pi^3}. \tag{21}$$

Here we replaced the W-boson propagator by it's point-like approximation ($q^2 \ll M_W^2$). Single particle energy spectra can be obtained from (20) by integration over all possible energies of unseen particles:

$$\frac{d\Gamma_B^{b\to ce^+\bar{\nu}_e}}{dx_e} = \int\limits_{1-x_e}^{1} dx_c \frac{d\Gamma_B^{b\to ce^+\bar{\nu}_e}}{dx_c dx_e} = 2\Gamma_b x_e^2 (3-2x_e), \tag{22}$$

$$\frac{d\Gamma_B^{b\to ce^+\bar{\nu}_e}}{dx_c} = \int\limits_{1-x_c}^{1} dx_e \frac{d\Gamma_B^{b\to ce^+\bar{\nu}_e}}{dx_c dx_e} = 2\Gamma_b x_c^2 (3-2x_c), \tag{23}$$

$$\frac{d\Gamma_B^{b\to ce^+\bar{\nu}_e}}{dx_\nu} = \int\limits_{0}^{1} dx \frac{d\Gamma_B^{b\to ce^+\bar{\nu}_e}}{dx_c dx_e} = 12\Gamma_b x_\nu^2 (1-x_\nu). \tag{24}$$

Following the SF method illustrated in Section 2 we can write double spectrum (20) with QCD and QED radiative corrections:

$$\frac{d\Gamma^{b\to ce^+\bar{\nu}_e}}{dx_c dx_e} = \int\limits_{x_c}^{1} \frac{dy_c}{y_c} \int\limits_{x_e}^{1} \frac{dy_e}{y_e} \frac{d\Gamma_B^{b\to ce^+\bar{\nu}_e}}{dy_c dy_e} D^{QCD}\left(\frac{x_c}{y_c}, L_c\right) D^{QED}\left(\frac{x_e}{y_e}, L_e\right)\left(1 - \frac{\alpha_s}{3\pi} G(y_c)\right), \tag{25}$$

where function $G(x)$ is the result of calculation of QCD-radiative corrections which was performed in [4]. Function $D^{QED}(x, L_e)$ is the structure function defined in (6) and $D^{QCD}(x, L_c)$ can be obtained from it by replacements $\alpha \to \frac{4\alpha_s}{3}$, $L_e = \ln\left(M_b^2/m_e^2\right) \to L_c = \ln\left(M_b^2/M_c^2\right)$.

The explicit form of $G(x) \equiv G(x, \eta, \xi)|_{\eta,\xi\to 0}$ is:

$$\begin{aligned} G(x) &= \ln^2(1-x) + 2\mathrm{Li}_2(x) + \frac{2}{3}\pi^2 + \\ &+ \frac{1}{12x^2(3-2x)}\left\{ 2x\left(49x^2 - 159x + 86\right) + 27\left(1-4x^2\right)\left(\mathrm{Li}_2\left(\frac{2}{3}(1-x)\right) - \mathrm{Li}_2\left(\frac{2}{3}\right)\right) + \right. \\ &+ \left.\left[2\left(-16x^3 + 114x^2 - 153x + 86\right) + 27\left(1-4x^2\right)\ln\left(\frac{1+2x}{3}\right)\right]\ln(1-x)\right\}. \end{aligned} \tag{26}$$

In the case of averaging over the c-quark induced jet we have:

$$\frac{d\Gamma^{b\to ce^+\bar{\nu}_e}}{dx_e} = \int\limits_{x_e}^{1} \frac{dy_e}{y_e} \int\limits_{0}^{1} \frac{dy_c}{y_c} \frac{d\Gamma_B^{b\to ce^+\bar{\nu}_e}}{dy_c dy_e} D^{QED}\left(\frac{x_e}{y_e}, L_e\right)\left(1 - \frac{\alpha_s}{3\pi} G(y_c)\right). \tag{27}$$

References

[1] T. Kinoshita, J. Math. Phys. **3**, 650 (1962).
[2] T. D. Lee and M. Nauenberg, Phys. Rev. **133**, B1549 (1964).
[3] M. Jezabek and J. H. Kuhn, Nucl. Phys. **B320**, 20 (1989).
[4] G. Corbo, Nucl. Phys. **B212**, 99 (1983).
[5] S. M. Berman, Phys. Rev. **112**, 267 (1958).
[6] T. Kinoshita and A. Sirlin, Phys. Rev. **107**, 593 (1957).
[7] A. Arbuzov, A. Czarnecki, and A. Gaponenko, Phys. Rev. **D65**, 113006 (2002), hep-ph/0202102.
[8] A. Arbuzov and K. Melnikov, Phys. Rev. **D66**, 093003 (2002), hep-ph/0205172.
[9] E. Bartos, E. A. Kuraev, and M. Secansky, (2008), 0811.4242.
[10] E. A. Kuraev and V. S. Fadin, Sov. J. Nucl. Phys. **41**, 466 (1985).
[11] L. B. Okun, Amsterdam, Netherlands: North-holland (1982) 361p.
[12] L. Michel, Proc. Phys. Soc. **A63**, 514 (1950).
[13] L. N. Lipatov, Sov. J. Nucl. Phys. **20**, 94 (1975).
[14] G. Altarelli and G. Parisi, Nucl. Phys. **B126**, 298 (1977).
[15] J. C. Collins, D. E. Soper, and G. Sterman, Nucl. Phys. **B250**, 199 (1985).
[16] V. B. Berestetsky, E. M. Lifshitz, and L. P. Pitaevsky, Oxford, Uk: Pergamon (1982) 652 P. (Course Of Theoretical Physics, 4).

Proceedings of the International School-seminar
"New Physics and Quantum Chromodynamics at external Conditions", pp. 9 − 14,
3-6 May 2009, Dnipropetrovsk, Ukraine

RADIATIVE MUON DECAY

O. M. Boyarkin[a], Boyarkina G.G.

Belarus State Pedogogical University, Minsk, Belarus

The effect of the neutrino dipole magnetic moment (MM) on the width of the radiative muon decay is investigated within the standard model (SM) and the left-right model (LRM). It was shown that this decay is an unobservable process from the point of view of the SM. In the LRM there are two kind of diagrams: (i) diagrams caused by the neutrino MM ($\mathcal{M}^n$); (ii) diagrams which do not take into account neutrino MM. The latter involve contributions coming both from virtual charged gauge bosons $\mathcal{M}^W$ and singly charged Higgs boson $\mathcal{M}^h$. At identical values of the model parameters, the contributions of the diagrams $\mathcal{M}^W$ and $\mathcal{M}^h$ are four orders of magnitude greater than the contributions of the diagrams $\mathcal{M}^n$. In this case the experimental upper limit on the radiative muon decay could be obtained under assumption of mass quasidegeneracy in the heavy neutrino sector. Since the contributions of $\mathcal{M}^W$ and $\mathcal{M}^h$ have opposite signs, the situation is possible, however, in which they compensate each other. In this case, the contributions of the diagrams that take into account the neutrino MM become dominant. At specific parameter values that are consistent with experimental data, it is then possible to obtain, for $\mathrm{Br}(\mu^- \to e^-\gamma)$, a value that is equal to the experimental upper limit on this branching ratio.

1 Introduction

The neutrino plays a key role in particle physics and cosmology. For example, neutrino oscillations, whose existence was conclusively confirmed at the SNO [1] and KamLAND boyarkin:KAML neutrino telescopes, are a source of a number of exotic phenomena in the lepton sector, such as resonance transitions, partial and complete flavor violation, CP and CPT violation. The discovery that the neutrino has a mass makes it a natural candidate for the role of a hot-dark-matter particle and enables us to estimate the mean matter density of the Universe, the age of the Universe, and its further fate. Not only does the introduction of heavy neutrinos in the theory help us to explain the smallness of the mass of the left-handed neutrinos via the "see-saw" mechanism, but this also makes it possible to relate baryogenesis with leptogenesis. Also, the neutrino is widely in applied investigations [2]. Neutrino astronomy provides a number of unique opportunities in relation to ordinary astronomy. The basis distinction of the former from the latter is that it carries a nearly invariable information about a progenitorial object. Even at the present time, it is feasible to obtain images (neutrinographs) of some closely lying cosmic objects. One can hope that, in the near future, it will even become possible to obtain neutrinographs of supernovae that belong to the type used to determine the properties of a cosmic vacuum and which lie at enormously large distances. Neutrino geotomography, which studies the internal structure of the Earth by means of a well-controlled neutrino beam, is yet another field of neutrino applications. However, neutrino astronomy and neutrino geotomography are both still in their infancy and will reach maturity only after the properties of the neutrinos are conclusively established and after highresolution neutrino telescopes are created. In the present study, we focus our attention on the neutrino dipole magnetic moment and its influence on the muon properties. The neutrino is a neutral particle, and its total bare Lagrangian does not involve any multipole moments. The appearance of the neutrino dipole magnetic moment is due to neutrino interaction with the vacuum, whose structure is determined by the choice of model. Our investigation will be performed within the standard model of electroweak interactions (SM) and within the theory based on the $SU(2)_L \times SU(2)_R \times U(1)_{B-L}$ gauge group (left-right model) [3]. In the SM supplemented with a $SU(2)_L$ right-handed neutrino singlet, the neutrino is a Dirac particle, the diagonal elements of its dipole magnetic moment being given by [4]

$$\mu_{\nu_l} = \frac{3eG_F}{8\sqrt{2}\pi^2} m_{\nu_l} = 3\times 10^{-19}\mu_B \left(\frac{m_{\nu_l}}{1\ \mathrm{eV}}\right), \qquad (1)$$

where μ_B is the Bohr magneton. By way of example, we indicate that, for the electron neutrino, whose mass is a few eV units according to modern experimental data, the dipole magnetic moment is $\mu_{\nu_e} \sim 10^{-19}\mu_B$ that is, it is of no physical interest. However, upper limits on the neutrino dipole magnetic moment that follow from experimental observations appear to be much higher. Laboratory experiments give the following values at a

e-mail: [a]boyarkin@front.ru

90% C.L. (for an overview, see [5])

$$\mu_{\nu_e} \leq 1.9 \times 10^{-10}\mu_B, \qquad \mu_{\nu_\mu} \leq 6.8 \times 10^{-10}\mu_B, \qquad \mu_{\nu_\tau} \leq 3.9 \times 10^{-7}\mu_B. \tag{2}$$

The left-right model (LRM) involves a set of extra particles not present in the SM. A traditional choice of Higgs sector that ensures the Majorana nature of the neutrino is the bidoublet

$$\Phi\left(\frac{1}{2},\frac{1}{2},0\right)$$

and two triplets

$$\Delta_L(1,0,2), \qquad \Delta_R(0,1,2),$$

where the quantum numbers of the $SU(2)_L, SU(2)_R$, and $U(1)_{B-L}$ gauge groups are indicated parenthetically. Upon spontaneous symmetry breaking, 14 physical Higgs bosons arise in the theory: four doubly charged scalars $\Delta^{(\pm\pm)}_{1,2}$, four singly charged scalars $h^{(\pm)}$ and $\tilde{\delta}^{(\pm)}$, four neutral scalars S_i $(i = 1,2,3,4)$, and two neutral pseudoscalars $P_{1,2}$. Available experimental data admit that some of these bosons have masses at the electroweak scale and that their coupling constants are on the same order of magnitude as the electroweak coupling constants. The LRM also includes three additional gauge bosons, $W_2^\pm$ and Z_2, the $W^\pm_{1,2}$ bosons being related to the W_L and W_R bosons as

$$W_1 = W_L c_\xi - W_R e^{-i\phi} s_\xi, \qquad W_2 = W_L e^{i\phi} s_\xi + W_R c_\xi \tag{3}$$

where W_L and W_R appear in the left- and right-handed currents, respectively; that is,

$$\mathcal{L}^L_{CC} = \frac{g_L}{2\sqrt{2}}\bar{l}(x)\gamma_\lambda(1+\gamma_5)\nu_l(x)W_{L\lambda}(x) + \frac{g_R}{2\sqrt{2}}\bar{l}(x)\gamma_\lambda(1-\gamma_5)N_l(x)W_{R\lambda}(x), \tag{4}$$

where ξ is the mixing angle; $c_\xi = \cos\xi$; $s_\xi = \sin\xi$ and ϕ is the phase that is responsible for CP violation. The theory also involves three extra particles. These are three right-handed neutrinos N_e, N_μ, and N_τ, which are mixtures of the three mass eigenstates $N_{1,2,3}$. It was shown in [6] that one of these heavy neutrinos can have a mass at the electroweak scale. It is obvious that, in the LRM, the contributions of the aforementioned particles lead to changes in the neutrino dipole magnetic moment. For the first time, the non-diagonal elements of the neutrino dipole magnetic moment were calculated in [7], where only the contributions of virtual gauge bosons were taken into account. The dipole magnetic moments $\mu_{\nu_a\nu_b}$ associated with light neutrinos exclusively are on the order of $10^{-22}\mu_B$ and are of no interest from the physical point of view. Thus, we are interested in $\mu_{N_aN_b}$ and $\mu_{N_a\nu_b}$, which are given by

$$\mu_{N_aN_b} \approx \frac{-3eg_L^2(m_{N_a}+m_{N_b})}{2^7\pi^2}\left(\frac{s_\xi^2 m_\tau^2}{m_{W_1}^4} + \frac{c_\xi^2 m_\tau^2}{m_{W_2}^4}\right)\mathrm{Im}\left[V^*_{\tau a}V_{\tau b}\right], \tag{5}$$

$$\mu_{N_a\nu_b} \approx \frac{eg_L^2}{8\pi^2}s_\xi c_\xi \frac{m_\tau}{m_{W_1}^2}\mathrm{Im}\left[e^{-i\phi}V^*_{\tau a}U_{\tau b}\right], \tag{6}$$

where

$$\nu_a = \sum_{l=e,\mu,\tau} U_{al}\nu_l, \qquad N_a = \sum_{l=e,\mu,\tau} V_{al}N_l. \tag{7}$$

We recall that the present-day constraints on the W_2 boson mass and the mixing angle ξ are

$$m_{W_2} \geq 736 \text{ GeV},$$

$$|\xi| < 3\times 10^{-3}.$$

Setting

$$m_{N_a} = m_{N_b} = 1 \text{ TeV}, \qquad \xi = 3\times 10^{-3}, \qquad m_{W_2} = 736 \text{ GeV}, \tag{8}$$

we then obtain the constraints

$$|\mu_{N_aN_b}| < 10^{-13}\mu_B, \qquad |\mu_{N_a\nu_b}| \leq 4\times 10^{-12}\mu_B \tag{9}$$

(hereafter, we assume that $g_L = g_R$). In the LRM, the neutrino can also possess a Dirac nature. In this case, the Higgs sector includes two doublets $\chi_L(2,1,1)$, $\chi_R(1,2,1)$ and one pseudoscalar real singlet $\sigma(1,1,0)$. Upon spontaneous symmetry breaking, the theory has two singly charged and six neutral physical Higgs bosons. In this version of the theory, the diagonal elements of the neutrino dipole magnetic moment are no longer zero and can be considerably larger than non-diagonal elements. The neutrino dipole magnetic moment associated with the heavy neutrino is given by [7]

$$\mu_{N_aN_a}=\frac{3eg_L^2m_{N_a}}{64\pi^2}\left(\frac{s_\xi^2}{m_{W_1}^2}+\frac{c_\xi^2}{m_{W_2}^2}\right)+\frac{eg_L^2}{8\pi^2m_{W_1}^2}s_\xi c_\xi m_\tau\mathrm{Re}(e^{-i\psi}V_{a\tau}^\dagger V_{\tau a}). \tag{10}$$

Substituting the numerical values from (8) into the above formula, we obtain

$$\mu_{N_aN_a}\approx 3.7\times 10^{-9}\mu_B. \tag{11}$$

We note that there are presently no experimental limits on the neutrino dipole magnetic moment of heavy neutrinos.

The objective of the present study is to examine the effect of the neutrino dipole magnetic moment on the radiative muon decay. Without allowance for the electromagnetic properties of the neutrino, this decay width was calculated within the SM [8], in various supersymmetric GUT [9], and in the LRM involving a Majorana neutrino (for an overview, see [10]]).

2 Calculation of branching ratio

In order to seek muon decays through the channel

$$\mu^-\to e^-\gamma \tag{12}$$

the MEGA Collaboration was organized at the Los Alamos Meson Physics Facility (LAMPF, USA). To date, this collaboration obtained the following upper limit on the branching ratio for radiative muon decay [11]:

$$\mathrm{Br}(\mu\to e\gamma)=\frac{\Gamma(\mu\to e\gamma)}{\Gamma(\mu\to\nu_\mu e\overline{\nu}_e)}<1.2\times10^{-11}, \tag{13}$$

where

$$\Gamma(\mu\to e\nu_\mu\overline{\nu}_e)=\frac{G_{\mathrm{F}}^2m_\mu^5}{192\pi^2}. \tag{14}$$

Since 2006, the investigations of decay (12) have been performed by the MEG Collaboration at the Paul Scherrer Institut (Switzerland). The goal of the MEG experiment is to improve the sensitivity in measuring $\mathrm{Br}(\mu\to e\gamma)$ to 10^{-14} [12]. If the decay $\mu\to e\gamma$ is detected in that experiment, it will be possible to measure the angular distribution of decay products and to obtain thereby additional criteria for establishing a true model of electroweak interactions.

First we perform calculation of the radiative muon decay within the LRM. We will use the LRM involving a Dirac neutrino. Let us consider diagrams that are generated by the neutrino dipole magnetic moment (MM). The neutrino MM induces the effective Lagrangian describing the electromagnetic interaction of the neutrino and having the form

$$\mathcal{L}_{\mathrm{eff}}=\sum_{i,k}\left[\mu_{\nu_i\nu_k}\overline{\nu}_i(p)\sigma_{\lambda\tau}q_\tau\nu_k(p')+\mu_{N_iN_k}\overline{N}_i(p)\sigma_{\lambda\tau}q_\tau N_k(p')+\right.$$

$$\left.+\mu_{\nu_iN_k}\overline{\nu}_i(p)\sigma_{\lambda\tau}q_\tau N_k(p')+\mu_{N_i\nu_k}\overline{N}_i(p)\sigma_{\lambda\tau}q_\tau\nu_k(p')\right]A_\lambda(q), \tag{15}$$

where

$$\sigma_{\lambda\tau}=\frac{i}{2}\left(\gamma_\tau\gamma_\lambda-\gamma_\lambda\gamma_\tau\right),\qquad q_\tau=(p'-p)_\tau.$$

For the sake of simplicity, we assume that only the electron and muon neutrinos are mixed, that is,

$$\begin{pmatrix}\nu_{eL}\\ \nu_{\mu L}\\ N_{eR}\\ N_{\mu R}\end{pmatrix}=\mathcal{O}\begin{pmatrix}\nu_1\\ \nu_2\\ N_1\\ N_2\end{pmatrix}, \tag{16}$$

where

$$\mathcal{O}=\begin{pmatrix}U&0\\0&V\end{pmatrix}\begin{pmatrix}c_{\varphi_e}&0&s_{\varphi_e}&0\\0&c_{\varphi_\mu}&0&s_{\varphi_\mu}\\-s_{\varphi_e}&0&c_{\varphi_e}&0\\0&-s_{\varphi_\mu}&0&c_{\varphi_\mu}\end{pmatrix}, \tag{17}$$

$$U=\begin{pmatrix}c_{\theta_\nu}&e^{i\beta_\nu}s_{\theta_\nu}\\-e^{-i\beta_\nu}s_{\theta_\nu}&c_{\theta_\nu}\end{pmatrix},\qquad V=\begin{pmatrix}c_{\theta_N}&e^{i\beta_N}s_{\theta_N}\\-e^{-i\beta_N}s_{\theta_N}&c_{\theta_N}\end{pmatrix}, \tag{18}$$

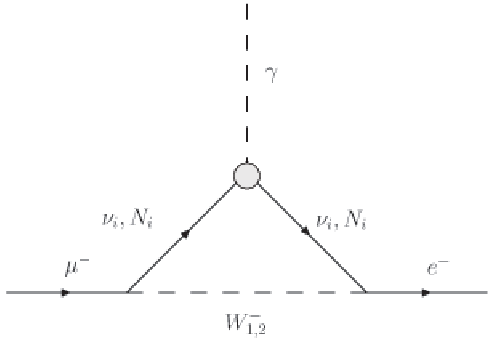

Figure 1.

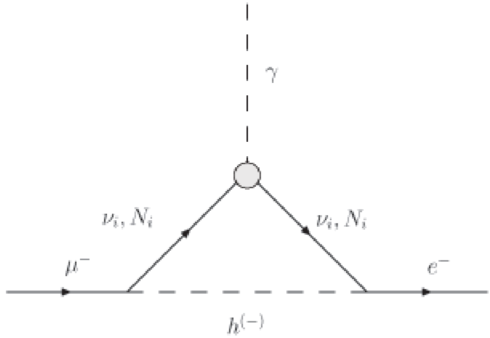

Figure 2.

φ_l is the angle of mixing between the light and heavy neutrinos in the lth generation, θ_ν (θ_N) is the angle of mixing between light (heavy) neutrinos belonging to different generations, $\beta_\nu(\beta_N)$ is the CP violating phase for the light (heavy) neutrino, $s_{\varphi_\mu}=\sin\varphi_\mu, c_{\varphi_\mu}=\cos\varphi_\mu$ etc. We restrict ourselves to determining the contributions of only the diagonal elements of the neutrino dipole magnetic moment. In the third order of perturbation theory, the corresponding Feynman diagrams are shown in Figs.1 and 2. One can see that there are two types of diagrams. The first is induced by the Lagrangians in (4) and (15), while the second is induced by the Lagrangian in (15) and the Lagrangian

$$\mathcal{L}_h^n=[\alpha_{lh\nu_l}\overline{\nu}_l(x)(1-\gamma_5)l(x)+\alpha_{lhN_l}N_l(x)(1+\gamma_5)l(x)]h^+(x). \tag{19}$$

The results of the calculations show that a dominant contribution comes from the diagrams in which the virtual lines are associated with heavy neutrinos. Moreover, only the diagrams involving W_2-boson exchange contribute substantially among all diagrams of the type in Fig.1. Summing the contributions of the diagrams in Figs.1 and 2, we obtain the following expression for the decay width:

$$\Gamma^n(\mu\to e\gamma)=\frac{32m_\mu^5}{(4\pi)^5}\left(I_N^{W_2}c_\xi^2+I_N^h\right)^2(c_{\theta_N}s_{\theta_N})^2. \tag{20}$$

Here, $I_N^{W_2}$ and I_N^h are the contributions of, respectively, the W_2 boson and the Higgs h-boson. Specifically, we have

$$I_N^{W_2}=\frac{g_L^2}{8}\left(D_{N_1}^{W_2}m_{N_1}\mu_{N_1N_1}c^2_{\varphi_\mu}-D_{N_2}^{W_2}m_{N_2}\mu_{N_2N_2}c^2_{\varphi_e}\right),$$

$$I_N^h=\alpha_{ehN}\alpha_{\mu hN}\left(D_{N_1}^{h}m_{N_1}\mu_{N_1N_1}c^2_{\varphi_\mu}-D_{N_2}^{h}m_{N_2}\mu_{N_2N_2}c^2_{\varphi_e}\right),$$

$$\begin{aligned}D_j^{W_k}=\int_0^1\Bigg\{&\frac{2x(1-x)}{b+m_\mu^2x^2}\ln\left|\frac{L_j^{W_k}+b+m_\mu^2x^2}{L_j^{W_k}}\right|+\frac{x(3x-1)}{m^2_{W_k}}\left[\frac{L_j^{W_k}}{b}\ln\left|\frac{L_j^{W_k}+b}{L_j^{W_k}}\right|-\right.\\&\left.-\frac{L_j^{W_k}}{b+m_\mu^2x^2}\ln\left|\frac{L_j^{W_k}+b+m_\mu^2x^2}{L_j^{W_k}}\right|+\ln\left|\frac{L_j^{W_k}+b}{L_j^{W_k}+b+m_\mu^2x^2}\right|\right]+\\&+\frac{m_\mu^2x^3(1-x)}{m^2_{W_k}(b+m_\mu^2x^2)^2}\left(b+m_\mu^2x^2-L_j^{W_k}\ln\left|\frac{L_j^{W_k}+b+m_\mu^2x^2}{L_j^{W_k}}\right|\right)\Bigg\}dx,\end{aligned}$$

$$b=x(m_e^2-m_\mu^2),\qquad L_j^{W_k}=(m_j^2-m^2_{W_k})x+m^2_{W_k},\qquad k=1,2,\qquad j=N_1,N_2,$$

$$D_j^h=\int_0^1\frac{x(1-x)}{b+m_\mu^2x^2}\ln\left|\frac{L_j^h+b+m_\mu^2x^2}{L_j^h}\right|dx,\qquad L_j^h=L_j^{W_k}(m_{W_k}\to m_h).$$

We note that the quantities $I_N^{W_2}$ and I_N^h are of the same sign.

In the LRM, radiative muon decay also receives contributions from the diagrams in Fig.3.

Among these, dominant contributions come from the diagrams involving heavy-neutrino exchanges. The corresponding decay width is given by

$$\Gamma^b(\mu\to e\gamma)=\frac{e^2m_\mu^5}{(4\pi)^5}\left(\mathcal{A}_N^{W_2}c_\xi^2+\mathcal{A}_N^h\right)^2(c_{\theta_N}s_{\theta_N})^2, \tag{21}$$

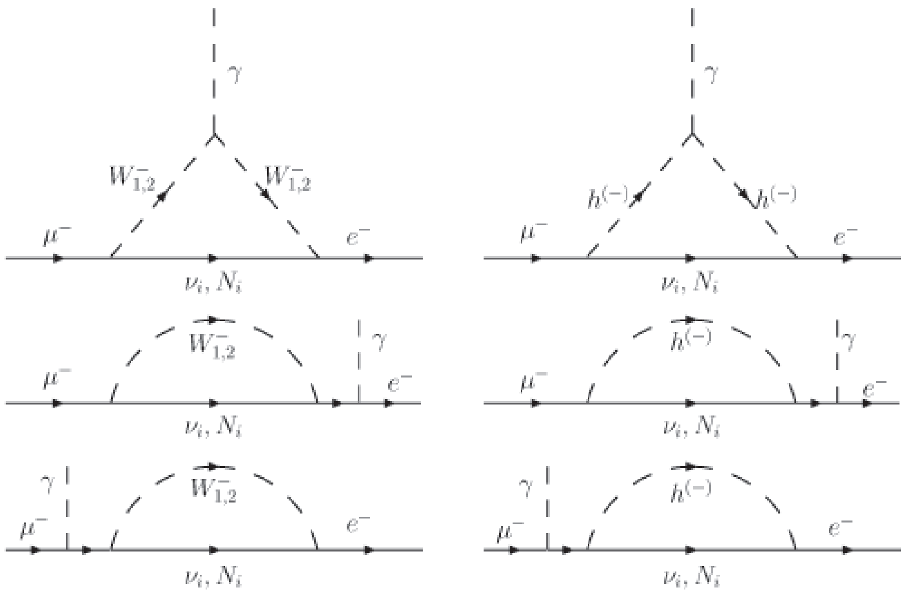

Figure 3.

where $\mathcal{A}_N^{W_2}$ and $\mathcal{A}_N^h$ are determined by the diagrams involving a W_2^- boson and a Higgs boson $h^{(-)}$, respectively. Specifically, we have

$$\mathcal{A}_N^{W_2} = \frac{g_L^2}{2}\left(B_{N_1}^{W_2}c^2_{\varphi_\mu} - B_{N_2}^{W_2}c^2_{\varphi_e}\right), \qquad \mathcal{A}_N^h = 4\alpha_{ehN_e}\alpha_{\mu hN_\mu}\left(B_{N_1}^h c^2_{\varphi_\mu} - B_{N_2}^h c^2_{\varphi_e}\right),$$

$$B_j^{W_k} = -\int_0^1 \left[\frac{x^2}{b+m_\mu^2x^2}\ln\left|\frac{L^j_{W_k}+b+m_\mu^2x^2}{L^j_{W_k}}\right| + \frac{x^2(1-2x)}{(b+m_\mu^2x^2)^2}\left(b+m_\mu^2x^2 - \right.\right.$$

$$\left.\left. -L^j_{W_k}\ln\left|\frac{L^j_{W_k}+b+m_\mu^2x^2}{L^j_{W_k}}\right|\right)\right]dx, \qquad L^j_{W_k} = (m^2_{W_k}-m_j^2)x + m_j^2,$$

$$B_j^h = \int_0^1 \frac{x^2(1-x)}{(b+m_\mu^2x^2)^2}\left(b+m_\mu^2x^2 - L_h^j\ln\left|\frac{L_h^j+b+m_\mu^2x^2}{L_h^j}\right|\right)dx, \qquad L_h^j = L^j_{W_k}(m_{W_k}\to m_h).$$

Because the sign of $\mathcal{A}_N^{W_2}$ is opposite to the sign of $\mathcal{A}_N^h$, the interference between the diagrams associated with charged gauge bosons and the diagrams generated by singly charged Higgs bosons is destructive. From expressions (20) and (21), it follows that the widths $\Gamma^n(\mu\to e\gamma)$ and $\Gamma^b(\mu\to e\gamma)$ are functions of $\Delta m_{ij} = m_i - m_j$, that decreases with decreasing Δm_{ij} and are zero in the limit of degenerate heavy neutrino masses.

In order to find the expression for the radiative decay width of the muon in the SM supplemented with an $SU(2)_L$ right-handed neutrino singlet, we must set $\mathcal{A}_N^h$ to zero in (21) and perform the following substitutions there:

$$B_{N_1}^{W_2}\to B_{\nu_1}^{W_1}, \qquad B_{N_2}^{W_2}\to B_{\nu_2}^{W_1}, \qquad \varphi_\mu,\varphi_e,\xi\to 0, \qquad \theta_N\to\theta_\nu. \tag{22}$$

Setting $\Delta m_\nu = m_{\nu_1} - m_{\nu_2} = 10^{-3}$ eV and taking into account relation (14), we obtain a hopelessly small value of $(\mathrm{Br}^b)^{SM}(\mu\to e\gamma)\sim 10^{-50}$. The inclusion of the neutrino MM does not change situation. Indeed, one can easily see that, upon making in (20) the substitutions

$$D_{N_1}^{W_2}\to D_{\nu_1}^{W_1}, \qquad D_{N_2}^{W_2}\to D_{\nu_2}^{W_1}, \qquad \varphi_\mu,\varphi_e,\xi\to 0, \qquad \theta_N\to\theta_\nu \tag{23}$$

and setting $I_N^h = 0$, the result becomes

$$(\mathrm{Br}^n)^{SM}(\mu\to e\gamma)\approx 4\times 10^{-47}.$$

Using Eqs.(20) and (21), one can obtain the expression for the radiative-decay width in the model relying on the same gauge group as the SM and involving two doublets of Higgs fields (2HDM). In this case, we must make, in the above formulas, the substitutions specified in Eqs.(22) and (23) and employ, in $\mathcal{A}_N^h$, 2HDM parameters

— namely, the H^- boson mass; the leptonic couplings of the H^- boson $\alpha_{lH\nu_l}$ and neutrino-magnetic-moment value of about $10^{-10}\mu_B$. An analysis shows that, in this case, the branching ratio for radiative muon decay is so small that this process cannot be detected experimentally. It follows that, from the point of view of the SM involving a Dirac neutrino, muon radiative decay is an unobservable effect.

It turns out that, at identical values of the model parameters, the contributions of gauge and Higgs bosons are on average four orders of magnitude greater than the contributions of the neutrino dipole MM. It should be stressed to obtain values in the range $\mathrm{Br}(\mu \to e\gamma) < 1.2 \times 10^{-11}$ it is necessary to have quasidegeneracy in the heavy neutrino sector.

However, there is one important case where the contributions of the neutrino MM play a leading role. Since $\mathcal{A}_N^{W_2}$ and $\mathcal{A}_N^h$ have opposite signs, they can cancel each other. One can readily show that, under the condition

$$4\alpha_{ehN_e}\alpha_{\mu hN_\mu}\int_0^1 (x^2-x^3)\left[\frac{c^2_{\varphi_\mu}}{L_h^{N_1}}-\frac{c^2_{\varphi_e}}{L_h^{N_2}}\right]dx \approx g_L^2\int_0^1 (x^2-x^3)\left[\frac{c^2_{\varphi_\mu}}{L_{W_2}^{N_1}}-\frac{c^2_{\varphi_e}}{L_{W_2}^{N_2}}\right]dx \qquad (24)$$

the width $\Gamma^b(\mu \to e\gamma)$ vanishes. In this case, an analysis reveals that, if only the term $I_N^{W_2}$ is taken into account in (20), a value of 10^{-12} or less can be obtained for branching ratio for radiative muon decay in the experimentally allowed region of the parameters of the left-right model [21]. But if I_N^h is on the same order of magnitude as $I_N^{W_2}$, $\mathrm{Br}^n(\mu \to e\gamma)$ may reach values of order 10^{-11}.

3 Conclusion

The objective of the present study was to determine the effect of the neutrino MM on the properties of the muon in the SM and in the LRM. We have investigated the radiative muon decay taking into account the neutrino MM. In the LRM involving a Dirac neutrino, this decay is described in the third order of perturbation theory by Feynman diagrams of two classes: (i) diagrams involving the neutrino electromagnetic vertex (Figs.1 and 2, $\mathcal{M}^n$) and (ii) diagrams disregarding the electromagnetic properties of the neutrino (Fig.3). The set of the latter diagrams in turn can be partitioned into diagrams involving virtual charged gauge bosons ($\mathcal{M}^W$) and diagrams involving a virtual singly charged Higgs boson ($\mathcal{M}^h$). It has been shown that, both in the SM supplemented with an $SU(2)_L$ right-handed neutrino singlet and in the SM supplemented with two doublets of Higgs fields, the branching ratio for the radiative muon decay is negligible. In other words, radiative muon decay is an unobservable process from the point of view of the SM. In the LRM involving a Dirac neutrino, the situation is the following. At identical values of the model parameters, the contributions of the diagrams in Fig.3 are four orders of magnitude greater than the contributions of the diagrams in Figs.1 and 2 ($\mathcal{M}^n$). In this case we can obtain the experimental upper limit on the radiative muon decay only under assumption of mass quasidegeneracy in the heavy neutrino sector. Since the contributions of $\mathcal{M}^W$ and $\mathcal{M}^h$ have opposite signs, the situation is possible, however, in which they compensate each other. In this case, the contributions of the diagrams that take into account the neutrino MM become dominant. At specific parameter values that are consistent with experimental data, it is then possible to obtain, for $\mathrm{Br}(\mu^- \to e^-\gamma)$, a value that is equal to the experimental upper limit on this branching ratio.

References

[1] Q. R. Ahmad *et al.* [SNO Collab.] Phys. Rev. Lett. **87**, 071301 (2001); **89**, 011301, 011302 (2002). boyarkin:KAML K. Eguchi *et al.* [KamLAND Collab.] Phys. Rev. Lett. **90**, 021802 (2003).

[2] O. M . Boyarkin, Physics of Massive Neutrinos, 2nd ed.(URSS, Moscow, 2006) [in Russian].

[3] R. N. Mohapatra and J. C. Pati, Phys. Rev. D **11**, 566 (1975); R. N. Mohapatra and G. Senjanovic, Phys. Rev. D **23**, 165 (1981); O. M. Boyarkin, Phys. Rev. D **50**, 2247 (1994).

[4] W. J. Marciano and A. I. Sanda, Phys. Lett. B **67**, 303 (1977); B. W. Lee and R. E. Shrock, Phys. Rev. D **16**, 1444 (1977).

[5] M. C. Gonzalez-Garcia and M. Maltoni, Phys. Rep. **460**, 1 (2008).

[6] O. M. Boyarkin, G. G. Boyarkina, Phys. Rev. D **70**, 113010 (2004).

[7] R. E. Shrock, Nucl. Phys. B **206**, 359 (1982); M. A. B. Beg , W. J. Marciano, and M. Ruderman, Phys. Rev. D **17**, 1395 (1978).

[8] T. P. Cheng and L. F. Li, Phys. Rev. D **16**, 1425 (1977); S. T. Petkov, Yad. Fiz. **25**, 641 (1977) [Sov. J. Nucl. Phys. **25**, 340 (1977)].

[9] F. Borzumati and A. Masiero, Phys. Rev. Lett. **57**, 961 (1986); K. Huitu, J. Maalampi, M. Raidal, and A. Santamaria, Phys. Lett. B **430**, 355 (1998).

[10] A. G. Akeroyd, M. Aoki, and Y. Okada, Phys. Rev. D **76**, 013004 (2007).

[11] M. L. Brooks *et al.* [MEGA Collab.], Phys. Rev. Lett. **83**, 1521 (1999).

[12] Y. Hisamatsu, Eur. Phys. J. C **52**, 477 (2007).

Proceedings of the International School-seminar
"New Physics and Quantum Chromodynamics at external Conditions", pp. 15 – 22,
3-6 May 2009, Dnipropetrovsk, Ukraine

QUARK GLUON PLASMA BAGS AS REGGEONS

K. A. Bugaev[a]

Bogolyubov Institute for Theoretical Physics, Kiev, Ukraine

Within an exactly solvable model I discuss the influence of the medium dependent finite width of quark gluon plasma (QGP) bags on their equation of state. It is shown that the large width of the QGP bags not only explains the observed deficit in the number of hadronic resonances, but also clarifies the reason why the heavy QGP bags cannot be directly observed as metastable states in a hadronic phase. I show how the model allows one to estimate the minimal value of the width of QGP bags being heavier than 2.5 GeV from a variety of the lattice QCD data and to get the minimal resonance width at zero temperature of about 600 MeV. The Regge trajectories of large and heavy QGP bags are established both in a vacuum and in a strongly interacting medium. It is shown that at high temperatures the average mass and width of the QGP bags behave in accordance with the upper bound of the Regge trajectory asymptotics (the linear asymptotics), whereas at low temperatures (below a half of the Hagedorn temperature T_H [1]) they obey the lower bound of the Regge trajectory asymptotics (the square root one). Thus, for temperatures below $T_H/2$ the spin of the QGP bags is restricted from above, whereas for temperatures above $T_H/2$ these bags demonstrate the typical Regge behavior consistent with the string models.

1 Introduction

Recently several ground shaking results in statistical mechanics of strongly interacting matter are obtained [2, 3, 4, 5, 6]. All of them are derived within the exactly solvable models. In [2, 3, 4, 5, 6] the surface tension of large QGP bags was included into the statistical description of the QGP equation of state (EOS). Such an inclusion not only allowed one to formulate the analytically solvable statistical models for the QCD tricritical [2] and critical [6] endpoint, but also to develop the finite width model of QGP bags [3, 4, 5] and to bring up the statistical description of the QGP EOS to a qualitatively new level of realism by establishing the Regge trajectories of heavy/large QGP bags both in a vacuum and in a medium [4, 5] using the lattice QCD data.

Here I would like to summarize the main results obtained in [2, 3, 4, 5, 6] and discuss the theoretical and experimental perspectives to study the properties of the strongly interacting matter EOS.

2 From the MIT Bag Model EOS to Finite Width Model

From its birth and up to now the MIT bag model [7] remains one of the most popular model EOS to describe the confinement phenomenon of the color degrees of freedom. It gives a very simple picture of a color confinement by considering the freely moving massless quarks and gluons inside the bubble with negative pressure, $-B_{bag}$, (for vanishing baryonic charge). Then the total pressure of a bag is

$$p_{bag} \;\equiv\; \sigma T^4 - B_{bag}\,, \quad \varepsilon_{bag} \;\equiv\; T \frac{d\,p_{bag}}{d\,T} - p_{bag} \;=\; 3\,\sigma T^4 + B_{bag}\,, \tag{1}$$

where $3\,\sigma$ is the usual Stefan-Boltzmann constant which can be trivially found for a given number of elementary degrees of freedom. The non-trivial feature of the bag model EOS is that the vacuum pressure, $-B_{bag}$, generates positive and large contribution to the bag energy density ε_{bag}.

In addition to a simplicity of the EOS (1) its other attractive features are based on the fact that the bag model also leads [8] to the Hagedorn mass spectrum of bags which was the first signal about the new physics above the Hagedorn temperature T_H. The easiest way to understand a special role of the Hagedorn mass spectrum, i.e. an exponentially increasing with mass m density of hadronic states $\rho_H(m) \sim exp\left(\frac{m}{T_H}\right)$ for $m \gg T_H$, is to consider the microcanonical ensemble of the test particles being in a thermal contact with the resonance of the exponential spectrum [9]. Then one can easily show that the exponential spectrum behaves as the perfect thermostat and perfect particle reservoir, i.e. it imparts its temperature T_H to particles which are in thermal contact with it and forces them to be in chemical equilibrium [9]. Therefore there is simply no reason to study such a system in the canonical ensemble or in grand canonical ensemble, i.e. to bring it into the contact with an external thermostat that has other temperature than T_H, since two thermostats of different

e-mail: [a]bugaev@th.physik.uni-frankfurt.de

temperatures cannot be in equilibrium. Perhaps these properties can explain the fast chemical equilibration of hadrons in an expanding fireball [10].

The first successful statistical model explaining the deconfinement phase transition (PT) from hadronic matter to QGP, gas of bags model (GBM) [8], is based on the MIT bag model and it interprets such a PT as a formation of the infinitely large bag. Further development in this direction led to many interesting findings [11, 12, 13], including an exact analytical solution for finite systems with a PT [11], but the most promising results were obtained only recently. The most hopeful of them are an inclusion of the quark gluon bags surface tension into statistical description [2, 6] and taking into account the finite width of large/heavy QGP bags [3, 4, 5]. Thus, the surface tension of QGP bags introduced in the quark gluon bag with surface tension model (QGBSTM) allows one to simultaneously describe the 1-st and 2-nd order deconfinement PT with the cross-over and generate the tricritical (QGBSTM1) [2] or critical endpoint (QGBSTM2) [6] at the vanishing value of the surface tension coefficient as required for the PT of liquid-vapor type [14, 15]. The finite width model (FWM) [3, 4, 5] naturally resolved *two conceptual problems* which, so far, were ignored by other statistical approaches for almost three decades: on one hand, the volume dependent width of large QGP bags easily explains a huge deficit in the number of observed hadronic resonances [16] with masses above 2.5 GeV predicted by the Hagedorn model [1] and used, so far, by the GBM and all its followers; and, on the other hand, the FWM shows that there is an inherent property of the strongly interacting matter EOS, the *subthreshold suppression*, which prevents the appearance of large QGP bags and strangelets inside of the hadronic phase even as metastable states in finite systems which are studied in nuclear laboratories. The latter effect explains the negative results of searches for strangelets and for not too heavy QGP bags, say with the mass of $10-15$ GeV, in various physical processes.

The most convenient way to study the phase structure of any statistical model similar to the GBM or QGBSTM is to use the isobaric partition [2, 6] and find its rightmost singularities. Hence, I assume that after the Laplace transform the FWM grand canonical partition $Z(V,T)$ generates the following isobaric partition:

$$\hat{Z}(s,T) \equiv \int\limits_0^\infty dV \exp(-sV)\ Z(V,T) = \frac{1}{[s - F(s,T)]}\,, \qquad (2)$$

where the function $F(s,T)$ contains the discrete F_H and continuous F_Q mass-volume spectrum of the bags

$$F(s,T) \equiv F_H(s,T) + F_Q(s,T) = \sum_{j=1}^{n} g_j e^{-v_j s}\phi(T,m_j) = + \int\limits_{V_0}^\infty dv \int\limits_{M_0}^\infty dm\ \rho(m,v)\exp(-sv)\,\phi(T,m)\ . \qquad (3)$$

The density of bags of mass m_k, eigen volume v_k and degeneracy g_k is given by $\phi_k(T) \equiv g_k\ \phi(T,m_k)$ with

$$\phi_k(T) \equiv \frac{g_k}{2\pi^2}\int\limits_0^\infty p^2 dp\ \exp\left[-\tfrac{(p^2\ +\ m_k^2)^{1/2}}{T}\right] = g_k \frac{m_k^2 T}{2\pi^2}\ K_2\left(\tfrac{m_k}{T}\right). \qquad (4)$$

The mass-volume spectrum $\rho(m,v)$ is the generalization of the exponential mass spectrum introduced by Hagedorn [1]. Similar to the GBM, the QGBSTM1 and the QGBSTM2, the FWM bags are assumed to have the hard core repulsion of the Van der Waals type which generates the suppression factor proportional to the exponential $\exp(-sv)$ of bag eigen volume v.

The first term of Eq. (3), F_H, represents the contribution of a finite number of low-lying hadron states up to mass $M_0 \approx 2.5$ GeV [3] which correspond to different flavors. This function has no s-singularities at any temperature T and can generate only a simple pole of the isobaric partition, whereas the mass-volume spectrum of the bags $F_Q(s,T)$ is chosen to generate an essential singularity $s_Q(T) \equiv p_Q(T)/T$ which defines the QGP pressure $p_Q(T)$ at zero baryonic densities [2]. Very recently our group discovered [6] absolutely new way to generate the rightmost singularity of the QGP which is a simple pole too. The latter is achieved by matching the deconfinement PT curve in the baryonic chemical potential and temperature plane with the curve of vanishing surface tension coefficient [6].

Here I use the parameterization of the spectrum $\rho(m,v)$ introduced in [3]. It assumes that

$$\rho(m,v) = \frac{\rho_1(v)\ N_\Gamma}{\Gamma(v)\ m^{a+\frac{3}{2}}}\exp\left[\tfrac{m}{T_H} - \tfrac{(m-Bv)^2}{2\Gamma^2(v)}\right], \quad \text{with} \quad \rho_1(v) = f(T)\,v^{-b}\ \exp\left[-\tfrac{\sigma(T)}{T}\,v^{\kappa}\right]. \qquad (5)$$

In fact, the FWM divides all hadrons into two groups depending on their width: the long (short) living hadrons belong to F_H (to F_Q). As one can see from (5) the mass spectrum has a Hagedorn like parameterization and the Gaussian attenuation around the bag mass Bv (B is the mass density of a bag of a vanishing width) with the volume dependent Gaussian width $\Gamma(v)$ or width hereafter. I will distinguish it from the true width defined as $\Gamma_R = \alpha\,\Gamma(v)$ ($\alpha \equiv 2\sqrt{2\ln 2}$). It is necessary to stress that the Breit-Wigner attenuation of a resonance mass cannot be used in the spectrum (5) because in case of finite width it would lead to a divergency of the mass integral in (2) or temperatures above T_H [3, 4, 5].

The normalization factor is defined as

$$N_\Gamma^{-1} \;=\; \int\limits_{M_0}^{\infty} \frac{dm}{\Gamma(v)} \exp\left[-\tfrac{(m-Bv)^2}{2\Gamma^2(v)}\right]. \tag{6}$$

Such a choice of mass-volume spectrum (5) is a natural extension of early attempts [11, 12, 13] to explore the bag volume as a statistically independent degree of freedom to derive an internal pressure of large bags. As it will be shown below such a simple parameterization not only allows one to resolve both of the conceptual problems discussed above, but, what is very important, it also gives us an exactly solvable model.

The volume spectrum in (5) contains the surface free energy ($\kappa = 2/3$) with the T-dependent surface tension which is parameterized as $\sigma(T) = \sigma_0 \cdot \left[\frac{T_c - T}{T_c}\right]^{2k+1}$ ($k = 0, 1, 2, ...$) [2, 17], where $\sigma_0 > 0$ can be a smooth function of temperature. For T being not larger than the (tri)critical temperature T_c such a parameterization is justified by the usual cluster models like the FDM [14, 18] and SMM [19, 20, 21], whereas the general consideration for any T can be driven by the surface partitions of the Hills and Dales model [17]. In Refs. [2, 6] it is argued that at low baryonic densities the first order deconfinement phase transition degenerates into a cross-over just because of negative surface tension coefficient for $T > T_c$. The other consequences of such a surface tension parameterization and the discussion of the absence of the curvature free energy in (5) can be found in [2, 5, 22].

The spectrum (5) has a simple form, but is rather general since both the width $\Gamma(v)$ and the bag mass density B can be medium dependent. It clearly reflects the fact that the QGP bags are similar to the ordinary quasiparticles with the medium dependent characteristics (life-time, most probable values of mass and volume). Now one can readily derive the infinite bag pressure for two choices of the width: the volume independent width $\Gamma(v) \equiv \Gamma_0$ and the volume dependent width $\Gamma(v) \equiv \Gamma_1 = \gamma v^{\frac{1}{2}}$. As will be seen below the latter resolves both of the conceptual problems discussed earlier, whereas the former parameterization I use for a comparison.

3 Subthreshold Suppression of Large and Heavy QGP Bags

Consider first the free bags. For large bag volumes ($v \gg M_0/B > 0$) the factor (6) can be found as $N_\Gamma \approx 1/\sqrt{2\pi}$. Similarly, one can show that for heavy free bags ($m \gg BV_0$, $V_0 \approx 1$ fm^3 [3], ignoring the hard core repulsion and thermostat)

$$\rho(m) \;\equiv \int\limits_{V_0}^{\infty} dv\, \rho(m,v) \;\approx\; \frac{\rho_1(\frac{m}{B})}{B\; m^{a+\frac{3}{2}}} \exp\left[\tfrac{m}{T_H}\right]. \tag{7}$$

It originates in the fact that for heavy bags the Gaussian in (5) acts like a Dirac δ-function for either choice of Γ_0 or Γ_1. Thus, the Hagedorn form of (7) has a clear physical meaning and, hence, it gives an additional argument in favor of the FWM. Also it gives an upper bound for the volume dependence of $\Gamma(v)$: the Hagedorn-like mass spectrum (7) can be derived, if for large v the width Γ increases slower than $v^{(1-\kappa/2)} = v^{2/3}$.

Similarly to (7), one can estimate the width of heavy free bags averaged over bag volumes and get $\overline{\Gamma(v)} \approx \Gamma(m/B)$. Thus, for $\Gamma_1(v)$ the mass spectrum of heavy free QGP bags must be the Hagedorn-like one with the property that heavy resonances have to develop the large mean width $\Gamma_1(m/B) = \gamma\sqrt{m/B}$ and, hence, they are hardly observable. Applying these arguments to the strangelets, I conclude that, if their mean volume is a few cubic fermis or larger, they should survive a very short time, which is similar to the results of Ref. [23] predicting an instability of such strangelets.

Note also that such a mean width is essentially different from both the linear mass dependence of string models [24] and from an exponential form of the nonlocal field theoretical models [25]. Nevertheless, as it will be demonstrated while discussing the Regge trajectories, the mean width $\Gamma_1(m/B)$ leads to the linear Regge trajectory of heavy free QGP bags for large values of the invariant mass squared.

Next let's calculate $F_Q(s,T)$ (3) for the spectrum (5) performing the mass integration. There are, however, two distinct possibilities, depending on the sign of the most probable mass:

$$\langle m \rangle \;\equiv\; Bv + \Gamma^2(v)\beta\,, \quad \text{with} \quad \beta \equiv T_H^{-1} - T^{-1}\,. \tag{8}$$

If $\boldsymbol{\langle m \rangle > 0}$ for $v \gg V_0$, one can use the saddle point method for mass integration to find the function $F_Q(s,T)$

$$F_Q^{+}(s,T) \approx \left[\frac{T}{2\pi}\right]^{\frac{3}{2}} \int\limits_{V_0}^{\infty} dv\; \frac{\rho_1(v)}{\langle m \rangle^a}\; \exp\left[\tfrac{(p^+ - sT)v}{T}\right] \tag{9}$$

and the pressure of large bags

$$p^+ \equiv T\left[\beta B + \frac{\Gamma^2(v)}{2v}\beta^2\right], \quad \text{for} \quad \Gamma(v) = \Gamma_1(v) \quad \Rightarrow \quad p^+ = T\left[\beta B + \frac{1}{2}\gamma^2\beta^2\right] \tag{10}$$

To get (9) one has to use in (3) an asymptotic form of the K_2-function $\phi(T,m) \simeq (mT/2\pi)^{3/2}\exp(-m/T)$ for $m \gg T$, collect all terms with m in the exponential, get a full square for $(m - \langle m \rangle)$ and make the Gaussian integration.

Since for $s < s^*_Q(T) \equiv p^+(v \to \infty)/T$ the integral (9) diverges at its upper limit, the partition (2) has an essential singularity that corresponds to the QGP pressure of an infinite large bag. One concludes that the width Γ cannot grow faster than $v^{1/2}$ for $v \to \infty$, otherwise $p^+(v \to \infty) \to \infty$ and $F^+_Q(s,T)$ diverges for any s. Thus, for $\boldsymbol{\langle m \rangle > 0}$ the phase structure of the FWM with $\Gamma(v) = \Gamma_1(v)$ is similar to the QGBSTM1 [2], but it can be also reformulated to have the phase structure of QGBSTM2 [6] by proper choice of the surface tension temperature dependence and value of the index $\tau > 2$. Comparing the v power of the exponential pre-factor in (9) to the continuous volume spectrum of bags of the QGBSTM1 and QGBSTM2, one finds that $a + b \equiv \tau$. The volume spectrum of bags $F^+_Q(s,T)$ (9) is of general nature and has a clear physical meaning. Choosing different T dependent functions $\langle m \rangle$ and $\Gamma^2(v)$, one obtains different equations of state.

It is possible to use the spectrum (9) not only for infinite system volumes, but also for finite volumes $V \gg V_0$. In this case the upper limit of integration should be replaced by finite V (see Refs. [11, 12] for details). This will change the singularities of partition (2) to a set of simple poles $s^*_n(T)$ in the complex s-plane which are defined by the same equation as for $V \to \infty$. Similarly to the finite V solution of the GBM [11, 12], it can be shown that for finite T the FWM simple poles may have small positive or even negative real part which would lead to a non-negligible contribution of the QGP bags into the total spectrum $F(s,T)$ (3). In other words, if the spectrum (9), was the only volume spectrum of the QGP bags, then there would exist a finite (non-negligible) probability to find heavy QGP bags ($m \gg M_0$) in finite systems at low temperatures $T \ll T_c$. Therefore, using the results of the finite volume GBM and SMM, one should conclude that the spectrum (9) itself cannot explain the absence of the QGP bags at $T \ll T_c$ and, hence, an alternative explanation of this fact is required.

Such an explanation corresponds to the case $\boldsymbol{\langle m \rangle \le 0}$ for $v \gg V_0$. From (8) one can see that for the volume dependent width $\Gamma(v) = \Gamma_1(v)$ the most probable mass $\langle m \rangle$ inevitably becomes negative at low T, if $0 < B < \infty$. In this case the maximum of the Gaussian mass distribution is located at resonance masses $m = \langle m \rangle \le 0$. This is true for any argument of the K_2-function in $F_Q(s,T)$ (3). Since the lower limit of mass integration M_0 lies above $\langle m \rangle$, then only the tail of the Gaussian mass distribution may contribute into $F_Q(s,T)$. A thorough inspection of the integrand in $F_Q(s,T)$ shows that above M_0 it is strongly decreasing function of resonance mass and, hence, only the vicinity of the lower limit of mass integration M_0 sizably contributes into $F_Q(s,T)$. Applying the steepest descent method and the K_2-asymptotic form for $M_0 T^{-1} \gg 1$ one obtains

$$F^-_Q(s,T) \approx \left[\frac{T}{2\pi}\right]^{\frac{3}{2}} \int\limits_{V_0}^{\infty} dv \frac{\rho_1(v) N_\Gamma\, \Gamma(v)\, \exp\left[\frac{(p^- - sT)v}{T}\right]}{M_0^a \left[M_0 - \langle m \rangle + a\,\Gamma^2(v)/M_0\right]}, \quad \text{with} \quad p^-\big|_{v \gg V_0} = \frac{T}{v}\left[\beta M_0 - \frac{(M_0 - Bv)^2}{2\,\Gamma^2(v)}\right] \tag{11}$$

where p^- defines the pressure of QGP bag.

It is necessary to stress that the last result requires $B > 0$ and it cannot be obtained for a weaker v-growth than $\Gamma(v) = \Gamma_1(v)$. Indeed, if $B < 0$, then the normalization factor (6) would not be $1/\sqrt{2\pi}$, but would become $N_\Gamma \approx [M_0 - \langle m \rangle]\,\Gamma^{-1}(v) \exp\left[\frac{(M_0 - Bv)^2}{2\,\Gamma^2(v)}\right]$ and, thus, it would cancel the leading term in pressure (11). Note, however, that the inequality $\boldsymbol{\langle m \rangle \le 0}$ for all $v \gg V_0$ with positive B and finite $p^-(v \to \infty)$ is possible for $\Gamma(v) = \Gamma_1(v)$ only. In this case the pressure of an infinite bag is

$$p^-(v \to \infty) = -T\,\frac{B^2}{2\,\gamma^2}\,. \tag{12}$$

Also it is necessary to point out that the only width $\Gamma(v) = \Gamma_1(v)$ does not lead to any divergency of the bag pressure in thermodynamic limit. This is clearly seen from Eqs. (10) and (11) since the multiplier $\Gamma^2(v)$ stands in the numerator of the pressure (10), whereas in the pressure (11) it appears in the denominator. Thus, if one chooses the different v-dependence for the width, then either p^+ or p^- would diverge for the bag of infinite size.

The new outcome of this case with $B > 0$ is that for $T < T_H/2$ [3, 4, 5] the spectrum (11) contains the lightest QGP bags having the smallest volume since every term in the pressure p^- (11) is negative. The finite volume of the system is no longer important because only the smallest bags survive in (11). Moreover, if such bags are created, they would have mass about M_0 and the width about $\Gamma_1(V_0)$, and, hence, they would not be distinguishable from the usual low-mass hadrons. Thus, the case $\boldsymbol{\langle m \rangle \le 0}$ with $B > 0$ leads to the *subthreshold suppression of the QGP bags* at low temperatures, since their most probable mass is below the mass threshold M_0 of the spectrum $F_Q(s,T)$. Note that such an effect cannot be derived within any of the GBM-kind models proposed earlier. The negative values of $\langle m \rangle$ that appeared in the expressions above serve as an indicator of a different physical situation comparing to $\langle m \rangle > 0$, but have no physical meaning since $\langle m \rangle \le 0$ does not enter the main physical observable p^-.

The obtained results give us a unique opportunity to make a bridge between the particle phenomenology, some experimental facts and the LQCD. For instance, if the most probable mass of the QGP bags is known along with the QGP pressure, one can estimate the width of these bags directly from Eqs. (10) and (11). To demonstrate the new possibilities let's now consider several examples of the QGP EOS and relate them to the above results. First, let's study the possibility of getting the MIT bag model pressure $p_{bag} \equiv \sigma T^4 - B_{bag}$ [7] by the stable QGP bags, i.e. $\Gamma(v) \equiv 0$. Equating the pressures p^+ and p_{bag}, one finds that the Hagedorn temperature is related to a bag constant $B_{bag} \equiv \sigma T_H^4$. Then the mass density of such bags $\frac{\langle m \rangle}{v}$ is identical to

$$B = \sigma T_H (T + T_H)(T^2 + T_H^2)\,, \tag{13}$$

and, hence, it is always positive. Thus, the MIT bag model EOS can be easily obtained within the FWM, but, as was discussed earlier, such bags should be observable.

The key point of the width estimation is based on the fact that the low T pressure (12) resembles the linear T dependent term in the LQCD pressure reported by several groups (for the full list of references see [4]). In [4] it is argued that the ansatz

$$B(T) = \sigma T_H^2 (T^2 + T T_H + T_H^2)\,, \tag{14}$$

not only gives the simplest possibility to fulfill all the necessary requirements to the mass density of QGP bags, but it also reproduces the LQCD pressure. Moreover, comparing ansatz (14) with the mass density (13) obtained for the pure MIT bag model pressure, one can see that they differ only by a term $\sigma T_H T^3$ which at low $T \leq 0.5\, T_H$ is a negligible correction to (14). Therefore, for low T the ansatz (14) looks quite reasonable because in this region it corresponds to the mass density of the most popular EOS of modern QCD phenomenology.

Using (14) it was possible to find out that the true width is independent for the number of quark flavors and of the color group number and is $\Gamma_R(V_0, T = 0) \approx 1.22\, V_0^{\frac{1}{2}}\, T_c^{\frac{5}{2}} \alpha \approx 600$ MeV and $\Gamma_R(V_0, T = T_H) = \sqrt{12}\, \Gamma_R(V_0, T = 0) \approx 2000$ MeV. These estimates clearly demonstrate that there is no way to detect the decays of such short living QGP bags even, if they are allowed by the subthreshold suppression.

4 Asymptotic Behavior of the QGP Bag Regge Trajectories

The behavior of the width of hadronic resonances was extensively studied almost forty years ago in the Regge poles method what was dictated by an intensive analysis of the strongly interaction dynamics in high energy hadronic collisions. A lot of effort was put forward [26, 27, 28] to elucidate the asymptotical behavior of the resonance trajectories $\alpha(S)$ for $|S| \to \infty$ (S is an invariant mass square in the reaction). Since the Regge trajectory determines not only the mass of resonances, but their width as well, it is worth to compare these results with the FWM predictions. Note that nowadays there is great interest in the behavior of the Regge trajectories of higher resonances in the context of the 5-dimensional string theory holographically dual to QCD [29] which is known as AdS/CFT.

In what follows I use the results of Ref. [28] which is based on the following most general assumptions: (I) $\alpha(S)$ is an analytical function, having only the physical cut from $S = S_0$ to $S = \infty$; (II) $\alpha(S)$ is polynomially restricted at the whole physical sheet; (III) there exists a finite limit of the phase trajectory at $S \to \infty$. Using these assumptions, it was possible to prove [28] that for $S \to \infty$ the upper bound of the Regge trajectory asymptotics at the whole physical sheet is

$$\alpha_u(S) = -g_u^2\, [-S]^{\nu}\ , \quad \text{with} \quad \nu \leq 1\,, \tag{15}$$

where the function $g_u^2 > 0$ should increase slower than any power in this limit and its phase must vanish at $|S| \to \infty$.

On the other hand, in Ref. [28] it was also shown that, if in addition to (I)-(III) one requires that the transition amplitude $T(s,t)$ is a polynomially restricted function of S for all nonphysical $t > t_0 > 0$, then the real part of the Regge tragectory does not increase at $|S| \to \infty$ and the trajectory behaves as

$$\alpha_l(S) = g_l^2 \left[-\, [-S]^{\frac{1}{2}} + C_l \right]\,, \tag{16}$$

where $g_l^2 > 0$ and C_l are some constants. Moreover, (16) defines the lower bound for the asymptotic behavior of the Regge trajectory [28]. The expression (16) is a generalization of a well known Khuri result [30]. It means that for each family of hadronic resonances the Regge poles do not go beyond some vertical line in the complex spin plane. In other words, it means that in asymptotics $S \to +\infty$ the resonances become infinitely wide, i.e. they are moving out of the real axis of the proper angular momentum J and, therefore, there are only a finite number of resonances in the corresponding transition amplitude. At first glance it seems that the huge deficit of heavy hadronic resonances compared to the Hagedorn mass spectrum supports such a conclusion. Since there is a finite number of resonance families [31] it is impossible to generate from them an exponential mass spectrum and, hence, the Hagedorn mass spectrum cannot exist for large resonance masses. Consequently, the GBM and its followers run into a deep trouble. However, it was possible to show [4] that the FWM with negative value of the most probable bag mass $\langle m \rangle \leq 0$ can help to resolve this problem as well.

Note that the direct comparison of the FWM predictions with the Regge poles asymptotics is impossible because the resonance mass and its width $\Gamma(v)$ are independent variables in the FWM. Nevertheless, one can relate their average values and compare them to the results of Ref. [28]. To illustrate this statement, let's recall the result on the mean Gaussian width of the free bags averaged with respect to their volume by the spectrum (7) (see two paragraphs after Eq. (7) for details)

$$\overline{\Gamma_1(v)} \approx \Gamma_1(m/B) = \gamma \sqrt{\frac{m}{B}}\,. \tag{17}$$

Using the formalism of [28], it can be shown that at zero temperature the free QGP bags of mass m and mean resonance width $\alpha\,\overline{\Gamma_1(v)}|_{T=0} \approx \alpha\,\gamma_0 \sqrt{\frac{m}{B_0}}$ precisely correspond to the following Regge trajectory

$$\alpha_r(S) = g_r^2 [S + a_r (-S)^{\frac{3}{4}}] \quad \text{with} \quad a_r = const < 0\,, \tag{18}$$

with $\gamma_0 \equiv \gamma(T=0)$ and $B_0 \equiv B(T=0)$ from (14). Indeed, using $S = |S| e^{i\,\phi_r}$ in (18), and expanding the second term on the right hand side of (18) and requiring $\mathrm{Im}\,[\alpha_r(S)] = 0$, one finds the phase of physical trajectory (one of four roots of one fourth power in (18)), which is vanishing in the correct quadrant of the complex S-plane, and going to the complex energy plane $E = \sqrt{S} \equiv M_r - i\frac{\Gamma_r}{2}$, one can also determine the mass M_r and the width Γ_r

$$\phi_r(S) \rightarrow \frac{a_r \sin\frac{3}{4}\pi}{|S|^{\frac{1}{4}}} \rightarrow 0^-\,, \quad M_r \approx |S|^{\frac{1}{2}} \quad \text{and} \quad \Gamma_r \approx -|S|^{\frac{1}{2}} \phi_r(S) = \frac{|a_r||S|^{\frac{1}{4}}}{\sqrt{2}} = \frac{|a_r| M_r^{\frac{1}{2}}}{\sqrt{2}}\,, \tag{19}$$

of a resonance belonging to the trajectory (18).

Comparing the mass dependence of the width in (19) with the mean width of free QGP bags (17) taken at $T = 0$, it is natural to identify them

$$a_r^{free} \approx -\alpha\,\gamma_0 \sqrt{\frac{2}{B_0}} = -4\,\gamma_0 \sqrt{\frac{\ln 2}{B_0}}\,, \tag{20}$$

and to deduce that the free QGP bags belong to the Regge trajectory (18). Such a conclusion is in line both with the well established results on the linear Regge trajectories of hadronic resonances [31] and with theoretical expectations of the dual resonance model [32], the open string model [33, 24], the closed string model [33] and the AdS/CFT [29]. Such a property of the FWM also gives a very strong argument in favor of both the volume dependent width $\Gamma(v) = \Gamma_1(v)$ and the corresponding mass-volume spectrum of heavy bags (5).

Next I consider the second way of averaging the mass-volume spectrum with respect to the resonance mass

$$\overline{m}(v) \;\equiv\; \int\limits_{M_0}^{\infty} dm \int \frac{d^3k}{(2\pi)^3}\, \rho(m,v)\; m\; e^{-\frac{\sqrt{k^2+m^2}}{T}} \left[\int\limits_{M_0}^{\infty} dm \int \frac{d^3k}{(2\pi)^3}\, \rho(m,v)\; e^{-\frac{\sqrt{k^2+m^2}}{T}} \right]^{-1}\,, \tag{21}$$

which is technically easier than averaging with respect to the resonance volume. The latter can be found in [4].

Using the results of Sect. 3 one can find the mean mass (21) for $T \geq 0.5\,T_H$ (or for $\langle m \rangle \geq 0$) to be equal to the most probable mass of bag from which one determines the resonance width:

$$\overline{m}(v) \approx \langle m \rangle \quad \text{and} \quad \Gamma_R(v) \approx 2\sqrt{2\ln 2}\;\Gamma_1\!\left[\frac{\langle m \rangle}{B + \gamma^2 \beta}\right] = 2\,\gamma \sqrt{\frac{2\ln 2\,\langle m \rangle}{B + \gamma^2 \beta}}\,. \tag{22}$$

These equations lead to a vanishing ratio $\frac{\Gamma_R}{\langle m \rangle} \sim \langle m \rangle^{-\frac{1}{2}}$ in the limit $\langle m \rangle \rightarrow \infty$. Comparing (22) with the mass and width (19) of the resonances described by the Regge trajectory (18) and applying absolutely the same logic which was used for the free QGP bags, I conclude that the location of the FWM heavy bags in the complex energy plane is identical to that one of resonances belonging to the trajectory (18) with

$$\langle m \rangle \approx |S|^{\frac{1}{2}} \quad \text{and} \quad a_r \approx -4\gamma \sqrt{\frac{\ln 2}{B + \gamma^2 \beta}}\,. \tag{23}$$

The most remarkable output of such a conclusion is that the medium dependent FWM mass and width of the extended QGP bags obey the upper bound for the Regge trajectory asymptotic behavior obtained for point-like hadrons [28]!

The extracted values of the resonance width coefficient along with the relation (14) for $B(T)$ allow us to estimate a_r as

$$a_r \approx -4 \sqrt{\frac{2\,T\,T_H}{2\,T - T_H} \ln 2}\,. \tag{24}$$

This expression shows that for $T \to T_H/2{+}0$ the asymptotic behavior (18) breaks down since the resonance width diverges at fixed $|S|$. I think such a behavior can be studied at NICA (Dubna) and/or FAIR (GSI, Darmstadt) energies. This can be seen from the following estimates. From (24) it follows that $a_r^2(T = T_H) \approx 22.18\, T_H$ and $a_r^2(T \gg T_H) \approx 11.09\, T_H$. In other words, for a typical value of the Hagedorn temperature $T_H \approx 190$ MeV (24) gives a reasonable range of the invariant mass $|S|^{\frac{1}{2}} \gg a_r^2(T = T_H) \approx 4.21$ GeV and $|S|^{\frac{1}{2}} \gg a_r^2(T \gg T_H) \approx 2.1$ GeV for which Eq. (18) is true. But then at $|S|^{\frac{1}{2}} \approx a_r^2(T = T_H) \approx 4.21$ GeV the asymptotic behavior (18) should be broken down and, hence, one may see the *resonances widening* at fixed S values and decreasing T.

Now it is possible to find the spin of the FWM resonances $J = \mathrm{Re}\, \alpha_r(\langle m\rangle^2) \;\approx g_r^2 \, \langle m\rangle \left[\langle m\rangle - \frac{a_r^2}{4}\right]$, which has a typical Regge behavior up to a small correction. Such a property can also be obtained within the dual resonance model [32], within the models of open [33] and closed string [33, 24], and within AdS/CFT [29]. These models support the relation between the spin and mass and justify it. Note, however, that in addition to the spin value the FWM determines the width of hadronic resonances. The latter allows one to predict the ratio of widths of two resonances having spins J_2 and J_1 and appearing at the same temperature T to be as follows

$$\Gamma_R\left[\frac{\langle m\rangle\big|_{J_2}}{(B+\gamma^2\beta)}\right]\left[\Gamma_R\left[\frac{\langle m\rangle\big|_{J_1}}{(B+\gamma^2\beta)}\right]\right]^{-1} \approx \sqrt{v|_{J_2}}\left[\sqrt{v|_{J_1}}\right]^{-1} \approx \sqrt{\langle m\rangle\big|_{J_2}}\left[\sqrt{\langle m\rangle\big|_{J_1}}\right]^{-1} \approx \left[\frac{J_2}{J_1}\right]^{\frac{1}{4}}, \qquad (25)$$

which, perhaps, can be tested at LHC.

Now let's analyze the low temperature regime, i.e. $T \leq 0.5 T_H$. Using previously obtained results from (21) one finds

$$\overline{m}(v) \;\approx\; M_0 \,, \qquad (26)$$

i.e. the mean mass is volume independent. Taking the limit $v \to \infty$, one gets the ratio $\frac{\Gamma(v)}{\overline{m}(v)} \to \infty$ which closely resembles the case of the lower bound of the Regge trajectory asymptotics (16). Similarly to the analysis of high temperature regime, from (16) one can find the trajectory phase and then the resonance mass M_r and its width Γ_r

$$\phi_r(S) \to -\pi + \frac{2|C_l||\sin(\arg C_l)|}{|S|^{\frac{1}{2}}}\,, \quad M_r \approx |C_l||\sin(\arg C_l)| \quad \text{and} \quad \Gamma_r \approx 2|S|^{\frac{1}{2}}\,. \qquad (27)$$

Again comparing the averaged masses and width of FWM resonances with their counterparts in (27), one finds a similar behavior in the limit of large width of resonances. Therefore, I conclude that at low temperatures the FWM obeys the lower bound of the Regge trajectory asymptotics of [28].

The above estimates demonstrate that at any temperature the FWM QGP bags can be regarded as the medium induced Reggeons which at $T \leq 0.5T_H$ (i.e. for $\langle m\rangle \leq 0$) belong to the Regge trajectory (16) and otherwise they are described by the trajectory (18). Of course, both of the trajectories (16) and (18) are valid in the asymptotic $|S| \to \infty$, but the most remarkable fact is that, to my knowledge, the FWM gives us the first example of a model which reproduces both of these trajectories and, thus, obeys both bounds of the Regge asymptotics. Moreover, since the FWM contains the Hagedorn-like mass spectrum at any temperature, the subthreshold suppression of QGP bags removes the contradiction between the Hagedorn ideas on the exponential mass spectrum of hadrons and the Regge poles method in the low temperature domain! Furthermore, the FWM opens a possibility to apply the Regge poles method to a variety of processes in a strongly interacting matter and account, at least partly, for some of the medium effects.

5 Conclusions

Here I present the novel statistical approach to study the QGP bags with medium dependent width. It is a further extension of the ideas formulated in [34]. I argue that the volume dependent width of the QGP bags $\Gamma(v) = \gamma\, v^{\frac{1}{2}}$ leads to the Hagedorn mass spectrum of heavy bags. Such behavior of a width allows us to explain a huge deficit of heavy hadronic resonances in the experimental mass spectrum compared to the Hadegorn model predictions. The key point of our treatment is the presence of Gaussian attenuation of bag mass.

Then it is shown that the Gaussian mass attenuation also allows one to "hide" the heavy QGP bags for $T \leq 0.5\, T_H$ by their *subthreshold suppression.* The latter occurs due to the fact that at low temperatures the most probable mass of heavy bags $\langle m\rangle$ becomes negative and, hence, is below the lower cut-off M_0 of the continuous mass spectrum. Consequently, only the lightest bags of mass about M_0 and of smallest volume V_0 may contribute into the resulting spectrum, but such QGP bags will be indistinguishable from the low-lying hadronic resonances with the short life-time. On the other hand the large minimal width, about 600 MeV, of bags being heavier than M_0 and large than V_0 prevents their experimental behavior for $T > 0.5\, T_H$, even, if they are allowed by the subthreshold suppression. Thus, the FWM naturally explains the absence of directly observable QGP bags and strangelets in the high energy nuclear and elementary particle collisions even as metastable states in hadronic phase.

Using the formalism of [28] it was shown that the average mass and width of heavy/large free QGP bags belong to the linear Regge trajectory (18). Similarly, it was found that at hight temperatures the average mass and width of the QGP bags behave in accordance with the upper bound of the Regge trajectory asymptotics (15) (linear trajectory), whereas at low temperatures they obey the lower bound of the Regge trajectory asymptotics (16) (square root trajectory). Such results create a new look onto the large and/or heavy QGP bags as the medium induced Reggeons and provide us with an alternative to the AdS CFT picture on the QGP bags. I would like to stress that it can be used not only to describe the deconfinement or cross-over and the corresponding phases, but for the metastable states of strongly interacting matter as well. Also as shown above such a coherent picture not only introduces new time scale into the heavy ion physics, but also naturally explains the existence of the tricritical or critical QCD endpoint due to the vanishing of the surface tension coefficient. Therefore, I am sure that further development of such a reach direction will lead to the major shift of the low energy paradigm of heavy ion physics and will shed light on the modification of the QCD (tri)critical endpoint properties in finite systems.

Acknowledgements. The research made in this work was supported in part by the Program “Fundamental Properties of Physical Systems under Extreme Conditions” of the Bureau of the Section of Physics and Astronomy of the National Academy of Science of Ukraine. This work was also supported in part by the Fundamental Research State Fund of Ukraine, Project No F28.2/014.

References

[1] R. Hagedorn, Suppl. Nuovo Cimento **3**, 147 (1965).
[2] K. A. Bugaev, Phys. Rev. **C 76**, 014903 (2007); Phys. Atom. Nucl. **71**, 1585 (2008); arXiv:0711.3169.
[3] K. A. Bugaev, V. K. Petrov and G. M. Zinovjev, Europhys. Lett. **85**, 22002 (2009); arXiv:0801.4869.
[4] K. A. Bugaev, V. K. Petrov and G. M. Zinovjev, Phys. Rev. **C 79**, 054913 (2009).
[5] K. A. Bugaev arXiv:0809.1023 [nucl-th].
[6] K. A. Bugaev, V. K. Petrov and G. M. Zinovjev, arXiv:0904.4420 [hep-ph].
[7] A. Chodos *et. al.*, Phys. Rev. **D 9**, 3471 (1974).
[8] J. I. Kapusta, Phys. Rev. **D 23**, 2444 (1981).
[9] L. G. Moretto, K. A. Bugaev, J. B. Elliott and L. Phair, Europhys. Lett. **76**, 402 (2006); arXiv:hep-ph/0511180; and K. A. Bugaev, J. B. Elliott, L. G. Moretto and L. Phair, arXiv:hep-ph/0504011.
[10] C. Greiner *et al.*, J. Phys. **G 31**, S725 (2005); C. Greiner, P. Koch-Steinheimer, F. M. Liu, I. A. Shovkovy and H. Stöcker, arXiv:nucl-th/0703079.
[11] K. A. Bugaev, Phys. Part. Nucl. **38**, (2007) 447; Acta Phys. Pol. **B 36**, 3083 (2005).
[12] K. A. Bugaev and P. T. Reuter, Ukr. J. Phys. **52**, (2007) 489.
[13] I. Zakout, C. Greiner, J. Schaffner-Bielich, Nucl. Phys. **A 781**, 150 (2007).
[14] M. E. Fisher, Physics **3**, 255 (1967).
[15] L. D. Landau and E.M. Lifshitz, *Statistical Physics*, (Fizmatlit, Moscow, 2001).
[16] W. Broniowski, W. Florkowski and L. Y. Glozman, Phys. Rev. **D 70**, 117503 (2004).
[17] K. A. Bugaev, L. Phair and J. B. Elliott, Phys. Rev. **E 72**, 047106 (2005); K. A. Bugaev and J. B. Elliott, Ukr. J. Phys. **52** (2007) 301.
[18] for a review see J. B. Elliott, K. A. Bugaev, L. G. Moretto and L. Phair, arXiv:nucl-ex/0608022.
[19] J. P. Bondorf *et al.*, Phys. Rep. **257**, 131 (1995).
[20] K. A. Bugaev, M. I. Gorenstein, I. N. Mishustin and W. Greiner, Phys. Rev. **C 62**, 044320 (2000); nucl-th/0007062; Phys. Lett. **B 498**, 144 (2001); nucl-th/0103075 and references therein.
[21] P. T. Reuter and K. A. Bugaev, Phys. Lett. **B 517**, 233 (2001).
[22] L. G. Moretto *et al.*, Phys. Rev. Lett. **94**, 202701 (2005); PoS CPOD2006:037 (2006).
[23] S. Yasui and A. Hosaka, Phys. Rev. **D 74**, 054036 (2006).
[24] see, for instance, I. Senda, Z. Phys. **C 55**, 331 (1992).
[25] A. C. Kalloniatis, S. N. Nedelko and L. Smekal, Phys. Rev. **D 70**, 094037 (2004) and references therein.
[26] for more references see M. Ida, Prog. Theor. Phys. **40**, 901 (1968).
[27] R. W. Childers, Phys. Rev. Lett. **21**, 868 (1968).
[28] A. A. Trushevsky, Ukr. J. Phys. **22**, 353 (1977).
[29] see, for instance, A. Karch *et al.,* Phys. Rev. **D 74**, 015005 (2006).
[30] N. N. Khuri, Phys. Rev. Lett. **18**, 1094 (1967).
[31] P. D. B. Collins, *An Introduction to Regge Theory and High-Energy Physics*, (Cambridge University Press, Cambridge, 1977).
[32] G. Veneziano, Nuovo Cim. **57**, 190 (1968).
[33] E. V. Shuryak, Prog. Part. Nucl. Phys. **62**, 48 (2009).
[34] D. B. Blaschke and K. A. Bugaev, Fizika **B 13**, 491 (2004); Prog. Part. Nucl. Phys. **53**, 197 (2004).

Proceedings of the International School-seminar
"New Physics and Quantum Chromodynamics at external Conditions", pp. 23 – 30,
3-6 May 2009, Dnipropetrovsk, Ukraine

VERY STRONG MAGNETIC FIELDS IN LATTICE QCD

P. V. Buividovich [1,2,a], M. N. Chernodub [3,4,2,b], E. V. Luschevskaya [1,2,c], M. I. Polikarpov [2,d]

[1] JIPNR "Sosny", National Academy of Science, Acad. Krasin str. 99, Minsk, 220109 Belarus
[2] Institute for Theoretical and Experimental Physics, B. Cheremushkinskaya 25, Moscow, 117218 Russia
[3] Laboratoire de Mathematiques et Physique Theorique, CNRS UMR 6083, Fédération Denis Poisson, Université de Tours, Parc de Grandmont, 37200, France
[4] Department of Mathematical Physics and Astronomy, University of Gent, Krijgslaan 281, S9, B-9000 Gent, Belgium

We discuss our recent results demonstrating that very strong external magnetic fields lead to (1) the enhancement of the chiral symmetry breaking [the quark condensate rises with the increase of the external magnetic field]; (2) the chiral magnetization of the QCD vacuum [spins of the quarks turn parallel to the external field]; (3) the chiral magnetic effect [a CP-odd generation of the electric current of quarks directed along the magnetic field].

1 Introduction

Noncentral heavy-ion collisions may create very strong magnetic field due to relative motion of electrically charged ions and the products of the collision. This fact ignited the interest of the scientific community towards an investigation of the properties of the strongly interacting matter exposed to the magnetic field. The QCD effects should be visible because the strength of the created magnetic field may be of the order of the hadron-scale, or higher. For example, at first moments ($\tau \sim 1\,\mathrm{fm/c}$) of Au-Au collision at Relativistic Heavy Ion Collider (RHIC) the strength of the magnetic field may reach $eB \sim (10-100\,\mathrm{MeV})^2$ [1, 2]. The strong magnetic fields will also be created in the future experiments at Facility for Antiproton and Ion Research (FAIR) at GSI, ALICE experiment at LHC, and at Nuclotron-based Ion Collider fAcility (NICA) at Dubna.

There are various vacuum effects associated which appear due to the presence of the strong magnetic fields (here we do not discuss interesting effects that may appear in a dense quark matter). Theoretically, the very strong magnetic fields may significantly modify the QCD phase diagram [3, 4, 5]. The magnetic fields increases the transition temperature and enhances the strength of the (phase) transition from the chirally broken (low temperature) phase to the chirally restored (high temperature) phase. Moreover, in the external magnetic field the transition – which is a smooth crossover in the absence of the fields – becomes a first order transition [3, 4, 5].

Also, the magnetic field stabilizes the chirally broken (low-temperature) phase of QCD enlarging the value of the chiral condensate and enhancing the chiral symmetry breaking. This result was obtained in various approaches using the chiral perturbation theory [6, 8], the Nambu-Jona-Lasinio model [9, 10, 11], the linear sigma model [12] and the AdS/QCD dual description [13]. In lattice simulations this effect was observed in our recent work [29]. In Section 3 we discuss essential results of [29].

Another effect of the strong enough magnetic field is a (para)magnetic response of the QCD vacuum: the external fields polarize the magnetic moments of the quarks and antiquarks, leading to appearance of the chiral magnetization of the vacuum. At relatively low magnetic fields the chiral magnetization is proportional to the strength of the magnetic field. The coefficient of the proportionality, the chiral magnetic susceptibility, was first discussed in Ref. [14] in order to analyze phenomenologically interesting nucleon magnetic moments. The value of the magnetic susceptibility – which was estimated using various analytical approaches [15, 16, 17, 18, 19, 21, 22, 23, 24] – can be measured in experiments on lepton pair photoproduction [25, 26], in radiative heavy meson decays [27] etc. As the strength of the field increases, the magnetization deviates from a linear function as it gets affected by logarithmic corrections [28]. At very strong fields the magnetization reaches an upper bound. The first lattice investigation of the chiral magnetization was performed in Ref. [30] (we discuss them in Section 4).

The magnetic fields may also lead to quite unusual effects due to nontrivial topological structure of the QCD vacuum [1, 31, 32, 33]. We discuss a particular realization of the Chiral Magnetic Effect (CME), which leads to a generation of an *electric* current along the direction of the *magnetic* field in a nontrivial topological backgrounds of gluons [1, 31]. The CME leads to a non-statistical asymmetry in the number of positively and negatively charged particles emitted on different sides of the reaction plane in the heavy ion collisions [34]. There are preliminary indications that this $\mathcal{CP}$-odd effect has been indeed observed by the STAR collaboration in experiments at RHIC [35, 36]. In our lattice studies we found the existence of the CME both at thermalized

e-mail: [a]buividovich@itep.ru, [b]maxim@itep.ru, [c]luschevskaya@itep.ru, [d]polykarp@itep.ru

ensembles of gluon fields and at specially prepared configurations with nontrivial topological charge [37]. A brief account of our results [37] is given in Section 5.

2 Physical setup and technical details of simulations

We utilize lattice QCD with the simplest $SU(2)$ gauge group because all studied effects originate in the chiral sector of QCD so that the number of colors is not crucial. In our simulations only valence quarks interact with the electromagnetic field, and the effects of the virtual quarks on gluons are neglected. Indeed, the inclusion of dynamical (sea) quarks makes the simulations computationally difficult, while the essential features of all mentioned effects remains intact in the quenched limit as well (an extended discussion is given in [29, 30, 37, 39]).

The chiral effects are best studied with massless fermions. In order to implement chirally symmetric massless fermions on the lattice, we use Neuberger's overlap Dirac operator [40]. We reduce the ultraviolet lattice artifacts using the tadpole-improved Symanzik action for the gluons. We introduce the magnetic field $B_\mu = B\delta_{\mu 3}$ into the Dirac operator by substituting $su\,(2)$-valued vector potential A_μ with $u\,(2)$-valued field. In infinite volume such substitution is,

$$A_\mu^{ij} \to A_\mu^{ij} + C_\mu \delta^{ij}\,, \qquad C_\mu = \frac{B}{2}\left(x_2\delta_{\mu 1} - x_1\delta_{\mu 2}\right)\,, \tag{1}$$

where C_μ is the $U(1)$ field. In the finite volume L^4 with periodic boundary conditions an additional x-dependent boundary twist for the fermion fields should be introduced [41], and the uniform magnetic field is forced to take quantized values [42],

$$qB = \frac{2\pi\, k}{L^2}\,, \qquad k \in \mathbb{Z}\,, \qquad q = \frac{1}{3}\,|e|\,, \tag{2}$$

where q is the absolute value of the electric charge of the d-quark. Note that in all Figures of this article we indicate the magnetic field strength in units of $qB \equiv eB/3$ and not in eB. In our simulations the *lowest* magnetic field takes values $\sqrt{eB} \sim (400 - 600\,\mathrm{MeV})^2$. Such fields are stronger than those expected at RHIC, while they are of the same order compared to the fields that will presumably be created at the LHC collisions [2].

In order to check the finite-volume effects we use two spatial lattice volumes, 14^3 and 16^3. We study the system at three different temperatures, $T/T_c = 0$, 0.82, 1.12 (the critical temperature in $SU(2)$ gauge theory is $T_c \approx 310\,\mathrm{MeV}$). In order to make sure that the influence of the finite ultraviolet cutoff is under proper control, we utilize three lattice spacings, $a = 0.089\,\mathrm{fm}$, $0.103\,\mathrm{fm}$, $0.128\,\mathrm{fm}$. Our spatial volumes are $L^3 = [(1.4\ldots2)\,\mathrm{fm}]^3$.

3 Enhancement of chiral condensate

The chiral condensate

$$\Sigma \equiv -\langle 0|\,\bar{q}q\,|0\rangle\,, \tag{3}$$

is commonly used order parameter for the chiral symmetry breaking in the theory with massless quarks. The condensate is zero if the chiral symmetry is unbroken. If the strength of magnetic field is larger than the pion mass (which is zero for massless quarks) but is still much smaller than the hadronic scale, one can use the chiral perturbation theory to calculate the field dependence of the chiral condensate. According to the original work [6], in a leading order in B, the chiral condensate $\Sigma\,(B)$ rises linearly with the field strength:

$$\Sigma\,(B) = \Sigma\,(0)\left(1 + \frac{eB\ln 2}{16\pi^2 F_\pi^2}\right)\,, \tag{4}$$

where $F_\pi \approx 130\,\mathrm{MeV}$ is the pion decay constant. The corrections due to nonvanishing pion mass may also be calculated [8].

The condensate (3) can be calculated using the Banks-Casher formula [43],

$$\Sigma = \lim_{\lambda\to 0}\lim_{V\to\infty}\frac{\pi\rho\,(\lambda)}{V} \tag{5}$$

where V is the total four-volume of Euclidean space-time. The density $\rho\,(\lambda)$ of eigenvalues λ_n of the Dirac operator $\mathcal{D} = \gamma^\mu\,(\partial_\mu - iA_\mu)$ is defined by

$$\mathcal{D}\psi_n = \lambda_n\psi_n\,, \qquad \rho\,(\lambda) = \langle\sum_n \delta\,(\lambda - \lambda_n)\rangle\,, \tag{6}$$

where ψ_n are the eigenmodes of the Dirac operator.

According to Eq. (5) the enhancement of the chiral condensate in the magnetic field means that the Dirac eigenvalues in the vicinity of $\lambda = 0$ should become denser as the magnetic fields increases. In order to check

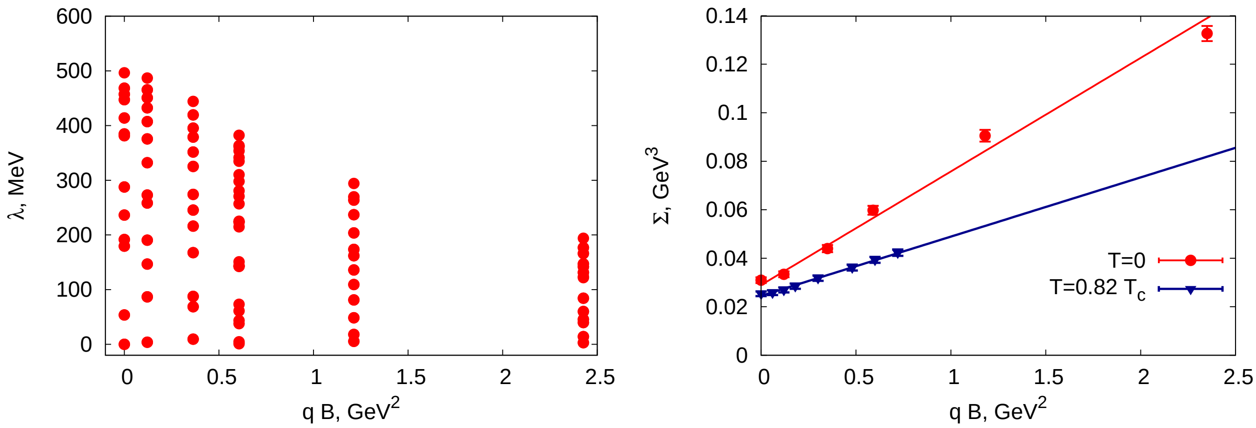

Figure 1. (left) Lowest twelve eigenvalues (including a zero mode) of the Dirac operator in a background of a typical gluon configuration *vs.* the magnetic field qB. (right) The chiral condensate *vs.* qB at two different temperatures T. The solid lines are the linear fits by the function (7). Figures are from Ref. [29].

this fact we plot in Figure 1(left) the dependence of lowest Dirac eigenvalues on the strength of the magnetic field. One can clearly see that the stronger the field, the smaller eigenvalues of the Dirac operator and the larger the density of the near-zero modes. This configuration has topological charge equal to one, and therefore the configuration contains one exact zero mode, $\lambda = 0$, in agreement with the Atyah-Singer theorem. The presence of the zero mode does not depend on the strength of the external field because the number of zero Dirac eigenmodes is equal to the topological charge of the gauge field configuration, while the topological charge is not affected by the Abelian magnetic field.

In Figure 1(right) we show the chiral condensate as the function of the magnetic field qB at zero temperature and at $T = 0.82\,T_c$. Following (4) we fit the chiral condensate by the linear function,

$$\Sigma\,(B) = \Sigma_0 \left(1 + \frac{eB}{\Lambda_B^2}\right)\,, \tag{7}$$

where Σ_0 and Λ_B are the fitting parameters.

The best fits are shown in Figure 1(right) by the solid lines. The best fit parameters at zero and nonzero temperatures are [29]:

$$T = 0: \qquad \Sigma_0^{\rm fit} = [(320 \pm 5)\ {\rm MeV}]^3\,, \qquad \Lambda_B^{\rm fit} = (1.53 \pm 0.11)\,{\rm GeV}, \tag{8}$$

$$T = 0.82\,T_c: \qquad \Sigma_0^{\rm fit} = [(291 \pm 1)\ {\rm MeV}]^3\,, \qquad \Lambda_B^{\rm fit} = (1.74 \pm 0.03)\,{\rm GeV}. \tag{9}$$

We see that the increase of temperature leads to a decrease the chiral condensate (as expected), and to a decrease the slope of the B-dependence.

The zero-field zero-temperature best fit value (8) of the chiral condensate, $\Sigma_0^{\rm fit}$, agrees very well with other numerical estimations in quenched $SU(2)$ gauge theory [44]. Surprisingly, the numerical value of the slope parameter Λ_B is quite close to the $T = 0$ result of the chiral perturbation theory (4), Ref. [6]:

$$\Lambda_B^{\rm th} = \frac{4\pi F_\pi}{\sqrt{\ln 2}} = 1.97\,{\rm GeV}\,. \tag{10}$$

The similarity between the theoretical prediction (10) and first principle $T = 0$ result (8) should be taken with care. Firstly, we are studying the quenched theory, in which the virtual charged pions are absent, and what we observe is the effect of the gauge fields. Secondly the strength of our weakest magnetic fields is still greater than the scale imposed by the zero-field chiral condensate, $\Sigma_0^{1/3}$. In this regime the prediction (4) of Ref. [6] should not work, in general, as the linear behavior is expected to be realized for much weaker fields. Thus, the observed linear enhancement of the chiral condensate even in the absence of the pion loops is intriguing feature of the non-Abelian gauge theory.

4 Magnetization of QCD vacuum

Quarks are spin-1/2 particle carrying magnetic moments. The magnetic moments are polarized by the external magnetic field. A natural quantitative measure of the polarization is given by the expectation value:

$$\langle \bar\Psi \Sigma_{\alpha\beta} \Psi \rangle = \chi(F)\, \langle \bar\Psi \Psi \rangle\, qF_{\alpha\beta}\,, \tag{11}$$

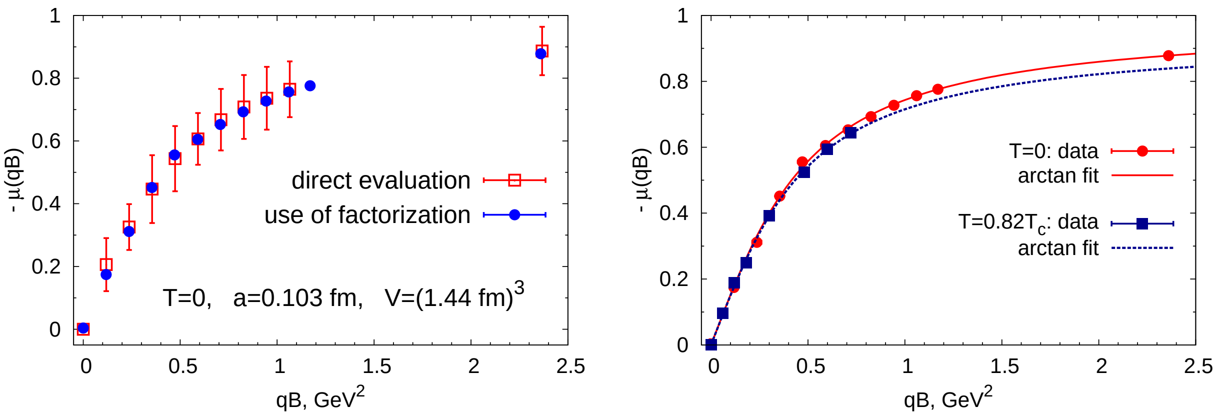

Figure 2. The magnetization μ *vs.* the magnetic field, qB. (left) Check of the factorization (14): the empty squares and the full circles show the nonfactorized (13) and factorized (15) definitions, respectively. (right) The magnetization μ at two temperatures. The lines correspond to the best fits (17). Figures are from Ref. [30].

where $\Sigma_{\alpha\beta} = \frac{1}{2i}[\gamma_\alpha\gamma_\beta - \gamma_\beta\gamma_\alpha]$ is the relativistic spin operator, $F_{\mu\nu} = \partial_\mu a_\nu - \partial_\nu a_\mu$ is the strength tensor of the electromagnetic field. Note that flavor and spinor indices are omitted in (11). Below we consider one quark flavor for simplicity.

The right hand side of Eq. (11) is proportional to the electromagnetic field strength tensor due to the Lorenz covariance. The proportionality to the chiral condensate $\langle\bar\Psi\Psi\rangle$ (evaluated at the external electromagnetic field F) allows us to disentangle nonlinear effects of the enhancement of the chiral condensate in the external magnetic field (discussed in the previous Section) from the effects of the quark's spin polarization. The strength of the vacuum polarization is characterized by a chiral magnetic susceptibility $\chi(F)$.

The (chiral) magnetization of the QCD vacuum in the external magnetic field $B = F_{12} = -F_{21}$ can be described by the dimensionless quantity

$$\mu(qB) = \chi(qB)\, qB \qquad \Longleftrightarrow \qquad \langle\bar\Psi\Sigma_{12}\Psi\rangle = \mu(qB)\langle\bar\Psi\Psi\rangle\,. \tag{12}$$

In [30] we derived a magnetization analogue of the Banks-Casher formula (5):

$$\langle\bar\Psi\Sigma_{\alpha\beta}\Psi\rangle = \lim_{\lambda\to 0}\Bigl\langle \frac{\pi\nu(\lambda)}{V}\int d^4x\, \psi^\dagger_\lambda(x)\,\Sigma_{\alpha\beta}\,\psi_\lambda(x)\Bigr\rangle\,. \tag{13}$$

Moreover, we have proven theoretically in [30] and also checked numerically, that the following factorization rule holds:

$$\langle\bar\Psi\,\Sigma_{\alpha\beta}\,\Psi\rangle = \langle\bar\Psi\Psi\rangle\Bigl\langle\int d^4x\, \psi^\dagger_\lambda(x)\,\Sigma_{\alpha\beta}\,\psi_\lambda(x)\Bigr\rangle\,. \tag{14}$$

The comparison of this formula with Eqs. (11) and (12) gives

$$\mu(qB) \equiv \chi(qF)\, qF_{\alpha\beta} = \lim_{\lambda\to 0}\Bigl\langle\int d^4x\, \psi^\dagger_\lambda(x;B)\,\Sigma_{12}\,\psi_\lambda(x;B)\Bigr\rangle\,, \tag{15}$$

where $\psi_\lambda(x;F)$ is the eigenmode of the Dirac operator in the external (magnetic) background field $B = F_{12}$.

We established the factorization property (14) for all studied values of the magnetic fields. The comparison of the left and right sides of Eq. (14) evaluated at the same set of configurations is shown in Figure 2(left). While both estimations agree with each other within error bars, the factorized definition (15) is much more accurate compared to the nonfactorized one (13).

We show in Figure 2(right) the magnetization for two different temperatures, $T = 0$ and $T = 0.82\,T_c$. The behavior of the magnetization is consistent with general expectations: at low magnetic fields the magnetization is linear indicating the existence of a nonzero susceptibility at vanishingly small external magnetic field. At high magnetic fields the quarks are fully polarized and the magnetization approaches the saturation regime,

$$\mu(qB) \to -1\,. \tag{16}$$

We fit our data by the function:

$$\mu^{\rm trig}_{\rm fit}(B) \quad = \quad \frac{2\mu_\infty}{\pi}\arctan\frac{\pi\chi_0 qB}{2\mu_\infty}\,, \tag{17}$$

with two fitting parameters: the zero-field susceptibility χ_0 and the infinite-field saturation parameter μ_∞. The fits – shown by the lines in Figure 2(right) – give the following values for the chiral susceptibility:

$$\chi_0 = \begin{cases} -1.547(6)\ \ \mathrm{GeV}^{-2} & \Lambda_{\mathrm{UV}} \sim 2\,\mathrm{GeV} \qquad T = 0 \\ -1.53(3)\ \ \mathrm{GeV}^{-2} & \Lambda_{\mathrm{UV}} \sim 1.5\,\mathrm{GeV} \qquad T = 0.82 T_c \end{cases} \tag{18}$$

where T is the temperature, and Λ_{UV} is the momentum scale, at which the susceptibility is evaluated (the momentum dependence is discussed, e.g., in [19]).

Other fitting functions were also discussed in [30]. For example, the specific (i.e., per atom) magnetization of a classical ideal paramagnetic gas is given by [20]

$$\mu^{\mathrm{class}}(B) \quad = \quad \mu \left[\coth \alpha(B) - \frac{1}{\alpha(B)} \right] , \qquad \alpha(B) = \frac{\mu B}{k_B T} , \tag{19}$$

where μ is the magnetic moment of a single molecule, T is temperature and k_B is the Boltzmann constant. The function in the brackets in Eq. (19) is often called the Langevin function.

The quantum analogue of the Langevin function (19) for a spin 1/2-particle is described by the Brillouin behavior:

$$\mu^{\mathrm{quant}}(B) = \mu \left[2 \coth 2\alpha(B) - \coth \alpha(B) \right] . \tag{20}$$

The atoms are supposed to be electrically neutral otherwise the paramagnetic magnetization – either classical (19) or quantum (20) – should be supplemented by a diamagnetic contribution due to Landau quantization (the motion of the atoms in transverse direction to the magnetic field is to be constrained to the Landau levels). In an electron gas the diamagnetic contribution provides an essential part of the total magnetization [20]. However, we do not consider the diamagnetic contribution of the quark's motion because of the paramagnetic nature of the condensate (11).

Our simulations show that the conventional functions, either classical formula (19) or quantum function (20) do not describe our numerical data.

An experimentally relevant and phenomenologically interesting quantity is the product $\chi\langle\bar{\Psi}\Psi\rangle$ at vanishing field [25, 26]. Our data gives the following result:

$$-\chi \, \langle \bar{\Psi}\Psi \rangle = 46(3)\,\mathrm{MeV} \qquad [\text{quenched limit}] . \tag{21}$$

which is surprisingly close to the estimation based on the QCD sum rules techniques [15, 16, 17, 18]:

$$-\chi \, \langle \bar{\Psi}\Psi \rangle = 50\,\mathrm{MeV} \qquad [\text{QCD sum rules}] . \tag{22}$$

5 Chiral Magnetic Effect

In brief, the physical mechanism behind the Chiral Magnetic Effect (CME) is as follows [1, 31]. A strong magnetic field forces the magnetic moment of quarks to turn parallel to the direction of the field. If the quarks are light (massless) then the left-handed quarks will move, say, towards the direction of the field while the right-handed quarks will move backwards. If there is an imbalance between left- and right-handed quarks, then a net electric current

$$j_\mu(x) = \bar{\psi}(x)\gamma_\mu\psi(x)$$

appears along the magnetic field [45, 46, 32, 33, 1, 31]. This longitudinal electric current may lead also to a spatial separation of the electric charges. The longitudinal current and the spatial charge separation are the consequences of the CME. The chiral imbalance may be created by topologically nontrivial configurations of gluon fields. Generally, the CME is a reflection of the $\mathcal{CP}$-odd structure of the vacuum.

In Ref. [37] we studied a spatial excess of the charge density due to the applied magnetic field,

$$j_0(x; B) = \langle j_0(x) \rangle_B - \langle j_0(x) \rangle_{B=0} .$$

The subtraction of the zero-field density removes all ultraviolet contributions providing us with a nonperturbative quantity originating due to the external magnetic field. In Figure 3 we demonstrate that the magnetic field applied to a typical gluon configuration leads to a spatial separation of the electric charges in an agreement with the CME. The effect increases as the magnetic field gets stronger.

In Figure 4 the profile of the longitudinal (parallel to the magnetic field) and transverse (perpendicular to the field) components of the quark's electric current in a background of a specially-prepared smooth instanton-like ($Q = 1$) configuration subjected to an external magnetic field. The CME is characterized by enhancement of the longitudinal current with respect to the transverse one. This property is clearly seen in the case of the instanton, Figure 4.

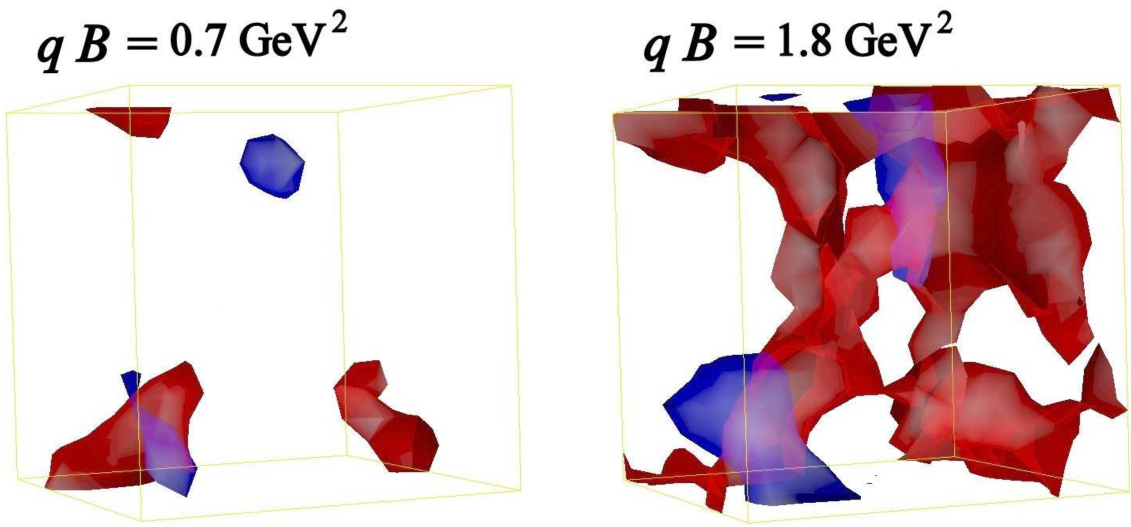

Figure 3. A visual evidence of the CME: A typical $T = 0$ gluon configuration: the excess of the positive (red) and negative (blue) electric charge due to magnetic field (directed vertically) $qB = 0.7\,\mathrm{GeV}^2$ (left) and $qB = 1.8\,\mathrm{GeV}^2$ (right). From Ref. [37].

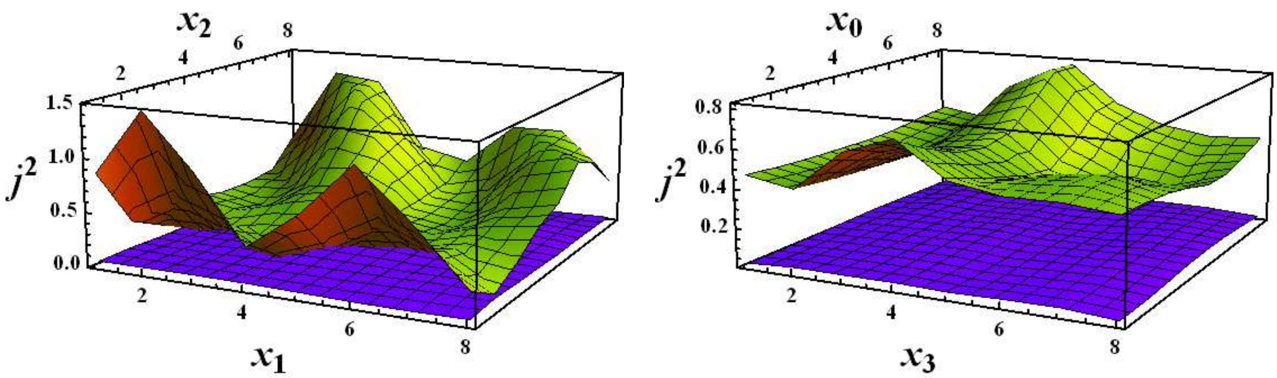

Figure 4. An instanton-like configuration with unit topological charge: a magnetic field induces the electric current (shown in arbitrary units). The upper (green) and lower (violet) surfaces are the longitudinal ($j_\parallel^2 = j_0^2 + j_3^2$) and the transverse ($j_\perp^2 = j_1^2 + j_2^2$) currents in the 12-plane (left) and in the 30-plane (right), Ref. [37].

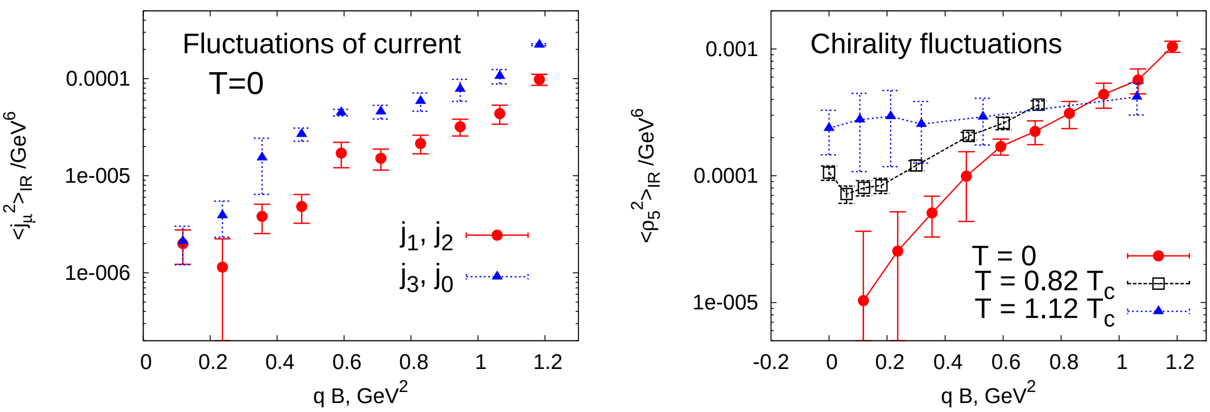

Figure 5. (left) The squares of the transverse (j_1, j_2) and longitudinal (j_3, j_0) components of the current *vs.* magnetic field qB at zero temperature. (right) The chirality squared *vs.* magnetic field qB at various temperatures T. Figures are from Ref. [37].

Coming back to real quantum configurations of the gluonic fields, we plot in Figure 5(left) the expectation values of the fluctuations of each component of the electric current at zero temperature. We do not distinguish the global topological charge of each configuration since the CME effect appears also locally (an extended discussion of this point is given in Ref. [37]). In agreement with the CME features, we observe the dominance of the longitudinal components of the electric current with respect to the transverse ones.

The CME crucially depends on the (local) imbalance between the left and right chiral modes given by the local chiral charge

$$\rho_5\left(x\right)=\bar{\psi}\left(x\right)\gamma_5\psi\left(x\right)\,.$$

The local strength of the chiral imbalance is characterized by the value of the chirality fluctuations, $\langle\rho_5^2\rangle$, which is shown in Figure 5(right) for three different temperatures. At $T=0$ the fluctuations quickly grow with the increase of the magnetic field. As the temperature increases the growth rate gets smaller, and in the deconfinement phase the rate is almost zero. Note that in the confinement phase ($T=0$) the chirality fluctuations at strong enough magnetic fields are as large as the fluctuations in the deconfinement phase. This allows us to suggest that the CME may be observed in a cold nuclear matter as well.

6 Conclusion

We have numerically demonstrated that the strong external magnetic fields reveal various nonperturbative properties of the QCD vacuum. We observed the enhancement of the chiral condensate in the external magnetic field. We calculated the chiral magnetization of the QCD vacuum. Finally, we demonstrated the existence of the chiral magnetic effect, which is an experimentally relevant feature of heavy ion collisions.

Acknowledgements. This work was partly supported by Grants RFBR Nos. 08-02-00661-a and 09-02-00629, grants for scientific schools Nos. NSh-679.2008.2 and Nsh-4961.2008.2, by the Russian Federal Agency for Nuclear Power, and by the STINT Institutional grant IG2004-2 025. P.V.B. is also partially supported by the Euler scholarship from DAAD, by a scholarship of the Dynasty Foundation and by the grant BRFBR F08D-005 of the Belarusian Foundation for Fundamental Research. The calculations were partially done on the MVS 50K at Moscow Joint Supercomputer Center.

References

[1] D. E. Kharzeev, L. D. McLerran, H. J. Warringa, Nucl. Phys. A **803**, 227 (2008) [arXiv:0711.0950 [hep-ph]].
[2] V. Skokov, A. Illarionov and V. Toneev, arXiv:0907.1396 [nucl-th];
[3] N. O. Agasian and S. M. Fedorov, Phys. Lett. B **663**, 445 (2008) [arXiv:0803.3156 [hep-ph]].
[4] E. S. Fraga and A. J. Mizher, Phys. Rev. D **78**, 025016 (2008) [arXiv:0804.1452 [hep-ph]].
[5] Nucl. Phys. A **820**, 103C (2009) [arXiv:0810.3693 [hep-ph]].
[6] I. A. Shushpanov and A. V. Smilga, Phys. Lett. B **402**, 351 (1997).
[7] N. O. Agasian and I. A. Shushpanov, Phys. Lett. B **472**, 143 (2000) [arXiv:hep-ph/9911254].
[8] T.D. Cohen, D.A. McGady, E.S. Werbos, Phys. Rev. C **76**, 055201 (2007) [arXiv:0706.3208 [hep-ph]].
[9] V.P.Gusynin, V.A.Miransky, I.A.Shovkovy, Nucl. Phys. B **462**, 249 (1996) [arXiv:hep-ph/9509320].
[10] S. P. Klevansky and R. H. Lemmer, Phys. Rev. D **39**, 3478 (1989).
[11] D. Ebert, K. G. Klimenko, M. A. Vdovichenko and A. S. Vshivtsev, Phys. Rev. D **61**, 025005 (1999) [arXiv:hep-ph/9905253].
[12] A. Goyal and M. Dahiya, Phys. Rev. D **62**, 025022 (2000) [arXiv:hep-ph/9906367].
[13] A. V. Zayakin, JHEP **0807**, 116 (2008) [arXiv:0807.2917 [hep-th]].
[14] B. L. Ioffe and A. V. Smilga, Nucl. Phys. B **232**, 109 (1984).
[15] I. I. Balitsky, A. V. Yung, Phys. Lett. B **129**, 328 (1983).
[16] V. M. Belyaev, Y. I. Kogan, Yad. Fiz. **40**, 1035 (1984).
[17] I. I. Balitsky, A. V. Kolesnichenko, A. V. Yung, Sov. J. Nucl. Phys. **41**, 178 (1985) [arXiv:hep-ph/8507307].
[18] P. Ball, V. M. Braun, N. Kivel, Nucl. Phys. B **649**, 263 (2003) [arXiv:hep-ph/0207307].
[19] A. E. Dorokhov, Eur. Phys. J. C **42**, 309 (2005) [arXiv:hep-ph/0505007].
[20] L.D. Landau and E.M. Lifshitz, Statistical Physics Part I, vol. 5 of Course of Theoretical Physics (Pergamon Press, Oxford, 1980); H. P. Myers, "Introductory solid state physics" (CRC Press, New York, 1997).
[21] A. E. Dorokhov, W. Broniowski and E. Ruiz Arriola, Phys. Rev. D **74**, 054023 (2006) [arXiv:hep-ph/0607171]; arXiv:0907.3374 [hep-ph].
[22] A. Vainshtein, Phys. Lett. B **569**, 187 (2003) [arXiv:hep-ph/0212231].
[23] A. Gorsky and A. Krikun, arXiv:0902.1832 [hep-ph].
[24] H. C. Kim, M. Musakhanov, M. Siddikov, Phys. Lett. B **608**, 95 (2005).
[25] V. M. Braun, S. Gottwald, D. Y. Ivanov, A. Schafer, L. Szymanowski, Phys. Rev. Lett. **89**, 172001 (2002).
[26] B. Pire, L. Szymanowski, Phys. Rev. Lett. **103**, 072002 (2009) [arXiv:0905.1258 [hep-ph]]; arXiv:0909.0098.

[27] J. Rohrwild, JHEP **0709**, 073 (2007) [arXiv:0708.1405 [hep-ph]].
[28] T. D. Cohen and E. S. Werbos, Phys. Rev. C 80, 015203 (2009) [arXiv:0810.5103].
[29] P.V. Buividovich, M.N. Chernodub, E.V. Luschevskaya, M.I. Polikarpov, *"Numerical study of chiral symmetry breaking in non-Abelian gauge theory with background magnetic field"*, arXiv:0812.1740 [hep-lat].
[30] P.V. Buividovich, M.N. Chernodub, E.V. Luschevskaya, M.I. Polikarpov, *"Chiral magnetization of non-Abelian vacuum: a lattice study"*, arXiv:0906.0488 [hep-lat].
[31] K. Fukushima, D.E. Kharzeev, H.J. Warringa, Phys. Rev. D **78**, 074033 (2008); H.J. Warringa, arXiv:0906.2803; D.E. Kharzeev, arXiv:0906.2808.
[32] D. Kharzeev, R.D. Pisarski, M. Tytgat, Phys. Rev. Lett. **81**, 512 (1998) [arXiv:hep-ph/9804221].
[33] D. Kharzeev, Phys. Lett. B **633**, 260 (2006) [arXiv:hep-ph/0406125].
[34] S. A. Voloshin, Phys. Rev. C **70**, 057901 (2004) [arXiv:hep-ph/0406311].
[35] S. A. Voloshin [STAR Collaboration], arXiv:0806.0029 [nucl-ex].
[36] H. Caines [STAR Collaboration], arXiv:0906.0305 [nucl-ex].
[37] P.V. Buividovich, M.N. Chernodub, E.V. Luschevskaya, M.I. Polikarpov, *"Numerical evidence of chiral magnetic effect in lattice gauge theory"*, arXiv:0907.0494 [hep-lat].
[38] P.V. Buividovich, M.N. Chernodub, E.V. Luschevskaya, M.I. Polikarpov, in preparation.
[39] V. G. Bornyakov, E. V. Luschevskaya, S. M. Morozov, M. I. Polikarpov, E. M. Ilgenfritz, M. Muller-Preussker, Phys. Rev. D **79**, 054505 (2009).
[40] H. Neuberger, Phys. Lett. B **417**, 141 (1998) [arXiv:hep-lat/9707022].
[41] M. H. Al-Hashimi and U. J. Wiese, Annals Phys. **324**, 343 (2009).
[42] P. H. Damgaard and U. M. Heller, Nucl. Phys. B **309**, 625 (1988).
[43] T. Banks and A. Casher, Nucl. Phys. B **169**, 103 (1980).
[44] S. J. Hands and M. Teper, Nucl. Phys. B **347**, 819 (1990).
[45] H. B. Nielsen and M. Ninomiya, Phys. Lett. B **130**, 389 (1983).
[46] M. A. Metlitski and A. R. Zhitnitsky, Phys. Rev. D **72**, 045011 (2005).

Proceedings of the International School-seminar
"New Physics and Quantum Chromodynamics at external Conditions", pp. 31 – 41,
3-6 May 2009, Dnipropetrovsk, Ukraine

EARLY PHYSICS WITH THE LHC

Ludwik Dobrzynski[a]

Laboratoire Leprince Ringuet - Palaiseau - France

The status of the Large Hadron Collider (LHC), ATLAS and CMS detectors commissioning is shortly reviewed. Both experiments are waiting for the promising signal hunting. The early data from LHC will first allow the check of the Standard Model (SM) predictions at $\sqrt{s} = 10$ and later at 14 TeV. The perspectives for early analyses are discussed, mainly as standard candles for detector understanding and simulation tuning. Few new physics searches are also presented. The high available energy will permit to be competitive with the past and ongoing experiments. Prospective searches about Higgs physics and the Beyond Standard Model (BSM) are presented for the CMS and ATLAS experiments as well as the searches for some supersymmetric and exotic particles predicted by several theoretical models.

1 Introduction

The LHC [1] assembled at CERN is a pp collider with a design center-of-mass energy of 14 TeV. LHC will collide protons or lead ions. Its first operation started in September 2008. The first collisions will be delivered in 2009. The gain in center of mass energy compared to the Tevatron will result in a large cross section increase [2] for high mass resonances as well as for SM processes. Hence, soon after LHC start-up, studies of Standard Model processes will not be limited by statistics. New processes, not yet excluded by past experiments, could become observable. Assuming successful operation, a delivered integrated luminosity of 10-20 pb^{-1} for 2009 can be foreseen.
The LHC has been built with the purpose of exploring new frontiers of particle physics. Possible excesses of events in real data, even with few hundred pb^{-1} of integrated luminosity, could be an indication of the existence of new particles. Larger luminosity will be required to have evidence of the existence of the Higgs boson and/or a wide spectrum of new particles predicted by supersymmetry and exotic models.
In general, the experiments at the LHC could provide answers or ingredients to answer some of the most fundamental open questions in particle physics, such as: the reality of the Higgs mechanism for generating gauge bosons and fermions masses, the problem of the hierarchy between the electroweak gauge boson scale and the Grand Unification or Planck scale, the existence of a supersymmetry, the existence of extra dimensions as predicted by various models inspired e.g. by string theory.

CMS [3] and ATLAS [4] are the two general purpose experiments built at the LHC to provide answers to those fundamental questions. Prospective studies have been performed in the physics groups of the CMS [2] and ATLAS [5] collaborations to optimize strategies for the search of the Higgs boson(s), of the supersymmetric particles and of some exotic particles, both with low and high integrated luminosity. Some of these studies will be developed in the present paper.

2 The experimental environment

Figure 1 present the layout of the experimental environment at CERN. The 27 km LHC underground ring will provide pp and lead-lead collisions to four experimental setup: ALICE, ATLAS, CMS, LHCb. In addition, two detectors devoted to access to the forward physics issued from the collisions: Totem and Castor are completing the experimental setups. The ATLAS and CMS are general purpose detectors designed to explore physics at the TeV energy scale. Each of them has a large acceptance and hermetic coverage. The various sub-detectors are: a silicon tracker with pixels and strips, electromagnetic and hadronic calorimeters, and muon chambers. Both detect with the highest precision leptons and both charged and neutral hadrons.

Both experiments, on 11 September 2008, have performed observation of the First Beam Induced Muons. At start-up the LHC machine provided single shots of LHC beam onto a collimator placed about at 150 m upstream of the detectors. These shots were used to synchronize the detectors beam monitoring system to the beam timing. Using the beam monitoring system as Trigger, Atlas and CMS recorded events in all sub-detectors except the silicon pixel and strip tracker which were left out of the run. In these shot events, more than 100 muons cross the volume of the detectors and illuminated a large fraction of all channels in the central detectors.

e-mail: [a]dobrzynski@llr.in2p3.fr

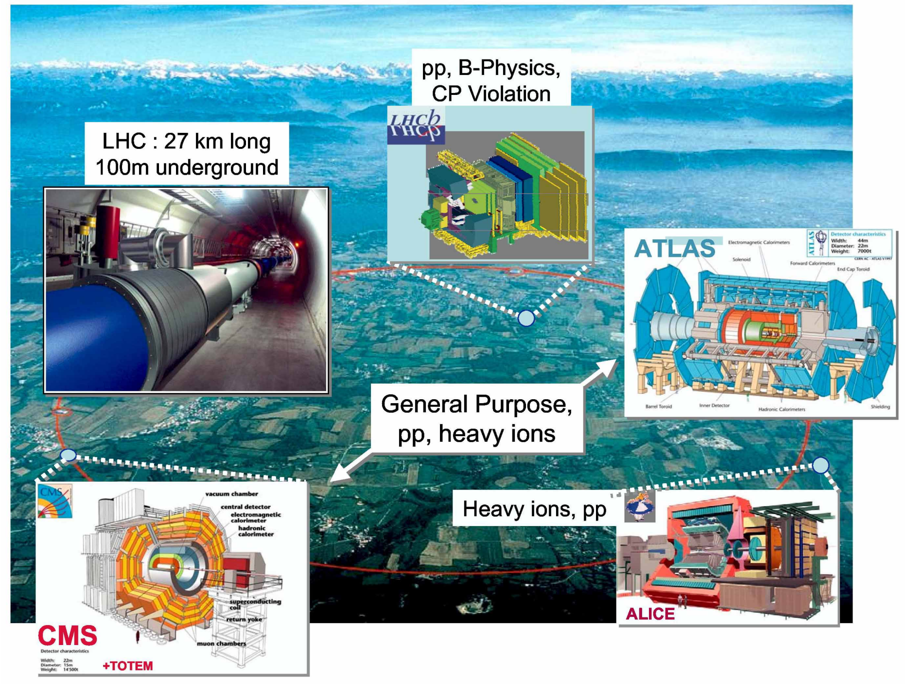

Figure 1. Overview of the CERN experimental environment.

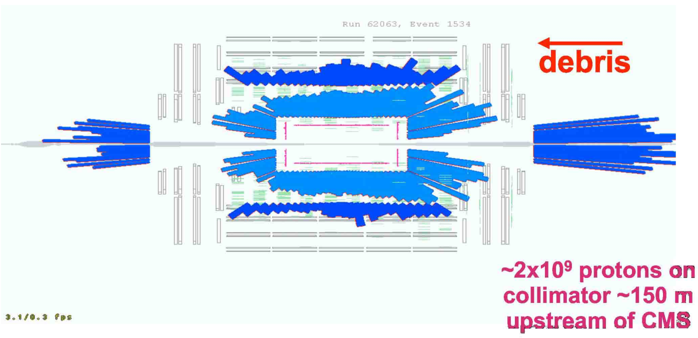

Figure 2. CMS detector energy response to muons produced by a LHC beam dumped onto collimators

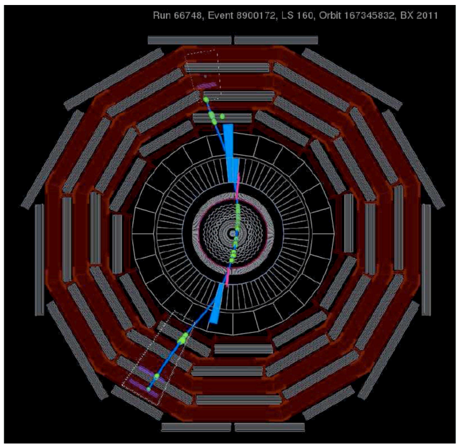

Figure 3. Response of the CMS detector to cosmics muons.

The first analysis results show clear correlations between sub-detectors in the energy recorded, as well as the angular predicted distribution of the deposited energy. In some of the events the energy recorded in ECAL and HCAL exceeded 1000 TeV. Figure 2 gives for the CMS detector a pattern view of the deposited energy.

In addition, current commissioning of the detectors with and without magnetic field uses cosmics tracks triggered by the muon system. Electronics alignment, timing improvements, calorimeter cell intercalibration are performed improving the detector response knowledge. Figure 3 shows a CMS view traversed by a cosmics track [7].

3 Standard Model process study at $\sqrt{s} = 10$ and 14 TeV.

The study of already known particles properties at a new accelerator is an important commissioning tool and interesting goal by testing the Monte Carlo predictions. Known resonances can be used as standard candles for calibration. Moreover, given the new kinematical regime due to the unprecedented center-of-mass energy, many expectations for standard phenomena, being extrapolated from measurements at much lower energy, have large uncertainties. Only the LHC data themselves will be able to constrain the empirical models used in these cases. This is essential to estimate the SM backgrounds to searches of new physics. This section presents a far from exhaustive list of SM topics which will be addressed with the early LHC data. Their impact to the detector knowledge or the MC tuning will also be addressed.

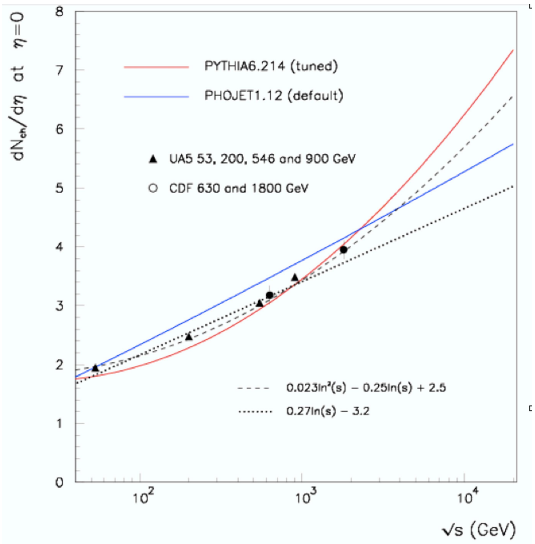

Figure 4. $dN/d\eta$ at $\eta = 0$ as function of the center of mass energy. The lines correspond to different model predictions.

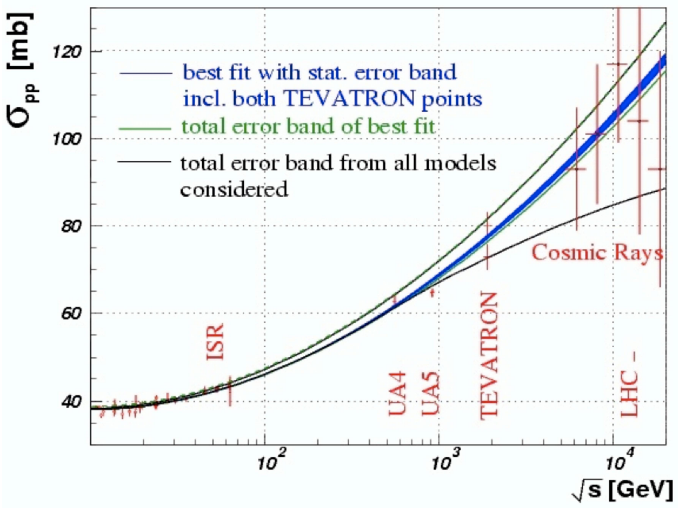

Figure 5. Total pp cross section as function of the center of mass energy. The lines correspond to different model predictions.

3.1 Soft hadronic physics

The study of charged hadron spectra [6] will probably be the first physics result with LHC pp collisions. Apart from its intrinsically importance for the models, it will define the number of charged tracks participating to each bunch crossing at the working LHC luminosity and defining how many extra particles from soft interactions will provide noise to the study of the hard process. Only the information from the Tracker will be needed for the analysis, but the track sample for this study should go as low as possible in p_T. Exclusive measurements can also be performed, thanks to the good capability of the Silicon Pixel and Strip Tracker to measure dE/dx, which can discriminate protons and kaons from pions in the low p_T region. Figure 4 shows our present knowledge of the charged hadron abundance and the large model dependent uncertainties at the LHC energy.

3.2 Total cross section measurement

A precise measuremnt of the pp total cross section is an important goal. As shown on figure 5 there is still an large uncertainty on the total pp cross section at high energy. Does the cross section continue to rise or are we approaching to some asymptotical region at the LHC energy. LHC results will discriminate between the models.

3.3 Underlying event [8]

The study of the underlying event deals with all the activities of a single pp interaction on top of the interesting hard process. Hence it covers several mechanisms: initial and final state radiation, the spectators, and multiple parton interactions, which is of particular interest today. While there are many sets of generator tunes describing Tevatron data, they have several differences when extrapolated to LHC energy.
The region transverse to the jet is expected to be particularly sensitive to the characteristics of the underling event. The study of the underlying event helps to tune energy dependence models, understand multiple parton interactions and improve the QCD understanding of pp collisions. The strategy, for comparing different models describing the underlying event, is to select events with two back-to-back jets and count the number of charged particles in the region transverse to the jets axis. Different models presented in figure 6 show significant differences at LHC energies when the average number of charged particles is drawn as a function of the leading charged jet transverse momentum.

3.4 Jet at LHC

Jets are the experimental signature of quarks and gluons. Jet algorithms are used to reconstruct unambiguously the jet properties. Inclusive dijet production is the most abundant hard scattering process at the LHC. The jets expected p_T spectrum [9] is shown in figure 7. In early running ($< 10pb^{-1}$), this is expected to be known within 10%.
The invariant mass of two leading cross section has at LHC large uncertainty. As shown on figure 8, we will reach at LHC, dijet masses up to 6 TeV about an order of magnitude higher as what can be observed at the Tevatron. Even a small amount of data is enough to exceed the Tevatron mass reach (1.4 TeV). Consequently

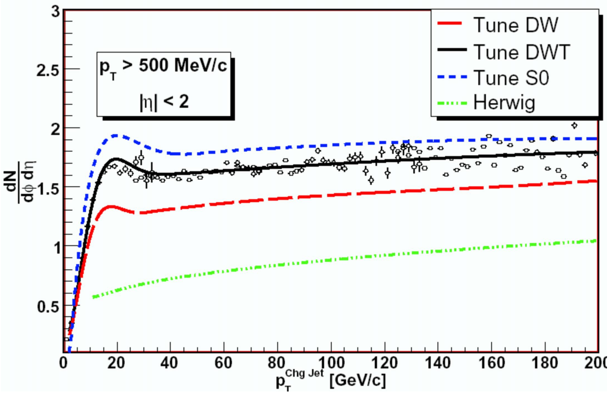

Figure 6. Densities $dN/d\eta d\phi$ for tracks with p_T $> 0.9 GeV/c$, as a function of the leading charged jet p_T , in the transverse region, for an integrated luminosity of 100 pb^{-1}.

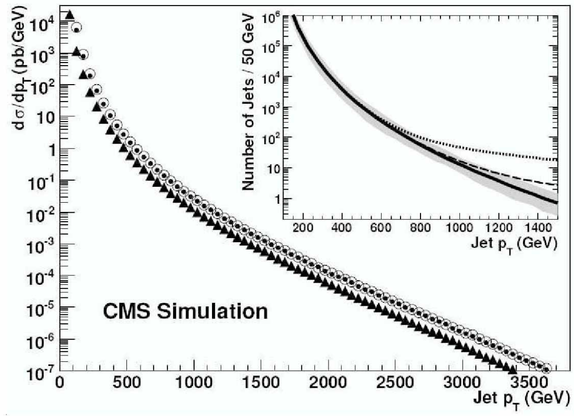

Figure 7. Jet p_T spectra : generator-level jets (black dots), raw reconstructed jets (black triangles), calibrated jets (open circles). The inset shows deviation from SM expected for contact interactions at a scale of 3 TeV (dots) and 5 TeV (brocken line), the grey band correspond to a scale uncertainty of 10 % on the jet calibration.

at LHC we will be sensitive to objects decaying to two jets (dijet resonances : q*, Z) as shown on figure 9 [10]. With 100 pb^{-1} a 2 TeV excited quark can be clearly seen. Present Tevatron limit for such resonances is M< 0.87 TeV.
Errors are expected to be dominated by the jet energy scale uncertainty which will be the dominant experimental systematic uncertainty.

3.5 J/Ψ

The observation of J/Ψ and its resonances at LHC will be important, as a test of QCD mechanisms, and as a commissioning tool for the detector. The main physics motivations for J/Ψ studies lies in the fact that none of the theory models for quarkonium production at hadron colliders explains successfully both polarization and differential cross section measurements [11]. LHC data, will allow to probe transverse momenta much higher than currently studied at the Tevatron. The reconstruction of the J/Ψ by selecting track pairs in a window around the known mass, will provide a very pure sample of muons providing the efficiency of muon selection in addition to a pure sample of muonic tracks. This could measure and correct the relative misalignment of the Tracker to the muon detectors. The peak position will be compared to the precisely known J/Ψ mass, used as a standard candle, in order to spot eventual biases in the momentum measurement due to a mismeasurement of the magnetic field. Figure 10, from Ref. [8], shows the expected peak in dimuon mass, for a statistics corresponding to 3 pb^{-1},

3.6 W/Z production [12]

The W and Z production cross section at 14 TeV is about 180 nb and 60 nb respectively, and is theoretically one of the best understood cross sections at hadron colliders. This, combined with the very clean signature for the electronic and muonic decay channels, makes W/Z production one of the best ways to determine the luminosity at the few % level, where most of the uncertainty will come from the imprecise knowledge on the Parton Distribution Functions (PDF), which can be in turn constrained by measurements of the rapidity distributions of W and Z, and of the W^+/W^- ratio. Furthermore, inclusive W/Z production serves as the starting point for more detailed analyses, such as measuring the boson p_T spectrum or looking for additional jets, which are important to understand the background to many low cross section channels. Moreover, Z $\rightarrow l^+l^-$ (l = e, μ) events provide a precious calibration reference, given the precise knowledge of the Z mass and width as measured at LEP, and a way to select pure $e/\mu/\tau$ samples useful for tag-and-probe methods. In the Z analysis as shown in figure 11 the main variable is the dileptonic invariant mass and the effect of detector misalignments.
ATLAS [5] has investigated the possibility of further constraining parton density functions (PDFs) using W decays into electrons. Re-fitting the ZEUS-S PDF to the e^+ and e^- rapidity distributions from Monte Carlo events the biggest improvement is seen in the parameter controlling the low-x gluon. This is not surprising as we will have access to x values down to about 10^{-4} with W and Z bosons at $\sqrt{s}$ = 14 TeV and the gluon being the dominant parton at this $Q^2 \sim (100GeV)^2$.

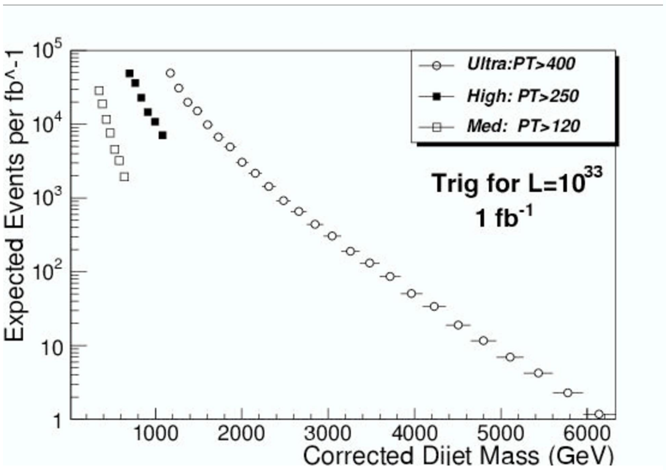

Figure 8. Dijet mass at LHC compared to what the Tevatron provide.

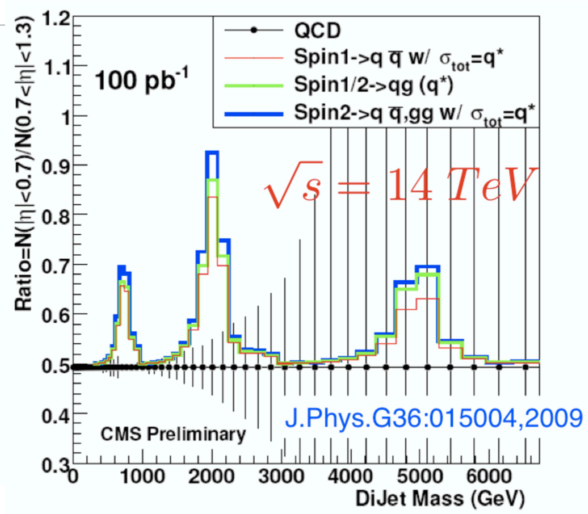

Figure 9. Dijet resonances as predicted by some models.

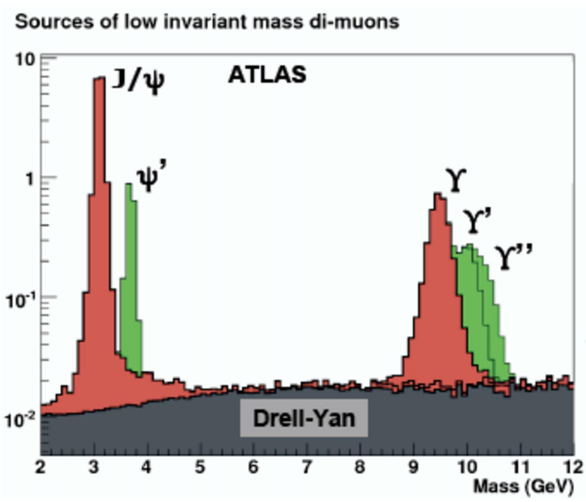

Figure 10. Heavy quark J/Ψ and Υ resonances in the ATLAS detector.

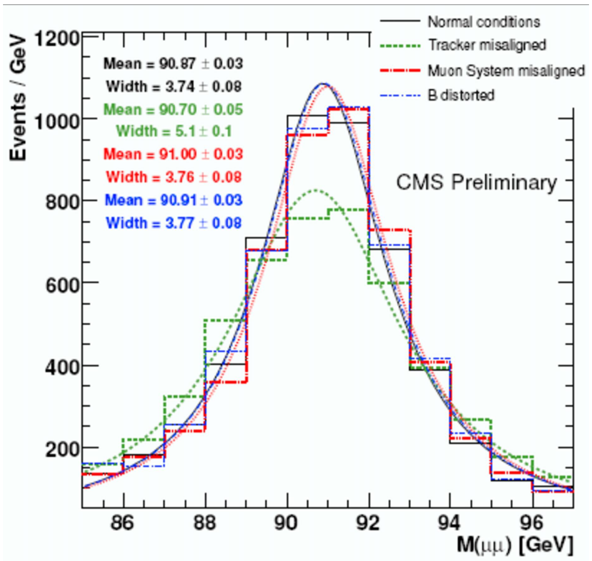

Figure 11. Muon pair effective mass in CMS for Z^0 events. The resolution evolution is studied as function of the tracker and muon chambers alignement.

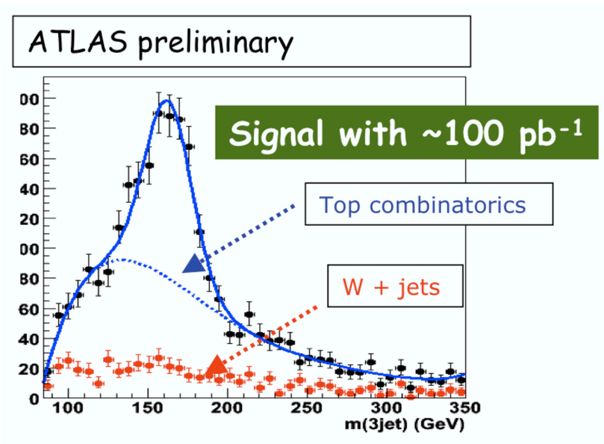

Figure 12. Top signal in ATLAS for 100 pb^{-1}.

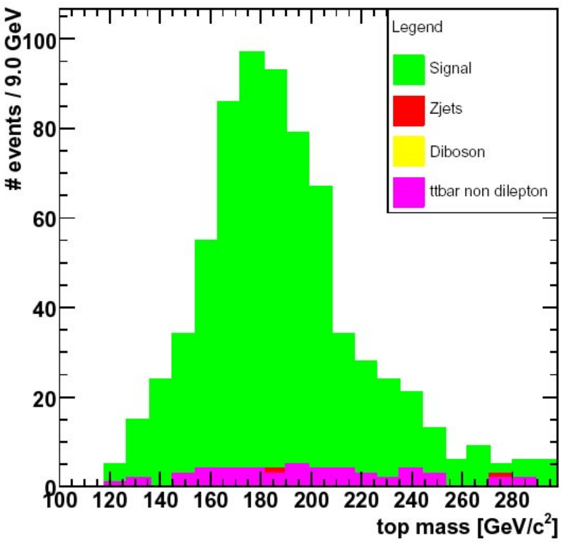

Figure 13. Top mass in CMS from dilepton events for 1 fb^{-1} integrated luminosity.

3.7 Top at LHC [13]

The top pair production cross section is more than hundred times larger at LHC compared to Tevatron (830 pb^{-1} at NLO [13] for LHC and 8pb^{-1} at the Tevatron [16]).The LHC will become rapidly a top factory at LHC and should allow to study the properties of top quarks in great detail.

The final states of top pair events are determined by the fact that the decays are almost exclusively into a W and a b quark and by the branching ratios of the W boson. Due to the fact that top pair events have all kinds of objects in the final state (electrons, muons, light and b jets and missing transverse energy), they will help to improve a large variety of reconstruction aspects: i.e. jet energy scale for instance. Furthermore, they are a background to many searches for new physics and therefore must be understood before a new signal can be claimed.

With 20 pb^{-1}, about 800 di-lepton and about 4700 semi-leptonic (e/μ) events are produced which should allow the observation of top pair events [13] rapidly (Figure 12). The analysis, described in [18] as shown on figure 13, starts from events triggered by the single or di-lepton trigger. At least two jets and two reconstructed isolated leptons with opposite charge have to be present in the event. The presence of the two neutrinos from the W decays induce a large missing transverse energy and a b-tag criterion for both b jets in the event. A kinematic fit imposing W mass allows to reconstruct a clear top mass peak (Figure 13). At starting even with 1 pb^{-1} one can already observe a signal as shown on Figure 14.

With more data, the production cross section can be measured as well as the measurements of the top mass and the other top properties.

4 Searches

The search for Higgs and supersymmetric particles have been the major guide to define the detector requirements and performance that are detailed in Ref. [1] and [2] for CMS and ATLAS. Detailed simulations of the detector closest to the real experimental set-up with miscalibration/misalignment conditions at start-up luminosity are used in the CMS and ATLAS studies presented here after. Advanced Monte Carlo physics generators have been used for signal and background simulation with the estimation of NLO for QCD and electroweak corrections.

4.1 BSM

ATLAS [5] and CMS [2] have a very rich program of searches, and LHC itself is commonly considered as a discovery machine in the HEP community, but most of the potential discoveries would require: high statistics; very good detector control (calibration, alignment); and very reliable prediction of the SM backgrounds in the signal region. All these three conditions will require a long running before being achieved. Nevertheless, a few examples exist of new particles or phenomena that could show up relatively early, with limited statistics and detector still far from ideal conditions.

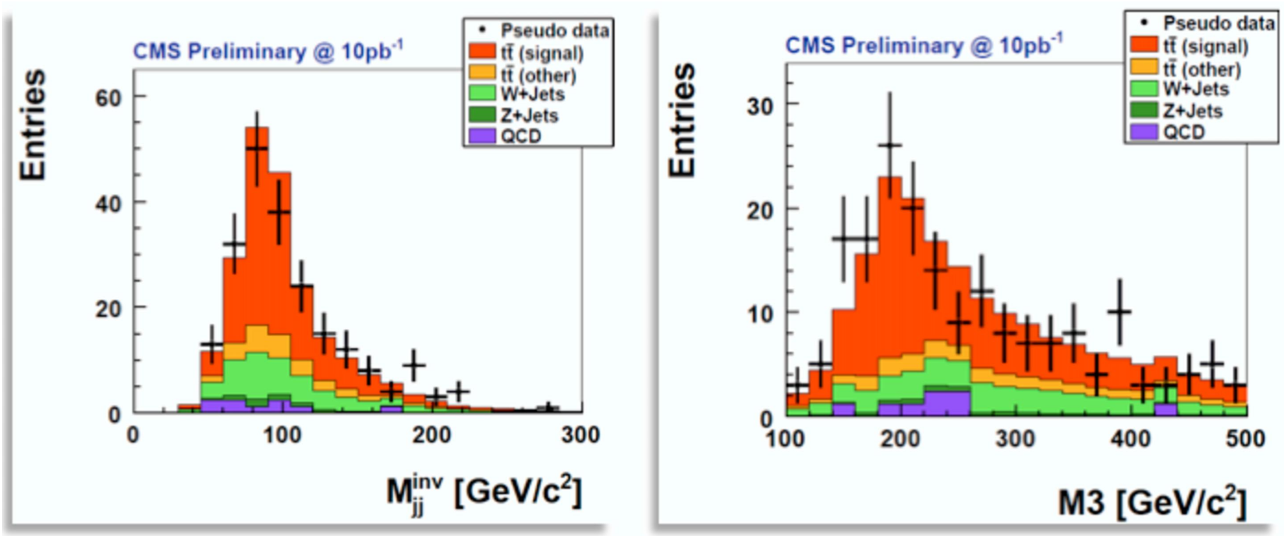

Figure 14. Top rediscovery in CMS for an integrated luminosity of $1pb^{-1}$. Left plot is the effective mass of the two highest energy jets giving a peak around the W mass. The right plot is the effective masss of the W jets and the third highest energy one providing a peak at the top mass.

Contact interactions and dijet resonances

Deviation from the SM in the jet spectra, or the appearance of peaks signaling resonances in the invariant mass distribution for dijet events are predicted from theories such as Technicolor [16], Extra Dimensions [17] and Contact Interactions [14], [18].
The inclusive cross section as a function of jet p_T is a first simple measure of QCD dijets which is sensitive to a 3 TeVcontact interaction with only 10 pb^{-1}. With the dijet mass distribution we expect to be able to observe resonances [10] with large cross sections, such as a 2 TeV excited quark which produces a convincing signal with only 100 pb^{-1}. Figure 9 shows, for Z^0 masses of 0.7, 2.0 and 5.0 TeV and cross section normalized to the q cross section, the expected signal for a Z^0 like spin 1 resonance, compared to the statistical uncertainty of the expected QCD background.

Exotics

New heavy neutral (Z') or charged (W') gauge bosons are predicted by several extensions of the Standard Model, such as E6 based GUTs [23], Little Higgs Models [18], Extra Dimensions [17]. A very useful benchmark for experimentalists is the Altarelli Reference Model [22] , also known as Sequential Standard Model (SSM) [26] In this model, the new gauge bosons are simply more massive replicas of the corresponding SM ones, with the same coupling constants.

As in the case of SM, the cleanest signatures for heavy gauge bosons are $\mathrm{W}' \to \mathrm{l}\nu$ [23] and $\mathrm{Z} \to \mathrm{l}^+\mathrm{l}^-$ ($\mathrm{l} = \mathrm{e}, \mu$). CMS prospects for W' search in the electronic [19] and muonic [24] channels are shown in figure 15 for the case of a 1 TeV W' with the same couplings as the W. Figure 16 shows the heavy Z' decay into τ τ leptons.

Other exotic massive gauge bosons are also expected in several theoretical models beyond the SM. In the sequential Standard Model [22], [26] (SSM) a Z-like boson, called Z', with the same couplings of the Z to fermions and gauge bosons and with O(TeV) mass is predicted. Other exotic scenarios based on extra dimension [17] predict the existence of a graviton with O(TeV) mass decaying in e^+e^-.

Search for di-muon resonances at O(1 TeV) mass were addressed too by CMS [**?**] and ATLAS [5]. Sources of background are di-muons from Drell Yan events and W+jets, Z+jets. The cross section times the branching ratio is between few fb^{-1} to few hundred fb^{-1} depending on the mass of the resonance and the theoretical model. Main backgrounds for those searches were di-electron events produced via Drell Yan mechanism, $\bar{t}t$ events with two electrons in the final state, QCD with jets faking electrons, W+jets, γ+jet and $\gamma\gamma$. The di-electron invariant mass spectrum for signal and background at 100 pb^{-1} is reported in figure 17. At high mass only few background events survive the selection giving an optimal signal to background rejection.

At the end of the analysis, after computing the integrated luminosity for 5 σ discovery at $\sqrt{s}$ = 14TeV as a function of the Z mass, it could be shown that few hundred pb^{-1} of integrated luminosity are needed to discover the Z with O(1 TeV) mass. Figure 18 gives the mass discovery potential as function of the required collected luminosity and for various models.

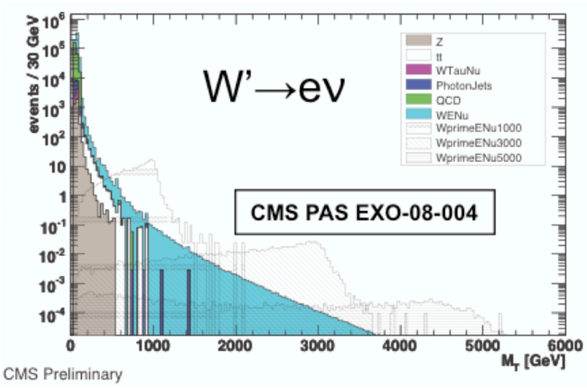

Figure 15. W' resonances production for differentes masses with the CMS detector

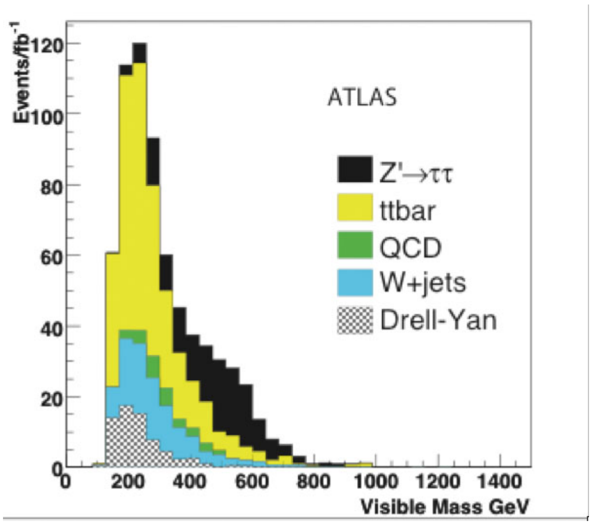

Figure 16. $Z' \rightarrow \tau\tau$ resonance producton in the Atals experiment.

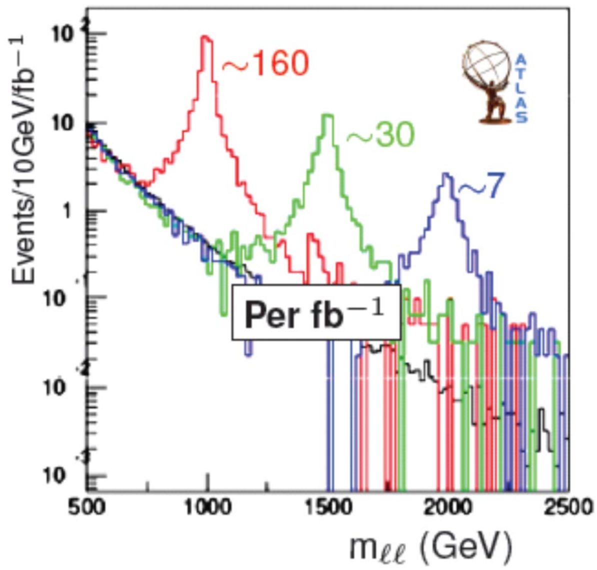

Figure 17. e^+e^- invariant mass spectrum for a 100 pb^{-1} integrated luminosity with 1, 1.5 and 2 TeV/c^2 Z signal, compared to SM background estimates for the Drell-Yan process, $\bar{t}t$, QCD di-jet, W+jet, γ+jet and $\gamma\gamma$.

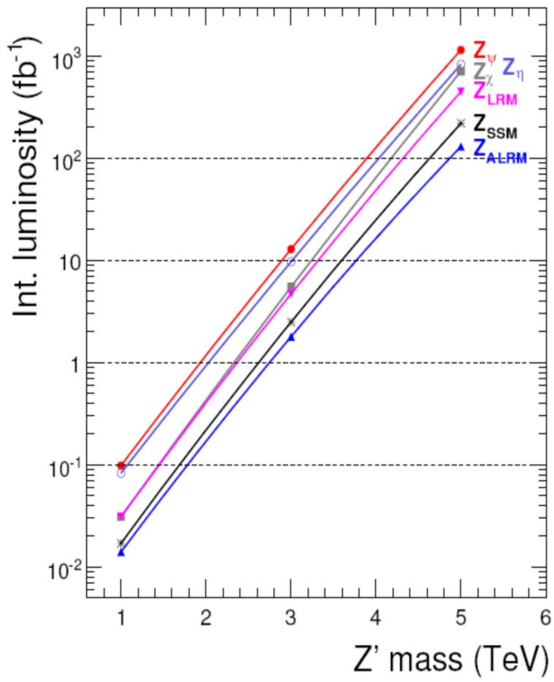

Figure 18. Z' mass sensibility, for viarious models, as function of the integrated luminosity

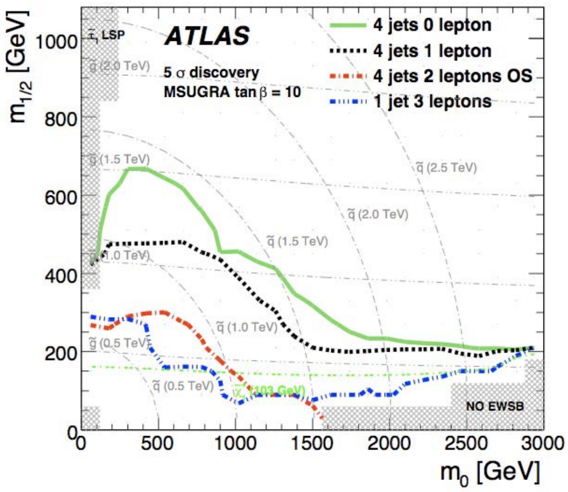

Figure 19. The 5σ discovery reach in the plane $(m_0;\ m_{1/2})$ in the case of four jets with one or more leptons in the final state and missing energy

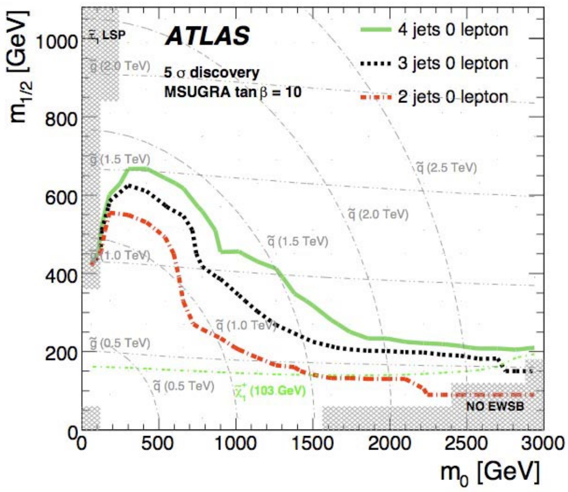

Figure 20. The $5sigma$ discovery reach in the plane $(m_0; m_{1/2})$ in the case of four jets with one or more leptons in the final state and missing energy

4.2 Susy

Hints of supersymmetry [20] are looked for at LHC via the production of squarks and gluinos, the supersymmetric partners of quark and gluons of the SM. The final state topologies of the supersymmetric events at LHC consist of multiple jets, often very energetic, with possibly some leptons and missing energy in the final state or simply with many leptons and missing energy. Most of the studies performed in CMS and ATLAS were done in the context of the Minimal Supersymmetric Standard Model (MSSM) with R-parity conservation and in the scenario of heavy squarks and gluinos. In order to reduce the number of free parameters of MSSM the hypotheses of minimal Supergravity (mSUGRA [21]) are used, in particular by assuming a common sfermion mass at GUT scale (m_0) and a common gaugino mass $(m_{1/2})$. Prospective analyses were developed to search for final states including jets, leptons and missing energy both in CMS [10] and in the ATLAS collaboration [25]. Typically some benchmark points of the parameter space of MSSM with mSUGRA hypotheses are used as starting points and scans of parameters around them is performed to derive conservative limits.

Concerning ATLAS [31] analyses, one possible inclusive signature consist of four jets and missing energy. The main backgrounds are $\bar{t}t$ and W/Z+jets events. Simple selection cuts are applied on the total transverse momentum of the jets, on the missing transverse energy, on the angle between the jet and the missing energy directions and on the effective mass of transverse momentum of the jets and leptons and missing transverse energy. Final state topologies with less than four jets and with one or more leptons were also studied. In figure 19 is reported the 5σ discovery reach in the plane $(m_0;\ m_{1/2})$ in the case of four jets with one or more leptons in the final state and missing energy; zero-lepton mode can probe close to 1.5 TeV for the minimum between the squark and the gluino mass, with 1 fb^{-1} of integrated luminosity; the four-jets topology seems to give the best results in zero-lepton mode, as derived from figure 20. Therefore ATLAS could discover signals with gluino and squark masses less than O(1 TeV) after having accumulated an integrated luminosity of about 1 fb^{-1}.

4.3 Higgs hunting

Direct searches for the SM Higgs particle at the LEP e^+e^- collider have led to a lower mass bound of $m_H > 114.4 GeV/c^2$ at 95% C.L. [27]. On-going direct searches at the Tevatron $\overline{p}p$ collider by the D0 and CDF experiments set constraints on the production cross-section for a SM-like Higgs boson in a mass range extending up to about 200 GeV/c^2 and allow to exclude his existence [28] with mass between 160 and 170 GeV/c^2. The main production mechanisms for SM Higgs particle at LHC are the gluon-gluon fusion mechanism, the associated production with W/Z bosons, the weak vector boson fusion processes and the associated Higgs production with heavy top or bottom quarks, as detailed in Ref. [29]. SM Higgs couples to fermions, gauge bosons and to itself. In the low mass region (namely $m_H < 130 GeV/c^2$) the dominant decay is in $\bar{b}b$ with a branching ratio between 60 and 90 %; $H \to \tau^+\tau^-, c\bar{c}, \gamma\gamma$ contribution to the total width is less that few %. In the high mass range the decay channels $H \to WW^*$ and $H \to ZZ^*$ play the main role given a clear signature of multi leptons in the final state. A prospective analysis about the $H \to WW \to ll\nu\nu$ decay chain was performed both in CMS [30] and in ATLAS [5]. The signature consists of two isolated high momentum leptons and missing energy related to the neutrinos escaping the detection. No hard jet in the central region of the acceptance is expected and it is not possible to reconstruct the Higgs mass peak due to the neutrinos. The main background comes from $\bar{t}t$

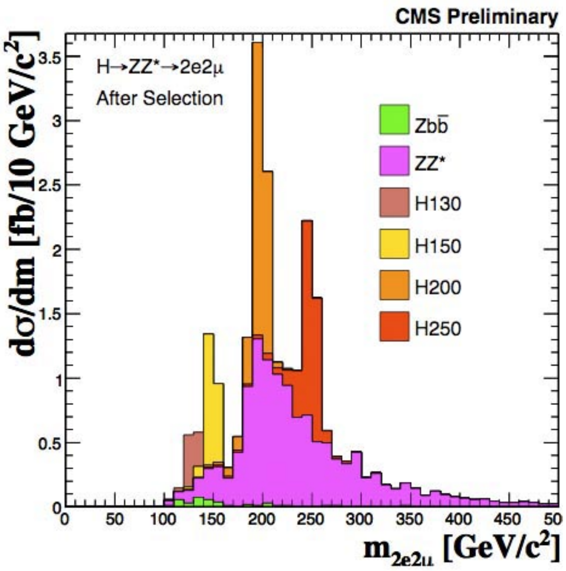

Figure 21. $2e2\mu$ invariant mass after the full selection corresponding to an integrated luminosity of 1 fb^{-1}.

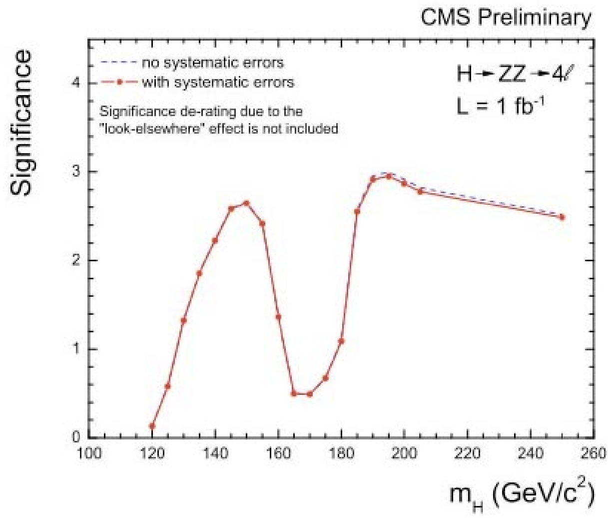

Figure 22. Significance for the signal observation in the $H \to ZZ \to 4l$ channel with an integrated luminosity of $1fb^{-1}$.

and di-boson events, di-leptons Drell-Yan type, tW and W+jets events in the topologies including two leptons in the final state. The analysis mainly consists of selecting events with high transverse momentum leptons and sufficient missing energy; a central jet veto strategy is used to select events with no hard jet in central rapidity region and the angular correlation between the leptons coming from Higgs decays is used as a discriminating observable.

In the case of $H \to ZZ$ decay channel, the topology of four leptons in the final state (electron and/or muons) was studied with an integrated luminosity of 1 and 30 fb^{-1} for CMS [32] and ATLAS [5] respectively; the irreducible background comes from the ZZ events with four leptons in the final state while contribitions from $Z\bar{b}b$ and $\bar{t}t$ events could be reduced. The four-lepton invariant mass spectrum obtained in the case $2e2\mu$ final state at the end of the selection is reported in figure 21. The significance for the signal observation with an integrated luminosity of 1 fb^{-1} is reported in figure 22, as obtained by the CMS collaboration.
Even if the branching ratio of the decay in two photons $H \to \gamma\gamma$ is less than % at low Higgs mass the clear signature of the final state makes that topology very promising. Background events come from the production of two isolated photons, which are usually referred to as irreducible, while reducible background sources are events with at least one fake photon. Fake photons are mostly due to the presence of a leading π^0 resulting from the fragmentation of a quark or a gluon.

5 Conclusions

The LHC is foreseen to deliver the first pp collisions in 2009. The ATLAS and CMS detector are ready for the first collision. Both luminosity and energy, hence cross sections, at the LHC will be much higher with respect to earlier experiments, meaning that soon very high statistics will be available, and the experiments will be soon sensitive to rare processes, including non-SM ones. To exploit the data it is important to understand rapidly the data and detectors response. For this, known particles will act as standard candles. Before claiming eventual discoveries, the CMS and ATLAS collaborations will have first to re-establish the SM, e.g., parameters related to Parton Distribution Functions, or to soft hadronic physics, or particular regions of kinematics for some final states which are also explored in beyond-SM searches.

Several interesting physics topics which can be pursued with both ATLAS and CMS with integrated luminosities between 10 and 1000 pb^{-1} have shortly been described. We all look forward to seeing the first data at energies never accessible before at a collider !

Acknowledgements. I thank all the authors of the specific CMS and Atlas studies reported in this paper, I would like also to thank the conference organizers for the invitation to give this talk.

References

[1] Lyndon Evans and Philip Bryant (editors), LHC Machine, 2008 JINST 3 S08001.

[2] Cross Sections in pp collisions at $\sqrt{s} = 14$ TeV, CMS Physics Analysis Summary EWK-07-001.

[3] The CMS experiment at the CERN LHC, CMS Collaboration, JINST 3 S08004, 2008.

[4] The ATLAS experiment at the CERN LHC, ATLAS Collaboration, JINST 3 S08003, 2008.

[5] Expected Performance of the ATLAS Experiment : Detector, Trigger and Physics, ATLAS Collaboration, CERN-OPEN-2008-020.

[6] The CMS Collaboration,Measurement of charged hadron spectra in pp collisions atps =14 TeV, CMS PAS QCD-07-001.

[7] C. Liu, N. Neumeister, Reconstruction of Cosmic and Beam-Halo Muons, CMS NOTE 2008/001

[8] The CMS Collaboration, Measurement of the Underlying Event in Jet Topologies using Charged Particle and Momentum Densities, CMS PAS QCD-07-003.

[9] A. Bhatti et al., CMS search plans and sensitivity to new physics with dijets, CMS NOTE 2008/019, J. Phys. G: Nucl. Part. Phys. 36 015004 [arXiv:hep-ex/0807.4961].

[10] SUSY searches with dijet events, CMS Collaboration, CMS PAS SUS-08-005.

[11] N. Brambilla et al, Heavy Quarkonium Physics, CERN Yellow Report, CERN-2005-005, [arXiv:hepph/ 0412158]. • CMS Collaboration, Charmonium production cross-section, CMS Physics Analysis Summary BPH-07-002.

[12] CMS Collaboration, Towards a measurement of the inclusive W $\rightarrow \mu\nu$ and Z $\rightarrow \mu^+\mu^-$ cross sections in pp collisions at $\sqrt{s} = 14$ TeV, CMS Physics Analysis Summary EWK-07-002.

[13] CMS Collaboration, Observability of Top Quark Pair Production in the Semileptonic Muon Channel with the first 10 pb^{-1} of CMS Data, CMS Physics Analysis Summary TOP-08-005. • S. C. M. Bentvelsen and M. Cobal, Top studies for the Atlas detector commissioning, ATL-PHYS-PUB-2005-024, ATL-COM-PHYS-2005-039, CERN, Geneva, 2005.

[14] K. D. Lane, Electroweak and Flavor Dynamics at Hadron Colliders [arXiv:hepph/9605257].

[15] CMS Collaboration, Search for high mass resonance production decaying into an electron pair in the CMS experiment, CMS Physics Analysis Summary EXO-08-001.

[16] K. Lane and S. Mrenna, The Collider Phenomenology of Technihadrons in the Technicolor Straw Man Model, Phys. Rev. D 67, 115011 (2003) [arXiv:hepph/0210299].

[17] L. Randall and R. Sundrum, A Large Mass Hierarchy from a Small Extra Dimension, Phys. Rev. Lett. 83, 3370 (1999) [arXiv:hepph/9905221]. • Search for high mass resonance production decaying into an electron pair in the CMS experiment, CMS Collaboration, CMS PAS EXO-08-001.

[18] T. Han, H. E. Logan, B. McElrath, L.-T. Wang, Phenomenology of the Little Higgs Model, Phys. Rev. D67 (2003) 095004 [arXiv:hepph/0301040].

[19] CMS Collaboration, Search for high mass resonance production decaying into an electron pair in the CMS experiment, CMS Physics Analysis Summary EXO-08-001.

[20] P. Fayet, Phys. Lett. B 64, 159 (196); P. Fayet, Phys. Lett. B 69, 489 (1977), Phys. Lett. B 84, 416 (1979); G.R. Farrar and P. Fayet, Phys. Lett. B 76, 575 (1978).

[21] H.P. Nilles, Phys. Rev. C 110, 1 (1984).

[22] G. Altarelli, B. Mele and M. Ruiz-Altaba, Searching for new heavy vector bosons IN PP COLLIDERS, Z. Phys. C45 (1989) 109.

[23] CMS Collaboration, Discovery potential of $W' \rightarrow e\nu$ at CMS, CMS Physics Analysis Sum. EXO-08-004.

[24] CMS Collaboration, Search for new high mass resonances decaying to muon pairs in the CMS experiment, CMS Physics Analysis Summary SBM-07-002.

[25] Prospects for SUSY discovery based on inclusive searches with the ATLAS detector, ATLAS Collaboration, ATL-PHYS-PROC-2009-038; ATL-COM-PHYS-2009-035.

[26] S. Dimopoulos and H. Georgi, NPB 193, 150 (1981)

[27] [3] R. Barate et al., LEP Working Group for Higgs boson searches, Search for the standard model Higgs boson at LEP, Phys. Lett. B 565, 61 (2003), arXiv:hep-ex/0306033.

[28] The TEVNPH Working Group for the CDF and D0 Collaborations, Combined CDF and D0 Upper Limits on Standard Model Higgs-Boson Production with up to 4.2 fb^{-1} of Data, FERMILAB-PUB-09-060-E, CDF Note 9713, D0 Note 5889, arXiv:0903.4001v1.

[29] The Anatomy of ElectroWeak Symmetry Breaking, LPT-Orsay-05-17 March 2005, arXiv:hepph/0503172v2.

[30] Search Strategy for a Standard Model e Higgs Boson Decaying to Two W Bosons in the Fully leptonic Final State, CMS Collaboration, CMS PAS HIG-08-006.

[31] Epected Performence of the Atlas Experiment : Detector, Trigger, Physics. ATLAS Collaboration. CERN-OPEN-2008-003.

[32] Search strategy for the Higgs boson in the ZZ^* decay 5 channel with the CMS experiment, CMS Collaboration, CMS PAS HIG-08-003.

Proceedings of the International School-seminar
"New Physics and Quantum Chromodynamics at external Conditions", pp. 42 – 47,
3-6 May 2009, Dnipropetrovsk, Ukraine

RARE DECAY $\pi^0 \to E^+E^-$ AS A TEST OF STANDARD MODEL

A.E. Dorokhov[a]

Joint Institute for Nuclear Research, Bogoliubov Laboratory of Theoretical Physics
114980, Moscow region, Dubna, Russia

Experimental and theoretical progress concerning the rare decay $\pi^0 \to e^+e^-$ is briefly reviewed. It includes the latest data from KTeV and a new model independent estimate of the decay branching which show the deviation between experiment and theory at the level of 3.3σ. The predictions for η and η' decays into lepton pair are presented. We also comment on the impact on the pion rare decay estimate of the data of BABAR collaboration on the pion transition form factor at large momentum transfer.

1 Introduction

Astrophysics observables tell us that 95% of the matter in the Universe is not described in terms of the Standard Model (SM) matter. Thus, the search for the traces of New Physics is a fundamental problem of particle physics. There are two strategies to look for the effects of New Physics: experiments at high energy and experiments at low energy. In high-energy experiments it is considered that due to a huge amount of energy the heavy degrees of freedom presumably characteristic of the SM extension sector are possible to excite. In low-energy experiments it is huge statistics that compensates the lack of energy by measuring the rare processes characteristic of such extensions. At present, there is no any evidence for deviation of SM predictions from the results of high-energy experiments and we are waiting for the LHC epoch. On the other hand, in low-energy experiments there are rough edges indicating such deviations. The most famous example is the muon $(g-2)$. Below it will be shown that due to recent experimental and theoretical progress the rare process $\pi^0 \to e^+e^-$ became a good SM test process and that at the moment there is a discrepancy between the SM prediction and experiment at the level of 3.3σ deviation.

2 KTeV data

In 2007, the KTeV collaboration published the result [1] for the branching ratio of the pion decay into an electron-positron pair

$$B^{\mathrm{KTeV}}_{\mathrm{no-rad}}\left(\pi^0 \to e^+e^-\right) = (7.48 \pm 0.38) \cdot 10^{-8}. \tag{1}$$

The result is based on observation of 794 candidate $\pi^0 \to e^+e^-$ events using $K_L \to 3\pi^0$ as a source of tagged π^0s. Due to a complicated chain of the process and a good technique for final state resolution used by KTeV this is a process with low background.

3 Classical theory of $\pi^0 \to e^+e^-$ decay

The rare decay $\pi^0 \to e^+e^-$ has been studied theoretically over the years, starting with the first prediction of the rate by Drell [2]. Since no spinless current coupling of quarks to leptons exists, the decay is described in the lowest order of QED as a one-loop process via the two-photon intermediate state, as shown in Fig. 1. A factor of $2\left(m_e/m_\pi\right)^2$ corresponding to the approximate helicity conservation of the interaction and two orders of α suppress the decay with respect to the $\pi^0 \to \gamma\gamma$ decay, leading to an expected branching ratio of about 10^{-7}. In the Standard Model contributions from the weak interaction to this process are many orders of magnitude smaller and can be neglected.

To the lowest order in QED the normalized branching ratio is given by

$$R\left(\pi^0 \to e^+e^-\right) = \frac{B\left(\pi^0 \to e^+e^-\right)}{B\left(\pi^0 \to \gamma\gamma\right)} = 2\left(\frac{\alpha}{\pi}\frac{m_e}{m_\pi}\right)^2 \beta_e\left(m_\pi^2\right)\left|\mathcal{A}\left(m_\pi^2\right)\right|^2, \tag{2}$$

where $\beta_e\left(q^2\right) = \sqrt{1-4\frac{m_e^2}{q^2}}$, $B\left(\pi^0 \to \gamma\gamma\right) = 0.988$. The amplitude $\mathcal{A}$ can be written as

e-mail: [a]dorokhov@theor.jinr.ru, This is an extended version of the talk.

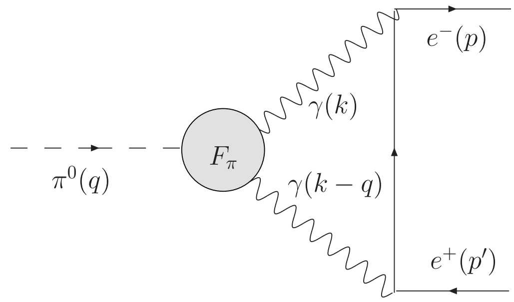

Figure 1. Triangle diagram for the $\pi^0 \to e^+e^-$ process with a pion $\pi^0 \to \gamma^*\gamma^*$ form factor in the vertex.

$$\mathcal{A}\left(q^2\right) = \frac{2i}{q^2}\int \frac{d^4k}{\pi^2} F_{\pi\gamma^*\gamma^*}\left(k^2,(k-q)^2\right) \frac{q^2k^2-(qk)^2}{\left(k^2+i\varepsilon\right)\left((k-q)^2+i\varepsilon\right)\left((k-p)^2-m_e^2+i\varepsilon\right)}, \tag{3}$$

$$\tag{4}$$

where $q^2 = m_\pi^2, p^2 = m_e^2$. $F_{\pi\gamma^*\gamma^*}$ is the form factor of the transition $\pi^0 \to \gamma^*\gamma^*$ with off-shell photons.

The imaginary part of $\mathcal{A}$ is defined uniquely as

$$\begin{aligned} \mathrm{Im}\mathcal{A}\left(q^2\right) &= \frac{\pi}{2\beta_e\left(q^2\right)} \ln\left(y_e\left(q^2\right)\right), \\ y_e\left(q^2\right) &= \frac{1-\beta_e\left(q^2\right)}{1+\beta_e\left(q^2\right)}. \end{aligned} \tag{5}$$

It comes from the contribution of real photons in the intermediate state and is model independent since $F_{\pi\gamma^*\gamma^*}(0,0) = 1$. Using inequality $|\mathcal{A}|^2 \geq (\mathrm{Im}\mathcal{A})^2$ one can get the well-known unitary bound for the branching ratio [3]

$$B\left(\pi^0 \to e^+e^-\right) \geq B^{\text{unitary}}\left(\pi^0 \to e^+e^-\right) = 4.69 \cdot 10^{-8}. \tag{6}$$

One can attempt to reconstruct the full amplitude by using a once-subtracted dispersion relation [5]

$$\mathcal{A}\left(q^2\right) = \mathcal{A}\left(q^2=0\right) + \frac{q^2}{\pi}\int_0^\infty ds \frac{\mathrm{Im}\mathcal{A}(s)}{s\left(s-q^2\right)}. \tag{7}$$

If one assumes that Eq. (5) is valid for any q^2, then one arrives for $q^2 \geq 4m_e^2$ at [6, 7, 8]

$$\mathrm{Re}\mathcal{A}\left(q^2\right) = \mathcal{A}\left(q^2=0\right) + \frac{1}{\beta_e\left(q^2\right)}\left[\frac{1}{4}\ln^2\left(y_e\left(q^2\right)\right) + \frac{\pi^2}{12} + \mathrm{Li}_2\left(-y_e\left(q^2\right)\right)\right], \tag{8}$$

where $\mathrm{Li}_2(z) = -\int_0^z (dt/t)\ln(1-t)$ is the dilogarithm function. The second term in Eq. (8) takes into account a strong q^2 dependence of the amplitude around the point $q^2 = 0$ occurring due to the branch cut coming from the two-photon intermediate state. In the leading order in $(m_e/m_\pi)^2$, Eq. (8) reduces to

$$\mathrm{Re}\mathcal{A}\left(m_\pi^2\right) = \mathcal{A}\left(q^2=0\right) + \ln^2\left(\frac{m_e}{m_\pi}\right) + \frac{\pi^2}{12}. \tag{9}$$

Thus, the amplitude is fully reconstructed up to a subtraction constant. Usually, this constant containing the nontrivial dynamics of the process is calculated within different models describing the form factor $F_\pi(k^2,q^2)$ [4, 5, 7, 9, 10]. However, it has recently been shown in [10] that this constant may be expressed in terms of the inverse moment of the pion transition form factor given in symmetric kinematics of spacelike photons

$$\mathcal{A}\left(q^2=0\right) = 3\ln\left(\frac{m_e}{\mu}\right) - \frac{5}{4} - \frac{3}{2}\left[\int_0^{\mu^2} dt \frac{F_{\pi\gamma^*\gamma^*}(t,t)-1}{t} + \int_{\mu^2}^\infty dt \frac{F_{\pi\gamma^*\gamma^*}(t,t)}{t}\right]. \tag{10}$$

Here, μ is an arbitrary (factorization) scale. One has to note that the logarithmic dependence of the first term on μ is compensated by the scale dependence of the integrals in the brackets. In this way two independent processes becomes related.

4 Importance of CLEO data on $F_{\pi\gamma^*\gamma}$

In order to estimate the integral in Eq. (10), one needs to define the pion transition form factor in symmetric kinematics for spacelike photon momenta. Since it is unknown from the first principles, we will adapt the available experimental data to perform such estimates. Let us first use the fact that $F_{\pi\gamma^*\gamma^*}(t,t) < F_{\pi\gamma^*\gamma^*}(t,0)$ for $t>0$ in order to obtain the lower bound of the integral in Eq. (10). For this purpose, we take the experimental results from the CELLO [11] and CLEO [12] Collaborations for the pion transition form factor in asymmetric kinematics for spacelike photon momentum which is well parameterized by the monopole form [12]

$$\begin{aligned} F^{\text{CLEO}}_{\pi\gamma^*\gamma^*}(t,0) &= \frac{1}{1+t/s_0^{\text{CLEO}}}, \\ s_0^{\text{CLEO}} &= (776\pm 22 \quad \text{MeV})^2 . \end{aligned} \tag{11}$$

For this type of the form factor one finds from Eq. (10) that

$$\mathcal{A}\left(q^2=0\right) > -\frac{3}{2}\ln\left(\frac{s_0^{\text{CLEO}}}{m_e^2}\right) - \frac{5}{4} = -23.2\pm 0.1. \tag{12}$$

Thus, for the branching ratio we are able to establish the important lower bound which considerably improves the unitary bound given by Eq. (6)

$$B\left(\pi^0 \to e^+e^-\right) > B^{\text{CLEO}}\left(\pi^0 \to e^+e^-\right) = (5.84\pm 0.02)\cdot 10^{-8}. \tag{13}$$

It is natural to assume that the monopole form is also a good parametrization for the form factor in symmetric kinematics

$$F_{\pi\gamma^*\gamma^*}(t,t) = \frac{1}{1+t/s_1}. \tag{14}$$

The scale s_1 can be fixed from the relation for the slopes of the form factors in symmetric and asymmetric kinematics at low t [13],

$$-\frac{\partial F_{\pi\gamma^*\gamma^*}(t,t)}{\partial t}\bigg|_{t=0} = -2\frac{\partial F_{\pi\gamma^*\gamma^*}(t,0)}{\partial t}\bigg|_{t=0}, \tag{15}$$

that gives $s_1 = s_0/2$. Note that a similar reduction of the scale is also predicted by OPE QCD from the large momentum behavior of the form factors: $s_1^{OPE} = s_0^{OPE}/3$ [14]. Thus, the estimate for $\mathcal{A}(0)$ can be obtained from Eq. (12) by shifting the lower bound by a positive number which belongs to the interval $[3\ln(2)/2, 3\ln(3)/2]$

$$\mathcal{A}\left(q^2=0\right) = -\frac{3}{2}\ln\left(\frac{s_1}{m_e^2}\right) - \frac{5}{4} = -21.9\pm 0.3. \tag{16}$$

With this result the branching ratio becomes

$$B\left(\pi^0 \to e^+e^-\right) = (6.23\pm 0.09)\cdot 10^{-8}. \tag{17}$$

This is 3.3 standard deviations lower than the KTeV result given by Eq. (1).

5 Other decay modes

The $\eta \to l^+l^-$ decay can be analyzed in a similar manner. As in the pion case, the CLEO Collaboration has parameterized the data for the η-meson in the monopole form [12]:

$$\begin{aligned} F^{\text{CLEO}}_{\eta\gamma^*\gamma^*}(t,0) &= \frac{1}{1+t/s_{0\eta}^{\text{CLEO}}}, \\ s_{0\eta}^{\text{CLEO}} &= (774\pm 29 \quad \text{MeV})^2 , \end{aligned} \tag{18}$$

which is very close to the relevant pion parameter. Then following the previous case (with evident substitutions), one finds the bounds for the $q^2 \to 0$ limit of the amplitude $\eta \to \mu^+\mu^-$ as

$$\mathcal{A}_\eta\left(q^2=0\right) > -\frac{3}{2}\ln\left(\frac{s_{0\eta}^{\text{CLEO}}}{m_\mu^2}\right) - \frac{5}{4} = -(7.2\pm 0.1), \tag{19}$$

and for $\eta \to e^+e^-$ one gets again Eq. (12). The obtained estimates allow one to find the bounds for the branching ratios

$$\begin{aligned} B\left(\eta \to \mu^+\mu^-\right) &< (6.23\pm 0.12)\cdot 10^{-6}, \\ B\left(\eta \to e^+e^-\right) &> (4.33\pm 0.02)\cdot 10^{-9}. \end{aligned} \tag{20}$$

It is important to note that for the decay $\eta \to \mu^+\mu^-$ we get the upper limit for the branching. This is because the real part of the amplitude for this process taken at the physical point $q^2 = m_\eta^2$ for the parameter $s_{0\eta}^{\mathrm{CLEO}}$ remains negative and a positive shift due to the change of the scale $s_{0\eta} \to s_{1\eta}$ reduces the absolute value of the real part of the amplitude $\left|\mathrm{Re}\mathcal{A}\left(m_\eta^2\right)\right|$. At the same time, considering the decays of π^0 and η into an electron-positron pair, the evolution to physical point (8) makes the real part of the amplitude to be positive for the parameter s_0^{CLEO} and the absolute value of the real part of the amplitude increases in changing the scales of the meson form factors.

The predicted branchings are given in the Table and compared with existing experimental data. The so-called unitary bound appears if in (2) only the imaginary part of the amplitude which is model independent is taken into account. The CLEO bound corresponds to the estimate of the real part of the amplitude basing on the CELLO and CLEO data on the meson transition from factors [10]. The fourth column of the Table contains the predictions where in addition the constraint from OPE QCD on the transition form factor for arbitrary photon virtualities is taken into account[10].

The results that take into account the mass corrections to the amplitude [20], mainly due to powers $(M/\Lambda)^2$, where M is the pseudoscalar meson mass and $\Lambda \approx M_\rho$ is characteristic scale of the pion transition form factor, are given in the fifth column of the Table. They are essentially visible for $\eta\,(\eta')$ meson decays. It is interesting that for η decay to muons the mass correction shifts the theoretical prediction in the direction to the unitary bound and thus opposite to the experimental result [16]. Thus, it would be very desirable to check experimentally the predicted bounds for the process $\eta \to \mu^+\mu^-$. Also note the recent measurement by the WASA/Celcius Collaboration [15] which improves the upper limit for the branching $\eta \to e^+e^-$.

For η' decays there appear new thresholds in addition to the two-photon one. In general, this violates the unitary bound because the correction A_z gains an imaginary part at $z = (M/\Lambda)^2 > 1$

$$\Delta\Im\mathcal{A} = -\frac{\pi}{\beta}\left(1 - \frac{1}{z}\right)^2 \ln\left(\frac{1+\beta}{1-\beta}\right)\Theta(z-1). \tag{21}$$

As it is seen from the table, this happens for the $\eta' \to \mu\mu$ channel. Nevertheless, it turns out that the predictions for this channel are quite accurate.

Table 1. Values of the branchings $B\left(P \to l^+l^-\right)$ obtained in our approach and compared with the available experimental results.

R_0	Unitary bound	CLEO bound	CLEO+OPE [10]	[20]	Experiment
$R_0\left(\pi^0 \to e^+e^-\right) \times 10^8$	≥ 4.69	$\geq 5.85 \pm 0.03$	6.23 ± 0.12	6.26	7.49 ± 0.38 [1]
$R_0\left(\eta \to \mu^+\mu^-\right) \times 10^6$	≥ 4.36	$\leq 6.23 \pm 0.12$	5.12 ± 0.27	4.64	5.8 ± 0.8 [16]
$R_0\left(\eta \to e^+e^-\right) \times 10^9$	≥ 1.78	$\geq 4.33 \pm 0.02$	4.60 ± 0.09	5.24	$\leq 2.7 \cdot 10^4$ [15]
$R_0\left(\eta' \to \mu^+\mu^-\right) \times 10^7$	≥ 1.35	$\leq 1.44 \pm 0.01$	1.364 ± 0.010	1.30	
$R_0\left(\eta' \to e^+e^-\right) \times 10^{10}$	≥ 0.36	$\geq 1.121 \pm 0.004$	1.178 ± 0.014	1.86	

6 Possible explanations of the effect

Therefore, it is extremely important to trace possible sources of the discrepancy between the KTeV experiment and theory. There are a few possibilities: (1) problems with (statistic) experiment procession, (2) inclusion of QED radiation corrections by KTeV is wrong, (3) unaccounted mass corrections are important, and (4) effects of new physics. At the moment, the last possibilities were reinvestigated. In [17], the contribution of QED radiative corrections to the $\pi^0 \to e^+e^-$ decay, which must be taken into account when comparing the theoretical prediction (17) with the experimental result (1), was revised. Comparing with earlier calculations [18], the main progress is in the detailed consideration of the $\gamma^*\gamma^* \to e^+e^-$ subprocess and revealing of dynamics of large and small distances. Occasionally, this number agrees well with the earlier prediction based on calculations [18] and, thus, the KTeV analysis of radiative corrections is confirmed. In [19, 20] it was shown that the mass corrections are under control and do not resolve the problem. So our main conclusion is that the inclusion of radiative and mass corrections is unable to reduce the discrepancy between the theoretical prediction for the decay rate (17) and experimental result (1).

7 $\pi^0 \to e^+e^-$ decay as a filtering process for low mass dark matter

If one thinks about an extension of the Standard Model in terms of heavy, of an order of 100 GeV or higher, particles, then the contribution of this sort of particles to the pion decay is negligible. However, there is a class of models for description of Dark Matter with a mass spectrum of particles of an order of 10 MeV [26]. This model postulates a neutral scalar dark matter particle χ which annihilates to produce electron/positron pairs:

$\chi\chi \to e^+e^-$. The excess positrons produced in this annihilation reaction could be responsible for the bright 511 keV line emanating from the center of the galaxy [27]. The effects of low mass vector boson U appearing in such model of dark matter were considered in [28] where the excess of KTeV data over theory put the constraint on coupling which is consistent with that coming from the muon anomalous magnetic moment and relic radiation [29]. Thus, the pion decay might be a filtering process for light dark matter particles.

8 Constraints from BABAR data

Let us now consider the amplitude $\pi^0 \to e^+e^-$ in the context of the constituent quark model [22, 23]. Within this model, the pion form factor is given by the quark-loop (triangle) (Fig. 1) diagram with momentum independent constituent quark mass. The result for the form factor in symmetric kinematics is given by [23]

$$F_{\pi\gamma^*\gamma^*}(t,t) = \frac{2M_Q^2}{\beta_Q t} \ln \frac{\beta_Q + 1}{\beta_Q - 1}, \tag{22}$$

where $\beta_Q = \sqrt{1 + \frac{4M_Q^2}{t}}$, and the amplitude at zero is

$$\mathcal{A}(0) = \frac{3}{2} \ln(\frac{m_e^2}{M_Q^2}) - \frac{17}{4}. \tag{23}$$

It is interesting to remind that in asymmetric kinematics the form factor has double logarithmic asymptotics at large momentum transfer $log^2(Q^2/M_q^2)$ [23]

$$F_{\pi\gamma\gamma^*}(t,0) = \frac{m_\pi^2}{m_\pi^2 + t} \frac{1}{2\arcsin^2(\frac{m_\pi}{2M_Q})} \{2\arcsin^2(\frac{m_\pi}{2M_Q}) + \frac{1}{2} \ln^2 \frac{\beta_Q + 1}{\beta_Q - 1}\}. \tag{24}$$

Recently BABAR collaboration announced new data [21] on pion transition form factor $F_{\pi\gamma\gamma^*}(t,0)$ at very large t up to 40 GeV^2. The data are in strong contradiction with massless QCD predicting asymptotic $1/t$ behavior with single logariphmic modulation in leading order. However, the BABAR data are well fitted by (24) if the parameter M_Q is taken as $M_Q = 135$ MeV. Then the amplitude at zero is $\mathcal{A}(0) = -20.98$ which is still far from numbers corresponding to KTeV: $\mathcal{A}(0) = -18.6 \pm 0.9$. In [24] it was also noted that in order to get reasonable estimate of the hadronic vacuum polarization to the anomalous magnetic moment of muon it is necessary to take the quark mass rather small $M_Q = 180$ MeV, the value which is close to the pion mass.

Within perturbative QCD one possible scenario to explain the form factor growth faster than expected is to assume that the full resummation of perturbative logarithms is important[1]. Indeed, sometime ago Manohar augmented [25] that for the pion transition form factor in kinematics when one photon is virtual and other is quasireal the resummation effects dominate its behavior at large fixed Q^2 and probably BABAR (if confirmed) observes these effects (logarithmic or powerlike).

5

Further independent experiments at KLOE, NA48, WASAatCOSY, BES III and other facilities will be crucial for resolution of the problem with the rare leptonic decays of light pseudoscalr mesons. Also it is important to confirm the theoretical base for maximally model independent prediction of the branchings by getting more precise data on the pion transition form factor in asymmetric as well in symmetric kinematics in wider region of momentum transfer that is soon expected from BABAR and BELLE collaborations.

Acknowledgements. We are grateful to the Organizers and personally professor V. Skalozub for a nice meeting and kind invitation to present our results.

References

[1] E. Abouzaid et al. Phys. Rev. **D75** (2007) 012004.
[2] S. Drell, Nuovo Cim. **XI** (1959) 693.
[3] M. Berman and D.A. Geffen, Nuovo Cim. **XVIII** (1960) 1192.
[4] L. Bergstrom, Z. Phys. **C14** (1982) 129.
[5] L. Bergstrom, E. Masso, L. Ametlier and A. Ramon, Phys. Lett. **B126** (1983) 117.
[6] G. D'Ambrosio and D. Espriu, Phys. Lett. **B175**, 237 (1986).
[7] M. J. Savage, M. E. Luke, and M. B. Wise, Phys. Lett. **B291**, 481 (1992), hep-ph/9207233.
[8] L. Ametller, A. Bramon, and E. Masso, Phys. Rev. **D48**, 3388 (1993), hep-ph/9302304.
[9] G. V. Efimov, M. A. Ivanov, R. K. Muradov, and M. M. Solomonovich, JETP Lett. **34**, 221 (1981).
[10] A. E. Dorokhov and M. A. Ivanov, Phys. Rev. **D75** (2007) 114007.

[1] I am indebted to A.A. Pivovarov for discussion this point.

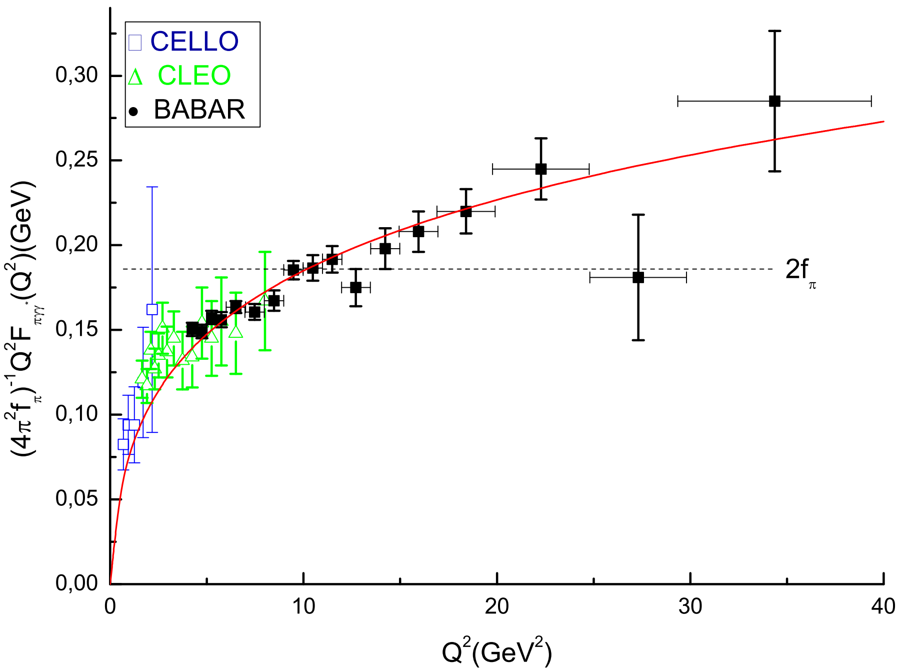

Figure 2. The transition form factor $\pi^0 \to \gamma^*\gamma$. The data are from CELLO [11], CLEO [12] and BABAR [21] Collaborations. The dashed line is massless QCD asymptotic limit. The solid line is the form factor calculated from massive triangle diagram, Eq. (24), with mass parameter taken as $M_q = 135$ MeV.

[11] H. J. Behrend *et al.* [CELLO Collaboration], Z. Phys. C **49** (1991) 401.

[12] CLEO, J. Gronberg *et al.*, Phys. Rev. **D57** (1998) 33.

[13] A. E. Dorokhov, A. E. Radzhabov and M. K. Volkov, Eur. Phys. J. A **21** (2004) 155 [arXiv:hep-ph/0311359].

[14] G. P. Lepage and S. J. Brodsky, Phys. Rev. D **22** (1980) 2157.

[15] M. Berlowski *et al.*, Phys. Rev. D **77** (2008) 032004.

[16] R. Abegg *et al.*, Phys. Rev. D **50** (1994) 92.

[17] A. E. Dorokhov, E. A. Kuraev, Yu. M. Bystritskiy and M. Secansky, Eur. Phys. J. C **55** (2008) 193, hep-ph/0801.2028.

[18] L. Bergstrom, Z. Phys. C **20** (1983) 135.

[19] A. E. Dorokhov and M. A. Ivanov, JETP Lett. **87** (2008) 531, hep-ph/0803.4493.

[20] A. E. Dorokhov, M. A. Ivanov and S. G. Kovalenko, arXiv:0903.4249 [hep-ph].

[21] Selina Li, Representing the BaBar Collaboration, Photon 2009 Conference, 11-15 May 2009, Hamburg, Germnany, http://photon09.desy.de; BABAR Collaboration, "Measurement of the $\gamma\gamma^* \to \pi^0$ transition form factor", arXiv:0905.4778.

[22] S. B. Gerasimov, Yad. Fiz. **29** (1979) 513 [Sov. J. Nucl. Phys. **29** (1979 ERRAT,32,156.1980) 259],

[23] L. Ametller, L. Bergstrom, A. Bramon and E. Masso, Nucl. Phys. B **228** (1983) 301.

[24] A. A. Pivovarov, Phys. Atom. Nucl. **66** (2003) 902 [Yad. Fiz. **66** (2003) 934] [arXiv:hep-ph/0110248].

[25] A. V. Manohar, Phys. Lett. B **244** (1990) 101.

[26] C. Boehm and P. Fayet, Nucl. Phys. B **683** (2004) 219 [arXiv:hep-ph/0305261].

[27] G. Weidenspointner *et al.*, arXiv:astro-ph/0601673.

[28] Y. Kahn, M. Schmitt, T. Tait, Phys. Rev. D **78** (2008) 115002, hep-ph/0712.0007.

[29] P. Fayet, Phys. Rev. **D75** 115017 (2007).

Proceedings of the International School-seminar
"New Physics and Quantum Chromodynamics at external Conditions", pp. 48 – 55,
3-6 May 2009, Dnipropetrovsk, Ukraine

DECONFINEMENT AND QCD CRITICAL POINT IN NUCLEUS-NUCLEUS COLLISIONS

Mark I. Gorenstein

Bogolyubov Institute for Theoretical Physics, Kiev, Ukraine

The energy dependence of hadron production in relativistic nucleus-nucleus collisions reveals the anomalies – *kink, horn*, and *step*. They have been predicted as the signals of the deconfinement phase transition and observed recently by NA49 collaboration in Pb+Pb collisions at the CERN SPS. This indicates the onset of the deconfinement in nucleus-nucleus collisions at about 30 A·GeV. The QCD critical point is expected to be experimentally seen as a non-monotonic dependence of the multiplicity fluctuations on atomic number A and/or bombarding energy E_{lab}.

1 Introduction

The data on nucleus-nucleus (A+A) collisions suggested that there is a significant change in the energy dependence of the pion and strangeness yields which is located between the top AGS (11 A·GeV) and SPS (158 A·GeV) energies. Based on the statistical approach it was speculated that the change is related to the onset of deconfinement at the early stage of A+A collisions, and a simplified quantitative model was developed, the Statistical Model of the Early Stage (SMES) [1]. The SMES predicted a sharp maximum in the multiplicity ratio of strange hadrons to pions at the beginning of the transition region. This prediction triggered a new experimental programme at the SPS – the energy scan programme – in which the NA49 experiment recorded central Pb+Pb collisions at several energies: 20, 30, 40, 80 and 158 A·GeV [2, 3]. The energy scan program at the CERN SPS results an observation of several 'anomalies' in the energy dependence of hadron production in the same domain of the collision energy. These 'anomalies' are interpreted as signals of the deconfinement phase transition in A+A collisions.

2 Signals of deconfinement: SMES predictions

An exact nature of the deconfinement phase transition may be different in different regions of the plane of temperature T and baryon chemical potential μ_B: a smooth crossover between hadron and quark-gluon phases at $\mu_B = 0$, and a 1-st order phase transition at large μ_B. A crossover seen from the lattice QCD at $\mu_B = 0$ corresponds to strong changes of the energy density ε in a narrow temperature interval $\Delta T \approx 10$ MeV. The energy density changes by about an order of magnitude, whereas the pressure remains approximately unchanged. Thus, even at $\mu_B = 0$, the deconfinement resembles a 1-st order transition. One may refer to the transition temperature interval as a 'generalized mixed phase'.

The *Kink* in Pion Multiplicity. The majority of all particles produced in high energy interactions are pions. Thus, pions carry basic information on the entropy created in the collisions. On the other hand, the entropy production should depend on the form of matter present at the early stage of collisions. A deconfined matter is expected to lead to the final state with higher entropy than that created by a confined matter. Consequently, it is natural to expect that the onset of creation of a deconfined matter should be signalled by an enhancement of the pion production. The simple intuitive argumentation can be further quantified within SMES assuming the generalized Fermi–Landau initial conditions: the initial volume is Lorenz-contracted, $V \propto \langle N_W \rangle \cdot (\sqrt{s_{NN}})^{-1}$, where $\sqrt{s_{NN}}$ is the c.m.s. energy of the nucleon pair. Clearly, a trivial dependence of the pion multiplicity on the size of colliding nuclei should be removed and thus a relevant observable is the ratio of the mean pion multiplicity $\langle \pi \rangle$ to the mean number of wounded nucleons $\langle N_W \rangle$. The initial energy density is given by $\varepsilon \propto gT^4 \propto (\sqrt{s_{NN}} - 2m_N) \cdot \sqrt{s_{NN}}$, where g is an effective number of internal degrees of freedom at the early stage and m_N is the nucleon mass. The pion multiplicity is proportional to the initial entropy, and the $\langle \pi \rangle / \langle N_W \rangle$ ratio can be thus calculated outside the transition region as

$$\frac{\langle \pi \rangle}{\langle N_W \rangle} \;\propto\; \frac{V\, g\, T^3}{\langle N_W \rangle} \;\propto g^{1/4} (\sqrt{s_{NN}} - m_N)^{3/4} (\sqrt{s_{NN}})^{-1/4} \;\equiv\; g^{1/4}\, F\ . \tag{1}$$

Therefore, the $\langle\pi\rangle/\langle N_W\rangle$ ratio increases linearly with Fermi's energy measure F outside the transition region, and the slope parameter is proportional to $g^{1/4}$ [4]. In the transition region, a steepening of the pion energy dependence is predicted, because of activation of partonic degrees of freedom, i.e. an effective number of internal degrees of freedom in the quark gluon plasma (QGP) is larger than in the hadron gas (HG): $g_{QGP} > g_{HG}$.

The *Horn* in Strangeness to Pion Ratio. The energy dependence of the strangeness to entropy ratio is a crucial signal of the deconfinement. The temperature dependence of a particle multiplicity is strongly dependent on the particle mass,

$$\langle N_i\rangle \;=\; \frac{g_i V}{2\pi^2}\int\limits_0^\infty p^2 dp\;\exp\left(-\;\frac{\sqrt{p^2+m_i^2}}{T}\right) \;=\; \frac{g_i V}{2\pi^2}\;m_i^2 T\;K_2\left(\frac{m_i}{T}\right)\;, \tag{2}$$

where g_i and m_i are respectively the degeneracy factor and particle mass, and K_2 is the modified Hankel function. For light hadrons ($m_l/T \ll 1$) one finds from Eq. (2), $\langle N_l\rangle \propto T^3$, whereas for heavy hadrons ($m_h/T \gg 1$) Eq. (2) leads to $\langle N_h\rangle \propto T^{3/2}\exp(-\,m_h/T)$. Within SMES at low collision energies, when the HG matter is produced, the strangeness to entropy ratio steeply increases with collision energy. This is due to a low temperature at the early stage and the high mass of the carriers of strangeness (the kaon mass). Thus, $m_K \gg T$ and the total strangeness is proportional to $T^{3/2}\exp(-\,m_K/T)$. On the other hand, the total entropy is approximately proportional to T^3. Therefore, the strangeness to pion ratio is approximately $T^{-3/2}\exp(-m_K/T)$ in the HG and strongly increases with the collision energy. When the transition to a deconfined matter is crossed, the mass of the strangeness carriers is significantly reduced ($m_s \cong 150$ MeV, the strange quark mass). Due to the low mass ($m_s < T$) the strangeness yield becomes approximately proportional to the entropy (both are proportional to T^3), and the strangeness to entropy (or pion) ratio becomes independent of energy in the QGP. This leads to a "jump" in the energy dependence from the larger value for confined matter to the value for deconfined matter. Thus, within the SMES, the non-monotonic energy dependence of the strangeness to entropy ratio is followed by a saturation at the deconfined value which is a direct consequence of the onset of deconfinement taking place at about 30 A·GeV [1].

The *Step* in Inverse Slope of Transverse Mass Spectra. The energy density at the early stage increases with increasing of collision energy. At low and high energies, when a pure confined or deconfined phase is produced, this leads to an increase of the initial temperature and pressure. This, in turn, results in an increase of the transverse expansion of a matter and consequently a flattening of the transverse mass spectra of final state hadrons. One may expect an 'anomaly' [5, 6, 7] in the energy dependence of the transverse hadron activity as the temperature and pressure are approximately constant in the mixed phase.

The experimental data on the transverse mass spectra are usually parameterized by a simple exponential dependence:

$$\frac{dN}{m_T dm_T} \;\cong\; C\;\exp\left(-\;\frac{m_T}{T^*}\right)\;, \tag{3}$$

where $m_T = (m^2+p_T^2)^{1/2}$. The inverse slope parameter T^* is sensitive to both the thermal and collective motion in the transverse direction. Hydrodynamical transverse flow with collective velocity v_T modifies the Boltzmann m_T-spectrum of hadrons. At low transverse momenta, it leads to the result (T_{kin} is a kinetic freeze-out temperature):

$$T^*_{low-p_T} \;\cong\; T_{kin} \;+\; \frac{1}{2}m\;v_T^2\;. \tag{4}$$

A linear mass dependence (4) of T^* is supported by the data for hadron spectra at small p_T. However, for $p_T >> m$ the hydrodynamical transverse flow leads to the mass-independent blue-shifted 'temperature':

$$T^*_{high-p_T} \;=\; T_{kin}\;\cdot\;\sqrt{\frac{1+v_T}{1-v_T}}\;. \tag{5}$$

Note that a simple exponential fit (3) neither works for light π-mesons, $T^*_{low-p_T}(\pi) < T^*_{high-p_T}(\pi)$, nor for heavy (anti)protons and (anti)lambdas, $T^*_{low-p_T}(p,\Lambda) > T^*_{high-p_T}(p,\Lambda)$ (see e.g., Refs. [8, 9]).

Kaons are the best and unique particles among measured hadron species for observing the effect of the modification of the equation of state due to the onset of the deconfinement in hadron transverse momentum spectra [7]. The arguments are the following: 1). the kaon m_T–spectra are only weakly affected by the hadron re-scattering and resonance decays during the post-hydrodynamic hadron cascade at the SPS and RHIC energies; 2). a simple one parameter exponential fit (3) is quite accurate for kaons in central A+A collisions at all energies, i.e. $T^*_{low-p_T}(K) \approx T^*_{high-p_T}(K)$ for kaons; 3). the high quality data on m_T-spectra of K^+ and K^- mesons in central Pb+Pb and Au+Au collisions are available in the full range of relevant energies. Thus, one expects [7] that T^* for kaons increases when either pure confined or deconfined phase is produced at the early stage of A+A collision, but T^* remains approximately constant when the initial matter is in a mixed phase state.

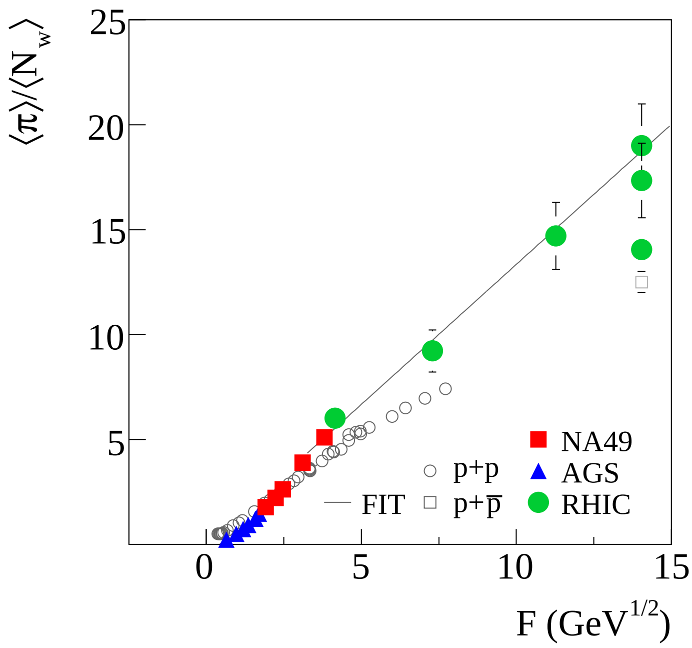

Figure 1. Energy dependence of the mean pion multiplicity per wounded nucleon measured in central Pb+Pb and Au+Au collisions (full symbols), compared to the corresponding results from $p + p(\bar{p})$ reactions (open symbols). The compilation of data is from Ref. [3].

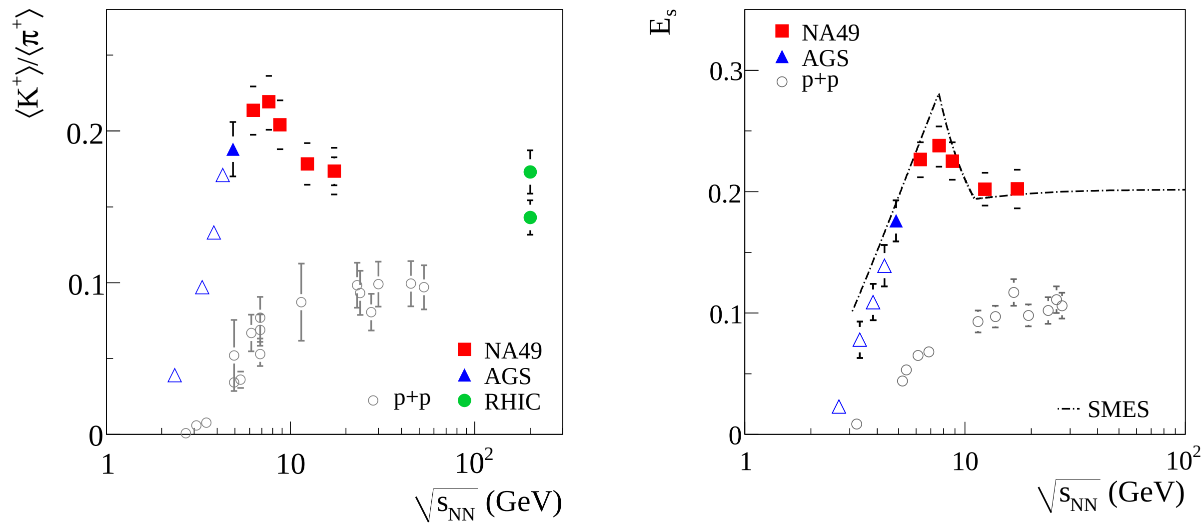

Figure 2. Left: Energy dependence of the $\langle K^+\rangle/\langle\pi^+\rangle$ ratio measured in central Pb+Pb and Au+Au collisions (full symbols) compared to the corresponding results from $p + p$ reactions (open circles). Right: Energy dependence of the relative strangeness production as measured by the E_s ratio (see text) in central Pb+Pb and Au+Au collisions (full symbols) compared to results from $p + p$ reactions (open circles). The compilation of data is from Ref. [3]. The dashed-dotted line in the figure shows the predictions of the SMES [1].

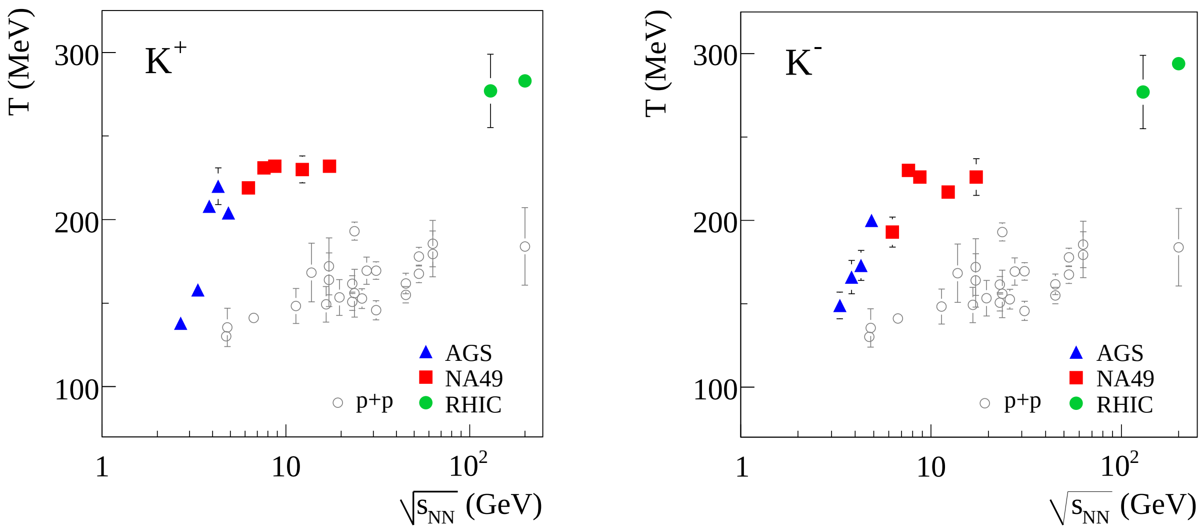

Figure 3. Energy dependence of the inverse slope parameter T^* of the transverse mass spectra of K^+ (left) and K^- mesons (right) measured at mid-rapidity in central Pb+Pb and Au+Au collisions. The $K^\pm$ slope parameters are compared to those from $p+p$ reactions (open circles). The compilation of data is from Ref. [3].

3 Signals of deconfinement: experimental results

The Pion Kink. The compilation of data [3] on the pion multiplicity in central Pb+Pb (Au+Au) collisions and $p+p(\bar{p})$ interactions is shown in Fig. 1. The mean pion multiplicity $\langle\pi\rangle = 1.5\,(\langle\pi^-\rangle + \langle\pi^-\rangle)$ per wounded nucleon is shown as a function F. The results from $p+p(\bar{p})$ interactions are shown by the open symbols. Up to the top SPS energy the mean pion multiplicity in $p+p$ interactions is approximately proportional to F. A fit of $\langle\pi\rangle/\langle N_W\rangle = bF$ yields a value of $b \cong 1.063$ GeV$^{-1/2}$. For central Pb+Pb and Au+Au collisions the energy dependence is more complicated. Below 40 A·GeV the ratio $\langle\pi\rangle/\langle N_W\rangle$ is lower in A+A collisions than in $p+p(\bar{p})$ interactions (pion suppression) while at higher energies this ratio is larger in A+A collisions than in $p+p(\bar{p})$ interactions (pion enhancement). A linear fit, $\langle\pi\rangle/\langle N_W\rangle = a+bF$ for $F < 1.85$ GeV$^{1/2}$ gives $a \cong -0.45$ and $b \cong 1.03$ GeV$^{-1/2}$. The slope parameter fitted in the range $F > 3.5$ GeV$^{1/2}$ is $b \cong 1.33$. This is shown by the solid line in Fig. 1 (the lowest point at the top RHIC energy was excluded from the fit). Thus, in the region 15–40 A·GeV between the highest AGS and the lowest SPS energy the slope increases by a factor of about 1.3. This increase of the slope for A+A collisions is interpreted within the SMES as due to an increase of the effective number of the internal degrees of freedom by a factor of $g_{QGP}/g_{HG} = (1.3)^4 \cong 3$ [1, 4]. It is caused by the creation of a transient state of deconfined matter at collision energies higher than 30 A·GeV.

The Strange Horn. One can argue that the strangeness to entropy ratio is closely proportional to the two ratios directly measured in experiments: the $\langle K^+\rangle/\langle\pi^+\rangle$ ratio and the $E_s = (\langle\Lambda\rangle + \langle K+\overline{K}\rangle)/\langle\pi\rangle$ ratio. The energy dependence of these full phase space ratios is plotted in Fig. 2 for central Pb+Pb (Au+Au) collisions and $p+p$ interactions as functions of collision energy. Kaons are the lightest strange hadrons and $\langle K^+\rangle$ accounts for about half of all the anti-strange quarks produced in Pb+Pb collisions at AGS and SPS energies. K^+ and K^0 carry a dominant fraction of all produced $\bar{s}$-quarks exceeding 95% in Pb+Pb collisions at 158 A·GeV if open strangeness is considered. Because $\langle K^+\rangle \cong \langle K^0\rangle$ in approximately isospin symmetric collisions of heavy nuclei, the K^+ yield is nearly proportional to the total strangeness production and only weakly sensitive to the baryon density. As a significant fraction of s-quarks (about 50% in central Pb+Pb collisions at 158 A·GeV) is carried by hyperons, the number of produced anti-kaons, K^- and $\overline{K}^0$, is sensitive to both the strangeness yield and the baryon density. In the E_s ratio all main carriers of strange and anti-strange quarks are included. The neglected contribution of $\overline{\Lambda}$ and other hyperons and anti-hyperons is about 10% at SPS energies. Both the $\langle K^+\rangle/\langle\pi^+\rangle$ and E_s ratios are approximately, within 5% at SPS energies, proportional to the ratio of total multiplicity of s and $\bar{s}$ quarks to the multiplicity of pions. It should be noted that the $\langle K^+\rangle/\langle\pi^+\rangle$ ratio is expected to be similar (within about 10%) for $p+p$, $n+p$, and $n+n$ interactions at 158 A·GeV, whereas the E_s ratio is independent of the isospin of nucleon-nucleon interactions.

For $p+p$ interactions both ratios show monotonic increase with energy. However, very different behavior is observed for central Pb+Pb (Au+Au) collisions. The steep threshold rise of the ratios characteristic for confined matter then settles into saturations at the level expected for deconfined matter. In the transition region (at low SPS energies) a sharp maximum is observed caused by a higher strangeness to entropy ratio in the confinend matter than in the deconfiend matter. As seen in Fig. 2 the measured dependence is consistent

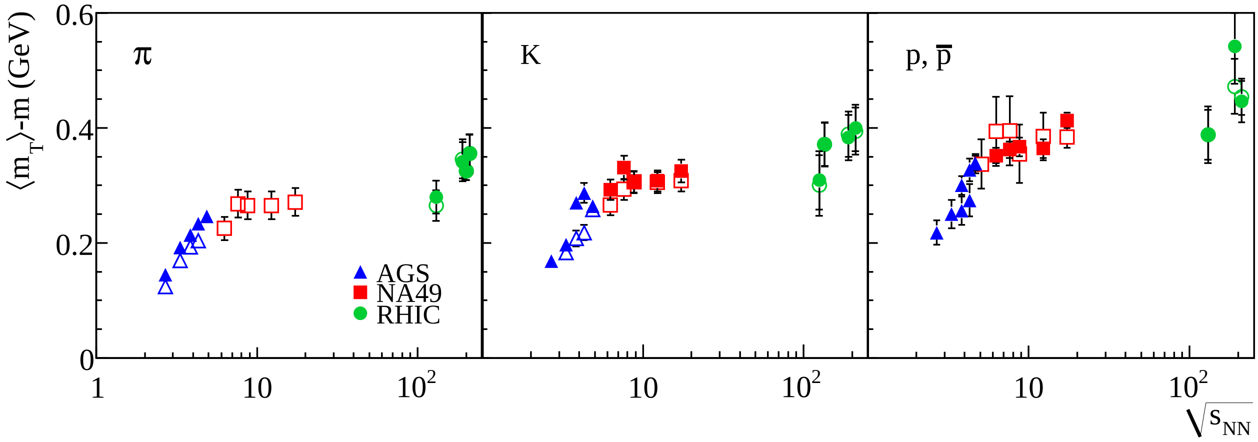

Figure 4. Energy dependence of the mean transverse mass, $\langle m_T \rangle - m$, measured at mid-rapidity in central Pb+Pb an Au+Au collisions for $\pi^{\pm}$ (left), $K^{\pm}$ (middle), and p and $\bar{p}$ (right). In the plots, positively (negatively) charged hadrons are indicated by the full (open) symbols. The compilation of data is from Ref. [3].

with that predicted within the SMES [1].

The Step in Slopes. The energy dependence of the inverse slope parameter fitted to the K^+ and K^- transverse mass spectra for central Pb+Pb (Au+Au) collisions is shown in Fig. 3.

The striking features of the data can be summarized and interpreted as follows. The T^* parameter increases strongly with collision energy up to the SPS energy point 30 A·GeV. This is an energy region where the creation of confined matter at the early stage of the collisions is expected. Increasing collision energy leads to an increase of the early stage temperature and pressure. Consequently the transverse activity of produced hadrons, measured by the inverse slope parameter, increases with increasing energy. The T^* parameter is approximately independent of the collision energy in the SPS energy range $30 - 158$ A·GeV. In this energy region the transition between confined and deconfined matter is expected to be located. The resulting modification of the equation of state "suppresses" the hydrodynamical transverse expansion and leads to the observed plateau structure in the energy dependence of the T^* parameter [7, 10]. At higher energies (RHIC data), T^* again increases with the collision energy. The equation of state at the early stage becomes again stiff, the early stage temperature and pressure increase with collision energy, and this results in increase of T^* too. The parameter T^* appears to increase smoothly in $p + p$ interactions as shown in the left panel of Fig.3.

For the transverse mass spectra of pions and protons the inverse slope parameter depends on the transverse mass interval used in the fit. The mean transverse mass $\langle m_T \rangle$ provides an alternative characterization of the m_T-spectra. The energy dependence of $\langle m_T \rangle - m$ for pions, kaons and (anti)protons is shown in Fig.4. The results shown in Fig.4 demonstrate that the approximate energy independence of $\langle m_T \rangle$ in the SPS energy range is a common feature for all particles investigated.

4 QCD critical point and event-by-event fluctuations

The event-by-event fluctuations in high energy A+A collisions are expected to be closely related to the transitions between different phases of QCD matter. By measuring the fluctuations one should observe anomalies from the onset of deconfinement and dynamical instabilities when the expanding system goes through the 1-st order transition line between the QGP and the hadron gas. Furthermore, the QCD critical point may be signaled by a characteristic pattern in enhanced fluctuations. A+A collisions in the SPS energy region are expected to be a suitable tool for a search of critical point signatures. Only recently first measurements of particle multiplicity fluctuations and transverse momentum fluctuations in A+A collisions have been performed. A theoretical analysis of multiplicity fluctuations for the hadron-resonance gas - in different statistical ensembles - has been performed in Ref. [11]. Independently, the multiplicity fluctuations in A+A collisions has been studied within a microscopic transport approach [12, 13]. We recall that particle number fluctuations are quantified by the ratio of the variance of the multiplicity distribution to its mean value, the scaled variance.

An ambitious experimental program for the search of the QCD critical point has been started by the NA61 Collaboration at the SPS [14]. The program includes a variation in the atomic number A of the colliding nuclei as well as an energy scan. This allows to scan the phase diagram in the plane of temperature T and baryon chemical potential μ_B near the critical point. One expects to 'locate' the position of the critical point by studying its 'fluctuation signals'. High statistics multiplicity fluctuation data will be required.

Ref. [15] studied the energy and system size dependence of event-by-event multiplicity fluctuations within the microscopic transport approaches Hadron-String-Dynamics (HSD) and Ultra-Relativistic-Quantum-Mole-

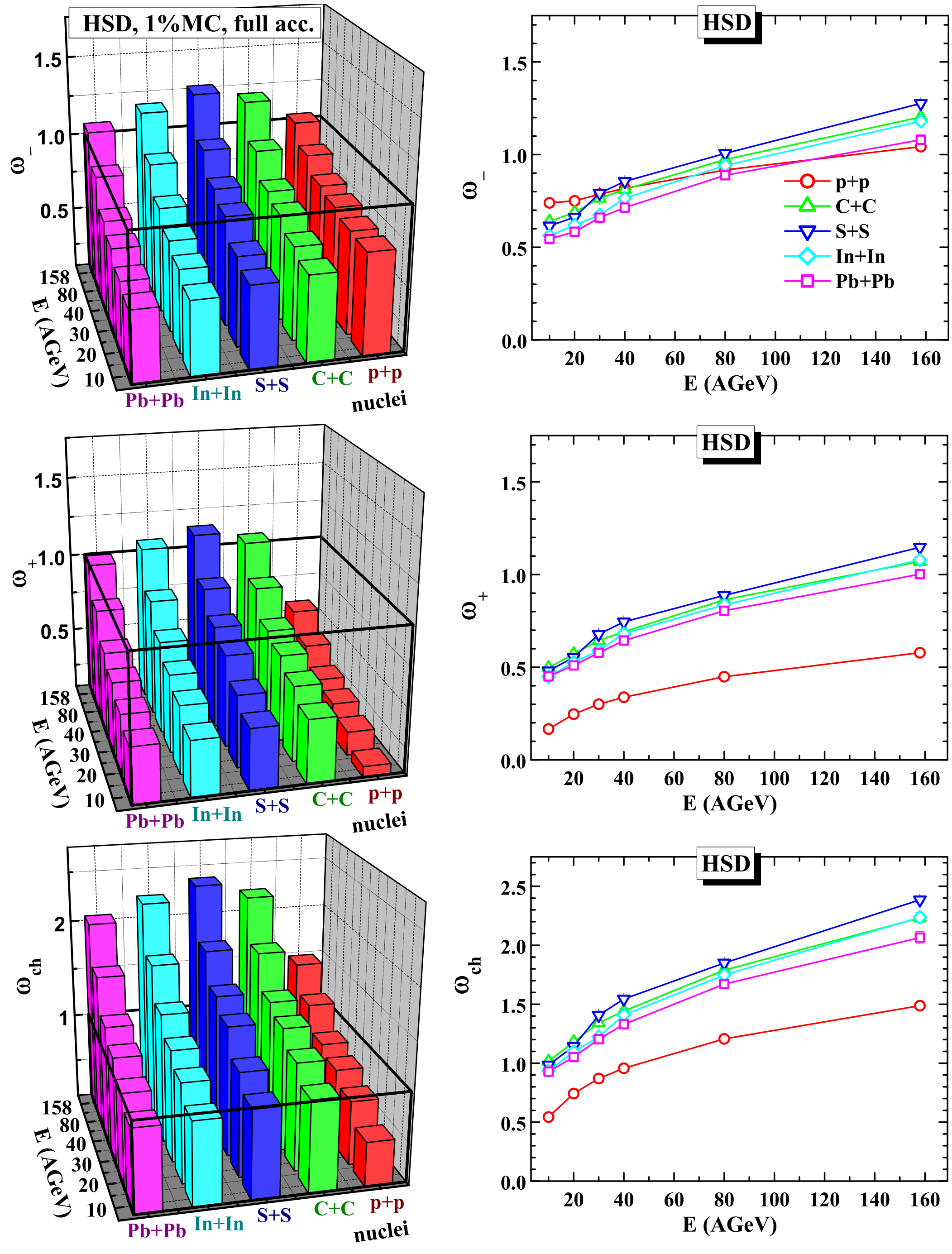

Figure 5. The HSD results for the scaled variances of particle number fluctuations of negative particles ω_{-} (upper panel), positive particles ω_{+} (middle panel), and all charged particles ω_{ch} (lower panel) in $A + A$ and p+p collisions for the full 4π acceptance in 3D (*left*) and 2D (*right*) projection. The 1% most central C+C, S+S, In+In, and Pb+Pb collisions are selected by choosing the largest values of the number of projectile participants N_P^{proj} at different collision energies E_{lab}=10, 20, 30, 40, 80, 158 AGeV. The errorbars indicate the estimated uncertainties in the model calculations. For p+p collisions the HSD results for all inelastic events are presented.

cular-Dynamics (UrQMD). These models provide a rather reliable description for the inclusive spectra of charged hadrons in A+A collisions from SIS to RHIC energies. There were considered C+C, S+S, In+In, and Pb+Pb collisions at the bombarding energies of 10, 20, 30, 40, 80, 158 AGeV. For a comparison and reference there were also presented the results of multiplicity fluctuations in p+p collisions at the same energies. This study thus was in full correspondence to the experimental program of the NA61 Collaboration [14]. The typical results are presented in Fig. 5.

The QCD critical point is expected to be experimentally seen as a non-monotonic dependence of the multiplicity fluctuations, i.e. a specific combination of atomic number A and bombarding energy E_{lab} could move the chemical freeze-out of the system close to the critical point and show a 'spike' in the multiplicity fluctuations. Since HSD and UrQMD do not include explicitly a phase transition from a hadronic to a partonic phase, we can not make a clear suggestion for the location of the critical point - it is beyond the scope of our hadron-string models. However, this study might be helpful in the interpretation of the upcoming experimental data since it will allow to subtract simple dynamical and geometrical effects from the expected QGP signal. The deviations of the future experimental data from the HSD and UrQMD predictions may be considered as an indication for the critical point signals.

Theoretical estimates give about 10% increase of the multiplicity fluctuations due to the critical point [16]. It is large enough to be observed experimentally within the statistics of NA61 [14]. To achieve this goal, it is necessary to have a control on other possible sources of fluctuations. One of such sources is the fluctuation of the number of nucleon participants. It has been found in Ref. [12] that these fluctuations give a dominant contribution to hadron multiplicity fluctuations in A+A collisions. On the other hand one can suppress the participant number fluctuations by selecting most central A+A collisions (see Ref. [12, 17] for details). That's why the NA61 Collaboration plans to measure central collisions of light and intermediate ions instead of peripheral Pb+Pb collisions. It is important to stress, that the conditions for the centrality selection in the measurement of fluctuations are much more stringent than those for mean multiplicity measurements. This issue has been discussed in detail in Ref. [15].

5 Conclusions

The energy scan program at the CERN SPS together with the measurements at lower (LBL, JINR, SIS, BNL AGS) and higher (BNL RHIC) energies yielded systematic data on energy dependence of hadron production in central Pb+Pb (Au+Au) collisions. Predicted signals of the deconfinement phase transition, namely anomalies in the energy dependence of hadron production – the *kink* [1, 4], *horn* [1] and *step* [7] – are simultaneously observed in the same domain of the low SPS energies. The anomalies in the energy dependence of the hadron production are seen in central A+A collisions and absent in the data of $p + p$ reactions. They indicate that the onset of the deconfinement in central Pb+Pb collisions is located at about 30 A·GeV.

The experimental program of searching for the QCD critical point includes a variation in the atomic number A of the colliding nuclei as well as an energy scan. One expects to 'locate' the position of the critical point by observing an anomalous increase of the 'fluctuation signals'. The results of Ref. [15] are essential for an optimal choice of colliding nuclei and bombarding energies for the experimental search of the QCD critical point.

Acknowledgements. I am thankful to Marek Gaździcki for fruitful collaboration. I am also thankful to Walter Greiner for his permanent support and encouraging of these studies.

References

[1] M. Gaździcki and M. I. Gorenstein, Acta Phys. Polon. **B 30**, 2705 (1999) [arXiv:hep-ph/9803462], and references therein.

[2] S.V. Afanasiev et al. [NA49 Collaboration], Phys. Rev. **C 66**, 054902 (2002).

[3] C. Alt et al. [NA49 Collaboration], arXiv:nucl-ex/0710.0118, and references therein.

[4] M. Gaździcki, Z. Phys. **C 66**, 659 (1995) and J. Phys. **G 23**, 1881 (1997).

[5] L. Van Hove, Phys. Lett. **B 118**, 138 (1982).

[6] C.M. Hung and E. Shuryak, Phys. Rev. Lett. **75**, 4003 (1995); Phys. Rev. **57**, 1891 (1997).

[7] M. I. Gorenstein, M. Gaździcki, and K. Bugaev, Phys. Lett. **B 567**, 175 (2003) [arXiv:hep-ph/0303041].

[8] D. Teaney, J. Lauret, and E.V. Shuryak, Phys. Rev. Lett. **86**, 4783 (2001) and nucl–th/0110037.

[9] M. I. Gorenstein, K. Bugaev, and M. Gaździcki, Phys. Rev. Lett. **88**, 132301 (2002), Phys. Lett. **B 544**, 127 (2002), Phys. Rev. **C 68**, 01790 (2003).

[10] M. Gaździcki, M.I. Gorenstein, F. Grassi, Y. Hama, T. Kodama, and O. Socolowski Jr., Braz. J. Phys. **34**, 322 (2004) [hep-ph/0309192].

[11] V.V. Begun *et al.*, Phys. Rev. C **70**, 034901 (2004); *ibid.* **71**, 054904 (2005); *ibid.* **74**, 044903 (2006); M. Hauer, V.V. Begun, and M.I. Gorenstein, arXiv:0706.3290 [nucl-th]; M. Hauer, arXiv:0710.3938 [nucl-th].

[12] V.P. Konchakovski, *et al.*, Phys. Rev. C **73**, 034902 (2006);

[13] V.P. Konchakovski, *et al.*, Phys. Rev. C **74**, 064911 (2006).

[14] M. Gazdzicki *et al.* [NA61 Collaboration], PoS C **POD2006**, 016 (2006) [arXiv:nucl-ex/0612007]; N. Antoniou *et al.* [NA61 Collaboration], "Study of hadron production in hadron nucleus and nucleus nucleus collisions at the CERN SPS," CERN-SPSC-P-330 (2006).

[15] V.P. Konchakovski, B. Lungwitz, M.I. Gorenstein, and E.L. Bratkovskaya, Phys. Rev. C **78**, 0249906 (2008).

[16] M.A. Stephanov, K. Rajagopal, and E.V. Shuryak, Phys. Rev. Lett. **81**, 4816 (1998); Phys. Rev. D **60**, 114028 (1999); M.A. Stephanov, Acta Phys. Polon. B **35**, 2939 (2004).

[17] M. Gaździcki and M. Gorenstein, Phys. Lett. B**640**, 155 (2006).

Proceedings of the International School-seminar
"New Physics and Quantum Chromodynamics at external Conditions", pp. 56 – 63,
3-6 May 2009, Dnipropetrovsk, Ukraine

Z'-BOSON: LEP RESULTS AS A GUIDE FOR THE LHC

A. V. Gulov[a], V. V. Skalozub[b]

Dnipropetrovsk National University, Dnipropetrovsk, Ukraine

The model-independent relations between low energy couplings of Z'-boson to fermions are used to uniquely pick out Z' signals by the data of LEP2 experiments. The maximum likelihood values of Z' couplings to leptons and quarks and the corresponding confidence intervals are estimated. These estimates may serve as a guide for experiments at the Tevatron and/or LHC.

1 Introduction

The precision test of the standard model (SM) at the LEP gave a possibility not only to determine all the parameters and particle masses at the level of radiative corrections but also afforded an opportunity for searching for signals of new heavy particles beyond the energy scale of it. On the base of the LEP2 experiments the low bounds on parameters of various models extending the SM have been estimated and the scale of new physics was obtained [1]–[3]. Although no new particles were discovered, a general believe is that the energy scale of new physics to be of order 1 TeV, that may serve as a guide for experiments at the Tevatron and LHC. In this situation, any information about new heavy particles obtained on the base of the present day data is desirable and important.

Numerous extended models include the Z' gauge boson – massive neutral vector particle associated with the extra $U(1)$ subgroup of an underlying group. Searching for this particle as a virtual state is widely discussed in the literature (see for references [4]–[6]). Such aspects as the mass of Z', couplings to the SM particles, $Z - Z'$ mixing and its influence in various processes and particles parameters, distinctions between different models are discussed in details. As concerned a searching for Z' in the LEP experiments and the experiments at Tevatron [7], it was carried out mainly in a model-dependent way. A wide class of popular models has been investigated and low bounds on the mass $m_{Z'}$ were estimated (see, [1]–[3]). As it is occurred, the low masses are varying in a wide energy interval 400-1800 GeV dependently on a specific model. These bounds are a little bit different in the LEP and Tevatron experiments. In this situation a model-independent analysis is of interest.

In the papers [8]–[11] of the present authors a new approach for the model-independent search for Z'-boson was proposed which, in contrast to other model-independent searches, gives a possibility to pick out uniquely this virtual state and determine its characteristics. The corresponding observables have also been introduced and applied to analyze the LEP2 experiment data. Our consideration is based on two constituents: 1) The relations between the effective low-energy couplings derived from the renormalization group (RG) equation for fermion scattering amplitudes. We called them the RG relations. Due to these relations, a number of unknown Z' parameters entering the amplitudes of different scattering processes considerably decreases. 2) When these relations are accounted for, some kinematics properties of the amplitude become uniquely correlated with this virtual state and the Z' signals exhibit themselves.

The RG relations allow to introduce observables correlated uniquely with the Z'-boson. Comparing the mean values of the observables with the necessary specific values, one could arrive at a conclusion about the Z' existence. The confidence level (CL) of these values has been estimated and adduced in addition. Without taking into consideration the RG relations the determination of Z'-boson requires a supplementary specification due to a larger number of different couplings contributing to the observables. Similar situation takes place in the "helicity model fits" of LEP Collaborations [1]–[3] when different virtual states contribute to each of the specific models (AA, VV, and so on). Therefore these fits had the goal to discover any signals of new physics independently of the particular states which may cause deviations from the SM. Note that the LEP Collaborations saw no indications of new contact four fermion interactions in these fits.

In Refs. [8, 10, 11] the one-parametric observables were introduced and the signals (hints in fact) of the Z' have been determined at the 1σ CL in the $e^+e^- \to \mu^+\mu^-$ process, and at the 2σ CL in the Bhabha process. The Z' mass was estimated to be 1–1.2 TeV. An increase in statistics could make these signals more pronounced and there is a good chance to discover this particle at the LHC.

In Ref. [12] the updated results of the one-parameter fit and the complete many-parametric fit of the LEP2 data were performed with the goal to estimate a possible signal of the Z'-boson with accounting for the final

e-mail: [a]gulov@dsu.dp.ua, [b]skalozubv@daad-alumni.de

data of the LEP collaborations DELPHI and OPAL [2, 3]. Usually, in a many-parametric fit the uncertainty of the result increases drastically because of extra parameters. On the contrary, in our approach due to the RG relations between the low-energy couplings there are only 2-3 independent parameters for the investigated leptonic scattering processes. As it was showed in Ref. [12], an inevitable increase of confidence areas in the many-parametric space was compensated due to accounting for all accessible experimental information. Therefore, the uncertainty of the many-parametric fit was estimated as the comparable with previous one-parametric fits. In this approach the combined data fit for all lepton processes is also possible.

As a result, we obtained the maximum likelihood values and the corresponding confidence intervals for Z' couplings to leptons and quarks derived from the LEP2 experimental data. These results may serve as a good input into the future LHC and ILC experiments and used in various aspects. To underline the importance of them we mention that there are many tools at the LHC for the identification of Z'. But many of them are only applicable if Z' is relatively light. The knowledge of the Z' couplings to SM fermions also have important consequences.

2 The Abelian Z' boson at low energies and relations between its couplings

Let us adduce a necessary information about the Abelian Z'-boson. This particle is predicted by a number of grand unification models. Among them the E_6 and $SO(10)$ based models [13] (for instance, LR, $\chi - \psi$ and so on) are often discussed in the literature. In all the models, the Abelian Z'-boson is described by a low-energy $\tilde{U}(1)$ gauge subgroup originated in some symmetry breaking pattern.

At low energies, the Z'-boson can manifest itself by means of the couplings to the SM fermions and scalars as a virtual intermediate state. Moreover, the Z-boson couplings are also modified due to a Z–Z' mixing. In principle, arbitrary effective Z' interactions to the SM fields could be considered at low energies. However, the couplings of non-renormalizable types have to be suppressed by heavy mass scales because of decoupling. Therefore, significant signals beyond the SM can be inspired by the couplings of renormalizable types. Such couplings can be derived by adding new $\tilde{U}(1)$-terms to the electroweak covariant derivatives in the Lagrangian [14, 15]

$$L_f = i\sum_{f_L} \bar{f}_L \gamma^\mu \left(\partial_\mu - \frac{ig}{2}\sigma_a W^a_\mu - \frac{ig'}{2}B_\mu Y_{f_L} - \frac{i\tilde{g}}{2}\tilde{B}_\mu \tilde{Y}_{f_L}\right) f_L + i\sum_{f_R} \bar{f}_R \gamma^\mu \left(\partial_\mu - ig' B_\mu Q_f - \frac{i\tilde{g}}{2}\tilde{B}_\mu \tilde{Y}_{f_R}\right) f_R, \quad (1)$$

where summation over all the SM left-handed fermion doublets, leptons and quarks, $f_L = (f_u)_L, (f_d)_L$, and the right-handed singlets, $f_R = (f_u)_R, (f_d)_R$, is understood. Q_f denotes the charge of f in positron charge units, $\tilde{Y}_{f_L} = \mathrm{diag}(\tilde{Y}_{f_u}, \tilde{Y}_{f_d})$, and $Y_{f_L} = -1$ for leptons and $1/3$ for quarks.

For general purposes we derive the RG relations for the Z' beyond the SM with two light Higgs doublets [8]. Z' interactions with the scalar doublets can be parametrized in a model-independent way as follows,

$$L_\phi = \sum_{i=1}^{2} \left| \left(\partial_\mu - \frac{ig}{2}\sigma_a W^a_\mu - \frac{ig'}{2}B_\mu Y_{f_L} - \frac{i\tilde{g}}{2}\tilde{B}_\mu \tilde{Y}_{\phi_i}\right)\phi_i \right|^2 . \quad (2)$$

In these formulas, $g, g', \tilde{g}$ are the charges associated with the $SU(2)_L, U(1)_Y$, and the Z' gauge groups, respectively, σ_a are the Pauli matrices, $\tilde{Y}_{\phi_i} = \mathrm{diag}(\tilde{Y}_{\phi_{i,1}}, \tilde{Y}_{\phi_{i,2}})$ is the generator corresponding to the gauge group of the Z' boson, and Y_{ϕ_i} is the $U(1)_Y$ hypercharge.

The Yukawa Lagrangian can be written in the form

$$L_{\text{Yuk.}} = -\sqrt{2}\sum_{f_L}\sum_{i=1}^{2}\left(G_{f_{d,i}}[\bar{f}_L \phi_i (f_d)_R + (\bar{f}_d)_R \phi_i^+ f_L] + G_{f_{u,i}}[\bar{f}_L \phi_i^c (f_u)_R + (\bar{f}_u)_R \phi_i^{c+} f_L]\right), \quad (3)$$

where $\phi_i^c = i\sigma_2 \phi_i^*$ is the charge conjugated scalar doublet.

The Lagrangian (2) leads to the Z–Z' mixing. The Z–Z' mixing angle θ_0 is determined by the coupling $\tilde{Y}_\phi$ as follows

$$\theta_0 = \frac{\tilde{g}\sin\theta_W \cos\theta_W}{\sqrt{4\pi\alpha_{\text{em}}}} \frac{m_Z^2}{m_{Z'}^2}\tilde{Y}_\phi + O\left(\frac{m_Z^4}{m_{Z'}^4}\right), \quad (4)$$

where θ_W is the SM Weinberg angle, and α_{em} is the electromagnetic fine structure constant. Although the mixing angle is a small quantity of order $m_{Z'}^{-2}$, it contributes to the Z-boson exchange amplitude and cannot be neglected at the LEP energies.

In what follows we will also use the Z' couplings to the vector and axial-vector fermion currents defined as

$$v_f = \tilde{g}\frac{\tilde{Y}_{L,f} + \tilde{Y}_{R,f}}{2}, \qquad a_f = \tilde{g}\frac{\tilde{Y}_{R,f} - \tilde{Y}_{L,f}}{2}. \quad (5)$$

The Lagrangian (1) leads to the following interactions between the fermions and the Z and Z' mass eigenstates:

$$\begin{aligned}\mathcal{L}_{Z\bar{f}f} &= \frac{1}{2}Z_\mu \bar{f}\gamma^\mu \left[(v^{\rm SM}_{fZ}+\gamma^5 a^{\rm SM}_{fZ})\cos\theta_0 + (v_f+\gamma^5 a_f)\sin\theta_0\right] f,\\ \mathcal{L}_{Z'\bar{f}f} &= \frac{1}{2}Z'_\mu \bar{f}\gamma^\mu \left[(v_f+\gamma^5 a_f)\cos\theta_0 - (v^{\rm SM}_{fZ}+\gamma^5 a^{\rm SM}_{fZ})\sin\theta_0\right] f,\end{aligned} \tag{6}$$

where f is an arbitrary SM fermion state; $v^{\rm SM}_{fZ}$, $a^{\rm SM}_{fZ}$ are the SM couplings of the Z-boson.

Since the Z' couplings enter the cross-section together with the inverse Z' mass, it is convenient to introduce the dimensionless couplings

$$\bar{a}_f = \frac{m_Z}{\sqrt{4\pi}m_{Z'}}a_f, \quad \bar{v}_f = \frac{m_Z}{\sqrt{4\pi}m_{Z'}}v_f, \tag{7}$$

which can be constrained by experiments.

Low energy parameters $\tilde{Y}_{\phi_{i,1}}$, $\tilde{Y}_{\phi_{i,2}}$, $\tilde{Y}_{L,f}$, $\tilde{Y}_{R,f}$ must be fitted in experiments. In most investigations they were considered as independent ones. In a particular model, the couplings $\tilde{Y}_{\phi_{i,1}}$, $\tilde{Y}_{\phi_{i,2}}, \tilde{Y}_{L,f}, \tilde{Y}_{R,f}$ take some specific values. In case when the model is unknown, these parameters remain potentially arbitrary numbers. However, this is not the case if one assumes that the underlying extended model is a renormalizable one. In the papers [8, 9] it was shown that the Abelian Z' couplings are correlated due to renormalizability:

$$\tilde{Y}_{\phi_{1,1}} = \tilde{Y}_{\phi_{2,1}} = \tilde{Y}_{\phi,2} \equiv \tilde{Y}_\phi, \qquad \tilde{Y}_{L,f} = \tilde{Y}_{L,f^*}, \qquad \tilde{Y}_{R,f} = \tilde{Y}_{L,f} + 2T_{3f}\,\tilde{Y}_\phi, \tag{8}$$

where f and f^* are the partners of the $SU(2)_L$ fermion doublet ($l^* = \nu_l, \nu^* = l, q^*_u = q_d$ and $q^*_d = q_u$), T_{3f} is the third component of weak isospin. In this case the SM Lagrangian appears to be invariant with respect to the $\tilde{U}(1)$ group associated with the Z'. The last relation in Eq.(8) ensures the $L_{\rm Yuk.}$ Eq.(3) is to be invariant with respect to the $\tilde{U}(1)$ transformations. We called the relations (8) the RG relations.

Introducing the Z' couplings to the vector and axial-vector fermion currents (5), the last line in Eq. (8) yields

$$v_f - a_f = v_{f^*} - a_{f^*}, \qquad a_f = T_{3f}\tilde{g}\tilde{Y}_\phi. \tag{9}$$

The couplings of the Abelian Z' to the axial-vector fermion current have a universal absolute value proportional to the Z' coupling to the scalar doublet.

These relations are model independent. In particular, they hold in all the known models containing the single Abelian Z' at low energies.

The RG relations give a possibility to reduce the number of fitted parameters and to introduce observables which uniquely pick out the Z' signals. The RG relations (8) influences the $Z - Z'$ mixing (4). The axial-vector coupling determines also the coupling to the scalar doublet and, consequently, the mixing angle. As a result, the number of independent couplings is significantly reduced.

3 Z' search in $e^+e^- \to \mu^+\mu^-, \tau^+\tau^-$ processes

Let us consider the processes $e^+e^- \to l^+l^-$ ($l = \mu, \tau$) with the non-polarized initial- and final-state fermions. In the lower order in $m^{-2}_{Z'}$ the Z' contributions to the differential cross-section of the process $e^+e^- \to l^+l^-$ are expressed in terms of four-fermion contact couplings, only. The tree-level contributions are described by 4 quadratic combinations of Z' couplings: $\bar{a}^2_e$, $\bar{v}_e\bar{v}_{\mu,\tau}$, $\bar{a}_e\bar{v}_e$, and $\bar{a}_e\bar{v}_{\mu,\tau}$. The first combination is sign-definite and can be used as a clear signal of the Abelian Z' boson.

In order to introduce the observable which selects the signal of the Abelian Z' boson we introduce the observable $\sigma_l(z)$ defined as the difference of cross sections integrated in some ranges of the scattering angle θ [9, 10]:

$$\sigma_l(z) \equiv \int_z^1 \frac{d\sigma_l}{d\cos\theta}d\cos\theta - \int_{-1}^z \frac{d\sigma_l}{d\cos\theta}d\cos\theta, \tag{10}$$

where z stands for the cosine of the boundary angle. The idea of introducing the z-dependent observable (10) is to choose the value of the kinematic parameter z to pick up the sign-definite contribution $\bar{a}^2_e$ and suppress others. Such a value, $z = z^*$, exists, which is the unique property of the Abelian Z' boson contribution to the cross-section.

The boundary angle z^* is defined by the maximization of the relative contribution of the factor at $\bar{a}^2_e$. The value $z^* \simeq 0.38$ is found, at which the factor at $\bar{a}^2_e$ contributes more than 95% of the observable

$$\Delta\sigma_l(z^*) = \sigma_l(z^*) - \sigma^{\rm SM}_l(z^*) \sim -\bar{a}^2_e < 0. \tag{11}$$

Thus, the observable $\Delta\sigma_l(z^*)$ selects the model-independent signal of this particle in the processes $e^+e^- \to l^+l^-$. It allows to use the data on scattering into $\mu\mu$ and $\tau\tau$ pairs in order to estimate the Abelian Z' coupling to the axial-vector lepton currents.

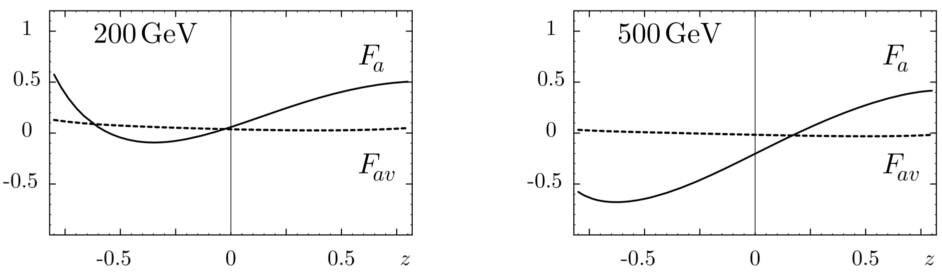

Figure 1. Factors $F_a(\sqrt{s}, z)$ (solid) and $F_{av}(\sqrt{s}, z)$ (dashed) in the normalized deviation of the differential cross-section $d\tilde{\sigma}/dz$ for $\sqrt{s} = 200$ and 500 GeV.

Although the observable can be computed from the differential cross-sections directly, it is also possible to recalculate it from the total cross-sections and the forward-backward asymmetries. The recalculation is based on the known fact that the differential cross-section of the $s-$channel process through the vector state can be approximated with a good accuracy by the two-parametric polynomial in the cosine of the scattering angle z. The recalculation procedure has the proper theoretical accuracy. Nevertheless, it allows to reduce the experimental errors on the observable, since the published data on the total cross-sections and the forward-backward asymmetries are more precise than the data on the differential cross-sections.

The introduced observable $\Delta\sigma_l(z^*)$ is analyzed on the base of the LEP2 data set on the total cross-sections and the forward-backward asymmetries [1]. The fit is performed by the χ^2-function. The $\mu\mu$, $\tau\tau$, and the complete $\mu\mu$ and $\tau\tau$ data lead to the following results:

$$\mu\mu: \quad \bar{a}^2 = 0.0000366^{+0.0000489}_{-0.0000486}, \qquad \tau\tau: \quad \bar{a}^2 = -0.0000266^{+0.0000643}_{-0.0000639},$$
$$\mu\mu \text{ and } \tau\tau: \quad \bar{a}^2 = 0.0000133^{+0.0000389}_{-0.0000387}. \tag{12}$$

As is seen, the more precise $\mu\mu$ data demonstrate the signal of about 1σ level. It corresponds to the Abelian Z'-boson with the mass of order 1.2–1.5 TeV if one assumes the value of $\tilde{\alpha} = \tilde{g}^2/4\pi$ to be in the interval 0.01–0.02. No signal is found by the analysis of the $\tau\tau$ cross-sections. The combined fit of the $\mu\mu$ and $\tau\tau$ data leads to the signal below the 1σ CL.

4 Search for Z' in $e^+e^- \to e^+e^-$ process

4.1 One-parameter fits

In our analysis, as the SM values of the cross-sections we use the quantities calculated by the LEP2 collaborations [2, 3, 16, 17]. They account for either the one-loop radiative corrections or initial and final state radiation effects (together with the event selection rules, which are specific for each experiment). As it is reported by the DELPHI Collaboration, there is a theoretical error of the SM values of about 2%. In our analysis this error is added to the statistical and systematic ones for all the Collaborations. As it was checked, the fit results are practically insensitive to accounting for this error.

The deviation from the SM is computed in the improved Born approximation. This approximation is sufficient for our analysis leading to the systematic error of the fit results less than 5-10 per cents.

The deviation from the SM of the differential cross-section for the process $e^+e^- \to e^+e^-$ can be expressed through quadratic combinations a^2, v_e^2, and $a/, v_e$ of couplings $a = a_e$, v_e. The factor at v_e^2 is a positive monotonic function of the cosine of the scattering angle z for the LEP2 center-of-mass energies $\sqrt{s} \simeq 200$ GeV. The same behavior is observed for higher energies. Such a property allows one to choose the factor to normalize the differential cross section. Then the normalized deviation of the differential cross-section reads [11]

$$\frac{d\tilde{\sigma}}{dz} = \bar{v}^2 + F_a(\sqrt{s}, z)\bar{a}^2 + F_{av}(\sqrt{s}, z)\bar{a}\bar{v} + \ldots, \tag{13}$$

and the normalized factors are shown in Fig 1. Now these factors are finite at $z \to 1$. Each of them in a special way influences the differential cross-section.

The factor at $\bar{v}^2$ is just the unity. Hence, $\bar{v}^2$ determines the level of the deviation from the SM value. The factor at $\bar{a}^2$ depends on the scattering angle in a non-trivial way. It allows to recognize the Abelian Z' boson, if the experimental accuracy is sufficient. The factor at $\bar{a}\bar{v}$ results in small corrections. Thus, effectively, the obtained normalized differential cross-section is a two-parametric function. It is possible to introduce the observables to fit separately each of these parameters.

Let us first proceed with the observable for $\bar{v}^2$. After normalization the factor at the vector-vector four-fermion coupling becomes the unity. The factor at $\bar{a}^2$ is a sign-varying function of the cosine of the scattering angle, which is small over the backward scattering angles for $\sqrt{s} = 200$ GeV (Fig. 1). So, to measure the value of $\bar{v}^2$ the normalized deviation of the differential cross-section has to be integrated over the backward angles. For the center-of-mass energy 500 GeV the factor at $\bar{a}^2$ is already a non-vanishing quantity for the backward scattering angles. The curves corresponding to intermediate energies are distributed in between two these curves. Since they are sign-varying ones at each energy point some interval of z can be chosen to make the integral to be zero. Thus, to measure the Z' coupling to the electron vector current $\bar{v}^2$ we introduce the integrated cross-section (13)

$$\sigma_V = \int_{z_0}^{z_0+\Delta z} (d\tilde{\sigma}/dz)dz, \tag{14}$$

where at each energy the most effective interval $[z_0, z_0 + \Delta z]$ is determined by the following requirements: 1) The relative contribution of the coupling $\bar{v}^2$ is maximal (more than 95%). Equivalently, the contribution of the factor at $\bar{a}^2$ is suppressed. 2) The length Δz of the interval is maximal. This condition ensures that the largest number of bins is taken into consideration.

The most efficient intervals are found [11]

$$-0.6 < z < 0.2, \quad \sqrt{s} = 200 \text{ GeV}, \qquad -0.3 < z < 0.7, \quad \sqrt{s} = 500 \text{ GeV}. \tag{15}$$

Therefore the observable (14) allows to measure the Z' coupling to the electron vector current $\bar{v}^2$ with the efficiency more than 95%.

Fitting the LEP2 final data with the one-parameter observable, we find the values of the Z' coupling to the electron vector current together with their 1σ uncertainties:

$$\begin{aligned} \text{ALEPH}: \quad \bar{v}_e^2 &= -0.11 \pm 6.53 \times 10^{-4} \qquad \text{DELPHI}: \bar{v}_e^2 = 1.60 \pm 1.46 \times 10^{-4} \\ \text{L3}: \quad \bar{v}_e^2 &= 5.42 \pm 3.72 \times 10^{-4} \qquad \text{OPAL}: \quad \bar{v}_e^2 = 2.42 \pm 1.27 \times 10^{-4} \\ \text{Combined}: \quad \bar{v}_e^2 &= 2.24 \pm 0.92 \times 10^{-4}. \end{aligned} \tag{16}$$

As one can see, the most precise data of DELPHI and OPAL collaborations are resulted in the Abelian Z' hints at one and two standard deviation level, correspondingly. The combined value shows the 2σ hint, which corresponds to $0.006 \leq |\bar{v}_e| \leq 0.020$.

In order to pick the axial-vector coupling $\bar{a}^2$ one needs to eliminate the dominant contribution coming from $\bar{v}^2$. Since the factor at $\bar{v}^2$ in the $d\tilde{\sigma}/dz$ equals unity, this can be done by summing up equal number of bins with positive and negative weights. In particular, the forward-backward normalized deviation of the differential cross-section appears to be sensitive mainly to $\bar{a}^2$. Such an observable was fitted by the LEP2 data. Since in the Bhabha process the effects of the axial-vector coupling are suppressed with respect to those of the vector coupling, the huge errors for $\bar{a}^2$ of order $10^{-3} - 10^{-4}$ were observed. The corresponding mean values are too large to be interpreted as a manifestation of some heavy virtual state beyond the energy scale of the SM.

Thus, the LEP2 data constrain the value of $\bar{v}^2$ at the 2σ CL which could correspond to the Abelian Z' boson.

4.2 Many-parameter fits

As the basic observable to fit the LEP2 experiment data on the Bhabha process we propose the differential cross-section

$$\left.\frac{d\sigma^{\text{Bhabha}}}{dz} - \frac{d\sigma^{\text{Bhabha},SM}}{dz}\right|_{z=z_i,\sqrt{s}=\sqrt{s_i}}, \tag{17}$$

where i runs over the bins at various center-of-mass energies $\sqrt{s}$. The final differential cross-sections measured by the ALEPH (130-183 GeV, [16]), DELPHI (189-207 GeV, [3]), L3 (183-189 GeV, [17]), and OPAL (130-207 GeV, [2]) collaborations are taken into consideration (299 bins).

As the observables for $e^+e^- \to \mu^+\mu^-, \tau^+\tau^-$ processes, we consider the total cross-section and the forward-backward asymmetry

$$\left.\sigma_T^{\ell^+\ell^-} - \sigma_T^{\ell^+\ell^-,\text{SM}}, \quad A_{FB}^{\ell^+\ell^-} - A_{FB}^{\ell^+\ell^-,\text{SM}}\right|_{\sqrt{s}=\sqrt{s_i}}, \tag{18}$$

where i runs over 12 center-of-mass energies $\sqrt{s}$ from 130 to 207 GeV. We consider the combined LEP2 data [1] for these observables (24 data entries for each process). These data are more precise as the corresponding differential cross-sections. Our analysis is based on the fact that the kinematics of s-channel processes is rather simple and the differential cross-section is effectively a two-parametric function of the scattering angle. The total cross-section and the forward-backward asymmetry incorporate complete information about the kinematics of the process and therefore are an adequate alternative for the differential cross-sections.

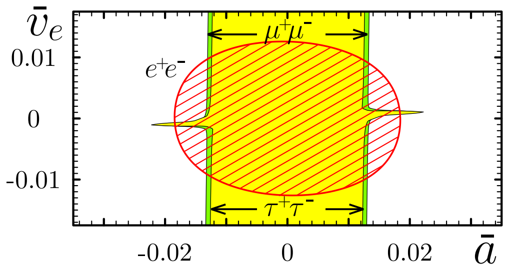

Figure 2. The 95% CL areas in the $(\bar{a}, \bar{v}_e)$ plane for the Bhabha, $e^+e^- \to \mu^+\mu^-$, and $e^+e^- \to \tau^+\tau^-$ processes.

The data are analysed by means of the χ^2 fit [12]. Denoting the observables (17)–(18) by σ_i, one can construct the χ^2-function,

$$\chi^2(\bar{a}, \bar{v}_e, \bar{v}_\mu, \bar{v}_\tau) = \sum_i \left[\frac{\sigma_i^{\rm ex} - \sigma_i^{\rm th}(\bar{a}, \bar{v}_e, \bar{v}_\mu, \bar{v}_\tau)}{\delta\sigma_i}\right]^2, \qquad (19)$$

where $\sigma^{\rm ex}$ and $\delta\sigma$ are the experimental values and the uncertainties of the observables, and $\sigma^{\rm th}$ are their theoretical expressions. The sum in Eq. (19) refers to either the data for one specific process or the combined data for several processes. By minimizing the χ^2-function, the maximal-likelihood estimate for the Z' couplings can be derived. The χ^2-function is also used to plot the confidence area in the space of parameters $\bar{a}$, $\bar{v}_e$, $\bar{v}_\mu$, and $\bar{v}_\tau$:

$$\chi^2 \le \chi^2_{\rm min} + \chi^2_{{\rm CL},\beta}(M), \qquad (20)$$

where $\chi^2_{{\rm CL},\beta}(M)$ is the β-level of the χ^2-distribution with M degrees of freedom.

In the Bhabha process, the Z' effects are determined by 3 linear-independent contributions coming from $\bar{a}^2$, $\bar{v}_e^2$, and $\bar{a}\bar{v}_e$ ($M = 3$). As for the $e^+e^- \to \mu^+\mu^-, \tau^+\tau^-$ processes, the observables depend on 4 linear-independent terms for each process: $\bar{a}^2$, $\bar{v}_e\bar{v}_\mu$, $\bar{v}_e\bar{a}$, $\bar{a}\bar{v}_\mu$ for $e^+e^- \to \mu^+\mu^-$; and $\bar{a}^2$, $\bar{v}_e\bar{v}_\tau$, $\bar{v}_e\bar{a}$, $\bar{a}\bar{v}_\tau$ for $e^+e^- \to \tau^+\tau^-$ ($M = 4$). Note that some terms in the observables for different processes are the same. Therefore, the number of χ^2 d.o.f. in the combined fits is less than the sum of d.o.f. for separate processes. Hence, the predictive power of the larger set of data is not drastically spoiled by the increased number of d.o.f. In fact, combining the data of the Bhabha and $e^+e^- \to \mu^+\mu^-$ ($\tau^+\tau^-$) processes together we have to treat 5 linear-independent terms. The complete data set for all the lepton processes is ruled by 7 d.o.f. As a consequence, the combination of the data for all the lepton processes is possible.

The parametric space of couplings ($\bar{a}$, $\bar{v}_e$, $\bar{v}_\mu$, $\bar{v}_\tau$) is four-dimensional. However, for the Bhabha process it is reduced to the plane ($\bar{a}$, $\bar{v}_e$), and to the three-dimensional volumes ($\bar{a}$, $\bar{v}_e$, $\bar{v}_\mu$), ($\bar{a}$, $\bar{v}_e$, $\bar{v}_\tau$) for the $e^+e^- \to \mu^+\mu^-$ and $e^+e^- \to \tau^+\tau^-$ processes, correspondingly. The predictive power of data is distributed not uniformly over the parameters. The parameters $\bar{a}$ and $\bar{v}_e$ are present in all the considered processes and appear to be significantly constrained. The couplings $\bar{v}_\mu$ or $\bar{v}_\tau$ enter when the processes $e^+e^- \to \mu^+\mu^-$ or $e^+e^- \to \tau^+\tau^-$ are accounted for. So, in these processes, we also study the projection of the confidence area onto the plane $(\bar{a}, \bar{v}_e)$.

The origin of the parametric space, $\bar{a} = \bar{v}_e = 0$, corresponds to the absence of the Z' signal. This is the SM value of the observables. This point could occur inside or outside of the confidence area at a fixed CL. When it lays out of the confidence area, this means the distinct signal of the Abelian Z'. Then the signal probability can be defined as the probability that the data agree with the Abelian Z' boson existence and exclude the SM value. This probability corresponds to the most stringent CL (the largest $\chi^2_{\rm CL}$) at which the point $\bar{a} = \bar{v}_e = 0$ is excluded. If the SM value is inside the confidence area, the Z' boson is indistinguishable from the SM. In this case, upper bounds on the Z' couplings can be determined.

The 95% CL areas in the $(\bar{a}, \bar{v}_e)$ plane for the separate processes are plotted in Fig. 2. As it is seen, the Bhabha process constrains both the axial-vector and vector couplings. As for the $e^+e^- \to \mu^+\mu^-$ and $e^+e^- \to \tau^+\tau^-$ processes, the axial-vector coupling is significantly constrained, only. The confidence areas include the SM point at the meaningful CLs, so the experiment could not pick out clearly the Abelian Z' signal from the SM. An important conclusion from these plots is that the experiment significantly constrains only the couplings entering sign-definite terms in the cross-sections.

The combination of all the lepton processes is presented in Fig. 3. There is no visible signal beyond the SM. The couplings to the vector and axial-vector electron currents are constrained by the many-parameter fit as $|\bar{v}_e| < 0.013$, $|\bar{a}| < 0.019$ at the 95% CL.

Why does the one-parameter fit of the Bhabha process show the 2σ CL hint whereas there is no signal in the two-parameter one? Our one-parameter observable accounts mainly for the backward bins. Therefore, the difference of the results can be inspired by the data sets used. To clarify this point, we perform the many-parameter fit with the 113 backward bins ($z \le 0$), only. The χ^2 minimum is found in the non-zero point

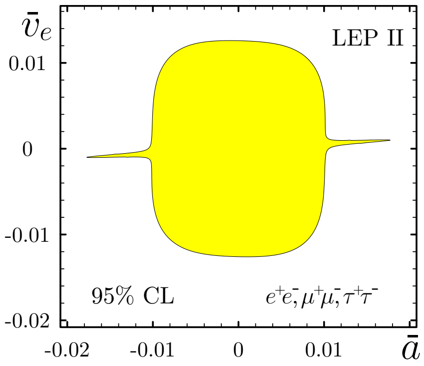

Figure 3. The projection of the 95% CL area onto the $(\bar{a}, \bar{v}_e)$ plane for the combination of the Bhabha, $e^+e^- \to \mu^+\mu^-$, and $e^+e^- \to \tau^+\tau^-$ processes.

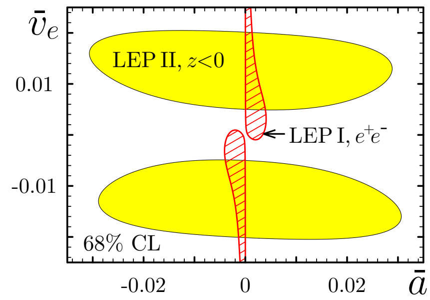

Figure 4. The 68% CL area in the $(\bar{a}, \bar{v}_e)$ plane from the backward bins of the Bhabha process in the LEP2 experiments (the shaded area). The hatched area is the 68% CL area from the LEP 1 data on the Bhabha process.

$|\bar{a}| = 0.0005$, $\bar{v}_e = 0.015$. This value of the Z' coupling $\bar{v}_e$ is in an excellent agreement with the mean value obtained in the one-parameter fit. The 68% confidence area in the $(\bar{a}, \bar{v}_e)$ plane is plotted in Fig. 4. There is a visible hint of the Abelian Z' boson at 1.3σ CL. So, the many-parameter fit is less precise than the analysis of the one-parameter observables.

At LEP1 experiments [18] the Z-boson couplings to the vector and axial-vector lepton currents (g_V, g_A) were precisely measured. The Bhabha process shows the 1σ deviation from the SM values for Higgs boson masses $m_H \geq 114$ GeV (see Fig. 7.3 of Ref. [18]). This deviation could be considered as the effect of the Z–Z' mixing. The deviations of g_V, g_A from their SM values are governed by the couplings $\bar{a}$ and $\bar{v}_e$,

$$g_V - g_V^{\mathrm{SM}} = -49.06\bar{a}\bar{v}_e, \quad g_A - g_A^{\mathrm{SM}} = 49.06\bar{a}^2. \tag{21}$$

Let us assume that the total deviation of theory from experiments follows due to the Z–Z' mixing. This gives an upper bound on the Z' couplings. In this way one can estimate whether the Z' boson is excluded by the experiments or not.

The 1σ CL area for the Bhabha process from Ref. [18] is converted into the $(\bar{a}, \bar{v}_e)$ plane in Fig. 4. The SM values of the couplings correspond to the top quark mass $m_t = 178$ GeV and the Higgs scalar mass $m_H = 114$ GeV. As it is seen, the LEP1 data on the Bhabha process is compatible with the Abelian Z' existence at the 1σ CL. The axial-vector coupling is constrained as $|\bar{a}| \leq 0.005$. This bound corresponds to $\bar{a}^2 \leq 2.5 \times 10^{-5}$, which agrees with the one-parameter fits of the LEP2 data for $e^+e^- \to \mu^+\mu^-, \tau^+\tau^-$ processes ($\bar{a}^2 = 1.3 \pm 3.89 \times 10^{-5}$ at 68% CL). On the other hand, the vector coupling constant $\bar{v}_e$ is practically unconstrained by the LEP1 experiments.

5 Discussion

For a convenience of readers, let us present the results of fits of the Z' parameters in terms of the popular notations [4, 5]. The Lagrangian reads

$$\mathcal{L}_{Z\bar{f}f} = \frac{1}{2} Z_\mu \bar{f}\gamma^\mu \left[(v_f^{\mathrm{SM}} + \Delta_f^V) - \gamma^5 (a_f^{\mathrm{SM}} + \Delta_f^A) \right] f, \qquad \mathcal{L}_{Z'\bar{f}f} = \frac{1}{2} Z'_\mu \bar{f}\gamma^\mu \left[(v'_f - \gamma^5 a'_f) \right] f, \tag{22}$$

with the SM values of the Z couplings

$$v_f^{\mathrm{SM}} = \frac{e\,(T_{3f} - 2Q_f \sin^2\theta_W)}{\sin\theta_W \cos\theta_W}, \qquad a_f^{\mathrm{SM}} = \frac{e\,T_{3f}}{\sin\theta_W \cos\theta_W},$$

where e is the positron charge, Q_f is the fermion charge in the units of e, $T_{3f} = 1/2$ for the neutrinos and u-type quarks, and $T_{3f} = -1/2$ for the charged leptons and d-type quarks.

The results of the fits of the Z' couplings to the SM leptons obtained from the analysis of the LEP experiments are adduced in the Tables 1-2. Remind that due to the universality of the axial-vector coupling a_f the same estimates take also place for quarks. First of all, one parameter fits of LEP experiments as well as the many-parameter fit for the e^+e^- backward bins show the hints of the Z' boson at the 1-2σ CL. Due to this fact, the fits allow to determine the maximum likelihood values of Z' parameters. In spite of uncertainties, these values can be used as a guiding line for the estimation of possible Z' effects in the LHC experiments. The maximum likelihood values are given in Table 1. As is seen, different fits and processes lead to the comparable values of the Z' parameters.

Table 1. The summary of the fits of the LEP data for the maximum likelihood values of the Z' couplings (22) to the SM fermions and of the $Z - Z'$ mixing angle θ_0. $M = \frac{m_{Z'}}{1\,\text{TeV}}$ denotes the unknown value of the Z' mass in TeV units.

Data	$\lvert\theta_0\rvert$, $\times 10^{-3}$	$\lvert v'_e\rvert$, $\times 10^{-1}$	$\lvert a'_f\rvert$, $\times 10^{-1}$	Δ_e^A, $\times 10^{-3}$
LEP1				
e^-e^+	$3.17 M^{-1}$	-	$1.38M$	0.437
LEP2, one-parameter fits				
e^-e^+	-	$5.83M$	-	-
$\mu^-\mu^+$	$5.42M^{-1}$	-	$2.36M$	1.278
$\mu^-\mu^+, \tau^-\tau^+$	$3.27M^{-1}$	-	$1.42M$	0.464
LEP2, many-parameter fits				
e^-e^+, $z < 0$	-	$5.84M$	-	-

Table 2. The summary of the fits of the LEP data for the confidence intervals for the Z' couplings (22) to the SM fermions and for the $Z - Z'$ mixing angle θ_0. $M = \frac{m_{Z'}}{1\,\text{TeV}}$ denotes the unknown value of the Z' mass in TeV units.

Data	CL	$\lvert\theta_0\rvert$, $\times 10^{-3}$	$\lvert v'_e\rvert$, $\times 10^{-1}$	$\lvert a'_f\rvert$, $\times 10^{-1}$	Δ_e^A, $\times 10^{-3}$
LEP1					
e^-e^+	68%	$(0; 4.48)M^{-1}$	-	$(0; 1.95)M$	$(0; 0.873)$
LEP2, one-parameter fits					
e^-e^+	95%	-	$(2.46; 7.87)M$	-	-
$\mu^-\mu^+$	95%	$(0; 10.39)M^{-1}$	-	$(0; 4.52)M$	$(0; 4.694)$
$\mu^-\mu^+$, $\tau^-\tau^+$	95%	$(0; 8.64)M^{-1}$	-	$(0; 3.75)M$	$(0; 3.244)$
LEP2, many-parameter fits					
e^-e^+, $\mu^-\mu^+$, $\tau^-\tau^+$	95%	$(0; 17.03)M^{-1}$	$(0; 5.06)M$	$(0; 7.40)M$	$(0; 12.607)$
e^-e^+, $z < 0$	68%	$(0; 27.61)M^{-1}$	$(1.68; 7.83)M$	$(0; 12.00)M$	$(0; 33.1288)$

In Table 2 we present the confidence intervals for the fitted parameters. With this Table one is able to estimate the uncertainty of the Z' couplings as well as the lower bounds on the parameters.

Thus, the results are in accordance at 68-95% CL with the existence of the not heavy Z', which has a good chance to be discovered at Tevatron and/or LHC.

References

[1] The LEP Collaborations ALEPH, DELPHI, L3, OPAL, and the LEP Electroweak Working Group, hep-ex/0612034.

[2] G. Abbiendi *et al.* [OPAL Collaboration], Eur. Phys. J. **C33** (2004) 173 [hep-ex/0309053]; Eur. Phys. J. **C6** (1999) 1; K. Ackerstaff *et al.* [OPAL Collaboration], Eur. Phys. J. **C2** (1998) 441.

[3] J. Abdallah *et al.* [DELPHI Collaboration], Eur. Phys. J. **C45** (2006) 589 [hep-ex/0512012].

[4] A. Leike, Phys. Rep. **317** (1999) 143.

[5] P. Langacker, arXiv:0801.1345 [hep-ph].

[6] T. Rizzo, hep-ph/0610104.

[7] A. Ferroglia, A. Lorca, and J.J. van der Bij, Annalen Phys **16** (2007) 563-578 [hep-ph/0611174].

[8] A. Gulov and V. Skalozub, Eur. Phys. J. **C17** (2000) 685.

[9] A. Gulov and V. Skalozub, Phys. Rev. **D61** (2000) 055007.

[10] V. Demchik, A. Gulov, V. Skalozub, and A. Tishchenko, Phys. Atom. Nucl. **67** (2004) 1312.

[11] A. Gulov and V. Skalozub, Phys. Rev. **D70** (2004) 115010.

[12] A. Gulov and V. Skalozub, Phys. Rev. **D76** (2007) 075008.

[13] J.Hewett and T.Rizzo, Phys. Rep. **183** (1989) 193.

[14] M. Cvetic and B.W. Lynn, Phys. Rev. **D35** (1987) 51.

[15] G. Degrassi and A. Sirlin, Phys. Rev. **D40** (1989) 3066.

[16] R. Barate *et al.* [ALEPH Collaboration], Eur. Phys. J. **C12** (2000) 183 [hep-ex/9904011].

[17] M. Acciarri *et al.* [L3 Collaboration], Phys. Lett. **B479** (2000) 101 [hep-ex/0002034].

[18] ALEPH Collaboration, DELPHI Collaboration, L3 Collaboration, OPAL Collaboration, SLD Collaboration, LEP Electroweak Working Group, SLD Electroweak Group, and SLD Heavy Flavour Group, Phys. Rept. **427** (2006) 257 [hep-ex/0509008].

Proceedings of the International School-seminar
"New Physics and Quantum Chromodynamics at external Conditions", pp. 64 – 71,
3-6 May 2009, Dnipropetrovsk, Ukraine

HEAVY FLAVOR PROBES OF QUARK-GLUON PLASMA

A. A. Isayev[a]

Kharkov Institute of Physics and Technology, Academicheskaya Str. 1, Kharkov, 61108, Ukraine
Kharkov National University, Svobody Sq., 4, Kharkov, 61077, Ukraine

Some aspects of heavy flavor probes of quark-gluon plasma (QGP) including quarkonia and open heavy flavor D- and B-mesons, aimed to study the properties of QGP, are discussed in this lecture note.

1 Introduction

Lattice QCD (LQCD) calculations predict that at a critical temperature $T_c \simeq 170\,\mathrm{MeV}$, corresponding to an energy density $\varepsilon_c \simeq 0.7\,\mathrm{GeV/fm}^3$, nuclear matter undergoes a phase transition to a deconfined state of quarks and gluons, called Quark-Gluon Plasma (QGP). At the modern collider facilities such as CERN supersynchrotron (SPS) (the nucleon-nucleon (NN) centre-of-mass energy for collisions of the heaviest ions is $\sqrt{s} = 17.3\,\mathrm{GeV}$), Relativistic Heavy Ion Collider (RHIC) at Brookhaven ($\sqrt{s} = 200\,\mathrm{GeV}$), and Large Hadron Collider (LHC) at CERN ($\sqrt{s} = 5.5\,\mathrm{TeV}$), which will start to operate soon, heavy-ion collisions are used to attain the energy density, exceeding ε_c. This makes the QCD phase transition potentially realizable within the reach of the laboratory experiments. The objective is then to identify and to assess suitable QGP signatures, allowing to study the properties of QGP. To that end, a variety of observables (probes) can be used [1, 2]. Further we will be mainly interested in heavy-flavour probes of QGP, i.e., utilizing the particles having c- and b-quarks.

A special role of heavy $Q = c, b$ quarks as probes of the medium created in heavy-ion collision (HIC) resides on the fact that their masses ($m_c \approx 1.3\,\mathrm{GeV}$, $m_b \approx 4.2\,\mathrm{GeV}$) are significantly larger than the typically attained ambient temperatures or other nonperturbative scales, $m_Q \gg T_c, \Lambda_{QCD} = 0.2\,\mathrm{GeV}$ [3]. This has several implications: (i) The production of heavy quarks is essentially constrained to the early, primordial stages of HIC. Hence, heavy quarks can probe the properties of the dense matter produced early in the collision. (ii) Thermalization of heavy quarks is "delayed" relative to light quarks. Heavy quarks could "thermalize" to a certain extent, but not fully on a timescale of the lifetime of the QGP. Therefore, their spectra should be significantly modified, but still retain memory about their interaction history, and, hence, represent an "optimal" probe. (iii) RHIC, and especially LHC experiments allow to reach very low parton momentum fractions x, where gluon saturation effects become important. Heavy quarks are valuable tools to study gluon saturation, since, due to their large masses, charm and bottom cross sections are calculable via perturbative QCD and their yield is sensitive to the initial gluon density.

The heavy-flavor hadrons we will be interested in include: 1) open charm $D = (c\bar{q})$ and open beauty $B = (b\bar{q})$ mesons composed of a heavy quark $Q = (c, b)$ and a light antiquark $\bar{q} = (\bar{u}, \bar{d})$. These mesons could be sensitive to the energy density of the medium through the mechanism of in-medium energy loss; 2) hidden charm [charmonia=$(c\bar{c})$] and hidden beauty [bottomonia=$(b\bar{b})$] mesons (called collectively heavy quarkonia) being the bound states of the charm quark-antiquark, or bottom quark-antiquark pairs, respectively. Heavy quarkonia could be sensitive to the initial temperature of the system through the dissociation due to color screening of the color charge that will be discussed later.

For detecting heavy flavor hadrons, different decay channels are used. At LHC, the ALICE experiment for detecting open charm will use the reconstructed hadronic decays like $D^0 \to K^-\pi^+$, $D^+ \to K^-\pi^+\pi^+$, etc., for detecting open beauty ALICE will use inclusive single lepton decays $B \to e + X$ (midrapidity), $B \to \mu + X$ (forward rapidity) and inclusive displaced charmonia decays $B \to J/\psi(\to e^+e^-) + X$. At RHIC, in PHENIX and STAR experiments direct measurement of open heavy flavors is currently complicated by the absence of the vertex detector. Due to that, the measurement of the spectra of open heavy flavors is based on the measurement of the spectra of heavy flavor (HF) electrons and positrons $[(e^+ + e^-)/2]$ from the semileptonic decays like $D^0 \to K^-e^+\nu_e$, $D^+ \to \bar{K}^0e^+\nu_e$, etc. These measurements are based on the fact that the decay kinematics of HF electrons/positrons largely conserves the spectral properties of the parent particles. In all of the above experiments, quarkonia are detected through their dilepton decays $Q\bar{Q} \to e^+e^-$ (midrapidity), $Q\bar{Q} \to \mu^+\mu^-$ (forward rapidity) $(Q = c, b)$.

e-mail: [a]isayev@kipt.kharkov.ua

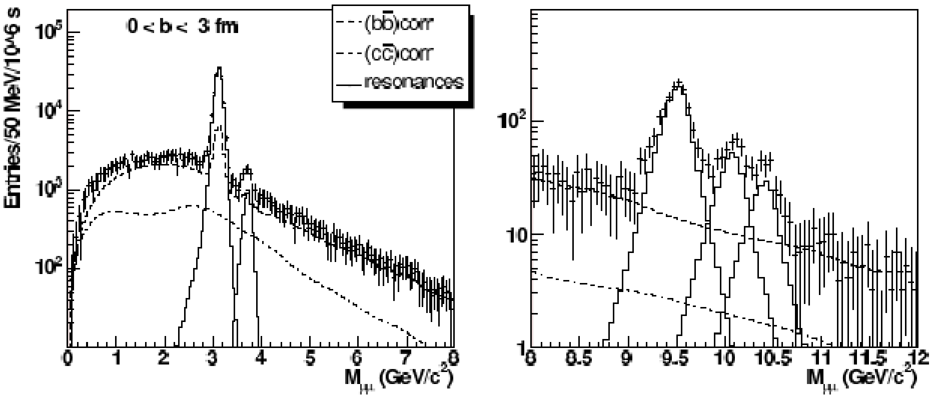

Figure 1. Left: Dimuon invariant mass spectra (after subtraction of the uncorrelated background) in central Pb-Pb collisions at LHC/ALICE for one year of data taking (10^6 s) and luminosity $5 \cdot 10^{26}\,\mathrm{cm}^{-2}\mathrm{s}^{-1}$ in the J/ψ mass region (PYTHIA calculations). Right: Same as on the left, but in the Υ mass region.

2 Heavy Flavor Probes of QGP: Quarkonia

We begin the discussion of heavy flavor probes of QGP with heavy quarkonia. The question we would like to address is: What could happen with quarkonium yields in HIC if QGP is really formed? In the above mensioned experiments, quarkonia are detected in the dielectron channel at midrapidity and in the dimuon channel at forward rapidity. For example, in the dimuon channel, signals of about $7 \cdot 10^5$ J/ψs and 10^4 Υs are expected in the most central Pb-Pb collisions at LHC/ALICE for one year of data taking at nominal luminosity (see Fig. 1 from [2]). If quarkonia will be completely suppressed by QGP, these signals will disappear, otherwise, in the case of enhancement of quarkonium yields, the peaks will be more pronounced as compared to the signals obtained in pp collisions after scaling them with the corresponding number of independent binary NN collisions.

Let us note that if the deconfinement phase transition really takes place in a dense medium created in HIC, then a color charge in the QGP will be screened analogously to the Debye screening of an electric charge in the electromagnetic plasma. As a result of color Debye screening of the heavy quark interaction in QGP, the binding energy of a bound state decreases and one can expect that this would lead to the suppression of quarkonium yields in HIC. This idea was first suggested by H. Matsui and H. Satz [4] who predicted that color Debye screening will result in the suppression of J/ψ meson ($c\bar{c}$ in the $^3S_1$ state, $M = 3.097\,\mathrm{GeV}$) yields.

However, soon it was realized that besides melting J/ψ mesons in QGP due to the screening of the color charge, there are also a few competing mechanisms which could explain the suppression of J/ψ production in heavy-ion collisions. These mechanisms are referred to as cold nuclear matter (CNM) effects. The first CNM effect is the absorption of J/ψ by nuclear fragments from colliding nuclei. Let us consider, e.g., the proton-nucleus collision. Once produced in the hard primary parton processes, J/ψ has to cross the length L of nuclear matter, before exiting the nucleus, and, when traversing nuclear matter, it can be absorbed by forthcoming nucleons of a nucleus. The production cross section of J/ψ is p-A collision can be parameterized as

$$\sigma_{pA}^{J/\psi} = A\sigma_{pp}^{J/\psi} e^{-\sigma_{abs}^{J/\psi}\varrho L}, \tag{1}$$

where $\sigma_{pp}^{J/\psi}$ is the production cross section of J/ψ in pp collisions and $\sigma_{abs}^{J/\psi}$ is the nuclear absorption cross section. From the global fit to the data on charmonium production in p-A collisions the value of $\sigma_{abs}^{J/\psi}$ can be extracted, in particular, at SPS (NA50 experiment) it was obtained that $\sigma_{abs}^{J/\psi} = 4.5 \pm 0.5$ mb.

The second CNM effect is related to shadowing of low momentum partons. This means the depletion of low momentum partons in nucleons bound in nuclei as compared to free nucleons. This effect can be accounted for in terms of the modification of the parton distribution functions in nucleon within the nucleus with respect to the parton distribution functions in a free nucleon:

$$R_i^A(x, Q^2) = \frac{f_i^A(x, Q^2)}{f_i^N(x, Q^2)} < 1, \quad i = q_v, q_{sea}, g. \tag{2}$$

Here "i" denotes valence quarks, sea quarks, and gluons, x is the parton momentum fraction, Q^2 is the momentum transfer squared. At the typical RHIC and LHC energies J/ψs are dominantly produced through the gluon fusion, $g + g \to J/\psi + g$, and the J/ψ yield is therefore sensitive to gluon shadowing. The underlying idea explaining the occurrence of gluon shadowing is that the gluon density strongly rises at small x to the point where gluon fusion, $gg \to g$, becomes significant. In the case of proton-nucleus and nucleus-nucleus collisions,

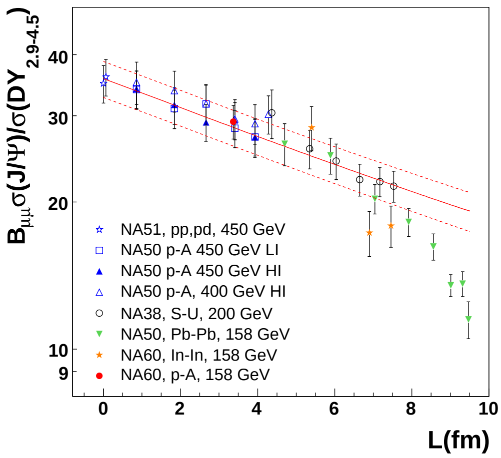

Figure 2. J/ψ yields normalized by Drell-Yan process, as a function of the nuclear thickness L, as measured at the SPS.

where nuclei with large mass number A are involved, the nonlinear effects are enhanced by the larger density of gluons per unit transverse area of the colliding nuclei. A direct consequence of nuclear shadowing is the reduction of hard-scattering cross sections in the phase-space region characterized by small-x incoming partons. For gluons, e.g., shadowing becomes important at $x \lesssim 5\times10^{-2}$. Note however that the strength of the reduction is constrained by the current experimental data only for $x \gtrsim 10^{-3}$.

After discussing CNM effects on the J/ψ production, let us consider the J/ψ production at CERN SPS experiments. Fig. 2 shows the J/ψ production cross section, where J/ψ are registered through their decay in the dimuon channel, normalized to the cross section of the Drell-Yan (DY) process [5]. The nuclear thickness parameter L parameterizes the number of participating nucleons and increases with centrality. At SPS energies, the DY process is not modified by the medium and its production cross section scales linearly with the number of binary NN collisions. Hence, this process can be used as unsuppressed reference process for the J/ψ production. The current interpretation of the obtained results is the following. The effects of cold nuclear matter are quantified in proton-nucleus collisions, where the energy density is not enough to reach the critical value for the formation of QGP. There is no anomalous suppression, beyond CNM effects, of the J/ψ yield in the collisions of light ions of sulfur ($A = 32$) with the heavy ions of uranium ($A = 238$). However, there is the anomalous suppression beyond the CNM effects in the central collisions of lead nuclei when the number of participating nucleons is the largest, and, to a certain extent, in the central collisions of the indium nuclei ($A = 115$) [6]. This could be considered as the signature of melting the charmonium states in quark-gluon plasma. At this point, it is also worth to note that some level of the J/ψ suppression could originate with the reduced feed-down to J/ψ from excited charmonium states (ψ', χ_c), which melt just above the QGP transition temperature.

Let us consider the J/ψ production at RHIC experiments, when the nucleon-nucleon center-of-mass energy for collisions of the heaviest ions increases by a factor 10 compared to the CERN SPS experiments. The J/ψ suppression can be characterized by a ratio called the nuclear modification factor

$$R_{AB}(p_T, y) = \frac{d^2N^{AB}_{J/\psi}/dp_T dy}{N_{coll} d^2N^{pp}_{J/\psi}/dp_T dy}, \tag{3}$$

obtained by normalizing the J/ψ yield in nucleus-nucleus collision by the J/ψ yield in $p+p$ collision at the same energy per nucleon pair times the average number of binary inelastic NN collisions. This ratio characterizes the impact of the medium on the particle spectrum. If heavy ion collision is a superposition of independent N_{coll} inelastic NN collisions, then $R_{AB} = 1$, whereas $R_{AB} < 1$ ($R_{AB} > 1$) corresponds to the case of the J/ψ suppression (enhancement). As we discussed already, at first, it is necessary to clarify the role of CNM effects on J/ψ production. At RHIC, CNM effects are studied in collisions of light deuteron and heavy gold nuclei, when the energy density reached in the collision is not enough for the formation of QGP. At RHIC energies, shadowing of partons is important and in the model calculations is implemented in two shadowing schemes for the nuclear parton distribution functions, the EKS model [7] and NDSG model [8]. The J/ψ break-up cross sections obtained for two shadowing schemes from the best fit to data, $\sigma_{\rm breakup} = 2.8^{+2.3}_{-2.1}$ mb (EKS) and $\sigma_{\rm breakup} = 2.6^{+2.2}_{-2.6}$ mb (NDSG), are consistent, within large uncertainties, with the corresponding value obtained at CERN SPS (although denoted differently, $\sigma_{\rm breakup}$ is the same quantity as $\sigma_{\rm abs}$, introduced earlier).

Let us now consider charmonium production in heavy ion collisions at RHIC. Fig. 3 shows the p_T-integrated J/ψ nuclear modification factor obtained in Au-Au collisions at RHIC/PHENIX experiment as a function of

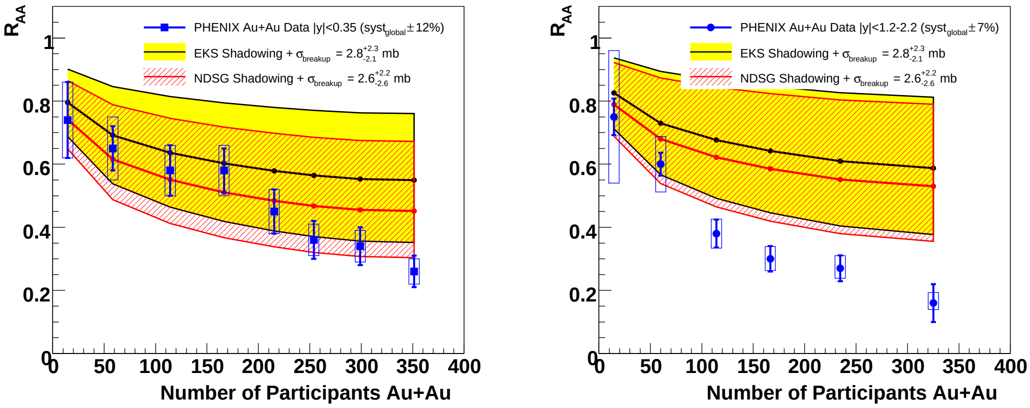

Figure 3. Left: J/ψ's R_{AA} for *Au-Au* collisions at midrapidity compared to a band of theoretical curves for the breakup values found to be consistent with the *d-Au* data. Both EKS and NDSG shadowing schemes are included. Right: Same as on the left but at forward rapidity.

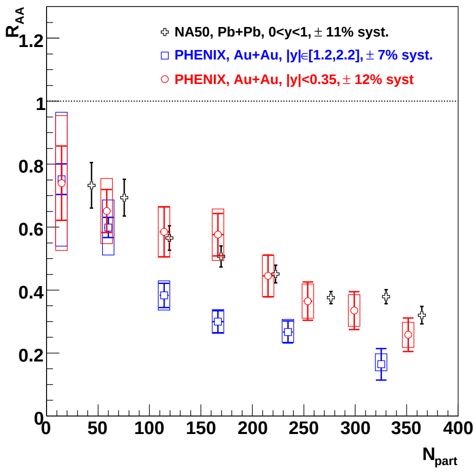

Figure 4. J/ψ nuclear modification factor for the most energetic SPS (Pb-Pb) and RHIC (Au-Au) collisions, as a function of the number of participants N_{part}.

centrality, parametrized by the number of participating nucleons at mid- (left panel) and forward (right panel) rapidity [9]. The PHENIX data are shown by blue symbols. The R_{AA} approaches unity for the peripheral collisions (small N_{part}) and goes down to approximately 0.2 at most central collisions (large N_{part}). To see the level of the anomalous suppression beyond the cold nuclear matter effects it is necessary to extrapolate the CNM effects obtained in d-Au collisions to the Au-Au collisions within the given shadowing scheme and the J/ψ break-up cross section. The results are shown by black and red curves with the corresponding error bands. It is seen that J/ψ production is significantly suppressed beyond CNM effects at forward rapidity (right) and suppression is less pronounced at midrapidity (left) in most central Au-Au collisions.

However, not all is still clear. Measurements of the J/ψ suppression by PHENIX collaboration at RHIC lead to some surprising features. Fig. 4 shows compiled data for the nuclear modification factor obtained in CERN SPS and RHIC PHENIX experiments. There are two surprising results in these measurements. First, the midrapidity suppression in PHENIX (the red boxes) is lower than the forward rapidity suppression (blue boxes) despite the experimental evidence that the energy density is higher at midrapidity than at forward rapidity, and, hence, one could expect that at midrapidity the J/ψs will be more suppressed due to higher density of color charges. Secondly, the nuclear modification factor R_{AA} at midrapidity in PHENIX (red boxes) and SPS (black crosses) are in agreement within error bars, a surprising result considering that the energy density reached at RHIC is larger than the one reached at SPS. This indicates that at RHIC energies additional mechanisms countering the suppression, could be operative.

Let us consider possible explanations of the above features. 1. Regeneration of J/ψs in the hot partonic phase from initially uncorrelated c and $\bar{c}$ quarks (quark coalescence model). If to compare the J/ψ suppression pattern at RHIC and SPS, J/ψs could be indeed more suppressed at RHIC than at SPS, but then regenerated

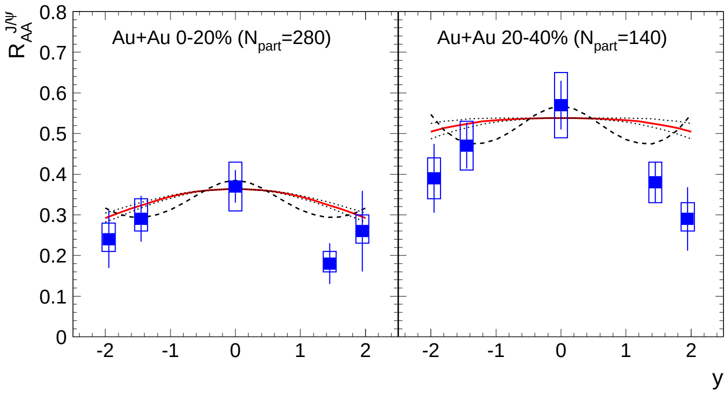

Figure 5. Rapidity dependence of J/ψ R_{AA} for two centrality classes in the statistical hadronization model. The data from the PHENIX experiment (symbols with errors) are compared to calculations (lines, see text).

during (or at the boundary of) the hot partonic phase from initially uncorrelated c and $\bar{c}$ quarks. If to compare the results at RHIC (midrapidity vs. forward rapidity), at midrapidity, due to higher energy density, there are more c and $\bar{c}$ to regenerate than at forward rapidity that could explain the stronger suppression at forward rapidity. Note that the total number of initial $c\bar{c}$ pairs is larger than 10 in the most central Au-Au collisions. Certainly, if regeneration is important at the RHIC conditions, it will be even more important at the LHC conditions where more than 100 $c\bar{c}$ pairs is expected to be produced in the central Pb-Pb collisions. 2. J/ψ production could be more suppressed at forward rapidity due to the nuclear shadowing effects. Standard gluon shadowing parametrizations do not tend to produce such an effect but they are poorly constrained by the data and further saturation effects are not excluded.

To show the complexity of the problem, let us consider some theoretical models for the charmonium production, which quite satisfactory describe the RHIC data but whose predictions for LHC are drastically different. First, in the *statistical hadronization model* (SHM) [10], it is assumed that: 1. All heavy quarks (charm and bottom) are produced in primary hard collisions and their total number stays constant until hadronization. 2. Heavy quarks reach thermal equilibrium in the QGP before the chemical freeze-out (hadronization). 3. All quarkonia are produced (nonperturbatively) through the statistical coalescence of heavy quarks at hadronization. Multiplicities of various hadrons are calculated with the grand canonical ensemble. The generation of J/ψ proceeds effectively if $c, \bar{c}$ quarks are free to travel over large distances implying deconfinement.

Fig. 5 shows the rapidity dependence of the nuclear modification factor, obtained in this model and the comparison with the rapidity dependence at PHENIX for two centrality bins. Two theoretical curves correspond to two fitting procedures, with one and two Gaussians of the J/ψ data in pp collisions. In both cases, calculations reproduce rather well (considering the systematic errors) the R_{AA} data. The model describes the larger suppression away from midrapidity. The maximum of R_{AA} at midrapidity in this model is due to the enhanced generation of charmonium around midrapidity, determined by the rapidity dependence of the charm production cross section. The centrality dependence of R_{AA} at $y = 0$ is shown in Fig. 6. The model reproduces quite well the decreasing trend with centrality seen in the RHIC data. Fig. 6 also shows the prediction of the model for the LHC. At much higher LHC energies, the charm production cross section is expected to be larger by about an order of magnitude. As a result, a totally opposite trend as a function of centrality is predicted, with R_{AA} exceeding unity for central collisions.

Let us consider *the comovers interaction model* (CIM) [11]. This model does not assume the deconfinement phase transition. Anomalous suppression of J/ψ (beyond CNM effects) is the result of the final state interaction of the $c\bar{c}$ pair with the dense medium produced in the collision (comovers interaction). The model consistently treats the initial and final state effects. The initial state effects include: 1) nuclear absorption of the preresonant $c\bar{c}$ pairs by nucleons of the colliding nuclei, 2) consistent treatment of nuclear shadowing for hard production of charmonium. The final state effects include absorption of the $c\bar{c}$ pairs by the dense medium created in the collision (interaction with comoving hadrons produced in the collision). The model does not assume thermodynamic equilibrium and, thus, does not use thermodynamic concepts. The density of charmonium is governed by the differential rate equation

$$\tau \frac{dn_{J/\psi}}{d\tau} = -\sigma_{co}[n_{co}(b,s,y)n_{J/\psi}(b,s,y) - n_c(b,s,y)n_{\bar{c}}(b,s,y)], \tag{4}$$

where n_{co} is the density of comovers, which is found in the dual parton model [12] together with the proper shadowing correction, σ_{co} is the cross section of J/ψ dissociation due to interactions with comovers, taken such as

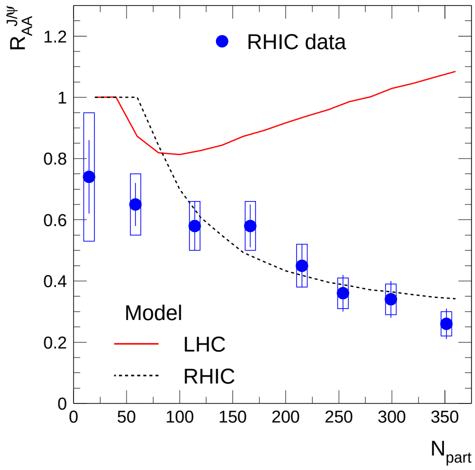

Figure 6. Centrality dependence of the J/ψ R_{AA} at midrapidity, according to the statistical hadronization model.

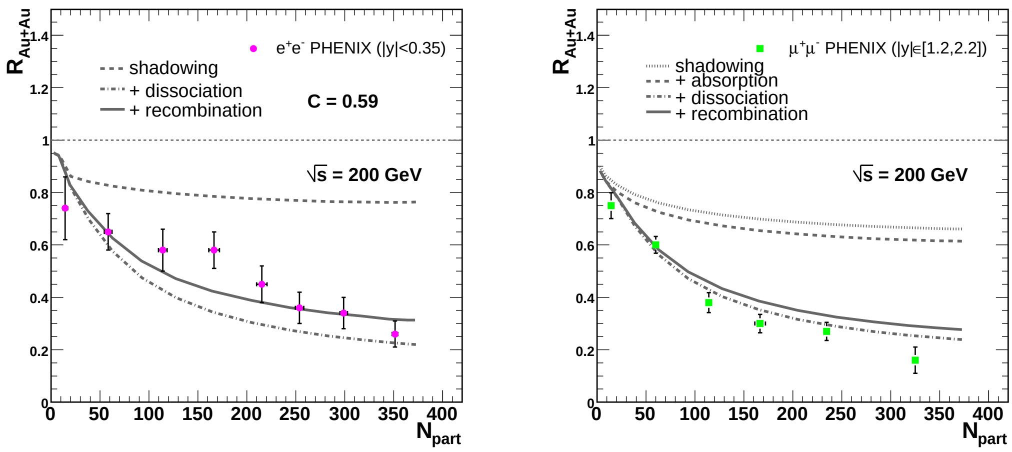

Figure 7. Results for J/ψ suppression in Au-Au collisions at RHIC at mid- (left panel), and forward (right panel) rapidities. The solid curves are the final results. The dashed-dotted ones are the results without recombination ($C = 0$). The dashed line is the total initial-state effect. The dotted line in the right panel is the result of shadowing. In the left panel the last two lines coincide.

to reproduce the low energy SPS experimental data (with $\sigma_{co} = 0.65$ mb). The first term on the right describes dissociation of charmonium due to interaction with comovers. The second term describes the recombination of charmonium and is proportional to the product of densities of charm quarks and antiquarks. The important feature of the CIM is that recombination of c-$\bar{c}$ quarks proceeds only locally, when the densities of quarks and antiquarks are taken at the same transverse coordinate s. This is different from the recombination in the SHM, where recombining quarks can be separated by large distance that implies deconfinement. The effective recombination cross section in the CIM is equal to the dissociation cross section due to the detailed balance. The results for the centrality dependence of the R_{AA} are shown in Fig. 7. At midrapidity, the experimental data are well reproduced by full theoretical calculations (solid curve) taking into account nuclear shadowing, dissociation by comovers and recombination from charm quark and antiquark pairs. At forward rapidity, the results also well agree with data, in particular, the J/ψ suppression at forward rapidity is somewhat larger that the suppression at midrapidity. Fig. 8 shows the predictions of the model for LHC. The parameter C encodes the recombination from c-$\bar{c}$ pairs and is vanishing in the absence of recombination. Although the density of charm grows substantially from RHIC to LHC, the combined effect of initial-state shadowing, absorption and comovers dissociation overcomes the effect of parton recombination. This is in sharp contrast with the predictions of SHM where a strong enhancement of the J/ψ yield with increasing centrality was predicted.

Thus, the J/ψ suppression is an interesting characteristic to search for QGP. But if J/ψ anomalous suppression (beyond CNM effects) was observed in HIC, there are a few competing mechanisms to explain that: 1. Charmonium is dissociated due to the genuine color screening in the deconfined medium. 2. Charmonium is dissociated through interactions with comoving hadrons in the medium formed in HIC. How to differ these

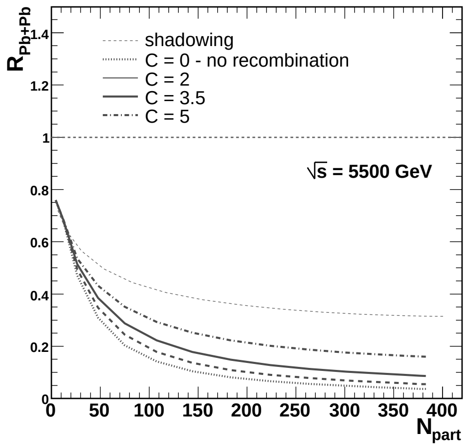

Figure 8. Results for J/ψ suppression in Pb+Pb at LHC ($\sqrt{s} = 5.5$ TeV) at mid-rapidities for different values of the parameter C. The upper line is the suppression due to initial-state effects (shadowing).

mechanisms? In CIM, the anomalous suppression sets in smoothly from peripheral to central collisions rather than in a sudden way when the corresponding dissociation temperature in the deconfined medium is reached. At SPS, current experimental errors still do not allow to disentangle these two mechanisms. However, even if the color screening mechanism is dominating, it is unclear what is really melted, directly produced J/ψs or originating from the feed-down of less bound charmonium states, χ_c ($\to J/\psi + X$), ψ' ($\to J/\psi + X$), which have lower dissociation temperatures. At RHIC and LHC conditions, the feed-down from B-meson decays becomes also important. Recombination enhances J/ψ production and much complicates the picture but its effect may be different depending on whether the deconfinement phase transition happened or not. It is even possible that after all J/ψs were melted in QGP they can be statistically regenerated at hadronization. True operative mechanisms of J/ψ production can be established only after studying all important dependences (from centrality, rapidity, collision energy $\sqrt{s}$,...) of all relevant observables with sufficient accuracy.

So far we considered the J/ψ production. Now let us briefly consider the perspective for bottomonia. One could expect that bottomonium production might be easier to understand than charmonium production due to the following reasons. 1. Since less than one $b\bar{b}$ pair is produced in one central Au-Au collision, the regeneration is negligible at the conditions of RHIC. Besides, only about 5 $b\bar{b}$ pairs are expected to be produced in a single central Pb-Pb collision at LHC. Hence, regeneration should play much less role in the beauty sector than in the charm sector. 2. Having higher masses, bottomonia originate from higher momentum partons and will less suffer from shadowing effects. 3. The absorptive cross section for Υ is by $40 - 50\,\%$ smaller than the corresponding cross section for J/ψ and ψ'.

These features should ease the separation of the anomalous suppression in the Υ's family.

3 Heavy Flavor Probes of QGP: Open Heavy Flavor Mesons

What qualitative effects could one expect to obtain when probing the dense matter by heavy quarks? As well known from electrodynamics, the bremsstrahlung off an accelerated heavy quark Q is suppressed by the large power of its mass $\sim (m_q/m_Q)^4$ as compared to light quarks. Therefore, gluon radiation off heavy quarks (i.e., radiative energy loss) is much suppressed relative to light quarks. Consequently, one could expect a decrease of high p_T suppression and of the elliptic flow coefficient v_2 [13] from light to charm to bottom quarks. Due to the above features, one should observe a pattern of gradually decreasing R_{AA} when going from the mostly gluon-originated light-flavor hadrons ($h^{\pm}$ and π^0) to D and to B mesons (gluons lose more energy than quarks since gluons have a higher color charge).

Let us now consider what the experiment tells us about the open heavy flavor p_T suppression and elliptic flow. Fig. 9 shows the nuclear modification factor and elliptic flow coefficient for HF electrons as functions of p_T, obtained in central collisions of gold nuclei at RHIC (closed circles) [14]-[17]. In contrast to the above expectations, the results for R_{AA}^{HF} show a strong suppression of HF decay electrons at $p_T > 2$ GeV/c, approaching at high p_T the level of suppression for π^0. This evidences that produced medium is quite dense for heavy quarks to lose energy as efficiently as light quarks do. The measurement of elliptic flow gives rather large value for v_2^{HF}. This means that HF electrons are involved in the collective motion being indicative of the collective flow of their parent particles as well. In Fig. 9, the results of some model considerations are also shown. The best description is provided by the model assuming the Brownian motion of heavy quarks within the framework of Langevin dynamics [18]. Let us consider the basic assumptions of this theory. Firstly, the thermal heavy quark

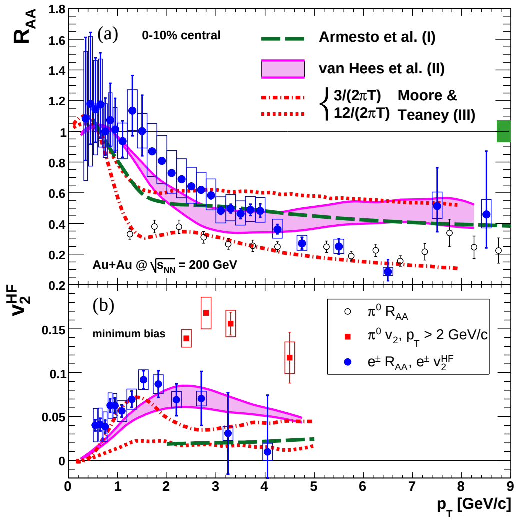

Figure 9. Nuclear modification factor (upper panel, central Au-Au) and elliptic flow (lower panel, minimum-bias Au-Au) of non-photonic electrons at RHIC, compared to theory. The band corresponds to the Langevin simulations based on an expanding fireball with effective heavy quark resonance interactions [18].

momentum $p^2 \sim mT$ (in nonrelativistic approximation) is much larger than the typical momentum transfer $Q^2 \sim T^2$ from a thermal medium to a heavy quark. Hence, the motion of a heavy quark in QGP can be represented as the Brownian motion, which can be described using the Langevin equation. Secondly, heavy quark loses its energy in elastic scattering processes with light partons. Besides, as evidenced from calculations of heavy and light meson correlators within LQCD, in QGP the D- and B-meson like resonant states exist up to $T < 2T_c$. Rescattering on these resonant states plays an important role in thermalizing heavy quarks. Thirdly, in order to get the spectrum of HF electrons, c- and b-quarks are to be hadronized into D- and B-mesons via quark coalescence (at low p_T) and fragmentation (at high p_T).

The analysis shows that resonance scattering decreases nuclear modification factor R_{AA}^{HF} and increases azimuthal asymmetry v_2^{HF}. Heavy-light quark coalescence in subsequent hadronization significantly amplifies v_2^{HF} and increases R_{AA}^{HF}, especially in the $p_T \simeq 2$ GeV/c region. The contribution from B-mesons to R_{AA}^{HF} and v_2^{HF} is estimated providing full calculations with c+b quarks and with only c quarks. The result is that the B-meson contribution increases R_{AA}^{HF} and decreases v_2^{HF}, and becomes important above $p_T \simeq 3$ GeV/c. Thus, one can conclude, that the combined effects of coalescence of heavy quarks Q with light quarks q, and of the resonant heavy-quark interactions are essential in generating strong elliptic flow v_2^{HF} of up to 10%, together with strong suppression of heavy flavor electrons with R_{AA}^{HF} about 0.5.

References

[1] ALICE: Physics Performance Report, V. 1. J. Phys. G **30**, 1517 (2004).
[2] ALICE: Physics Performance Report, V. 2. J. Phys. G **32**, 1295 (2006).
[3] R. Rapp and H. van Hees, Preprint arXiv: 0803.0901.
[4] T. Matsui and H. Satz, Phys. Lett. B **178**, 416 (1986).
[5] E. Scomparin (NA60 Collaboration), J. Phys. G **34**, S463 (2007).
[6] R. Arnaldi (NA60 Collaboration), J. Phys. G **35**, 104133 (2008)
[7] K. J. Eskola, V. J. Kolhinen, and R. Vogt, Nucl. Phys. A **696**, 729 (2001).
[8] D. deFlorian and R. Sassot, Phys. Rev. D **69**, 074028 (2004).
[9] A. Adare et al. (PHENIX Collaboration), Phys. Rev. Lett. **98**, 232301 (2007); A. Adare et al. (PHENIX Collaboration) Phys. Rev. C **79**, 059901 (2009).
[10] A. Andronic, P. Braun-Munzinger, K. Redlich, and J. Stachel, Phys. Lett. B **652**, 259 (2007).
[11] A. Capella, L. Bravina, E.G. Ferreiro, A.B. Kaidalov, et al., J. Phys. G **35**, 104156 (2008).
[12] A. Capella, U. Sukhatme, C.I. Tan, J. Tran Thanh Van, Phys. Rept. **236**, 225 (1994).
[13] A. A. Isayev, Report at the TESHEP School (Buymerovka, Ukraine), July, 2008 [arXiv:0810.4762].
[14] A. Adare et al. (PHENIX Collaboration), Phys. Rev. Lett. **98**, 172301 (2007).
[15] B. I. Abelev et al. (STAR Collaboration), Phys. Rev. Lett. **98**, 192301 (2007).
[16] D. Hornback et al. (PHENIX Collaboration), J. Phys. G **35**, 104113 (2008).
[17] V. G. Riabov, Phys. Atom. Nucl. **72**, 509 (2009).
[18] H. van Hees, V. Greco, and R. Rapp, Phys. Rev. C **73**, 034913 (2006).

Proceedings of the International School-seminar
"New Physics and Quantum Chromodynamics at external Conditions", pp. 72 – 77,
3-6 May 2009, Dnipropetrovsk, Ukraine

EXTRA DIMENSIONS IN INTERACTIONS OF COSMIC NEUTRINOS

A.V. Kisselev[a]

Institute for High Energy Physics, Protvino, Russia

Theories with extra spacial dimensions are reviewed. A significance of high energy cosmic neutrinos for a detection of effects coming from extra dimensions is underlined. Neutrino telescopes and their sensitivity to a diffuse neutrino flux are describes.

1 Cosmic rays and high energy neutrinos

One of the main problems in astroparticle physics is the origin and nature of extragalactic cosmic rays (CRs). While the spectrum of the CRs can be measured up to very high energies (see Fig. 1), their origin remains unclear.

The protons (nuclei) and photons cannot provide full information on astrophysical "accelerators". The protons and nuclei with energies up to 10^{20} eV are deflected by the galactic magnetic fields, while the photons with energies higher than 1 TeV are absorbed when interacting with the cosmic gamma-ray background. The neutrino is a unique cosmic messenger, since it is a neutral weakly interacting particle. The astrophysical neutrinos point back to their source and travel long distances without interaction.

The expected fluxes of high energy cosmic neutrinos is low, as well as the flux of high energy cosmic rays. In what follows, we will be interested in cosmic particles with energies above 10^{14} eV.

Ultra-high energy protons interact with the cosmic microwave background (CMB) via resonance photo-production,

$$p + \gamma_{\rm CMB} \to \Delta^+ \to p\,\pi^0,\ n\pi^+ \,. \tag{1}$$

The threshold energy of the process is equal to $6 \cdot 10^{19}$ eV. This effect, known as the Greisen-Zatsepin-Kuzmin (GZK) cutoff [1], limits the origin of high energy protons to a distance of the order of 100 Mpc. Recent data from HiRes collaboration [2] and Auger collaborations [3] say in favor of the GZK cutoff.

It is assumed that accelerated protons produce charged pions when interacting with matter or radiation:

$$p + p \to NN + \text{pions}, \quad p + \gamma \to n + \pi^+ \,, \tag{2}$$

either in their source (actice galactic nuclei, gamma-ray bursts) or in their travel to the Earth. Then the neutrinos are produced via decays:

$$\pi^+ \to \mu^+ + \nu_\mu, \quad \mu^+ \to e^+ + \nu_{\rm e} + \bar{\nu}_\mu \,. \tag{3}$$

The following flavor ratio results from (3): $\nu_{\rm e} : \nu_\mu : \nu_\tau = 1 : 2 : 0$. However, due to neutrino oscillations, the neutrino flux near the Earth will have equal fraction of all flavors: $\nu_{\rm e} : \nu_\mu : \nu_\tau = 1 : 1 : 1$.

Upper bound on diffuse neutrino flux $\Phi_\nu(E_\nu)$ was derived in [4]:

$$E_\nu\,\Phi_\nu(E_\nu) < 4 \cdot 10^{-8}\,\mathrm{GeV\,cm^{-1}c^{-1}sr^{-1}} \,. \tag{4}$$

Given GZK cutoff, there should exist so-called guaranteed (or GZK) neutrino flux [24]. As a result of pion decays (3) the neutrinos are produced. The predictions for the GZK flux vary from rather low neutrino flux to most optimistic one [6] which is close to the Waxman–Bahcall bound (4).

In contrast to"cosmic accelerators", in top-down models [7] the CRs are produced as a result of a decay of massive objects (topological defects, cosmic string, X-particles with masses $> 10^{22}$ eV). All these models predict the photon dominance in the CR spectrum. They are strongly constrained by the recent data on the photon fraction in CRs [8].

2 Theories with extra spacial dimensions

The consideration of the space-time with extra spacial dimensions is motivated by the string theory. The string theory is self-consistent only if $D = 10$, where D means the total number of dimensions. Since our world has (1+3) dimensions, six extra dimensions should be compactified.

e-mail: [a]alexandre.kisselev@ihep.ru

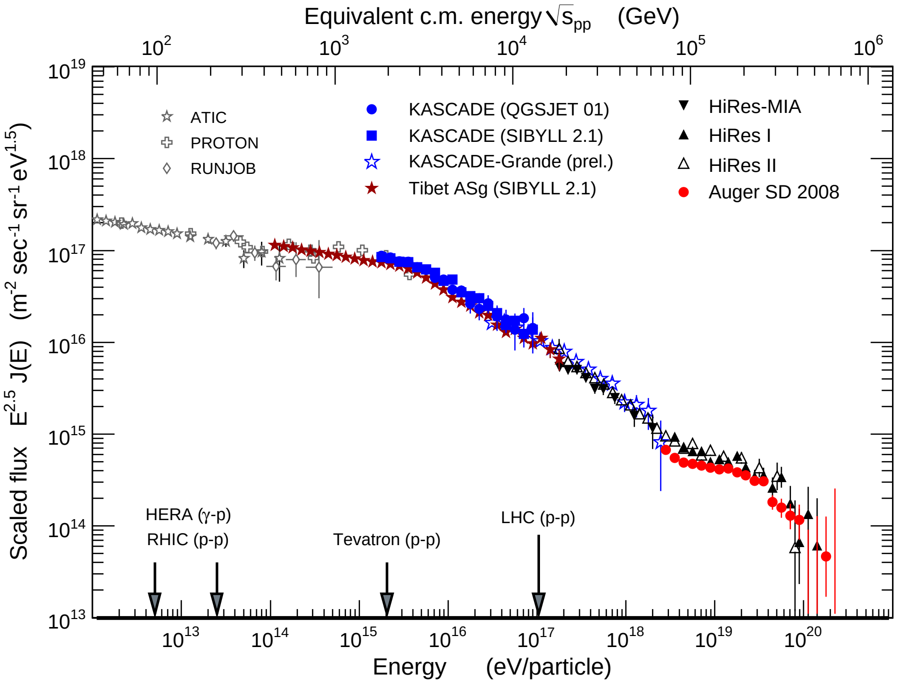

Figure 1. The CR spectrum.

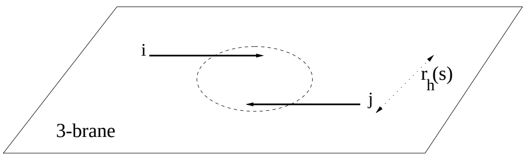

Figure 2. The black hole production.

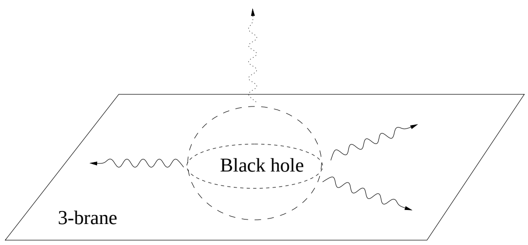

Figure 3. The black hole decay.

The large extra dimension scenario with the flat metric was proposed in [9] (ADD model). Background metric of the space-time looks like:

$$ds^2 = g_{\mu\nu}\, dx^\mu dx^\nu + \eta_{ab}\, dy^a dy^b\,, \tag{5}$$

where $\{x^\mu\}$ are the coordinates in four-dimensional space-time ($\mu = 0, 1, 2, 3$), and $\{y^a\}$ are the coordinate in $n = D - 4$ extra dimensions ($a, b = 1 \dots n$).

Stating from D-dimensional action, one can derive the following hierarchy relation [9]:

$$\bar{M}_{\rm Pl}^2 = (2\pi R_c)^n\, \bar{M}_D^{2+n}\,. \tag{6}$$

Here $\bar{M}_{\rm Pl}$ is the (reduced) Planck mass, $\bar{M}_D$ is the (reduced) fundamental gravity scale, R_c is the size of extra dimensions. Given strong gravity in D dimensions, $\bar{M}_D \sim 1$ TeV, we get form (6) that $R_c = 10^{-3}$ cm, 10^{-7} cm, 10^{-12} cm, for $n = 2, 3, 6$, respectively. Note that $R_c = 10^8$ km for $n = 1$.

The Standard Model (SM) fields are assumed to be confined to a (1+3)-dimensional brane embedded into a $(4 + n)$-dimensional space-time (bulk) in which the gravity lives. From the point of view of 4-dimensional observer, D-dimensional massless graviton looks like an infinite set of Kaluza-Klein (KK) modes with the masses $m_k \sim k/R_c$ ($k = 0, 1, \dots$). The coupling constant of both massless and massive gravitons with the SM fields is very small, $G_N = 1/M_D^2$. Nevertheless, cross sections for the production of KK gravitons appear to be proportional to $(\sqrt{s})^n/M_D^{2+n}$ where $\sqrt{s}$ is the invariant collision energy.

The gravitons in the ADD model are massive stable spin-2 particles. Experimental signature is an imbalance in missing mass of final states with a continuous mass distribution.

The hierarchy problem, i.e. unnaturally large ratio of the gravity scale ($\sim 10^{19}$ GeV) to the electroweak scale ($\sim 10^2$ GeV) is one of the most important problem of the modern physics. This problem is solved in the ADD scenario by introducing the new large scale R_c (6). The model which does solve the hierarchy problem most economically is the Randall-Sundrum (RS) model with a single extra dimensions and warped background metric [10]:

$$ds^2 = e^{2\kappa(\pi r - |y|)}\, \eta_{\mu\nu}\, dx^\mu dx^\nu + dy^2 \,. \tag{7}$$

Here $y = r\,\theta$ $(-\pi \leq \theta \leq \pi)$, r is the radius of the extra dimension. The parameter κ defines the scalar curvature in five dimensions. Note that the points (x^μ, y) and $(x^\mu, -y)$ are identified, and the periodicity condition, $(x^\mu, y) = (x_\mu, y + 2\pi r_c)$, is imposed. The tensor $\eta_{\mu\nu}$ is the Minkowski metric.

It is assumed that there are two 3-dimensional branes with equal and opposite tensions located at the points $y = 0$ (called the Plank brane) and $y = \pi r_c$ (referred to as the TeV brane). All SM fields are confined to the TeV brane, while the gravity propagates in five dimensions. The following relation between the 4-dimensional (reduced) Planck mass and (reduced) gravity scale in five dimensions can be derived:

$$\bar{M}_{\rm Pl}^2 = \frac{\bar{M}_5^3}{\kappa}\left(e^{2\pi\kappa r} - 1\right) \,. \tag{8}$$

The masses of the Kaluza-Klein (KK) graviton excitations are proportional to the curvature parameter κ: $m_k = x_k \kappa$ $(k = 1, 2 \ldots)$ where x_k are zeros of the Bessel function $J_1(x)$. The coupling of the massive graviton to the SM fields is proportional to TeV^{-1}.

Effects related with the extra dimension were searched for at the Tevatron collider in the processes:

$$p + \bar{p} \to \mathrm{jet} + \not{E}_\perp \,, \qquad p + \bar{p} \to \gamma + \not{E}_\perp. \tag{9}$$

No deviation from the SM were seen, and the region $\bar{M}_D < 1$ TeV is now excluded by the data. The RS model with the small curvature was checked by DELPHI collaboration. The lower limit obtained is $\bar{M}_5 > 0.92$ TeV.

3 Production of multidimensional black holes

When the impact parameter of colliding particles becomes smaller than the Schwarzschild radius [12],

$$R_{\rm S}(\sqrt{s}) = \bar{M}_D^{-1}\,(\sqrt{s}/\bar{M}_D)^{1/(n+1)} \,, \tag{10}$$

the black hole (BH) should be produced (see Fig. 2). The cross section of the BH production is given by the geometric formula [13]:

$$\sigma(\sqrt{s}) \simeq \pi\, R_{\rm S}^2(\sqrt{s}) \,. \tag{11}$$

It is assumed that $R_{\rm S}(M_{\rm BH}) \ll R_c$, where $M_{\rm BH}$ is the mass of the BH. The semiclassical description of the BH production is valid provided $M_{\rm BH} > M_D$.

The cross section for the neutrino-nucleon scattering is given by more complicated formula:

$$\sigma_{\nu N \to \rm BH}(\sqrt{s}) = \sum_{a = q, \bar{q}, g} \int_{x_{\min}}^{1} dx_a\, f_a(x_a)\, \sigma_{\nu a \to \rm BH}(x_a \sqrt{s}) \,, \tag{12}$$

where $f_a(x_a)$ is the distribution function of the parton of the type a, and $x_{\min} = M_{\rm BH}/\sqrt{s}$.

The lifetime of the BH is $\sim 10^{-26}$ c. There are several stages of the BH decay, the most important one is the Schwarzschild stage. At this stage the BH emits particles as a black body with the Hawking temperature $T_{\rm H} = (n+1)/(4\pi R_{\rm S})$ [14]. Note that the BH decays predominantly into the SM particles [15] (see Fig. 3).

The experimental signatures of BH decay are very distinct: the large multiplicity, flavor blindness, direct leptons and photons with energies ~ 100 GeV. The expected ratio of the hadronic decay mode to leptonic mode is 5 : 1.

4 Neutrino telescopes

The neutrino astronomy require the huge size to record a sufficient number of neutrino events. The detection technique is the observation of the Cherenkov light induced by interactions of cosmic neutrinos when traversing natural media such the ice of the South Pole or the water of deep oceans or lakes.

The AMANDA telescope, deployed in the ice of the South Pole [16] (Fig. 4), has been taking data since more than a decade. Its successor, IceCube telescope [17] (Fig. 4), is operating and it will be completed in the end of 2011. The ice act as a shield for down-going muons. On the other hand, it is transparent to the Cherenkov light emitted by the shower or up-going muons. The latter come from neutrinos traversing the Earth.

The IceCube is optimized for detection of the muons induced by muonic neutrinos:

$$\nu_\mu + N \to \mu + X \,. \tag{13}$$

The number of the neutrino events for the period T is given by

$$N_{\rm ev} = 2\pi\, A_{\rm eff}\, T \int dE_\nu \int d\cos\theta_z \Phi_\nu(E_\nu)\, P_{\nu\to\mu}(E_\nu, \cos\theta_z) \,, \tag{14}$$

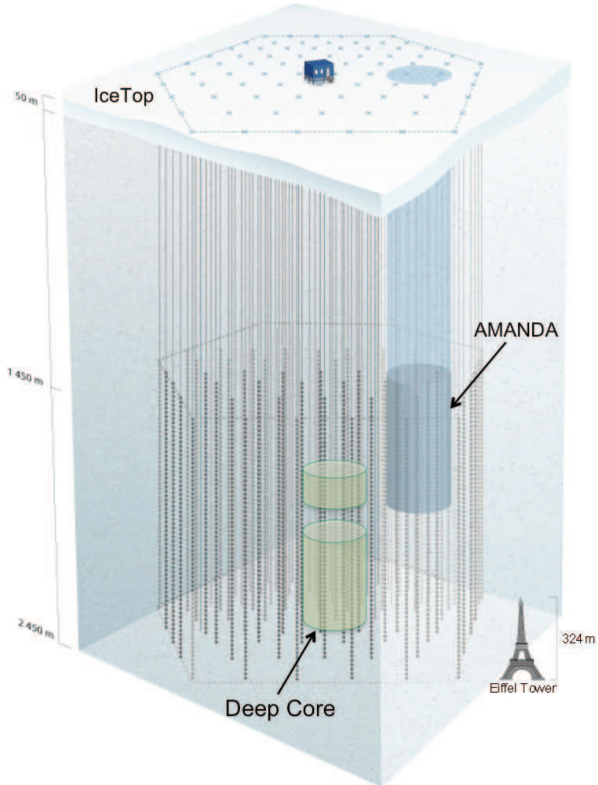

Figure 4. The IceCube neutrino telescope.

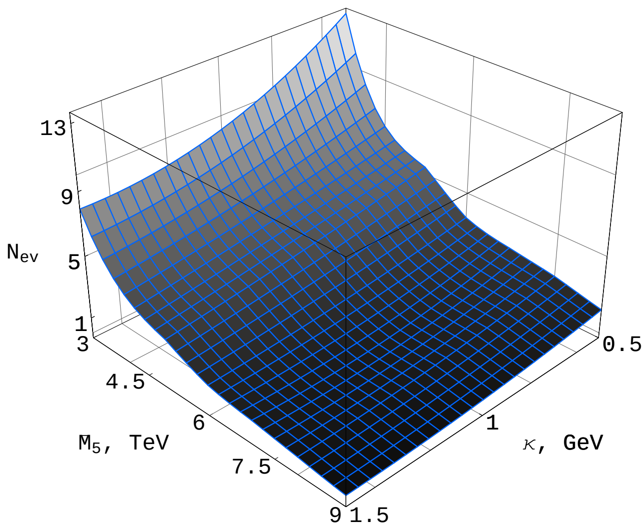

Figure 5. The number of inclined events at the Auger detector (RS scenario with the small curvature).

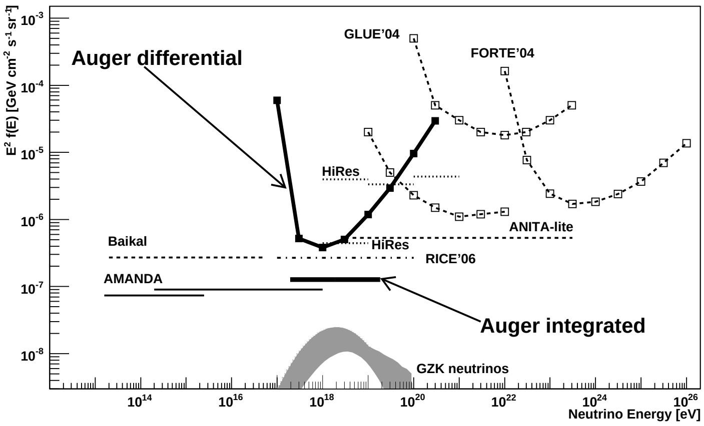

Figure 6. The experimental limits on the diffuse neutrino flux (converted to a single flavor).

where $A_{eff} = 1$ km^2 is the effective area of the detector, θ_z is zenith angle, $P_{\nu\to\mu}$ describes detection probability.

The electronic neutrino initiates an electromagnetic cascade via the process $\nu_{\rm e} + N \to {\rm e} + X$. The high energy tau neutrinos can produce so-called double-bang events [18].

In its full set-up, the IceCube telescope will be sensitive to the following diffuse neutrino flux ($2 \cdot 10^{14}$ eV $< E_\nu < 10^{18}$ eV):

$$E_\nu \, \Phi_\nu(E_\nu) < 1.5 \cdot 10^{-8} \, \mathrm{GeV \, cm^{-1} c^{-1} sr^{-1}} \, . \tag{15}$$

The Baikal neutrino telescope [19] operates since 1993 at the depth 1 km. The modern detector Baikal NT200+ has the effective volume $\sim 10^7$ m^3. There are plans to enlarge it up to 0.4 km^3 - 1.0 km^3. In the Mediterranean Sea, the ANTARES telescope [20] is taking data since 2008 in its full configuration. The first project in the Mediterranean Sea was the NESTOR detector [21] that started in 1989. It is located close to Pylos at the depth 4000 km. The NEMO projects [22] stated in 1998 is closed to Capo Passero with the depth of 3500 km. However, the low expected fluxes of the cosmic neutrinos call for a km^3-scale detector under the see. Such a telescope, KM3Net [23], was initiated in 2008. Its construction is expected to start by 2011.

5 Inclined air showers at the Auger Observatory

In order to discriminate neutrino induced events from events initiated by protons, nuclei or photons, it was suggested to search for quasi-horizontal (inclined) events with $\theta_z > 70^\circ$ [24] (see also [25]).

High energy cosmic particles produce extensive air showers (EASs) in the atmosphere. For the inclined events induced by the protons, only muonic component of the shower reaches the ground detector, that enable to select high energy neutrino events at the Auger Observatory [26]. The number of inclined events which can be detected by the Auger ground array is given by

$$\frac{dN_{\rm ev}}{dt} = \int_{E_{\rm th}}^{E_{\rm max}} dE_\nu \int_0^1 dy \, \theta(E_{\rm sh} - E_{\rm th}) \, \frac{d\sigma(E_\nu)}{dy} \, \Phi(E_\nu) \, A_{\rm eff}(E_{\rm sh}, E_\nu) \; , \tag{16}$$

where $E_{\rm sh} = yE_\nu$ is the shower energy. Effective aperture of the detector, $A_{\rm eff}(E_{\rm sh})$, is defined by its geometrical size, neutrino attenuation factor and detector efficiency. As one can see from (16), the number of EASs rises with the increase of neutrino-nucleon cross section $\sigma_{\nu N}(E_\nu)$ and neutrino flux $\Phi(E_\nu)$.

In Fig. 5 the expected number of the neutrino events in the RS scenario with the small curvature is presented [27]. The other predictions for the inclined event rate at the Auger detector can be found in [28].

There exist interesting events induced by so-called Earth-skimming tau neutrinos [29]. The up-going tau neutrinos turn into tau leptons in the Earth's crust. Then these tau leptons with energy $> 10^{19}$ eV can cross the crust and produce a shower in the atmosphere at altitude of 0-2500 m.

In contrary to the inclined events, the number of EASs initiated by Earth-skimming tau neutrinos decreases with the increase of $\sigma_{\nu N}(E_\nu)$. Thus, the simultaneously determining the cosmic neutrino flux and high energy neutrino cross section is possible by comparing the inclined and Earth-skimming events.

The EAS can be also induced by decay products of the BH. The estimates show that the BH production cross sections dominate SM neutrino-nucleon cross section at neutrino energy $> 10^{15}$ eV (10^{16} eV) [30].

Up to now, no signals from cosmic neutrinos were seen, but only upper limits on the diffuse neutrino flux were obtained by different collaborations [31] (see Fig. 6). Nevertheless, the expectation is that future 1 km^3-size IceCube and KM3Net telescopes, as well as Auger Observatory will be able to detect the cosmic neutrinos in a few years.

References

[1] K. Greizen, Phys. Rev. Lett. **16**, 748 (1966); G. T. Zatsepin and V. A. Kuzmin. Sov. Phys. JETP Lett. **4**, 78 (1966).

[2] R.U. Abbasi *et al.*, (HiRes Collab.), Phys. Rev. Lett. **100**, 101101 (2008).

[3] J. Abraham *et al.* (Pierre Auger Collab.), Phys. Rev. Lett. **101**, 061101 (2008).

[4] E. Waxmann and J.N. Bahcall, Phys. Rev. D **59**, 023002 (1999); J.N. Bahcall and E. Waxman, Phys. Rev. D **64**, 023002 (2001).

[5] V.S. Berezinsky and G.T. Zatsepin, Phys. Lett. **28B**, 423 (1969); Sov. J. Nucl. Phys. **11**, 111 (1970); V.S. Berezinsky and A.Yu. Smirnov, Phys. Lett. B **48**, 269 (1974); F.W. Stecker, Astrophys. J. **228**, 919 (1979).

[6] O.E. Kalashev, V. Kuzmin, D. Semikoz and G. Sigl, Phys. Rev. D **66**, 063004 (2002).

[7] C.T. Hill, D.N. Schramm and T.D. Walker, Phys. Rev. D **36**, 1007 (1987); P. Bhattacharjee, C.T. Hill, and D.N. Schramm, Phys. Rev. Lett **69**, 567 (1992); S. Yoshida, H. Dai, C.C.H. Jui, and P. Sommers, 1997, Astrophys. J. **479**, 547 (1997).

[8] M. Risse *et al.* (Pierre Auger Collab.), Nucl. Phys. Proc. Suppl. **190**, 223 (2009).

[9] N. Arkani-Hamed, S. Dimopoulos and G. Dvali, Phys. Lett. B **429**, 263 (1998); Phys. Rev. D **59**, 086004 (1999); I. Antoniadis *et al.*, Phys. Lett. B **436**, 257 (1998).

[10] L. Randall and R. Sundrum, Phys. Rev. Lett. **83**, 3370 (1999).

[11] A.V. Kisselev and V.A. Petrov, Phys. Rev. D **71**, 124032 (2005); G.F. Giudice, T. Plehn and A. Strumia, Nucl. Phys. B **706**, 455 (2005); A.V. Kisselev, Phys. Rev. D **73**, 024007 (2006).

[12] R.C. Myers and M.J. Perry, Ann. Phys. **172**, 304 (1986); P.C. Argyres, S. Dimopoulos and J. March-Russel, Phys. Lett. B **441**, 96 (1998).

[13] K.S. Thorne, in *Magic without magic: John Archibald Wheeler*, ed. J. Klauder Freeman (San Francisco, 1972), p. 231; T. Bank and W. Fisher, arXiv:hep-th/9906038; S. Dimopoulos and G. Landsberg, Phys Rev. Lett. **87**, 161602 (2001); S.B. Giddings and S. Thomas, Phys. Rev. D **65**, 056010 (2002).

[14] S.W. Hawking, Commun. Math. Phys. **43**, 199 (1975).

[15] R. Emparan, G.T. Horowitz and R.C. Myers, JHEP **1**, 007 (2000); Phys Rev. Lett. **85**, 499 (2000).

[16] R. Wischnewski *et al.* (AMANDA Collab.), Nucl. Phys. Proc.

[17] J. Ahrens *et al.* (IceCube Collab.), Nucl. Phys. Proc. Suppl. **118**, 338 (2003).

[18] J.G. Learned, Astropart. Phys. **3**, 267 (1995)

[19] G. Domogatsky *et al.* (Baikal Collab.), Nucl. Phys. Proc. Suppl. **110**, 504 (2002).

[20] T. Montaruli *et al.* (ANTARES Collab.), Nucl. Phys. Proc. Suppl. **110**, 513 (2002).

[21] P.K. Grieder *et al.* (NESTOR Collab.), Nucl. Phys. Proc. Suppl. **97**, 105 (2001).

[22] P. Piattelli *et al.* (NEMO Collab.) Nucl. Phys. Proc. Suppl. **165**, 172 (2007).

[23] C. Markou *et al.* (KM3NeT Collab.) Nucl. Instrum. Meth. A **595**, 54 (2008).

[24] V.S. Berezinsky and G.T. Zatsepin, Phys. Lett. B **28**, 423 (1969); V.S. Berezinsky and A.Yu. Smirnov, Astrophys. Space Science **32**, 461 (1975).

[25] K.S. Capelle, J.W. Cronin, G. Parente and E. Zas, Astropart. Phys. **8**, 321 (1998); X. Bertou *et al.*, Astropart. Phys. **17**, 183 (2002); E. Zas, New J. Phys. **7**, 130 (2005).

[26] D. Zavrtanik (Auger Collab.), Nucl. Phys. Proc. Suppl. **85**, 324 (2000); J. Abraham *et al.*, Nucl. Instrum. Methords A **523**, 50 (2004).

[27] A.V. Kisselev, The Open Astronomy J. **2**, 12 (2009).

[28] L.A. Anchordoqui *et al.*, JCAP **06**, 013 (2005); L.A. Anchordoqui *et al.*, Astropart. Phys. **25**, 14 (2006).

[29] D. Fargion, Astrophys. J. **570**, 909 (2002); J.L. Feng, Phys. Rev. Lett. **88**, 161102 (2002).

[30] J.L. Feng, Phys. Rev. Lett. **88**, 021303 (2002); L.A. Anchordoqui J.L. Feng, H. Goldberg and A.D. Shapere, Phys. Rev. D **65**, 124027 (2002); R. Emparan, M. Masip and R. Rattazzi, Phys. Rev. D **65**, 064023 (2002); L.A. Anchordoqui, J.L. Feng, H. Goldberg and A.D. Shapere, Phys. Lett. B **594**, 363 (2004).

[31] J. Abraham *et al.* (Pierre Auger Collab.), Phys. Rev. Lett. **100**, 211101 (2008).

Proceedings of the International School-seminar
"New Physics and Quantum Chromodynamics at external Conditions", pp. 78 – 85,
3-6 May 2009, Dnipropetrovsk, Ukraine

SUPERSTRING MODELS WITH REALISTIC CRITICAL DIMENSION

A. J. Nurmagambetov[a]

A.I. Akhiezer Institute for Theoretical Physics, NSC Kharkov Institute of Physics and Technology, Kharkov, Ukraine

Extra dimensions are predicted by Strings, but their existence does not experimentally verified. Such a situation stimulates searching for signals from extra dimensions on modern factories on the one hand, on the other hand it stimulates looking for String theories being already consistent in the observed number of space-time dimensions. Models of superstrings with realistic critical dimension are discussed in this notes.

1 Introduction

One of the most fascinating predictions of String theory is the existence of extra dimensions required for quantum consistency of strings. Extra dimensions, the presence of which was very sceptically conceived at early days of String theory, have become the standard *de facto* in the construction of various Unification models of fields and have received a lot of attention on the particle physics community side.

Searching for signals from extra dimensions on modern experimental factories is a good way to put String theory on the test. Unfortunately, up to date there are not any experimental observations in favor of extra dimensions. Therefore, a possibility of living in the World without extra dimensions has not a priori to be ruled out. This fact stimulates searching for String based Unification models being already consistent in the observed number of space-time dimensions.

In this notes I discuss models of supersymmetric strings which fall into such a criterion. To make the notes self-contained I begin with a brief discussion of extra dimensions in frameworks of String theory. Then, I discuss benefits and drawbacks of two most popular scenarios of Unification models with extra dimensions, the Kaluza-Klein scenario and the Brane World model. Next, I consider a formulation of String theory which is consistent, i.e. anomaly free, in $D = 4$, and outline some of features of the construction. My conclusions with summary of the results are collected in the end of the paper.

2 Extra dimensions in Strings

As I have noted in the above, the quantum consistency of String theory implies living in extra-dimensional world. This conclusion comes from an infinite-dimensional algebra of quantum operators [1]

$$[\hat{L}_m, \hat{L}_n] = (m-n)\hat{L}_{m+n} + A(m)\delta_{m+n}, \qquad A(m) = \frac{1}{12}D(m^3 - m), \tag{1}$$

which corresponds to a classical infinite-dimensional algebra

$$\{L_m, L_n\} = -i(m-n)L_{m+n}, \tag{2}$$

generating conformal transformations on a two-dimensional strings' world-sheet.

The difference between quantum and classical Virasoro algebras (1), (2) consists in the central element of the algebra $A(m)$. This term is absent in (2), and appears after the normal ordering of quantum oscillators entering the Virasoro generators $\hat{L}_m$. The central extension of (1) encodes the conformal anomaly in the quantized theory, and it manifestly depends on the space-time dimension. In fact, $A(m)$ is only a part of the total anomaly coefficient, since the classical Virasoro operators generate the residual world-sheet symmetry after the conformal gauge fixing. Following the Faddeev-Popov recipe ghosts have to be introduced, and their contribution into the anomaly coefficient is [1]

$$A^{b,c}(m) = \frac{1}{6}(m - 13m^3).$$

The total anomaly coefficient

$$A^{total}(m) = A(m) + A^{b,c}(m) + 2a_{open}m. \tag{3}$$

also contains the contribution from the open string intercept a_{open}.

e-mail: [a]ajn@kipt.kharkov.ua

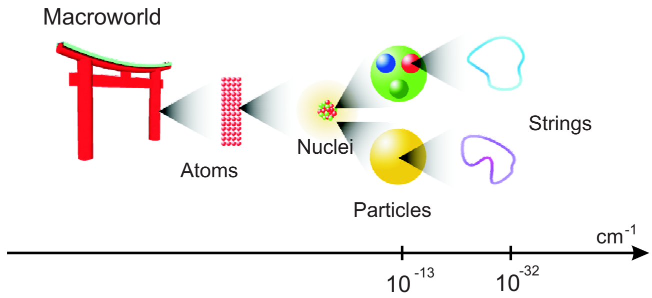

Figure 1. The Stringy World.

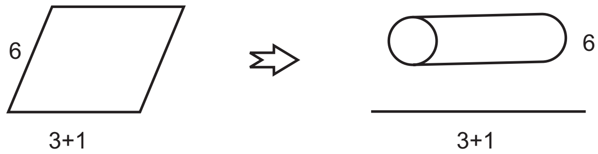

Figure 2. The Kaluza-Klein picture.

The anomaly absence, i.e. $A^{total}(m) = 0$, implies the space-time dimension D=26 and the string intercept $a_{open} = 1$. The same result holds for a closed bosonic string [1].

In the case of Neveu-Schwarz-Ramond (open) superstring (NSR superstring [2]) the Virasoro algebra is modified with two additional graded commutators, that leads to the set of two total anomaly coefficients. Depending on boundary conditions on world-sheet fermions two sectors of quantum oscillators appears: the Ramond (R) sector with

$$\begin{cases} A^{total}(m) = \frac{D}{8}m^3 + \frac{1}{6}(m - 13m^3) + \frac{1}{12}(11m^3 - 2m) + 2a^R_{open}m \\ \\ B^{total}(m) = \frac{D}{2}m^2 - 5m^2 + 2a^R_{open} \end{cases} \tag{4}$$

and the Neveu-Schwarz (NS) sector, where

$$\begin{cases} A^{total}(m) = \frac{D}{8}(m^3 - m) + \frac{1}{6}(m - 13m^3) + \frac{1}{12}(11m^3 + m) + 2a^{NS}_{open}m \\ \\ B^{total}(m) = \frac{D}{2}(m^2 - \frac{1}{4}) + (\frac{1}{4} - 5m^2) + 2a^{NS}_{open} \end{cases} \tag{5}$$

From $A(m) = 0$, $B(m) = 0$ it follows the critical dimension D=10 and the string intercepts $a^R_{open} = 0$, $a^{NS}_{open} = 1$.

Therefore, the presence of extra dimensions is an intrinsic property of the consistently quantized String theory. We get 22 space-like extra dimensions in bosonic string theory and 6 extra spatial dimensions for superstrings. The superstring case is more preferable since we have not the tachyonic vacuum state here: $a_{open} = 1$ corresponds to the tachyonic vacuum, while $a^R_{open} = 0$ leads to a well-defined zero-energy vacuum state. Though we have $a^{NS}_{open} = 1$ in the Neveu-Schwarz sector of superstring, we get rid off the tachyon state taking the Gliozzi-Scherk-Olive (GSO) projection [3]. Once the GSO projection is applied the spectrum of states in NS+R sectors possesses D=10 space-time supersymmetry.

In what follows I will mainly focus on the superstring case, where the number of extra dimensions is 6.

3 Living with Extra Dimensions

From the String theory point of view, our World looks as follows

To make a contact of String theory living in ten-dimensional world to observable physics in D=4 a special procedure of compactifying the extra dimensions has to be realized. There are many ways to this end, but the right way, which would reproduce main properties of the Standard Model (or its minimal supersymmetric extension), is up to date missed.

Dealing with extra dimensions one may wonder what is their size and what is the nature of extra dimensions? In the Kaluza-Klein picture [4] the extra dimensions have a small size that leads to appearing very massive particles after the compactification, with masses $M \sim 1/l_{comp.}$ ($l_{comp.}$ is a characteristic length of a compactified dimension).

Massive modes coming from the Kaluza-Klein compactification are too massive to be ever experimentally observed, so the best one can do is to consider massless modes, corresponding in part to the gauge bosons of

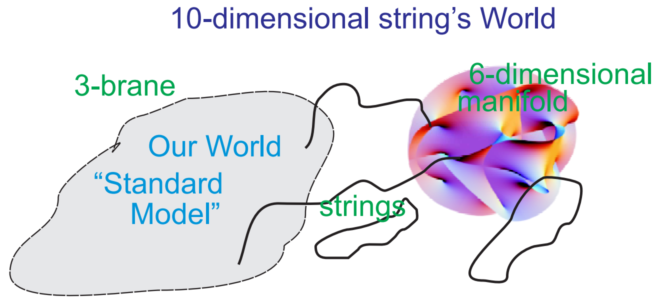

Figure 3. The Brane-World picture.

the SM symmetry group $SU(3) \times SU(2) \times U(1)$, or an extended symmetry group including the SM group as a subgroup.

Common drawbacks of the Kaluza-Klein scheme consist in:

- *Unsatisfactory spectrum of particles appearing upon the reduction which does not fit well the spectrum of the SM fields.*

  The desired spectrum of the Kaluza-Klein massless modes has to be realistic. A part of this spectrum should correspond to the gauge bosons of the Standard Model that puts restrictions on the type of the internal six-dimensional manifolds. However, the way of getting masses for the rest of the modes and establishing their correspondence to other Standard Model fields is an open task [5].

- *Gauge hierarchy problem still takes place.*

  The Kaluza-Klein scenario does not resolve the hierarchy problem, the gravity scale still remains near the Plank scale.

- *Typically four rather than three generations of quarks and leptons.*

  The exact number of generations coming after the dimensional reduction is strongly depended on geometrical and topological characteristics of internal six-dimensional manifolds. Roughly speaking, the number of fermion generations is twice less than the main topological number of the internal manifold (the Betti number). It turns out that the minimal Betti number for phenomenologically relevant internal manifolds is equal to 8 (Calabi-Yau manifolds), hence the number of generations is 4. A way to resolve this problem is to consider special manifolds of a Calabi-Yau type with the relevant Betti number [6], or to reduce on orbifolds [7] which are not manifolds in a common sense. Another perspective direction is to consider branes intersections [8] within the Brane World scenario (see below).

- *Masses and chiralities of fermions.*

  After the reduction fermions received masses of the compactification scale order, i.e. huge masses. Massless fermions comes from the zero-eigenvalue states of the Dirac operator on a compact internal manifold. In most phenomenologically interesting cases such zero-eigenvalue states do not exist. Another problem is to recover chiral fermions after the reduction. It may not be correctly resolved within the standard Kaluza-Klein scheme (see e.g. [9] and Refs. therein).

- *Large cosmological constant.*

  This point becomes important in context of String theory application to Cosmology and astrophysics, since we have definitely known that the right cosmological constant is small.

Problems with Kaluza-Klein motivated searching for other scenarios. One of them became popular last decade is the Brane World scenario [10].

Within the Brane World (BW) scenario it is supposed that fields of the SM do confine on a 4-dimensional brane (3-brane). A 3-brane is embedded in a higher-dimensional World. Gravity takes a special place in the BW picture since gravity does not confine on a 3-brane and gets trapped in high dimensions.

From the String theory point of view the BW picture looks like

A 3-brane is embedded into ten-dimensional space-time, a connection between 3-brane and extra dimensions is realized through strings. What is important in such a scheme is that extra dimensions are large. It leads to essential decreasing of the effective Plank scale on a Brane, that resolves the hierarchy problem.

Substantial progress in the Stringy BW has been achieved, nevertheless several important problems still remain open:

- *How to break Supersymmetry in a correct way?*

  Indeed, once we are talking about a 3-brane, it naturally appears in type IIB supersymmetric String theory. One may wonder why it is so necessary to deal with Superstring theory? The answer is we would like to have a joint coupling constant in high energies that provides by supersymmetry, and we would like to have a unified theory of gravity and the SM fields that is realized in String theory. However, the SM is not a supersymmetric theory, hence the way of supersymmetry breaking has to be found.

- *How to set up the right cosmological constant in the end?*

  I recall that *Anti-de-Sitter* space is actively exploited within the BW. Hence, all the machinery of the AdS/CFT correspondence is applied here. But we have to recover the right, *de-Sitter* space, cosmological constant in the end, which is the experimentally verified cosmological constant driving the late-time acceleration of Universe.

- *The predicted gravity scale is over TeV, but should we believe in that?*

  The BW scenario is a proposal for the resolving the hierarchy problem. However, we have not any signals on TeV quantum gravity (as well as on extra dimensions) up to date that makes the point questionable.

4 Living without Extra Dimensions

Living in extra dimensional World makes possible to resolve some of the fundamental problems of the Standard Model. At the same time the major worry on extra-dimensions is the absence of any experimental signals in favor of their existence. Once living in extra-dimensional World will be experimentally verified, it will get rid of any doubts on them, and on String theory, which predicts extra dimensions, as well. Currently, all possible ways of constructing Unification models, with or without extra dimensions, are needed to be taken into account on equal footing.

4.1 SUSY algebra and supersymmetric strings in extended superspaces

I have noted String theory is good enough to unify gravity with other interactions. But could we find a comprehensive String theory with realistic critical dimensions?

To get an answer let me begin with reviewing an irrelevant at first sight subject. In 1988 Curtright [11] made an analysis of the maximally extended SUSY algebra in D=11 (M-theory algebra [12], [13]). The algebra in particular includes [13]

$$\{Q,Q\} = \gamma^a P_a + \gamma^{ab}\mathfrak{P}_{ab} + \gamma^{abcde}\mathfrak{P}_{abcde}. \tag{6}$$

The right hand side of (6) contains different types of 'momenta'. Dynamical charge P_a corresponds to the standard momenta, other 'momenta' are topological charges corresponding to 'electrically' charged membrane and 'magnetically' charged 5-brane. Clearly,

$$\mathfrak{P}_{ab} = -\mathfrak{P}_{ba}, \qquad \mathfrak{P}_{abcde} = \mathfrak{P}_{[abcde]}.$$

Membranes and five-branes appear in eleven-dimensional M-theory, however there is not a room for strings there.

What happens if charges on the r.h.s. of (6) will be treated in more democratic way? They are different, of course, the dynamical momenta have the conjugated coordinates, whilst topological charges have not. To reach charges democracy Curtright proposed, instead of the standard D=11 superspace (X^a, θ^α), an 'extended' D=11 superspace $(X^a, Z^{ab}, Z^{abcde}, \theta^\alpha)$ [11], where Z^{ab}, Z^{abcde} are "coordinates" conjugated to topological charges $\mathfrak{P}_{ab}$, $\mathfrak{P}_{abcde}$. Curiously enough, there exists a room for superstrings in such an extended superspace.

A general form of the Curtright's superstring action looks as follows [11]

$$S = \int d^2\xi \sqrt{-\det(\omega^a_\mu \omega_{\nu a} + \alpha\omega^{ab}_\mu \omega_{\nu ab} + \beta\omega^{abcde}_\mu \omega_{\nu abcde})} + S_{WZ}. \tag{7}$$

The building blocks of the action consist of the pull-back of D=11 Volkov-Akulov superform $\omega^a_\mu = \partial_\mu X^a + i\bar\theta\gamma^a\partial_\mu\theta$, its extensions to tensorial-type coordinates $\omega^{ab}_\mu = \partial_\mu Z^{ab} + i\bar\theta\gamma^{ab}\partial_\mu\theta$ and $\omega^{abcde}_\mu = \partial_\mu Z^{abcde} + i\bar\theta\gamma^{abcde}\partial_\mu\theta$. Two parameters α, β are constants fixed by supersymmetry in the end, and the last terms of the action is the Wess-Zumino term. The term by Wess and Zumino was introduced in (7) to reach the invariance of the action under a local fermionic symmetry, the so-called kappa-symmetry, taking an important place in theory of supersymmetric extended objects. Nevertheless, in the original Curtright's paper the kappa-invariance of the action was rather claimed than exactly proved.

Now what about D=4? A similar extension of D=4 superspace was considered by Amorim and Barcelos-Neto [14], and a line of they reasoning was almost the same.

The maximally extended N=1 D=4 superalgebra in particular contains [12]

$$\{Q, Q\} = \gamma^a P_a + \gamma^{ab}\mathfrak{P}_{ab}. \tag{8}$$

Adding new tensor-type coordinates $Z^{ab} = -Z^{ba}$, which are conjugated to 'momenta' $\mathfrak{P}_{ab}$, we get an extended superspace $(X^a, Z^{ab}, \theta^\alpha)$. $\mathfrak{P}_{ab}$ is commonly treated as a topological charge (due to a D=4 membrane), but treating it dynamically it's possible to construct a Green-Schwarz-type superstring in the extended superspace

$$S = \int d^2\xi \sqrt{-\det(\omega^a_\mu \omega_{\nu a} + \alpha\omega^{ab}_\mu \omega_{\nu ab})} + S_{WZ}. \tag{9}$$

The notation in (9) is that of (7).

I postpone the discussion of (9) to the end of the paper, currently focussing on the superconformal algebra in the extended superspace and on the superstring critical dimension.

4.2 Superconformal algebra in tensorial superspace and superstring's critical dimension

To calculate the critical dimension of tensorial superstring let us turn back to the bosonic string case. As it has been noted in the above the total conformal anomaly coefficient (eq. (3))

$$A^{total}(m) = \frac{1}{12}D(m^3 - m) + \frac{1}{6}(m - 13m^3) + 2a_{open}m$$

contains contributions from bosonic fields X^a, conformal (anti)ghosts and the string intercept.

One could notice that

- The critical dimension is calculated from setting the terms proportional to m^3 to zero.
- D bosonic coordinates X^a contribute the relative coefficient D.
- The conformal (anti)ghosts contribute the relative coefficient '-26' independently on the number of space-time dimensions.

Hence, we need 26 bosonic coordinates X^a to compensate the ghosts contribution, $+26 - 26 = 0$.

In the NSR superstring case one of the total superconformal anomaly coefficients has the following form

$$A^{total}(m) = \left(\frac{D}{12}\cdot 1 + \frac{D}{12}\cdot\frac{1}{2}\right)m^3 + \frac{1}{6}(m - 13m^3) + \frac{1}{12}(11m^3 - 2m) + 2a^R_{open}m. \tag{10}$$

It's easy to recognize the contributions of bosonic X^a, fermionic conformal (anti)ghosts, bosonic superconformal (anti)ghosts and the contribution of the string intercept. But what about the second term of (10)?

This term contains the contribution of the world-sheet fermionic superpartners ψ^a of the bosonic coordinates X^a. Clearly, the fermionic superpartners contribute only 1/2 of the corresponding bosonic coefficient.

Hence, to calculate the critical dimension the following mnemonic rule may be used [1]:

- D bosons get the coefficient D.
- The input of D fermions (boson's superpartners) is $D/2$.
- The (super)conformal ghosts give '-26' for conformal (fermionic) ghosts, and superconformal (bosonic-type) ghosts contribute '$+11$'.

The difference '$-26+11 = -15$' has to be compensated with contributions of additional bosonic and/or fermionic fields, one of the realizations of which are bosonic coordinates X^a and their world-sheet superpartners ψ^a.

Let us fix the space-time dimension $D = 4$. Four bosonic coordinates X^m and their four world-sheet superpartners ψ^m contribute the coefficient $4 + 4/2 = +6$. On account of ghosts contribution it is necessary to compensate the coefficient equal to$-15 + 6 = -9$. There are different routes to this end. Say, if one were to use 6 'internal' coordinates y^i and their superpartners ψ^i $(i = 1, \dots, 6)$, this choice would be transformed into the standard $4 + 6 = 10$ set of coordinates of the NSR superstring in the end.

Another productive choice suggested by $D = 4$ $N = 1$ superalgebra structure is to consider 6 additional tensorial-type coordinates $Z^{mn} = -Z^{nm}$ together with their world-sheet superpartners $\Psi^{mn} = -\Psi^{nm}$ [15]. This set of coordinates contribute the required coefficient $+9$, hence we arrive at the consistent quantum formulation of superstring in the *observable number of space-time dimensions.*

5 New set of coordinates and benefits of their introduction

We have established the existence of a NSR-type superstring formulation with realistic critical dimension. The price we paid to this end is the extension of the conventional space-time with additional tensorial-type bosonic coordinates. Let me take an extensive treatment of new coordinates in the so extended space.

Note that the bosonic subset (X^m, Z^{mn}) could be embedded into the unique set of tensorial coordinates Z^{MN}, but in $D = 5$.

$$Z^{\tilde{m}5} \rightsquigarrow X^m, \qquad Z^{\tilde{m}\tilde{n}} \rightsquigarrow Z^{mn}, \quad \tilde{m} = 0, \ldots, 3 \tag{11}$$

The world-sheet superpartners of X^m and Z^{mn} can also be recasted into the single world-sheet fermion Ψ^{MN}

$$\Psi^{\tilde{m}5} \rightsquigarrow \psi^m, \qquad \Psi^{\tilde{m}\tilde{n}} \rightsquigarrow \psi^{mn}, \quad \tilde{m} = 0, \ldots, 3$$

Therefore, in the NSR-type formulation we are dealing with tensorial-type coordinates Z^{MN} which are scalars w.r.t. the world-sheet diffeomorphisms, and with their superpartners Ψ^{MN} which are a world-sheet spinors. If we calculate the Virasoro-like superalgebra of the NSR-type string with embedding coordinates (Z^{MN}, Ψ^{MN}) when we get

$$\begin{cases} A^{\text{total}}(m) = \frac{1}{12}(\frac{D(D-1)}{2} + \frac{D(D-1)}{4})m^3 + \frac{1}{6}(m - 13m^3) + \frac{1}{12}(11m^3 - 2m) + 2a^R_{open} m \\ B^{\text{total}}(m) = \frac{D(D-1)}{4} m^2 - 5m^2 + 2a^R_{open}. \end{cases} \tag{12}$$

Clearly, the critical dimension is $D = 5$ in the case, and we arrive at new formulation of superstring theory living in five-dimensional space-time endowed with coordinates Z^{MN}. This parametrization includes, as a four-dimensional part, the standard set of vector-type coordinates X^m, hence coordinates Z^{MN} are more fundamental than X^m, and the tensorial string theory in $D = 5$ is more fundamental than its four-dimensional analog. This situation may be considered as a remnant of the M-theory–String theory relation, when the more fundamental theory is formulated in a space-time of one spatial dimension higher.

Another consequence of introducing the new space-time parametrization may be viewed from the following observation. Calculating the Virasoro-like superalgebra for the NSR-type $D = 5$ tensorial string theory we have used the canonical relation between Z^{MN} and their conjugate generalized momenta $\mathfrak{P}_{MN}$

$$\{\mathfrak{P}^{MN}(\sigma), Z^{KL}(\sigma')\}_{PB} = \frac{1}{2} T^{-1} \left(\eta^{MK}\eta^{NL} - \eta^{ML}\eta^{NK}\right) \delta(\sigma - \sigma'),$$

When we pass to operators, the generalized momenta become $\hat{\mathfrak{P}}_{MN} = -i\partial_{MN}$, $\partial_{MN} Z^{MN} = \frac{1}{2} D(D-1)$.

Hence, in tensorial space there is an exotic *one-form* of the Yang-Mills-type $\mathcal{A} = \mathcal{A}_{MN} dZ^{MN}$. Its strength tensor is

$$\mathcal{F}_{MN,KL} = \partial_{MN}\mathcal{A}_{KL} - \partial_{KL}\mathcal{A}_{MN} + i[\mathcal{A}_{MN}, \mathcal{A}_{KL}] \tag{13}$$

and the action functional for such a field looks like

$$S = \frac{1}{4} \mathrm{Tr} \int d\Omega_D \, \mathcal{F}_{MN,KL} \mathcal{F}^{MN,KL},$$

where $d\Omega_D$ is the invariant volume form in a tensorial space. The one-form field $\mathcal{A}$ is an analog of a non-abelian Yang-Mills gauge field in the conventional space-time. It corresponds to the massless mode in the spectrum of open tensorial string.

In the spectrum of the closed tensorial superstring we meet other exotic massless modes $G_{MN|PQ}$ and $B_{MN|PQ}$ corresponding to graviton and the Kalb-Ramond antisymmetric tensor fields of the standard superstring spectrum.

The 'graviton' mode $G_{MN|PQ}$ possesses the following properties

$$G_{MN|PQ} = -G_{NM|PQ} = -G_{MN|QP} = G_{PQ|MN}$$

which formally the same as that of the curvature tensor in the conventional space.

For a 'Kalb-Ramond' field we have

$$B_{MN|PQ} = -B_{NM|PQ} = -B_{MN|QP} = -B_{PQ|MN}.$$

The remaining massless mode in the spectrum is a 'dilaton' Φ.

Having such exotic modes in the spectrum it is very important to understand the dynamics of these fields. The action functional for the 'dilaton' and the 'Kalb-Ramond' fields is more or less predictable. It is likely

$$S = \int d\Omega_5 \left(\frac{1}{2} \, \partial_{MN}\Phi\partial^{MN}\Phi + \frac{1}{12} \, H_{MN,\; KL|PQ} H^{MN,\; KL|PQ} \right),$$

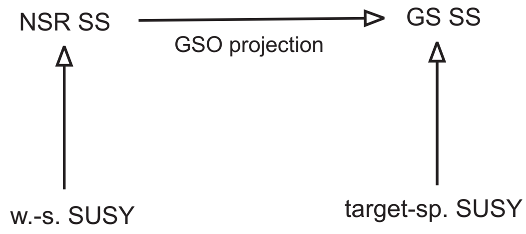

Figure 4. NSR-GS connection.

where the 'Kalb-Ramond' field strength is defined by

$$H_{MN,\ KL|PQ} = \partial_{MN} B_{KL|PQ} + \partial_{PQ} B_{MN|KL} + \partial_{KL} B_{PQ|MN}.$$

As for the effective action of 'graviton' $G_{MN|PQ}$, its structure is unclear. It could be recovered from calculations of the 3-point tree amplitude of interacting strings in the low-energy approximation (as, for instance, in [17]) and I postpone this task for further studies.

6 Summary and Conclusions

We have discussed a reformulation of superstring theory, the critical dimension of which coincides with the observable space-time dimension.

To recover the critical dimension $D = 4$ an extension of the standard space-time is required. New elements which have to be taken into account are tensorial-type bosonic coordinates. From the point of view of the string world-sheet theory, it does not matter what kind of bosonic coordinates need to be added to compensate the superconformal anomaly. They could be scalars, vectors or tensors under the space-time Poincare. The main point is that they are scalars with respect to the world-sheet diffeomorphisms.

One may wonder, that is a rule for selecting new coordinates then? What kind of the coordinates have to be selected to parameterize the target space? It turns out that the choice of the string's coordinates describing an immersion of the string world-sheet into a target superspace is governed by the structure of a target space superalgebra.

Let me discuss the target-space – world-sheet correspondence in more detail. There are two independent formulations of superstrings:

1. Neveu-Schwarz-Ramond with the world-sheet supersymmetry;

2. Green-Schwarz with the manifest target-space supersymmetry.

As I have noted these formulations are equivalent in $D = 10$, since their quantum spectra coincide (after truncation of the NSR spectrum with the GSO projection) and their critical dimensions are the same.

The world-sheet SUSY in the NSR formulation just says that there are world-sheet scalars and their superpartners under the world-sheet supersymmetry. However, it doesn't say anything on properties of these variables under the target-space Poincare transformations.

In its turn, properties of the string coordinates in the Green-Schwarz formulation are fixed. Indeed, a part of the space-time SUSY algebra is

$$\{Q, Q\} = \gamma^a P_a + \dots$$

and string coordinates are defined as ones conjugated to P_a. They are vector-type coordinates X^a with respect to the target-space Poincare. Precisely this type of the coordinates enter the standard NSR string action. Extending the space-time to superspace recovers the rest of the coordinates entering the Green-Schwarz superstring action, the space-time fermions θ^α. They are the target-space superpartners of X^a.

Hence, the relation between NSR and GS superstrings observes an independent interpretation, in which properties of the space-time SUSY, manifest in the GS formulation, govern the choice of the space-time coordinates to describe the NSR string.

Let me now turn to the Green-Schwarz-type action (9). This action is based on the target space supersymmetry algebra involving the supercharges anticommutator (8). If we give a credit to having a correspondence between NSR and GS formulations in the extended superspace $(X^m, Z^{mn}, \theta^\alpha)$, the NSR-type tensorial superstring variables are (X^m, Z^{mn}) together with their world-sheet superpartners (ψ^m, Ψ^{mn}).

As for the NSR-type tensorial superstring the bosonic subset (X^m, Z^{mn}) of the Green-Schwarz-type tensorial superstring coordinates could be embedded into the unique set of tensorial coordinates Z^{MN}, but in $D = 5$.

$$Z^{\tilde{m}5} \rightsquigarrow X^m, \qquad Z^{\tilde{m}\tilde{n}} \rightsquigarrow Z^{mn}, \quad \tilde{m} = 0, \dots, 3 \tag{14}$$

The # of fermionic target-space superpartners θ^α is the same in $D = 5$ and $D = 4$. Therefore, it is possible to reformulate the superstring model solely in terms of (Z^{MN}, θ^α) coordinates that essentially simplifies the Green-Schwarz-like tensorial superstring action [16] and proving its kappa-invariance. Moreover, the consistency of the Green-Schwarz-type superstring model in $D = 5$ tensorial superspace (Z^{MN}, θ^α) (kappa-invariance of the action) also requires [16]

$$G_{M[N|PQ]} = 0$$

This condition just says that the field $G_{MN|PQ}$ is in the [2,2] irreducible rep. over the Lorentz in $D = 5$ tangent space.

At the same time I should note that the Green-Schwarz-type formulation of tensorial superstring in $D = 4$ (or equivalently in $D = 5$) extended superspace faces with several questionable points. First of all one may encounter an apparent mismatch between bosonic and fermionic degrees of freedom in the case. Hence, it is necessary to understand the root of the problem. A helpful way to this end is to recover the spectrum of open/closed tensorial strings in different formulations and to figure out an analog of the GSO projection to relate spectra of tensorial superstrings. Perhaps, applying the machinery of the twistor-like superembedding approach [18], [19] (and Refs. therein), which ‘closes’ the diagram on Fig.4, may be useful to this end. Another intriguing problem is to construct the effective action of massless modes to check a correspondence of the approach to that of [20] where a new concept of the area metric was introduced.

Acknowledgements. It is a pleasure to thank Organizers of NPQCD09 School-Seminar for the kind hospitality in Dnipropetrovsk. I am very thankful to Vladimir Skalozub and Vladimir Vanyashin for numerous conversations during the School-Seminar, and to Igor Bandos and Victor Berezovoj for enlightened discussions on the subject of this notes. Partial support from the INTAS Grant # 05-08-7928 and the NASU-RFFI project # 38/50-2008 is acknowledged.

References

[1] M.B. Green, J.H. Schwarz and E. Witten, *Superstring theory*, (Cambridge, Cambridge University Press, 1987).
[2] P. Ramond, Phys. Rev. D **3**, 2415 (1971);
A. Neveu and J.H. Schwarz, Nucl. Phys. B **31**, 86 (1971).
[3] F. Gliozzi, J. Scherk and D. Olive, Nucl. Phys. B **122**, 253 (1977).
[4] M.J. Duff, B.E.W. Nilsson and C.N. Pope, Phys. Rep. **130**, 1 (1986).
[5] V. Braun, Y.-H. He, B.A. Ovrut and T. Pantev, JHEP **0605**, 043 (2006) [hep-th/0512177].
[6] P. Candelas and R. Davies, New Calabi-Yau Manifolds with Small Hodge Numbers, arXiv:0809.4681[hep-th].
[7] S. Ramos-Sanchez, Towards Low Energy Physics from the Heterotic String, arXiv:0812.3560[hep-th].
[8] T. Kimura and S. Mizoguchi, Yet Another Alternative to Compactification – Heterotic Five-branes Explain Why Three Generations in Nature, arXiv:0905.2185[hep-th].
[9] F. Cianfrani and G. Montani, Review on Extended Approaches in the Kaluza-Klein Model, arXiv:0904.0574[gr-qc].
[10] L. Randall and R. Sundrum, Phys. Rev. Lett. **83**, 3370 (1999) [hep-ph/9905221]; *ibid.* **83**, 4690 (1999) [hep-th/9906064].
[11] T. Curtright, Phys. Rev. Lett. **60**, 393 (1988).
[12] J.W. van Holten and A. van Proeyen, J. Phys. A **15**, 3763 (1982).
[13] E. Sezgin, Phys.Lett. B **392**, 323 (1997) [hep-th/9609086].
[14] R. Amorim and J. Barcelos-Neto, Z. Phys. C **64**, 345 (1994).
[15] R. Amorim and J. Barcelos-Neto, Z. Phys. C **58**, 513 (1993).
[16] A.J. Nurmagambetov, Visnyk of Kharkov Natl. Univ. **1(41)**, 21 (2009).
[17] R.I. Nepomechie, Phys. Rev. D **32**, 3201 (1985).
[18] D.P. Sorokin, Phys.Rept. **329**, 1 (2000) [hep-th/9906142].
[19] I.A. Bandos, J.A. de Azcarraga and C. Miquel-Espanya, JHEP **0607**, 005 (2006) [hep-th/0604037].
[20] F.P. Schuller and M.N.R. Wohlfarth, Nucl. Phys. B **747**, 398 (2006) [hep-th/0508170].

Proceedings of the International School-seminar
"New Physics and Quantum Chromodynamics at external Conditions", pp. 86 – 90,
3-6 May 2009, Dnipropetrovsk, Ukraine

FREEZE-OUT PROCESS IN HYDRODYNAMICALLY EXPANDING SYSTEMS

Yu. M. Sinyukov, S. V. Akkelin, Iu. A. Karpenko

Bogolyubov Institute for Theoretical Physics, Kiev, Ukraine

The freeze out process of continues particle liberation in hydrodynamically expanding systems, created in relativistic heavy ion collisions, is discussed within the kinetic theory approach. We point out the basic shortcomings of the Cooper-Frye freeze-out prescription and introduce improved freeze-out prescription based on the saddle point approximation of the emission function. It is shown that the corresponding freeze-out hypersurface σ depends on the values of p and that for such a hypersurface there is no negative contributions to the momentum spectra from non-space-like parts of σ. Conditions of applicability of the generalized sudden freeze-out approximation are discussed.

1 Introduction

A prescription of particle momentum freeze-out is needed for any hydrodynamical model applied for description of relativistic heavy ion collisions. Because system formed is quite small, the picture of continuous medium is destroyed at small finite time. Since the system expands fast, the latter is not constant in configuration space but depends on the position $\mathbf{r}$ of the fluid elements: $t_\sigma(\mathbf{r})$. The set of these points $(t_\sigma(\mathbf{r}), \mathbf{r})$ in the Minkowski space forms the hypersurface σ corresponding to the outer boundary of the applicability of hydrodynamics. The sudden freeze-out implies that the spectra are formed just on this hyperurface where, formally, an ideal fluid transforms into an ideal gas. The particle momentum spectra then can be expressed by the well-known Cooper-Frye formula [1]:

$$p^0 n(p) = p^0 \frac{d^3N}{d^3p} \approx \int\limits_\sigma d\sigma_\mu p^\mu f_{\texttt{1.eq.}}(x,p). \tag{1}$$

The freeze-out hypersurface is typically associated with an isotherm. In current analysis of A+A collisions the corresponding temperature is in the region $T = 90 - 150$ MeV and is fixed, typically, from the best fit of the spectra.

Any isotherm contains usually non-space-like parts, which lead to unphysical negative contributions to spectra for the particles with momenta directed inward the system, $p_\mu d\sigma_\mu < 0$. There is no common phenomenological prescription, based on Heaviside step functions $\theta(p_\mu d\sigma_\mu)$, which allows one to eliminate the negative contributions to the momentum spectra when $p^\mu d\sigma_\mu < 0$. The prescription, proposed in [2], eliminates the negative contributions in the way which preserves the number of particles in the fluid element crossing the freeze-out hypersurface. Therefore it takes into account that at the final stage the system is the only holder of emitted particles. Another prescription [3] ignores the particle number conservation considering decaying hadronic system rather as a star - practically unlimited reservoir of emitted photons/particles. The both prescriptions have a problem with momentum-energy conservation laws at freeze-out.

But the most serious problem is the obvious conflict of the Cooper-Frye prescription (CFp) with simple observation: to provide sudden transformation of the liquid to ideal gas one needs to switch suddenly cross-sections between particles from very big values to very small ones [4] that cannot happen in reality. The reason of particle liberation is another: it is the gradual change of the ratio between the rate of system expansion and the rate of collisions, so that particles should be emitted continuously. Nevertheless, in Ref. [5] it was advanced an idea of duality in hydro-kinetic approach to A+A collisions: though the process of particle liberation, described by the emission function, is non-equilibrium and gradual, the observable spectra can yet be expressed by means of the Cooper-Frye prescription based on locally equilibrium distribution function. The conclusive step towards an analytical and numerical realization of this idea is done in Ref. [6] where hydro-kinetic approach is developed: it overcomes all above mentioned problems by considering the continuous dynamical freeze-out that is consistent with Boltzmann equations and conservation laws. The aim of this work is, following the lines and ideas presented in Refs. [5, 6], to point out the shortcomings of the CFp when applied for description of freeze-out processes in relativistic A+A collisions, and to propose the way how the sudden freeze-out approximation can be applied for such processes.

2 Freeze-out of expanding systems within kinetic Boltzmann approach

Let us start from Boltzmann equation. It has the general form:

$$\frac{p^\mu}{p^0}\frac{\partial f_i(x,p)}{\partial x^\mu} = G_i(x,p) - L_i(x,p). \tag{2}$$

The expressions $G_i(x,p)$ and $L_i(x,p) = R_i(x,p)f_i(x,p)$ are so-called (G)ain and (L)oss terms for the particle of species i. Typically, R_i is a rate of collisions of i-th particle. Below we will omit index i, the corresponding expression can be related then, e.g., to pions.

The probability $\mathcal{P}_{t\to t'}(x,p)$ for a particle to reach the point $x' = (t', \mathbf{r}')$ starting from the point $x = (t, \mathbf{r})$ without collisions is

$$\mathcal{P}_{t\to t'}(x,p) = \exp\left(-\int\limits_t^{t'} d\bar{t}R(\overline{x}_t, p)\right), \tag{3}$$

where

$$\overline{x}_t = (\bar{t}, \mathbf{r} + \frac{\mathbf{p}}{p^0}(\bar{t}-t)).$$

In terms of this probability, the Boltzmann equation can be rewritten in the following integral form

$$f(t,\mathbf{r},p) = f(t_0, \mathbf{r} - \frac{\mathbf{p}}{p^0}(t-t_0), p)\mathcal{P}_{t_0\to t}(t_0, \mathbf{r} - \frac{\mathbf{p}}{p^0}(t-t_0), p) + \int\limits_{t_0}^{t} G(\tau, \mathbf{r} - \frac{\mathbf{p}}{p^0}(t-\tau), p)\mathcal{P}_{\tau\to t}(\tau, \mathbf{r} - \frac{\mathbf{p}}{p^0}(t-\tau), p)d\tau. \tag{4}$$

Let us integrate the distribution (4) over the space variables to represent the particle momentum density at large enough time, $t\to\infty$, when particles in the system stop to interact. To simplify notation let us introduce the escape probability for the particle with momentum p in the point $x = (t, \mathbf{r})$ to leave system without collisions: $\mathcal{P}(t,\mathbf{r},p) \equiv \mathcal{P}_{t\to(\tau\to\infty)}(t,\mathbf{r},p)$. Then the result can be presented in the general form found in Ref. [4]:

$$n(t\to\infty, p) \equiv n(p) = \int d^3r f(t_0, \mathbf{r}, p)\mathcal{P}(t_0, \mathbf{r}, p) + \int d^3r \int\limits_{t_0}^{\infty} dt' G(t', \mathbf{r}, p)\mathcal{P}(t', \mathbf{r}, p). \tag{5}$$

The first term in Eq. (5) describes the contribution to the momentum spectrum from particles that are emitted from the very initial time, while the second one describes the continuous emission with emission density $S(x,p) = G(t,\mathbf{r},p)\mathcal{P}(t,\mathbf{r},p)$ from 4D volume delimited by the initial and final (where particles stop to interact) 3D hypersurfaces.

In what follows we will use the (generalized) relaxation time approximation proposed in [4], which is the basis of the hydro-kinetic approach, described in detail in [6]. Namely, it was argued [4] that there is such a local equilibrium distribution function $f_{l.eq.}(T(x), u^\nu(x), \mu(x))$ that, in the region of not very small densities where term $G \sim S$ gives noticeable contribution to particle spectra, the function f is approximately equal to that one which would be obtained if all functions in r.h.s. of Eq. (4) calculated by means of that function $f_{l.eq.}$. The function $f_{l.eq.}$ is determined from the local energy-momentum conservation laws based on the non-equilibrium function f in the way specified in [6]. Then, in accordance with this approach we use

$$R(x,p) \approx R_{l.eq.}(x,p), G \approx R_{l.eq.}(x,p)f_{l.eq.}(x,p). \tag{6}$$

The “relaxation time” $\tau_{rel} = 1/R_{l.eq.}$ grows with time in this method.

3 Saddle point approximation of the emission function and particle momentum spectra

Let us generalize now the Cooper-Frye prescription of sudden freeze-out. For this aim we apply the saddle point method to calculate the integral in the expression for spectra (5) with account of (6). To simplify notation we neglect the contribution to the spectra from hadrons which are already free at the initial thermalization time $t_0 \sim 1$ fm/c and thus omit the first term in (4).

To provide straightforward calculations leading to the Cooper-Frye form let us shift the spacial variables, $\mathbf{r}' = \mathbf{r} + \frac{\mathbf{p}}{p_0}(t_0 - t')$, in (5) aiming to eliminate the variable t' in the argument of the function R which is the integrand in $\mathcal{P}(t', \mathbf{r}, p)$. Then

$$n(p) \approx \int d^3r' \int\limits_{t_0}^{\infty} dt' f_{\mathtt{l.eq.}}(t', \mathbf{r}' + \frac{\mathbf{p}}{p_0}(t'-t_0), p)Q(t', \mathbf{r}', \mathbf{p}), \tag{7}$$

where

$$Q(t',\mathbf{r}',p) = R(t',\mathbf{r}'+\frac{\mathbf{p}}{p_0}(t'-t_0),p)\exp\left\{-\int\limits_{t'}^{\infty} R(s,\mathbf{r}'+\frac{\mathbf{p}}{p_0}(s-t_0),p)ds\right\} \tag{8}$$

Note that

$$Q(t',\mathbf{r}',p) = \frac{d}{dt'}P(t',\mathbf{r}',\mathbf{p}), \tag{9}$$

where $P(t',\mathbf{r}',p)$ is connected with the escape probability $\mathcal{P}$:

$$P(t',\mathbf{r}',p) = \mathcal{P}(t',\mathbf{r}'+\frac{\mathbf{p}}{p_0}(t'-t_0),p). \tag{10}$$

Therefore

$$\int\limits_{t_0}^{\infty} dt' Q(t',\mathbf{r}',p) = 1-\mathcal{P}(t_0,\mathbf{r}',p) \approx 1. \tag{11}$$

The saddle point $t_\sigma(\mathbf{r},p)$ is defined by the standard conditions:

$$\begin{aligned} &\frac{dQ(t',\mathbf{r}',p)}{dt'}|_{t'=t'_\sigma} = 0, \\ &\frac{d^2Q(t',\mathbf{r}',p)}{dt'^2}|_{t'=t'_\sigma} < 0. \end{aligned} \tag{12}$$

Then one can get from (9), (10) the condition of the maximum of emission:

$$-\frac{p^\mu\partial_\mu R(t',\mathbf{r},p)}{R(t'_\sigma,\mathbf{r},p)}|_{t'=t'_\sigma,\mathbf{r}=\mathbf{r}'+\frac{\mathbf{p}}{p_0}(t'_\sigma-t_0)} = p_0 R(t'_\sigma,\mathbf{r}'+\frac{\mathbf{p}}{p_0}(t'_\sigma-t_0),p)\,. \tag{13}$$

If one neglects terms $\mathbf{p}^*\partial_{\mathbf{r}^*}R$ in l.h.s. and supposes that in the rest frame (marked be asterisk) of the fluid element with four-velocity $u(x)$ the collision rate, $R^*(x,p) = \frac{p_0R(x,p)}{p^\mu u_\mu}$, does not depend on particle momentum: $R^*(x) \approx \langle v^*\sigma\rangle(x)n^*(x)$ (here $n(x)$ is particle density, σ is the particle cross-section, v is the relative velocity, $< ... >$ means the average over all momenta), then the conditions (13) are equivalent to the requirement that at the temporal point of maximum of the emission function the rate of collisions is equal to the rate of system expansion [6]. This is the heuristic freeze-out criterion for sudden freeze-out [7]. However, as we will demonstrate, the neglect of momentum dependence leads to quite significant errors.

To pass to the Cooper-Frye representation we use the variables which include the saddle point:

$$\mathbf{r} = \mathbf{r}'+\frac{\mathbf{p}}{p_0}(t'_\sigma(\mathbf{r}',p)-t_0). \tag{14}$$

Then the expression for the spectrum takes the form:

$$n(p) \approx \int d^3r\left|1-\frac{\mathbf{p}}{p_0}\frac{\partial t_\sigma}{\partial\mathbf{r}}\right|\int\limits_{t_0}^{\infty} dt' S(t',\mathbf{r},p), \tag{15}$$

where the emission density in saddle point representation is ($t_\sigma \equiv (t_\sigma(\mathbf{r},p))$

$$\begin{aligned} S(t',\mathbf{r},p) &= f_{\mathtt{1.eq.}}(t',\mathbf{r}+\frac{\mathbf{p}}{p_0}(t'-t_\sigma),p) \\ &\times R(t_\sigma,\mathbf{r},p)\mathcal{P}(t_\sigma,\mathbf{r},p)\exp(-(t'-t_\sigma)^2/2D^2(t_\sigma,\mathbf{r},p)). \end{aligned} \tag{16}$$

According to Eq. (3) $\mathcal{P}(t_\sigma,\mathbf{r},p) = e^{-1}$, since the freeze-out zone is the region of the last collision for the particle. Then the normalization condition for Q (Q is presented by the bottom line in (16)) allows one to determine the temporal width of the emission at the point $(t_\sigma(\mathbf{r},p),\mathbf{r},p)$:

$$D(t_\sigma,\mathbf{r},p) = \frac{e}{\sqrt{2\pi}}\frac{1}{R(t_\sigma,\mathbf{r},p)} \approx \tau_{\mathtt{rel}}(t_\sigma,\mathbf{r},p). \tag{17}$$

Therefore if the temporal homogeneity length $\lambda(t,\mathbf{r},p)$ of the distribution function $f_{\mathtt{1.eq.}}$ near the 4-point $(t_\sigma(\mathbf{r},p),\mathbf{r})$ is much larger than the width of the emission zone, $\lambda(t_\sigma,\mathbf{r},p) \gg \tau_{\mathtt{rel}}(t_\sigma,\mathbf{r},p)$, then one can approximate $f_{\mathtt{1.eq.}}(t',\mathbf{r}+\frac{\mathbf{p}}{p_0}(t'-t_\sigma),p)$ by $f_{\mathtt{1.eq.}}(t_\sigma,\mathbf{r},p)$ in Eq. (15) and perform integration over t' accounting for normalizing condition (11). As a result we get from (15) and (16) the momentum spectrum in a form similar to the Cooper-Frye one (1):

$$p^0 n(p) = p^0 \frac{d^3N}{d^3p} \approx \int\limits_{\sigma(p)} d\sigma_\mu p^\mu f_{\mathtt{l.eq.}}(x,p). \tag{18}$$

It is worthy to note that the representation of the spectrum through emission function (5) is the result of the integration of the total non-equilibrium distribution function $f(x,p)$, Eqs. (4), (6), over the asymptotical hypersurface in time, while the approximate representation of the spectrum, Eq. (18), uses only the local equilibrium part $f_{\mathtt{l.eq.}}$ of the total function $f(x,p)$ at the set of points of maximal emission - at hypersurface $(t_\sigma(\mathbf{r},p),\mathbf{r})$.

4 Conditions of applicability for the sudden freeze-out approximation

Now let us summarize the conditions when the Cooper-Frye form for sudden freeze-out can be used. They are the following:

i) For each momentum $\mathbf{p}$, there is a region of $\mathbf{r}$ where the emission function as well as the function Q, Eq. (8), have a clear maximum. The temporal width of the emission D, defined by Eq. (16), which is found to be equal to the relaxation time (inverse of collision rate), should be smaller than the corresponding temporal homogeneity length of the distribution function: $\lambda(t_\sigma,\mathbf{r},p) \gg D(t_\sigma,\mathbf{r},p) \simeq \tau_{\mathtt{rel}}(t_\sigma,\mathbf{r},p)$.

ii) The contribution to the spectrum from the residual region of $\mathbf{r}$, where the saddle point method (Gaussian approximation (16) and/or condition $\tau_{\mathtt{rel}} \ll \lambda$) is violated, does not affect essentially the particle momentum density.

If these conditions are satisfied, then the momentum spectra can be presented in the Cooper-Frye form despite the fact that actually it is not sudden freeze-out and the decoupling region has a finite temporal width $\tau_{rel}(t_\sigma,\mathbf{r},p)$.

The analytical results as for the temporal width of the spectra agree remarkably with the numerical calculations of pion emission function within hydro-kinetic model (HKM) [6]. For example, near the point of maximum, $\tau = 16.5$ fm/c, $r = 0, p_T = 0.2$ GeV, the "experimental" temporal width D_{HKM} obtained by numerical solution of the complete hydro-kinetic equations is $D_{HKM} \approx 4.95$ fm (see Fig. 1, left). Our theoretical estimate is $D = \frac{e}{\sqrt{2\pi}R} \approx 5.00$ fm, since the rate of collisions in this phase-space point is $R(\tau_\sigma(\mathbf{r},p) = 16.5$ fm/c, $\mathbf{r} = 0, p_T=$ 0.2 GeV, $p_L = 0) \approx 0.217$ c/fm.

It is worthy to emphasize that such a generalized Cooper-Frye representation is related to freeze-out hypersurfaces that depend on the momentum $\mathbf{p}$ and typically do not enclose the initially dense matter. In Fig. 1, one can see the structure of the emission domains for different p_T in HKM [6] for initially (at τ=1 fm/c) Gaussian energy density profile with ϵ_{max}= 6 GeV/fm^3. The maximal emission regions for different p_T are crossed by isotherms with different temperatures: 80 MeV for low momenta and 135 MeV for high ones. This is completely reflected in the concave structure of the transverse momentum spectrum as one can see in Fig. 2.

If a part of the hypersurface $t_\sigma(\mathbf{r},p)$ is non-space-like and corresponds to the maximum of the emission of particles with momentum $\mathbf{p}$, directed outward the system, the same part of the hypersurface cannot correspond to the maximal emission for particles with momentum directed inward the system. It is clear that the emission function at these points is close to zero for such particles. Even formally, in the Gaussian approximation (16) for Q, validated in the region of its maximal value, the integral $\int\limits_{t_\sigma}^{\infty} dsR(s,\mathbf{r}+\frac{\mathbf{p}}{p^0}(s-t_\sigma(\mathbf{r},p),p) \gg 1$, if particle world line crosses almost the whole system. The latter results in $Q \to 0$ and, therefore, completely destroys the saddle-point approximation (12) for Q and then the Cooper-Frye form (18) for spectra. Recall that if a particle crosses some non-space-like part of the hypersurface σ moving inward the system, this corresponds to the condition $p^\mu d\sigma_\mu < 0$ [2]. Hence the value $p^\mu d\sigma_\mu(p)$ in the generalized Cooper-Frye formula (18) should be always positive: $p^\mu d\sigma_\mu(p) > 0$ across the hypersurface where fairly sharp maximum of emission of particles with momentum $\mathbf{p}$ is situated; and so requirement $p^\mu d\sigma_\mu(p) > 0$ is a necessary condition for $t_\sigma(\mathbf{r},p)$ to be a true hypersurface of the maximal emission. It means that hypersurfaces of maximal emission for a given momentum $\mathbf{p}$ may be open in the space-time, not enclosing the high-density matter at the initial time t_0, and different for different $\mathbf{p}$. Therefore, there are no negative contributions to the particle momentum density from non-space-like sectors of the freeze-out hypersurface, that is a well known shortcoming of the Cooper-Frye prescription [2, 3]; the negative contributions could appear only as a result of utilization of improper freeze-out hypersurface that roughly ignores its momentum dependence and so is common for all $\mathbf{p}$. If, anyhow, such a common hypersurface will be used, e.g. as the hypersurface of the maximal particle number emission (integrated over $\mathbf{p}$), there is no possibility to justify the approximate expression for momentum spectra similar to Eq. (18).

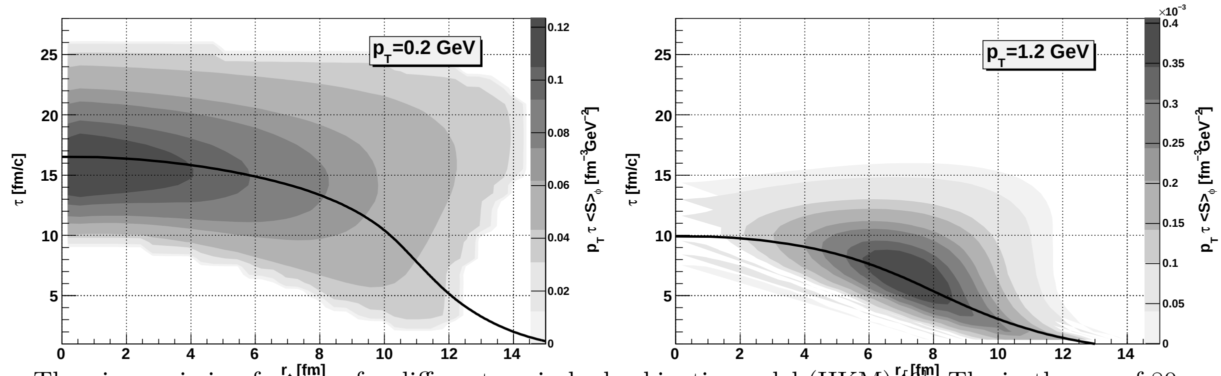

Figure 1. The pion emission function for different p_T in hydro-kinetic model (HKM) [6]. The isotherms of 80 MeV (left) and 135 MeV (right) are superimposed.

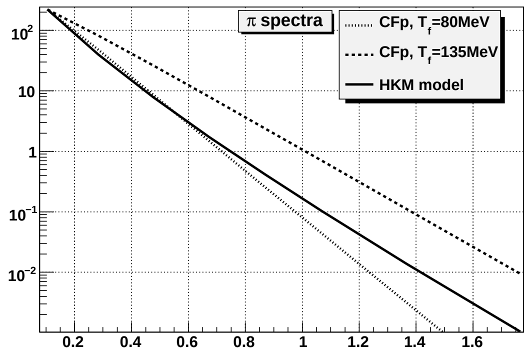

Figure 2. Transverse momentum spectrum of π^- in HKM, compared with the sudden freeze-out ones at temperatures of 80 and 160 MeV with arbitrary normalization.

5 Conclusions

We demonstrated that the widely used phenomenological Cooper-Frye prescription [1] for calculation of particle spectrum is too rough because the freeze-out hypersurface is considered there as common for all momenta of particles. The Cooper-Frye formula, however, could be applied in an improved (but still rather approximate) form accounting for direct momentum dependence of the freeze-out hypersurface $\sigma(p)$; the latter corresponds to the maximum of emission function $S(t_\sigma(\mathbf{r},p),\mathbf{r},p)$ at fixed momentum $\mathbf{p}$ in an appropriate region of $\mathbf{r}$. If such a hypersurface $\sigma(p)$ is found, the condition of applicability of the Cooper-Frye formula for given $\mathbf{p}$ is that the width of the maximum, which in the simple cases - e.g., for one component system or at domination of elastic scatterings - is just the relaxation time (inverse of collision rate), should be smaller than the corresponding temporal homogeneity length of the distribution function. Then the idealization of a freeze-out hypersurface may be justified (despite freeze-out is not sharp and has the finite temporal width), though an accurate determination of the corresponding hypersurface requires a nontrivial dynamical calculations.

Acknowledgements. This work was supported by the Program "Fundamental Properties of Physical Systems under Extreme Conditions" of the Bureau of the Section of Physics and Astronomy of NAS of Ukraine.

References

[1] F. Cooper, G. Frye, Phys. Rev. D**10**, 186 (1974).

[2] Yu.M. Sinyukov, Z. Phys. C**43**, 401 (1989).

[3] K.A. Bugaev, Nucl. Phys. A**606**, 559 (1996).

[4] Yu.M. Sinyukov, S.V. Akkelin, Y. Hama, Phys. Rev. Lett. **89**, 052301 (2002).

[5] S.V. Akkelin, M.S. Borysova, Yu.M. Sinyukov, Acta Phys. Hung. A: Heavy Ion Physics **22**, 165 (2005).

[6] S.V. Akkelin, Y. Hama, Iu.A. Karpenko, and Yu.M. Sinyukov, Phys. Rev. C**78**, 034906 (2008).

[7] J. Bondorf, S. Garpman, J. Zimanyi, Nucl. Phys. A**296**, 320 (1978); K.S. Lee, U. Heinz, E. Schnedermann, Z. Phys. C**48**, 525 (1990); F.S. Navarra, M.C. Nemes, U. Ornik, and S. Paiva, Phys. Rev. C**45**, R2552 (1992); E. Schnedermann, U. Heinz, Phys. Rev. C**47**, 1738 (1993)

Section Talks

Proceedings of the International School-seminar
"New Physics and Quantum Chromodynamics at external Conditions", pp. 92 – 94,
3-6 May 2009, Dnipropetrovsk, Ukraine

NEW RESULTS ON LATTICE MEASUREMENTS OF GLUON MAGNETIC MASS WITH GPGPU TECHNOLOGY

S. Antropov, V. Demchik[a], V. Skalozub[b]

Dnipropetrovsk National University, Dnipropetrovsk, Ukraine

$SU(2)$ gluodynamics at high temperature in external Abelian and non-Abelian magnetic field is investigated on a lattice with General Purpose computation on Graphics Processing Units (**GPGPU**) technology. Both type magnetic fluxes are introduced by means of twisted boundary conditions. It is shown that non-Abelian $SU(2)$ monopole-antimonopole magnetic fields form a screened flux tube, whereas Abelian magnetic fields form the screened magnetic tube with increasing temperature dependent field strength. The usage of GPGPU technology makes it possible to obtain the essential performance speed-up in comparison with a serial execution (up to 70 times).

1 Introduction

On the middle of 1970th 't Hooft and Mandelstam [4] proposed that condensation of magnetic monopoles could be responsible for the confinement mechanism. If the vacuum state of a non-Abelian gauge theory is characterized by the presence of a monopole condensate, this screens the monopole-antimonopole interaction which should therefore exhibit a Yukawa-like behavior [1]. If there is no condensate whatever, one should expect instead a Coulombic interaction between the monopoles, as is the case in classical $SU(2)$ theory.

The main aim of the present paper is to study the high-temperature phase of $SU(2)$ lattice gauge theory in the presence of Abelian and non-Abelian magnetic fields. In the latter case we consider the field generated by a monopole-antimonopole pair. To estimate the behavior of magnetic fields a large amount of simulation data is needed. Unfortunately, traditional computational resources are lack to perform the detail analysis. In our case, we use the GPGPU technology which allows to study the large lattices up to 32×64^3. As it is shown in the present investigation, the accounting for large lattices leads to decreasing of magnetic mass in both the cases of Abelian and non-Abelian magnetic fields. Some details of MC simulations on the ATI GPUs could be found in [5] and in references therein.

2 MC details and numerical results

In performed MC simulations we use the hypercubic lattice $L_t \times L_s^3$ with hypertorus geometry. The temperature is incorporated in the formalism in a standard way, "indirectly" through the lattice asymmetry in temporal direction ($L_t < L_s$). The standard Wilson action is used,

$$S_W = \beta \sum_x \sum_{\mu<\nu} \left[1 - \frac{1}{2}\,\mathrm{Tr}\,\mathbf{U}_{\mu\nu}(x) \right], \tag{1}$$

$$\mathbf{U}_{\mu\nu}(x) = \mathbf{U}_\mu(x)\mathbf{U}_\nu(x+a\hat{\mu})\mathbf{U}_\mu^\dagger(x+a\hat{\nu})\mathbf{U}_\nu^\dagger(x), \tag{2}$$

where $\beta = 4/g^2$, g is a bare coupling.

The link variables $\mathbf{U}_\mu(x)$ are the $SU(2)$ matrices and can be decomposed in terms of the unity, I, and Pauli σ_j, matrices in the color space,

$$\mathbf{U}_\mu(x) = IU_\mu^0(x) + i\sigma_j U_\mu^j(x). \tag{3}$$

Each global buffer cell in the GPU comprises four 32-bit numbers (single precision). Thus, it is natural to store all components of link matrices ($U_\mu^0(x)$, $U_\mu^1(x)$, $U_\mu^2(x)$ and $U_\mu^3(x)$) as one GPU-cell.

Lattice data are stored with the single precision, MC updating are performed with the single precision whereas all averaging measurements were performed with the double precision to avoid error accumulations.

The constant homogeneous magnetic flux is introduced on a lattice by applying the twisted boundary conditions (see [9] and references therein). The magnetic field of monopole-antimonopole string is introduced by the procedure of DeGrand and Toussaint [6].

e-mail: [a]vadimdi@yahoo.com, [b]skalozub@daad-alumni.de

Table 1. Fit results for monopole-antimonopole pair and Abelian magnetic field, respectively

	Monopole string			**Abelian field**		
Fit function	χ^2	C	m	χ^2	C	m
$C\exp(-mr)$	35.2	0.047	$0.227^{+0.040}_{-0.036}$	901.8	0.063	$0.0244^{+0.0006}_{-0.0006}$
$C\exp(-m^2r^2)$	60.6	0.019	$0.113^{+0.011}_{-0.011}$	1924.4	0.035	$0.0157^{+0.0002}_{-0.0002}$
C/r	342.0	0.031		7.090	0.911	
$C/r\exp(-mr)$	19.1	0.125	$0.095^{+0.038}_{-0.030}$	7.086	0.912	$0.0000125^{+0.00052}_{-0.00054}$
$C/r\exp(-m^2r^2)$	36.1	0.087	$0.075^{+0.013}_{-0.014}$	7.090	0.911	$0.000155^{+0.00229}_{-0.00242i}$
C/r^2	1.19	0.437		31400	28.13	
$C/r^2\exp(-m^2r^2)$	0.81	0.441	$0.00837^{+0.014}_{-0.013i}$	7550	18.26	$0.0182i$
C/r^4	218.3	14.75		159500	248.9	
$C/r^4\exp(-m^4r^4)$	215.0	14.75	$0.000547i$	161000	10.0	0.0

Table 2. Performance comparison of serial (CPU) and parallel (GPU) Monte Carlo simulations for pure $SU(2)$ gluodynamics on some lattices

	4×8^3	4×16^3	4×24^3	4×32^3	8×16^3	8×24^3
CPU, sec.	30	274	1985	3796	744	2060
GPU, sec.	5.0	11.4	28.5	63.1	18.9	53.4
Speed-up, times	6.1	24.1	69.8	60.2	39.4	38.6

For each lattice geometry $L_t \times L_s^3$, we have fitted the effect of magnetic field with the lattice plaquette average by means of different functions:

$$\langle U_{untwisted}\rangle - \langle U_{twisted}\rangle = f(m, L_s). \tag{4}$$

The fit results are shown in Table 1. There are different fit functions with the corresponding values of χ^2 function and the values of fit parameters for cases of monopole-antimonopole string and Abelian magnetic field, respectively.

As one can see, the best fit function for magnetic field of monopole-antimonopole string is $C/r^2\exp(-m^2r^2)$, so non-Abelian $SU(2)$ monopole-antimonopole magnetic fields form screened flux tubes. Such behavior is in a good correspondence with the results known from the literature [1, 2]. It should be noted that the fit function C/r^2 has the close value of χ^2 function, this is essentially the case of zero magnetic mass $m = 0$.

The best fit function for the case of the Abelian magnetic field is $C/r\exp(-mr)$ with a small value of the magnetic mass $m = 0.0000125$ with symmetric confidence area near the zero. So, this case corresponds to the screened magnetic tube with increasing field strength.

The fit results for the Abelian magnetic field is shown in figure 1. The maximum-likelihood estimate of different fit functions by the whole data set is shown as the solid curves. The mean values and the 95% confidence intervals are shown as the points for each lattice spatial size. As it is also seen, the maximum-likelihood estimate of $f(m, L_s)$ for functions of C/r form is in good accordance with all the data points, because the corresponding solid lines are located in the 95% confidence intervals of all points.

The performance comparison of serial and parallel MC simulations for different lattices is collected in Table 2. In the first row the lattice geometry is shown. The next row contains the execution time of Fortran-program, compiled with the trial version of Intel Fortran compiler 11 (last available version). The execution time of GPU-oriented program is shown in the third row. The total speed-up of parallel (GPU) MC simulations in comparison with serial (CPU) one is shown in the last row. It can be seen that for small lattices (4×8^3, 4×16^3) the gain in productivity is not too high (6.1 and 24.1 times, respectively). But for larger lattices it varies from 38.6 to 69.8 times.

3 Conclusion

We have investigated the different hypothesis for the behavior of the magnetic fields in pure $SU(2)$ gluodynamics at high temperature. It was determined that non-Abelian $SU(2)$ monopole-antimonopole magnetic fields form screened flux tube. Abelian magnetic fields form a screened magnetic field tube with increasing field strength. The screening magnetic mass is different, it is less for Abelian magnetic fields.

In our investigation we have shown that the usage of GPGPU technology leads to significant performance increase in comparison with a serial execution (up to 69.8 times). This technology makes possible to study

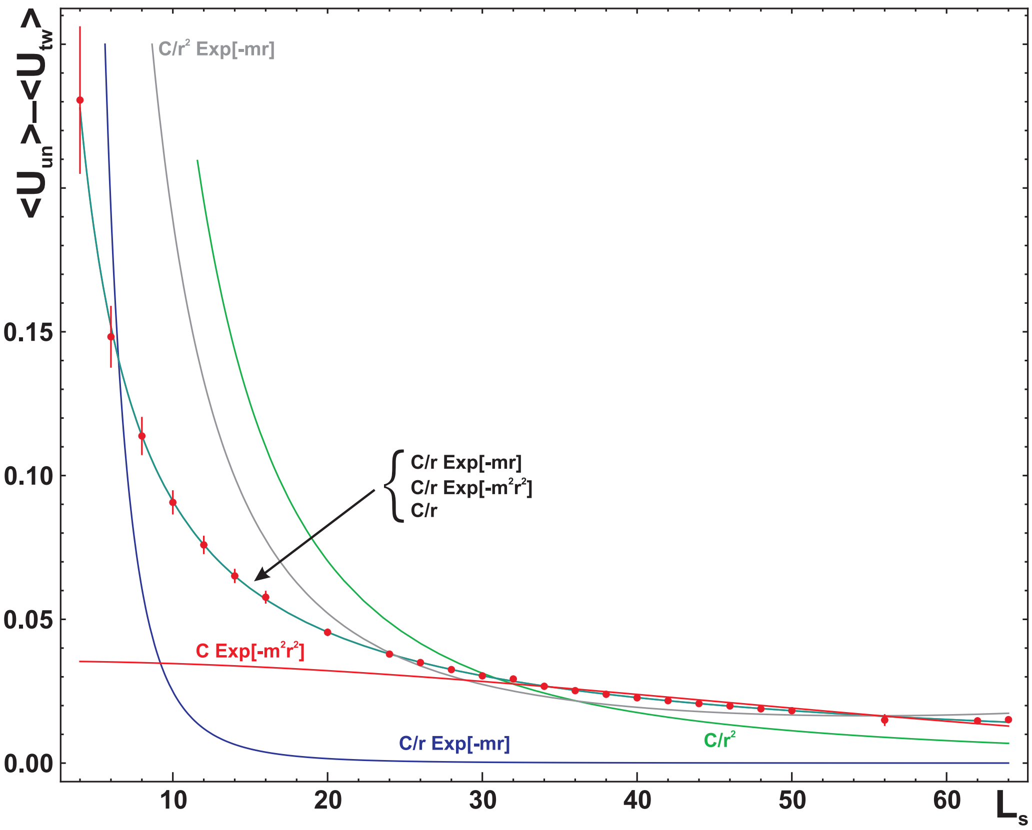

Figure 1. Fit results for Abelian magnetic field

large lattices (32×64^3 and larger could be studied on PC). Due to extreme growth of compute performance the modern GPU cards even may vie with CPU cluster systems. So, we hope that GPGPU technology will open new facilities in simulations of high-energy physics.

References

[1] C. Hoelbling, C. Rebbi and V. A. Rubakov, Phys. Rev. D **63** (2001) 034506 [arXiv:hep-lat/0003010].

[2] Ph. de Forcrand, C. Korthals-Altes and O. Philipsen, Nucl. Phys. B **742** (2006) 124 [arXiv:hep-ph/0510140].

[3] G. 't Hooft, Nucl. Phys. B **79** (1974) 276.

[4] G. 't Hooft, in High Energy Physics, ed. A. Zichichi (Editrice Compositori Bologna, 1976); S. Mandelstam, Phys. Rept. **23** (1976) 245.

[5] V. Demchik and A. Strelchenko, arXiv:0903.3053 [hep-lat].

[6] T. A. DeGrand and D. Toussaint, Phys. Rev. D **25** (1982) 526.

[7] M. Creutz, Phys. Rev. D **36** (1987) 515.

[8] E. M. Ilgenfritz, M. L. Laursen, G. Schierholz, M. Muller-Preussker and H. Schiller, Nucl. Phys. B **268** (1986) 693.

[9] V. Demchik and V. Skalozub, arXiv:hep-lat/0601035.

Proceedings of the International School-seminar
"New Physics and Quantum Chromodynamics at external Conditions", pp. 95 – 99,
3-6 May 2009, Dnipropetrovsk, Ukraine

IDENTIFICATION OF HEAVY GAUGE Z' BOSONS AT THE ILC

A. A. Babich[a], N. V. Karpenko[b], A. V. Tsytrinov[c], A. A. Pankov [d]

Pavel Sukhoi Technical State University, Gomel, Belarus

The potential of the e^+e^- International linear collider (ILC) to search for and distinguish between new neutral gauge bosons signals predicted within various classes of models with extended gauge sector in fermion pair production processes was examined. The presented analysis is based on the polarized differential observables which provides higher sensitivity of the studied processes to Z' boson parameters with respect to the integrated observables. The discovery and identification reaches of the new neutral gauge bosons within the classes of E_6 and LR models and also ALR and SSM models were determined.

1 Introduction

The Standard Model (SM) of strong and electroweak interactions, based on the gauge symmetry $SU(3)_C \times SU(2)_L \times U(1)_Y$, has achieved many successes in describing the experimental data within the range of energies available today. In particular, it has been tested to the level of its loop radiative corrections in the high precision LEP experiments. Nevertheless, it is widely believed that it is not the ultimate truth. Indeed, besides the fact that it has too many parameters which are merely incorporated by hand, it does not unify the electromagnetic, weak and strong forces in a satisfactory way since the coupling constants of the three gauge groups are different and independent. Therefore, one would expect the existence of a more fundamental theory in which the SM is naturally embedded and which reduces to it at present energies.

Among the candidates for this more fundamental picture, grand unified theories are the most appealing ones. In particular, the exceptional group E_6, which contains the popular subgroups $SU(5)$ and $SO(10)$, has received most of the attention in recent years [1]. A general prediction of grand unified theories is the existence of additional gauge bosons Z'. Indeed, in the breaking of these symmetries down to the SM gauge group, it is possible that some additional group factors survive at low energies, allowing for at least one extra neutral gauge boson with a mass not far from the scale of the electroweak symmetry breaking. This additional boson could then be light enough to generate observable effects at the next generation of electron-positron or hadron colliders.

Depending on the assumed luminosity of the machine, the nature of the Z' as well as its decay branching fractions, discovery limits range up to 4-5 TeV at the LHC. At e^+e^- ILC, since their presently planned energies do not exceed one TeV, the possibility of directly producing a new gauge boson is more limited than at LHC. However, even if a new Z' is too heavy to be produced as a resonance, it could give rise to virtual effects which are measurable. As a matter of fact, due to the clean environment of e^+e^- annihilation, high precision measurements can be performed and masses considerably higher than the maximum center of mass energy can be probed. In addition, because of the much larger number of experimental observables which can be measured with a high accuracy, the possibility of identifying the model origin of the new gauge boson is not as limited as in the case of the LHC. The study of the effects of the new gauge boson at the LHC and ILC would then be complementary.

In this paper, we shall study the possible effects of one extra neutral gauge boson at high energy e^+e^- colliders, concentrating on two general effective theories: $SU(2)_L \times U(l)_Y \times U(1)_{Y'}$ originating from the E_6 model and left-right models [1] based on an $SU(2)_L \times SU(2)_R \times U(1)$ symmetry. We shall assume that the new Z' boson will be heavier than the total energy of the ILC so that it can reveal its existence only through virtual effects which could be measurable in a high precision experiment.

The paper is organized as follows. The next section is devoted to the discussion of the main features of the effective Z' models which will be considered and the observables under study. In section III, we present the numerical analysis and constraints on Z' masses. Section IV contains concluding remarks.

2 Differential cross sections and Z' models

We consider the fermion pair production process

$$e^+ + e^- \to f + \bar{f}, \tag{1}$$

e-mail: [a]babich@gstu.gomel.by, [b]chiffa@np.by, [c]tsytrin@gstu.gomel.by, [d]pankov@ictp.it

with $f \neq t$ at the ILC with c.m. energy $\sqrt{s} = 0.5\,\text{TeV}$ and polarized electron and positron beams. For the process Eq. (1), limiting ourselves to the cases $f \neq t$, we can neglect fermion masses with respect to $\sqrt{s}$, and express the amplitude in the Born approximation including the γ, Z and Z' s-channel exchanges. With P_e and $P_{\bar{e}}$ the longitudinal polarizations of the electron and positron beams, respectively, and θ the angle between the incoming electron and the outgoing fermion in the c.m. frame, the differential cross section can be expressed as [2]:

$$\frac{d\sigma(P^-,P^+)}{dz} = \frac{D}{4}\left[(1-P_{\text{eff}})\left(\frac{d\sigma_{\text{LL}}}{dz}+\frac{d\sigma_{\text{LR}}}{dz}\right)+(1+P_{\text{eff}})\left(\frac{d\sigma_{\text{RR}}}{dz}+\frac{d\sigma_{\text{RL}}}{dz}\right)\right], \tag{2}$$

where $z = \cos\theta$; L, R are the helicity indexes. Here,

$$P_{\text{eff}} = \frac{P_e - P_{\bar{e}}}{1 - P_e P_{\bar{e}}} \tag{3}$$

is the effective polarization, $|P_{\text{eff}}| \leq 1$, and $D = 1 - P_e P_{\bar{e}}$. For Bhabha scattering differential cross sections can be written as [3, 4]

$$\begin{aligned}\frac{d\sigma(P^-,P^+)}{dz} &= \frac{(1+P^-)(1-P^+)}{4}\frac{d\sigma_{\text{R}}}{dz}+\frac{(1-P^-)(1+P^+)}{4}\frac{d\sigma_{\text{L}}}{dz}+\\ &+\frac{(1+P^-)(1+P^+)}{4}\frac{d\sigma_{\text{RL},t}}{dz}+\frac{(1-P^-)(1-P^+)}{4}\frac{d\sigma_{\text{LR},t}}{dz},\end{aligned} \tag{4}$$

where

$$\frac{d\sigma_{\text{L}}}{dz} = \frac{d\sigma_{\text{LL}}}{dz}+\frac{d\sigma_{\text{LR},s}}{dz}, \qquad \frac{d\sigma_{\text{R}}}{dz} = \frac{d\sigma_{\text{RR}}}{dz}+\frac{d\sigma_{\text{RL},s}}{dz}. \tag{5}$$

The helicity cross sections

$$\begin{aligned}\frac{d\sigma_{\text{LL}}}{dz} &= \frac{2\pi\alpha^2_{\text{e.m.}}}{s}\left|G_{\text{LL},s}+G_{\text{LL},t}\right|^2, \qquad \frac{d\sigma_{\text{RR}}}{dz} = \frac{2\pi\alpha^2_{\text{e.m.}}}{s}\left|G_{\text{RR},s}+G_{\text{RR},t}\right|^2,\\ \frac{d\sigma_{\text{LR},t}}{dz} &= \frac{d\sigma_{\text{RL},t}}{dz} = \frac{2\pi\alpha^2_{\text{e.m.}}}{s}\left|G_{\text{LR},t}\right|^2, \qquad \frac{d\sigma_{\text{LR},s}}{dz} = \frac{d\sigma_{\text{RL},s}}{dz} = \frac{2\pi\alpha^2_{\text{e.m.}}}{s}\left|G_{\text{LR},s}\right|^2.\end{aligned} \tag{6}$$

are expressed through the helicity amplitudes $G_{\alpha\beta,i}$ $(\alpha,\beta = \text{L},\text{R})$ as

$$\begin{aligned}G_{\text{LL},s} &= u\left(\frac{1}{s}+\frac{g^2_{\text{L}}}{s-M^2_Z}+\frac{g'^2_{\text{L}}}{s-M^2_{Z'}}\right), \quad G_{\text{LL},t} = u\left(\frac{1}{t}+\frac{g^2_{\text{L}}}{t-M^2_Z}+\frac{g'^2_{\text{L}}}{t-M^2_{Z'}}\right),\\ G_{\text{RR},s} &= u\left(\frac{1}{s}+\frac{g^2_{\text{R}}}{s-M^2_Z}+\frac{g'^2_{\text{R}}}{s-M^2_{Z'}}\right), \quad G_{\text{RR},t} = u\left(\frac{1}{t}+\frac{g^2_{\text{R}}}{t-M^2_Z}+\frac{g'^2_{\text{R}}}{t-M^2_{Z'}}\right),\\ G_{\text{LR},s} &= t\left(\frac{1}{s}+\frac{g_{\text{R}}\,g_{\text{L}}}{s-M^2_Z}+\frac{g'_{\text{R}}\,g'_{\text{L}}}{s-M^2_{Z'}}\right), \quad G_{\text{LR},t} = s\left(\frac{1}{t}+\frac{g_{\text{R}}\,g_{\text{L}}}{t-M^2_Z}+\frac{g'_{\text{R}}\,g'_{\text{L}}}{t-M^2_{Z'}}\right).\end{aligned} \tag{7}$$

Here $u, t = -s(1 \pm z)/2$, $g_{\text{R}} = \text{tg}\theta_W$ and $g_{\text{L}} = -\text{ctg}2\,\theta_W$, θ_W - Weinberg angle. The helicity amplitudes (7) are written in approximation $M_Z \ll \sqrt{s} \ll M_{Z'}$.

Polarized cross section (2) for s-channel lepton processes $e^+e^- \to l^+l^-$ $(l = \mu, \tau)$ is produce from (4) after removing t-channel contributions. For estimating cross sections of c- and b-quark pair production in amplitudes it is necessary to consider the electric charges of final fermions, their coupling constants with Z- and Z'-bosons and color factor $N_C \simeq 3\,(1 + \alpha_s/\pi)$.

In the following analysis, cross sections will be evaluated including initial- and final-state radiation by means of the program ZFITTER [5], which has to be used along with ZEFIT, adapted to the present discussion, with $m_{\text{top}} = 175$ GeV and $m_H = 120$ GeV. One-loop SM electroweak corrections are accounted for by improved Born amplitudes, such that the forms of the previous formulae remain the same. Concerning initial-state radiation, a cut on the energy of the emitted photon $\Delta = E_\gamma/E_{\text{beam}} = 0.9$ is applied for $\sqrt{s} = 0.5$ TeV in order to avoid the radiative return to the Z peak, and increase the signal originating from the contact interaction contribution.

For estimation of radiation corrections for Bhabha scattering we used method of structure functions [6]. Cross sections can be written as [7]:

$$d\sigma^{\text{rad}}(q^2) = \int dx_1 dx_2 D(x_1,q^2)D(x_2,q^2)d\sigma((1-x_1x_2)q^2)(1+\delta_{fe})\Theta(\text{cuts}), \tag{8}$$

where $D(x, q^2)$ is electron (positron) structure function.

Table 1. Left- and right-handed couplings of the first generation of SM fermions to the Z' gauge bosons, in units of $1/c_W$ for the E_6 and LR models, and $1/s_W c_W\sqrt{1-2s_W^2}$ for the ALR model, where $c_W = \cos\theta_W$, $s_W = \sin\theta_W$.

E_6 model				
fermions (f)	ν	e	u	d
$g_L^{f'}$	$3A+B$	$3A+B$	$-A+B$	$-A+B$
$g_R^{f'}$	0	$A-B$	$A-B$	$-3A-B$
Left-Right model (LR)				
$g_L^{f'}$	$\frac{1}{2\,\alpha_{LR}}$	$\frac{1}{2\,\alpha_{LR}}$	$-\frac{1}{6\,\alpha_{LR}}$	$-\frac{1}{6\,\alpha_{LR}}$
$g_R^{f'}$	0	$\frac{1}{2\,\alpha_{LR}}-\frac{\alpha_{LR}}{2}$	$-\frac{1}{6\,\alpha_{LR}}+\frac{\alpha_{LR}}{2}$	$-\frac{1}{6\,\alpha_{LR}}-\frac{\alpha_{LR}}{2}$
Alternative Left-Right model (ALR)				
$g_L^{f'}$	$-\frac{1}{2}+s_W^2$	$-\frac{1}{2}+s_W^2$	$-\frac{1}{6}s_W^2$	$-\frac{1}{6}s_W^2$
$g_R^{f'}$	0	$-\frac{1}{2}+\frac{3}{2}s_W^2$	$\frac{1}{2}-\frac{7}{6}s_W^2$	$\frac{1}{3}s_W^2$

As numerical inputs, we shall assume the commonly used reference values of the identification efficiencies: $\epsilon = 95\%$ for l^+l^-; $\epsilon = 60\%$ for $b\bar{b}$; $\epsilon = 35\%$ for $c\bar{c}$. In order to evaluate the statistical uncertainty we take $L = 100$ fb^{-1} (half for each polarization orientation) with uncertainty $\delta L/L = 0.5\%$, and a fiducial experimental angular range $|\cos\theta| \le 0.99$. Also, regarding electron and positron degrees of polarization, we shall consider the values: $|P_e| = 0.8$; $|P_{\bar{e}}| = 0.5$, with $\delta P_e/P_e = \delta P_{\bar{e}}/P_{\bar{e}} = 0.5$ %.

The list of Z' models that will be considered in our analysis is the following:

(i) The three possible $U(1)$ Z' scenarios originating from the exceptional group E_6 spontaneous breaking. They are defined in terms of a mixing angle β, and the couplings are as in Tab. 1. The specific values $\beta = 0$, $\beta = \pi/2$ and $\beta = \arctan(-\sqrt{5/3})$, correspond to different E_6 breaking patterns and define the popular scenarios Z'_χ, Z'_ψ and Z'_η, respectively.

(ii) The left-right models, originating from the breaking of an $SO(10)$ grand-unification symmetry, and where the corresponding $Z'_{\rm LR}$ couples to a combination of right-handed and $B-L$ neutral currents (B and L denote lepton and baryon currents), specified by a real parameter $\alpha_{\rm LR}$ bounded by $\sqrt{2/3} \le \alpha_{\rm LR} \le \sqrt{2}$. Corresponding Z' couplings are reported in Tab. 1. We fix $\alpha_{\rm LR} = \sqrt{2}$, which corresponds to a pure L-R symmetric model (LRS).

(iii) The $Z'_{\rm ALR}$ predicted by the 'alternative' left-right scenario.

(iv) The so-called sequential $Z'_{\rm SSM}$, where the couplings to fermions are the same as those of the SM Z.

All numerical values of the Z' couplings needed for the amplitudes are collected in Table 1, where: $A = \cos\beta/2\sqrt{6}$ and $B = \sqrt{10}\sin\beta/12$ are used.

3 Numerical analysis and constraints on Z' masses

Heavy resonances appearing in the clean Drell-Yan channel may be the first new physics to be observed at the LHC. In this section we assume that the Z' has been discovered in *pp* collisions as a mass peak or bump at the LHC and we want to discuss how to elucidate the origin of this new gauge boson at the ILC. In other words, we make the hypothesis that a Z' signal is effectively observed (so that the SM is excluded at a certain C.L.) and the data is consistent with one of the Z' models. We want to assess the level at which this Z' model, that we call "true" model, can be expected to be distinguishable from the other ones, that may compete with it as sources of the deviations from the SM and that we call "tested" models, for any values of their mass $M_{Z'}$. Quantitatively, this amounts to determine the foreseeable "identification reach" on the "true" model.

To illustrate the numerical procedure leading to the determination of an "identification reach", it should be useful to work out explicitly a definite example, and assume that the "true" non-standard model is a E_6 model with some value of $\cos\beta$ and $M_{Z'}$. Then, we may take as "tested" model anyone of the Z' models and, for definiteness, let us choose the LR model.

We can introduce a relative deviation of an observable $\mathcal{O}$ predictions arising from the chosen Z' model ($Z'_{\rm LR}$):

$$\Delta\mathcal{O} = \frac{\mathcal{O}(Z'_{\rm LR}) - \mathcal{O}(Z'_{\rm E_6})}{\mathcal{O}(Z'_{\rm E_6})}. \tag{9}$$

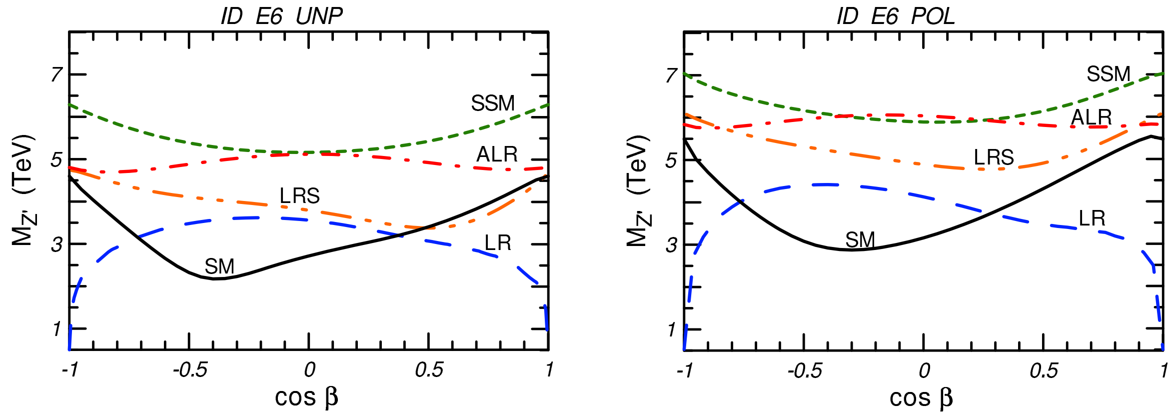

Figure 1. Left panel: Exclusion reaches on $M_{Z'}$ at 95% C.L. obtained from combination of all unpolarized processes $e^+e^- \to f\bar{f}$ at $\sqrt{s} = 0.5$ TeV and $\mathcal{L}_{\rm int} = 100 fb^{-1}$ in the case when E_6 models are assumed to be the "true" models while the the ones (SSM, LR, LRS, ALR and SM) are take as the tested models. Right panel: Similar, but for the polarized processes.

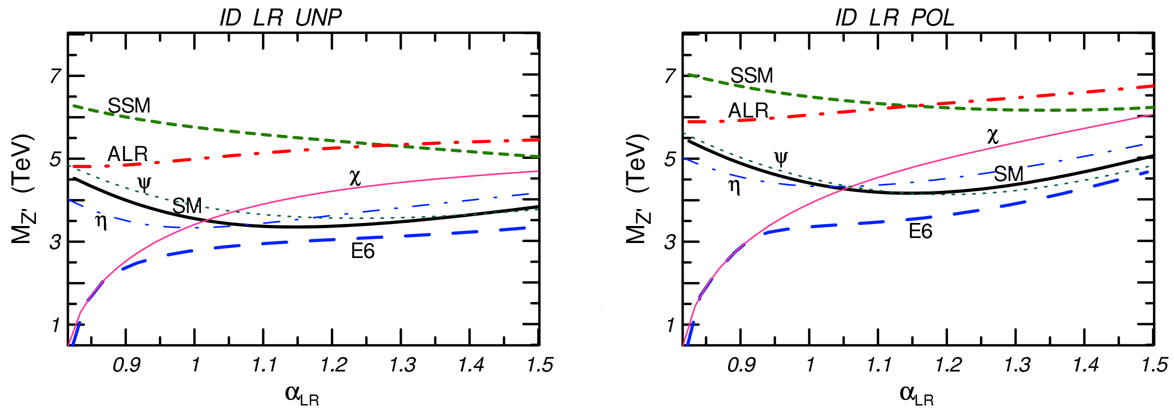

Figure 2. Same as Fig. 1 but for LR models.

As the observables $\mathcal{O}$ in (9) in this analysis we will use polarizing differential cross sections (2) and (4), $\mathcal{O} = {\rm d}\sigma(P^-, P^+)/{\rm d}z$.

According to the definition (9), one can introduce χ^2 function,

$$\chi^2 = \sum_f \chi_f^2, \tag{10}$$

where

$$\chi_f^2 = \sum_{\{P^-,\ P^+\}} \sum_{\rm bins} \left(\frac{\Delta \mathcal{O}_f^{\rm bin}}{\delta \mathcal{O}_f^{\rm bin}} \right)^2 . \tag{11}$$

Here $\Delta\mathcal{O}_f$ is defined in Eq. (9), and the uncertainty $\delta\mathcal{O}_f$ is referred to the E_6 model prediction of the observable $\mathcal{O}_f$. $\delta\mathcal{O}_f$ combines both the statistical and systematic uncertainties. The inequality that defines the confusion region between the two Z' models, E_6 and LR, at the 95% C.L. can be determined from

$$\chi^2(\mathcal{O}_f) \leq 3.84. \tag{12}$$

Fig. 1- 3 show the exclusion reaches on $M_{Z'}$ (95% C.L.) obtained from unpolarized and polarized processes $e^+e^- \to f\bar{f}$ for all set of Z' models. We find that irrespective of the availability of longitudinal polarization, an excellent distinction between E_6 and LR models can be obtained in the Z' mass range up to 2 TeV. In all cases, longitudinal polarization is valuable and would allow to extend the capability to distinguish between E_6 and LR models up to Z' masses of about 2.5 TeV.

4 Concluding remarks

In this paper, we examined the potential of the e^+e^- ILC to search for and distinguish between new neutral gauge bosons signals predicted within various classes of models with extended gauge sector in fermion pair

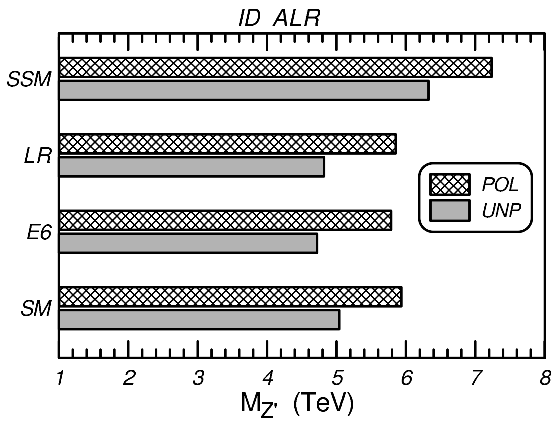

Figure 3. Exclusion reaches on $M_{Z'}$ at 95% C.L. obtained from combination of all unpolarized processes $e^+e^- \to f\bar{f}$ at $\sqrt{s} = 0.5$ TeV and $\mathcal{L}_{\rm int} = 100 fb^{-1}$ in the case when ALR model (left panel) and SSM model (right panel) are assumed to be the 'true' models while the rest ones are take as the tested models. In two cases the whole classes of E_6 model with $|\cos\beta| \leq 1$ and LR models with $\sqrt{2/3} \leq \alpha_{\rm LR} \leq \sqrt{2}$ are excluded.

production processes. The presented analysis is based on the polarized differential observables which provides higher sensitivity of the studied processes to Z' boson parameters with respect to the integrated observables. The discovery and identification reaches of the new neutral gauge bosons within the classes of E_6 and LR models and also ALR and SSM models were determined. In particular, it was shown that the polarized experiments at the electron-positron collider with the energy of 0.5 TeV and integrated luminosity of 100 fb^{-1} allow to identify the whole set of Z' models under consideration ($Z'_{\rm SSM}$, Z'_ψ, Z'_η, Z'_χ, $Z'_{\rm LRS}$ and $Z'_{\rm ALR}$) for $M_{Z'} < 6 \cdot \sqrt{s}$, and also, substantially improve the corresponding reaches obtained from unpolarized experiments.

Acknowledgements. This research has been partially supported by the Abdus Salam ICTP and the Byelorussian Republican Foundation for Fundamental Research.

References

[1] J. L. Hewett and T. G. Rizzo, Phys. Rept. **183** (1989) 193.
[2] A. A. Pankov and N. Paver, Phys. Rev. D **72**, 035012 (2005).
[3] A. A. Pankov and N. Paver, Eur. Phys. J. C **29**, 313 (2003).
[4] A. A. Pankov, N. Paver and A. V. Tsytrinov, Phys. Rev. D **73**, 115005 (2006).
[5] D. Y. Bardin, P. Christova, M. Jack, L. Kalinovskaya, A. Olchevski, S. Riemann and T. Riemann, Comput. Phys. Commun. **133**, 229 (2001).
[6] For reviews see, e.g., O. Nicrosini and L. Trentadue, in *Radiative Corrections for e^+e^- Collisions*, ed. J. H. Kühn 25 (Springer, Berlin, 1989), p. 25; in *QED Structure Functions, Ann Arbor, MI, 1989*, ed. G. Bonvicini, AIP Conf. Proc. No. 201 (AIP, New York, 1990), p. 12.
[7] A. Leike, Phys. Rept. **317** (1999) 143.

Proceedings of the International School-seminar
"New Physics and Quantum Chromodynamics at external Conditions", pp. 100 – 103,
3-6 May 2009, Dnipropetrovsk, Ukraine

DESCRIPTION OF NONEQUILIBRIUM BOSE GAS IN THE PRESENCE OF CONDENSATE

N. N. Bannikova[a], A. I. Sokolovsky[b]

Dnipropetrovsk National University, Dnipropetrovsk, Ukraine

The kinetics of spatially nonuniform Bose gas with the Bose-Einstein condensate is investigated on the basis of the Bogolyubov reduced description method. The system is described by the amplitude of the condensate wave function, the velocity of the condensate, and the distribution function of the Bogolyubov quasi-particles. A generalization of the Bogolyubov transformation for strong nonuniform states is proposed. A boundary condition for the Liouville equation is formulated, and an integral equation for the statistical operator of the gas is derived. The evolution equation for the parameters of reduced description is obtained, which gives a generalization of the Gross-Pitaevskii equation for the condensate in the presence of quasi-particles.

1 Introduction

Despite of many studies of non-equilibrium states of the Bose gas with the Bose-Einstein condensate (see, for example, [1, 2]), there are several aspects which have to be justified. It is concerned of set of parameters, which describe the system, and approach to description of spatially nonuniform states. Paper [1] proposed a solution of this problem, but it used for construction of kinetics of the system a complicated method of the ergodic relations [3]. Some states of the Bose gas with the condensate are described by the Gross-Pitaevskii equation (see, for example, [4]). However, there is a problem of derivation of this equation and investigation corrections to it [5].

In this work using ideas of paper [1] based on the Bogolyubov reduced description method (see, for example, [3]) we improve consideration of nonuniform kinetic states of the system. This allows to build integral equation for nonequilibrium statistical operator (SO) of the gas solvable in perturbation theory in interaction of particles and gradients of the reduced description parameters.

2 Basic equations of the theory

The kinetic stage of evolution of Bose gas of identical particles is studied in this work. The Hamiltonian of the gas has the form:

$$\hat{H} = \hat{H}_0 + \hat{\Phi},$$
$$\hat{H}_0 = \frac{\hbar^2}{2m}\int_V d^3x \frac{\partial\psi^+(x)}{\partial x_n}\frac{\partial\psi(x)}{\partial x_n}, \quad \hat{\Phi} = \frac{1}{2}\int_V d^3x \int d^3x' \Phi(|x'|)\psi^+(x+x')\psi^+(x)\psi(x)\psi(x+x'). \tag{1}$$

Here V is volume of the system, m is the particle mass, $\Phi(r)$ denotes the interaction potential, and $\psi(x), \psi^+(x)$ are the field operators.

Nonequilibrium states of the system are completely described by its SO $\rho(t)$, which satisfies the quantum Liouville equation

$$\dot{\rho}(t) = -\frac{i}{\hbar}[\hat{H}, \rho(t)]. \tag{2}$$

In the presence of the Bose-Einstein condensate the following value is not equal to zero

$$\psi(x,t) = \mathrm{Sp}\rho(t)\psi(x) \tag{3}$$

and it is called the condensate wave function. Local velocity of the condensate $\upsilon_n(x,t)$ is defined by formulae

$$\upsilon_n(x,t) = \frac{\hbar}{m}\frac{\partial\varphi(x,t)}{\partial x_n}, \quad \psi(x,t) = \eta(x,t)e^{i\varphi(x,t)}, \quad (\eta(x,t) > 0, 2\pi > \varphi(x,t) \geq 0). \tag{4}$$

Here weak nonuniform states are studied, in which amplitude $\eta(x,t)$ and velocity $\upsilon_n(x,t)$ depend on coordinates weak. Formulae (4) show that it is convenient to investigate states of the system in reference system of local rest of the condensate. The corresponding transition is made by unitary transformation

$$\rho_1(t) = U_1(\varphi(t))\rho(t)U_1^+(\varphi(t)), \quad U_1(\varphi)\psi(x)U_1^+(\varphi) = \psi(x)e^{\varphi(x)}. \tag{5}$$

e-mail: [a]bnndnu@mail.ru, [b]alexsokolovsky@mail.ru

Then the condensate is extracted with the transformation

$$\rho_2(t) = U_2(\eta(t))\rho_1(t)U_2^+(\eta(t)), \quad U_2(\eta)\psi(x)U_2^+(\eta) = \psi(x) + \eta(x). \tag{6}$$

On this basis perturbation theory in interaction is built with estimations $\Phi(r) \sim \lambda^2, \eta(x,t) \sim \lambda^{-1}$. It is equivalent to a resummation procedure in the framework of simple perturbation theory in interaction. Besides, after transformation (6) zero momentum Bose amplitudes a_0 can be omitted ($\psi(x) = V^{-1/2}\sum_k a_k e^{ikx}$). This allows to avoid difficulties in calculations based on the Wick-Bloch-de Dominicis theorem. Here we describe kinetic states of the Bose gas not only with the condensate wave function $\psi(x,t)$ but with distribution function of the the Bogolyubov quasi-particles too. Transition to quasi-particle picture is performed with unitary transformation

$$\rho_3(t) = U_3(\eta(t))\rho_2(t)U_3^+(\eta(t)), \quad U_3(\eta) = \exp\frac{1}{2}\int dx_1dx_2\chi(x_1 - x_2, \eta(x_1))\{\psi(x_1)\psi(x_2) - h.c.\} \tag{7}$$

($\chi(x,\eta)$ is an auxiliary function and $\chi(x,\eta)^* \equiv \chi(x,\eta), \chi(-x,\eta) \equiv \chi(x,\eta)$). This transformation is our generalization of the Bogolyubov one for the case of spatially nonuniform states. Then the Wigner distribution function of quasi-particles $f_k(x,t)$ is given by the formula $f_k(x,t) = \mathrm{Sp}\rho_3(t)\hat{f}_k(x)$, where $\hat{f}_k(x)$ is the corresponding Wigner operator. Further, our investigation of weak nonuniform states of the system is simplified in the Bar'yakhtar-Peletminsky picture of spatial dependance

$$\rho(x,t) = U_4(x)\rho_3(t)U_4^+(x), \quad U_4(x)\psi(x')U_4^+(x) = \psi(x' - x). \tag{8}$$

As a result of the previous definitions evolution equations for SO $\rho(x,t)$ and parameters $\xi_\mu(x,t) : \eta(x,t)$, $\upsilon_n(x,t)$, $f_k(x,t)$ can be written in the form

$$\dot{\rho}(x,t) = -\frac{i}{\hbar}[\hat{R}(x,\eta(t),\upsilon(t),\rho(t)),\rho(x,t)], \qquad \dot{\xi}_\mu(x,t) = M_\mu(x,\eta(t),\upsilon(t),\rho(t)), \tag{9}$$

where $\hat{R}(x,\eta,\upsilon,\rho)$, $M_\mu(x,\eta,\upsilon,\rho)$ are known functionals of $\eta(x), \upsilon_n(x), \rho(x)$.

Our investigation of nonequilibrium states of the Bose gas with condensate is based on the Bogolyubov functional hypothesis

$$\rho(x,t) \xrightarrow[t\gg\tau_0]{} \rho(x,\xi(t,\rho_0)) \qquad (\xi_\mu(x,t) \xrightarrow[t\gg\tau_0]{} \xi_\mu(x,t,\rho_0), \quad \rho_0 \equiv \rho(t=0)), \tag{10}$$

where τ_0 is a transition time to reduced description of the system with parameters $\xi_\mu(x,t,\rho_0)$. Here we introduced a special notation for the reduced description parameters at long times $\xi_\mu(x,t,\rho_0)$ and stressed that SO $\rho(x,\xi)$ does not depend on initial state ρ_0 of the gas. Functional hypothesis (10) and relations (9) give equations of the structure

$$\dot{\rho}(x,\xi(t,\rho_0)) = -\frac{i}{\hbar}[\hat{H}(x,\xi(t,\rho_0)),\rho(x,\xi(t,\rho_0))], \qquad \dot{\xi}_\mu(x,t,\rho_0) = L_\mu(x,\xi(t,\rho_0)) \qquad (t \gg \tau_0), \tag{11}$$

where $\hat{H}(x,\xi)$, $L_\mu(x,\xi)$ are functionals of $\xi_\mu(x)$ defined by SO $\rho(x,\xi)$

$$\hat{H}(x,\xi) \equiv \hat{R}(x,\eta,\upsilon,\rho(\xi)), \qquad L_\mu(x,\xi) \equiv M_\mu(x,\eta,\upsilon,\rho(\xi)).$$

In this paper functionals $\rho(x,\xi), L_\mu(c,\xi)$ are calculated in perturbation theory in gradients of the reduced description parameters

$$\partial^m\xi(x,t,\rho_0)/\partial x_{n_1}\ldots\partial x_{n_m} \sim g^m \qquad (g = r_0/L, \quad g \ll 1), \tag{12}$$

and interparticle interaction (small parameter λ). Here r_0 is radius of interparticle forces $\Phi(r)$ and L is characteristic size of spatial inhomogeneities in the system. Fourier transformation $\chi_k(\eta)$ of function $\chi(x,\eta)$ in the generalized Bogolyubov transformation (7) is defined by formulae

$$\hat{H}^{(0,0)}(x,\xi) = \hat{H}_B(\eta(x)) + \upsilon_n(x)\hat{P}_n, \qquad \hat{H}_B(\eta) \equiv \sum_k \varepsilon_k(\eta)a_k^+a_k, \quad \hat{P}_n \equiv \sum_k k_n\hbar a_k^+a_k \tag{13}$$

($A^{(m,n)}$ is of the order $g^m\lambda^n$ contribution to a value A). This demand leads to expressions

$$\tanh\chi_k = (\varepsilon_k + \alpha_k)/\beta_k, \qquad \varepsilon_k = \sqrt{\alpha_k^2 - \beta_k^2} \tag{14}$$

($\alpha_k = \varepsilon_k^0 + \beta_k, \quad \varepsilon_k^0 = (k\hbar)^2/2m, \quad \beta_k = \nu_k\eta^2, \quad \nu_k = \int dx\Phi(|x|)e^{ikx}$). Function $\varepsilon_k(\eta)$ is spectrum of the Bogolyubov quasi-particles.

Relations (11) show that SO $\rho(x,\xi)$ satisfies equation

$$\sum_{\mu}\int_V dx'\frac{\delta\rho(x,\xi)}{\delta\xi_\mu(x')}L_\mu(x',\xi)=-\frac{i}{\hbar}[\hat{H}(x,\xi),\rho(x,\xi)] \tag{15}$$

with addition conditions

$$\mathrm{Sp}\rho(x,\xi)\hat{f}_k(0)=f_k(x),\qquad \mathrm{Sp}\rho(x,\xi)a_k=0, \tag{16}$$

which are consequences of above definitions of the reduced description parameters $\xi_\mu(x,t,\rho_0)$.

According to Bogolyubov Liouville equation (15) has not unique solution and to obtain a proper its solution one need a boundary condition written in the terms of evolution of the system in physical direction of time. We obtain the necessary condition from the relation

$$U_B(\tau,\eta)\rho_0U_B^+(\tau,\eta)\xrightarrow[\tau\to+\infty]{}U_B(\tau,\eta)\rho_q(Z(\mathrm{Sp}\rho_0\hat{f}))U_B^+(\tau,\eta)\qquad (U_B(t,\eta)=e^{-\frac{i}{\hbar}t\hat{H}_B(\eta)},\quad \mathrm{Sp}\rho_0a_k=0), \tag{17}$$

which describes evolution of initial SO ρ_0 produced by the Bogolyubov Hamilton operator of quasi-particles $\hat{H}_B(\eta)$. Formulae of the type (17) are a consequence of the Bogolyubov principle of spatial weakening of correlations and were based in [3]. In fact this relation is the functional hypothesis (10) taken in the leading approximation of the perturbation theory. The right hand side of the relation (17) contains quasi-equilibrium SO of the gas

$$\rho_q(Y)=\exp\{F(Y)-V^{-1}\sum_k\int_V dxY_k(x)\hat{f}_k(x)\},\quad \mathrm{Sp}\rho_q(Y)=1;\qquad \mathrm{Sp}\rho_q(Z(f))\hat{f}_k(x)=f_k(x) \tag{18}$$

(the last formula defines functional $Z_k(x,f)$). The initial condition is obtained from (17) after substitution $\rho_0\to\rho(x=0,\xi),\eta\to\eta(x)$. Transformation of the result to the Bar'yakhtar-Peletminsky picture (8) gives its final form

$$U_B(\tau,\eta(x))\rho(x,\xi)U_B^+(\tau,\eta(x))\xrightarrow[\tau\to+\infty]{}U_B(\tau,\eta(x))\rho_q(x,Z(f))U_B^+(\tau,\eta(x)). \tag{19}$$

Here $\rho_q(x,Y)$ is quasi-equilibrium SO in the mentioned picture and for big volume of the system V

$$\rho_q(x,Y)=\exp\{F(x,Y)-V^{-1}\sum_k\int_V dx'Y_k(x+x')\hat{f}_k(x')\},\quad \mathrm{Sp}\rho_q(x,Y)=1;\quad \mathrm{Sp}\rho_q(x,Z(f))\hat{f}_k(0)=f_k(x) \tag{20}$$

(normalization function $F(x,Y)$ depend on x). Boundary condition (19)can be rewritten in a more simple form

$$\lim_{\tau\to+\infty}U_B(\tau,\eta(x))\{\rho(x,\xi)-\rho_q(x,Z(f))\}U_B^+(\tau,\eta(x))=0. \tag{21}$$

Using this relation on the basis of the Liouville equation (15) we obtain the following integral equation for SO $\rho(x,\xi)$

$$\rho(x,\xi)=\rho_q(x,Z(f))+\int_0^{+\infty}d\tau U_B(\tau,\eta(x))\left\{\frac{i}{\hbar}[\rho_q(x,Z(f)),\hat{H}_B(\eta(x))]+\right.$$
$$\left.+\frac{i}{\hbar}[\rho(x,\xi),\hat{H}(x,\xi)-\hat{H}_B(\eta(x))]-\sum_\mu\int dx'\frac{\delta\rho(x,\xi)}{\delta\xi_\mu(x')}L_\mu(x',\xi)\right\}U_B^+(\tau,\eta(x)). \tag{22}$$

Integral equation (22) is solvable in the perturbation theory in gradients g and interaction λ. The leading contribution to SO $\rho(x,\xi)$ has the form

$$\rho^{(0,0)}(x,\xi)=w(f(x)),\quad w(f)\equiv\exp\{F(f)-\sum_k Z_k(f)a_k^+a_k\};\qquad \mathrm{Sp}w(f)=1,\quad \mathrm{Sp}w(f)a_k^+a_k=f_k. \tag{23}$$

Therefore, all further calculations can be fulfilled with the Wick-Bloch-de Dominicis theorem.

3 Generalized Gross-Pitaevskii equation

Developed theory gives evolution equations for variables $\eta(x,t,\rho_0),\upsilon_n(x,t,\rho_0),f_k(x,t,\rho)$ and for asymptotic value $\varphi(x,t,\rho_0)$ of the phase $\varphi(x,t)$ of the condensate wave function $\psi(x,t)$. So, we obtained a close set of equations for distribution function $f_k(x,t,\rho)$ of quasi-particles and for asymptotic value of the condensate wave function $\psi(x,t,\rho_0)$. The Gross-Pitaevskii equational is closed equation for the condensate wave function (see, for example, [4]). Therefore, our set of equations is a generalization of this equation for the case, in which in the system there are quasi-particles in kinetic state. Our consideration confirm results of our paper [1] and gives new possibilities for investigation of the higher order contribution in gradients. The results will be discussed in another paper.

Here we consider the case of absence of quasi-particles, in which $f_k(x,t,\rho_0)=0$, in more detail. It is assumed for simplicity that small parameters of the developed theory are equal $g=\lambda$. This restriction is not serious because gradients of reduced description parameters decrease with time. In the terms of amplitude and phase of the condensate wave function our generalized Gross-Pitaevskii equations have the form:

$$\dot\eta = -\upsilon_n \frac{\partial\eta}{\partial x_n} + \left\{ \frac{1}{2\eta}\left(\frac{\eta}{2}\frac{\partial}{\partial\eta} - 1\right) n_0(\eta) - \frac{\eta}{2} \right\} \frac{\partial\upsilon_n}{\partial x_n},$$

$$\hbar\dot\varphi = -m\mu_0(\eta) - \frac{m\upsilon^2}{2} + \frac{\hbar^2\Delta\eta}{2m\eta} - a\frac{\partial}{\partial x_n}\left(\eta\frac{\partial\eta}{\partial x_n}\right), \tag{24}$$

where terms of the order λ^3 are omitted ($a \equiv \frac{4\pi}{3}\int_0^{+\infty} dr r^4 \Phi(r)$). These equations contain density of particle number $n_0(\eta)$ and chemical potential $\mu_0(\eta)$ of the gas at $T=0$ as a function of η

$$n_0(\eta) = \eta^2 + \frac{1}{2}\int \frac{d^3k}{(2\pi)^3}\frac{\alpha_k - \varepsilon_k}{\varepsilon_k} + O(\lambda^2), \qquad \mu_0(\eta)m = \nu_0 n_0 + \frac{1}{4\eta}\frac{\partial}{\partial\eta}\int \frac{d^3k}{(2\pi)^3}(\varepsilon_k - \alpha_k) + O(\lambda^4). \tag{25}$$

According to [4] usual Gross-Pitaevskii equations can be obtained from (25) in approximation $n_0(\eta)=\eta^2, \mu(\eta) = \nu_0\eta^2/m, a=0$. Our corrections are a result of a consequent investigation of dynamics of the Bose gas on the basis of the reduced description method.

The rigorous mathematical derivation of the Gross-Pitaevskii equations was presented in [5], but without any corrections to usual equations.

4 Conclusion

In this work kinetic theory of the Bose gas in the presence of the Bose-Einstein condensate was discussed on the basis of the Bogolyubov reduced description method (functional hypothesis). The condensate wave function and distribution of the Bogolyubov quasi-particles were chosen as a reduced description parameters. The Bogolyubov transformation, which introduces these quasi-particles, was generalized for spatially nonuniform states. This allowed to formulate a boundary condition to the Liouville equation consistent with the Bar'yakhtar-Peletminsky picture of spatial dependance of statistical operator. The boundary condition used to transform the Liouville equation into integral equation solvable in a perturbation theory in small interaction of the Bose particles and gradients of the reduced description parameters. The obtained results simplified and in some places corrected results of paper [1]. Corrections to the Gross-Pitaevskii equation for the condensate wave function are found, which take into account presence of the quasi-particles and effects of the rigorous dynamics of the system. On this basis the waves and vortexes in the condensate at zero and finite temperatures will be studied in another paper. The suggested method can be used as a basis for further investigations of non-equilibrium processes in other quantum systems, in particular, in helium II.

Acknowledgements. The research made in this work was supported by the State Foundation for Fundamental Research of Ukraine under project No. 25.2/102

References

[1] Peletminsky S.V., Sokolovsky A.I., Shchelokov V.S., Theor. Math. Phys. **30**, 57-72 (1977) (in Russian).
[2] Walser R., Williams J., Cooper J. and Holland M., Phys. Rev. **A 59**, 3878-3889 (1999).
[3] Akhiezer A.I., Peletminsky S.V. *Methods of Statistical Physics*, Oxford: Pergamon Press, 1981.
[4] Landau L.D. and Lifshitz E.M. *Statistical Physics. Part 2*, Oxford: Pergamon Press, 1980.
[5] Lieb E. H., Seiringer R., Yngvason J., Phys. Rev. **A 61**, 043602 (2000).

Proceedings of the International School-seminar
"New Physics and Quantum Chromodynamics at external Conditions", pp. 104 – 107,
3-6 May 2009, Dnipropetrovsk, Ukraine

CLASSICAL STOCHASTIC DYNAMICS AND EXTENDED $N = 4$ SUPERSYMMETRIC QUANTUM MECHANICS

V.P. Berezovoj[a], G.I. Ivashkevych[b]

A.I.Akhiezer Institute for Theoretical Physics of National Scientific Center "Kharkov Institute of Physics and Technology", Kharkov, Ukraine

This work is aimed at demonstrating the possibility to construct new exactly-solvable stochastic systems by use of the extended supersymmetric quantum mechanics ($N = 4$ $SUSY$ QM) formalism. A feature of the proposed approach consists in $N = 4$ $SUSY$ QM the fact that probability densities and so obtained new potentials, which enter the Langevin equation, have a parametric freedom. The latter allows one to change the potentials form without changing the temporal behavior of the dispersion function.

1 $N = 4$ $SUSY$ QM

Let us get started with a brief discussion of the $N = 4$ $SUSY$ QM structure and constructing within its framework isospectral Hamiltonians [1, 2]. The $N = 4$ $SUSY$ QM Hamiltonian has the following form:

$$H_{\sigma_1,\sigma_2} = \frac{1}{2}(p^2 + V_2^2(x) + \sigma_3^{(1)} V_2^1(x)) \equiv \frac{1}{2}(p^2 + V_1^2(x) + \sigma_3^{(2)} V_1^1(x)) \tag{1}$$

where we have introduced ($\hbar = m = 1$):

$$V_i(x) = W'(x) + \frac{1}{2}\sigma_3^{(i)} \frac{W''(x)}{W'(x)} \tag{2}$$

$W(x)$ is a superpotential, $\sigma_3^{(i)}$ are matrices which commute to each other and have the eigenvalues ± 1

$$\sigma_3^{(1)} = \sigma_3 \otimes 1, \sigma_3^{(2)} = 1 \otimes \sigma_3 \tag{3}$$

Supercharges Q_i of the extended supersymmetric mechanics form the algebra:

$$\{Q_i, \bar{Q}_k\} = 2\delta_{ik} H; \{Q_i, Q_k\} = 0; i, k = 1, 2 \tag{4}$$

And admit the form:

$$Q_i = \sigma_-^{(i)}(p + iV^{(i+1)}(x)),\ \bar{Q}_i = \sigma_+^{(i)}(p - iV^{(i+1)}(x)) \tag{5}$$

Constructing isospectral Hamiltonians within the $N = 4$ $SUSY$ QM is based on the fact that four Hamiltonians cast into one supermultiplet. Let us take as an initial one of the Hamiltonians

$$H_{\sigma_1,\sigma_2} = \tfrac{1}{2}(p - i\sigma_1 V_{\sigma_2}(x))(p + i\sigma_1 V_{\sigma_2}(x)) + \varepsilon \equiv \tfrac{1}{2}(p - i\sigma_2 V_{\sigma_1}(x))(p + i\sigma_2 V_{\sigma_1}(x)) + \varepsilon \tag{6}$$

where

$$V_{\sigma_2}(x) = W'(x) + \frac{1}{2}\sigma_2 W''(x)/W'(x), \tag{7}$$

and ε is the so-called factorization energy. In what follows the energy level will be counted from ε.

Consider an auxiliary equation:

$$H_{\sigma_1}^{\sigma_2}\varphi(x) = \varepsilon\varphi(x) \tag{8}$$

Its general solution $\varphi(x, \varepsilon, c)$ is the linear combination of two independent solutions $\varphi^{(1)}(x, \varepsilon)$ and $\varphi^{(2)}(x, \varepsilon)$. The expression for $W(x)$ in terms of $\varphi(x, \varepsilon, c)$ has the from of:

$$W(x) = \frac{\sigma_1}{2} \ln \left(1 + \lambda \int_{x_i}^{x} dx' \left[\varphi(x', \varepsilon, c)\right]^{2\sigma_1\sigma_2}\right) \tag{9}$$

where λ, x_i are two new parameters.

e-mail: [a]berezovoj@kipt.kharkov.ua, [b]giv@kipt.kharkov.ua

For definiteness we will consider $\sigma_1 = \sigma_2 = -1$. Then, relations in the above can be presented in the form of:

$$H_+^- = H_-^- - \frac{d^2}{dx^2}\ln\varphi(x,\varepsilon,c),\ \ \psi_+^-(x,E) = \frac{1}{\sqrt{2(E-\varepsilon)}}\frac{W\left\{\varphi(x,\varepsilon,c)\psi_-^-(x,E)\right\}}{\varphi(x,\varepsilon,c)} \tag{10}$$

$$\begin{gathered} H_+^+ = H_-^- - \tfrac{d^2}{dx^2}\ln(1+\lambda\int\limits_{x_i}^{x}dx'\,[\varphi(x',\varepsilon,c)]^2) \\ \psi_+^+(x,E) = \psi_-^-(x,E) - \frac{\lambda\varphi(x,\varepsilon,c)}{1+\lambda\int\limits_{x_i}^{x}dx'[\varphi(x',\varepsilon,c)]^2}\int\limits_{x_i}^{x}dx'^2\varphi(x',\varepsilon,c)\psi_-^-(x',E) \end{gathered} \tag{11}$$

In the case when $\varphi(x,\varepsilon,c)$ is a ground state eigenfunction of the initial Hamiltonian, wave function of ground state H_+^+ has a form:

$$\psi_+^+(x,E_0) = N_0\frac{\varphi(x,\varepsilon)}{1+\lambda\int\limits_{x_i}^{x}dx'\,[\varphi(x',\varepsilon)]^2} \tag{12}$$

2 Construction of stochastic models associated with $N = 4$ $SUSY$ QM.

The Fokker-Plank equation is equivalent to the Langevin equation, however the Fokker-Plank is used more widely in physics, since it is formulated in more common for the probability density $m_t^{\pm}(x,x_0)$ language. The Fokker-Plank equation takes the form [3, 4]:

$$\begin{gathered} \tfrac{\partial}{\partial t}m_t^{\pm}(x,x_0) = \tfrac{D}{2}\tfrac{\partial^2}{\partial x^2}m_t^{\pm}(x,x_0) \pm \tfrac{\partial}{\partial x}\Phi(x)m_t^{\pm}(x,x_0) \\ m_{t=0}^{\pm}(x,x_0) = \langle\delta(x-x_0)\rangle\,;\ U_{\pm}(x) = \mp\int\limits_0^x dz\Phi(z) \end{gathered} \tag{13}$$

with $U_{\pm}(x)$ to be the potential entering the Lagevin equation. The Fokker-Plank equation describes the stochastic dynamics of particles in potentials U_+ and $U_- = -U_+$. Substituting

$$m_t^{\pm}(x,x_0) = \exp\left\{-\left[U_{\pm}(x) - U_{\pm}(x_0)\right]/D\right\}K_{\pm}(x,t) \tag{14}$$

the Fokker-Plank equation transforms into the Schrodinger equation with imagine time:

$$\begin{gathered} -D\tfrac{\partial}{\partial t}K_{\pm}(x,t) = \left\{-\tfrac{D^2}{2}\tfrac{\partial^2}{\partial x^2} + \tfrac{1}{2}\left[\Phi^2(x) \pm D\Phi'(x)\right]\right\}K_{\pm}(x,t) = H_{\pm}K_{\pm}(x,t) \\ K_{\pm}(x,t) = \langle x\left|\exp\left\{-tH_{\pm}/D\right\}\right|x_0\rangle \end{gathered} \tag{15}$$

in which the diffusion constant can be treated as the "Plank" constant. As in the previous case, let us consider H_-^- to the initial Hamiltonian.

$$\begin{gathered} H_-^- = \tfrac{1}{2}\left[p^2 + \left(V_2^{(-)}(x)\right)^2 - DV_2^{(-)\prime}(x)\right] \\ V_2^{(-)}(x) = W'(x) - \tfrac{D}{2}\tfrac{d}{dx}\ln|W'(x)| \equiv -D\tfrac{d}{dx}\ln\varphi(x,\varepsilon,c) \end{gathered} \tag{16}$$

The force entering the corresponding Langevin equation:

$$F(x) = -\tfrac{dU_-^-(x)}{dx} = D\tfrac{d}{dx}\ln\varphi(x,\varepsilon,c),\ \ U_-^-(x) = -D\ln\varphi(x,\varepsilon,c) \tag{17}$$

Then, in the same to the $N = 2$ $SUSY$ QM way, there is the relation $U_+^- = -U_-^-$. It directly follows from the fact that H_+^- is obtained from H_-^- with changing $V_2^{(-)}(x)$ to $-V_2^{(-)}(x)$.

Hence, there is the relation between the stochastic dynamics in a potential and that of in an inverse potential.

Further consideration is based on an important property of $N = 4$ $SUSY$ QM, which consists in having the symmetry of $H_{\sigma_1}^{\sigma_2}$ under $\sigma_1 \leftrightarrow \sigma_2$. It leads to:

$$H_+^-(x,p) = \frac{1}{2}\bar{Q}_1^{(-)}Q_1^{(-)} \equiv \frac{1}{2}Q_2^{(+)}\bar{Q}_2^{(+)} = H_-^+(x,p) \tag{18}$$

If the first equation points to the expression of $H^{(+)}$ in terms of $Q_1(\bar{Q}_1)$, the second one is $H^{(-)}$ in terms of supercharges $Q_2(\bar{Q}_2)$. Though the supercharges of $H^{(+)}$ and $H^{(-)}$ are essentially different:

$$\begin{gathered} H_+^-(x,p) = \tfrac{1}{2}Q_2^{(+)}\bar{Q}_2^{(+)} = \tfrac{1}{2}\left[p^2 + \left(V_1^{(+)}(x)\right)^2 - DV_1^{(+)\prime}(x)\right] \\ V_1^{(+)}(x) = \tfrac{d}{dx}(W + \tfrac{D}{2}\ln|W'(x)|) \equiv D\tfrac{d}{dx}\ln\left|\frac{\varphi(x,\varepsilon,c)}{1+\lambda\int\limits_{x_i}^{x}dx'[\varphi(x',\varepsilon,c)]^2}\right| = \tfrac{dU_-^+}{dx} \end{gathered} \tag{19}$$

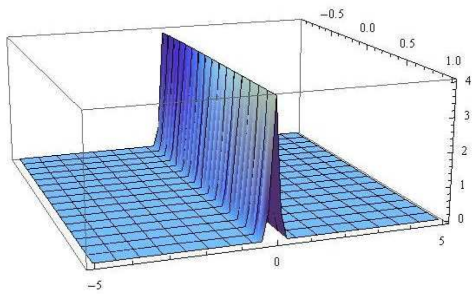

Figure 1. Dependence of $m^+_{+,t}(x,0)$ on x and λ at $z=1$.

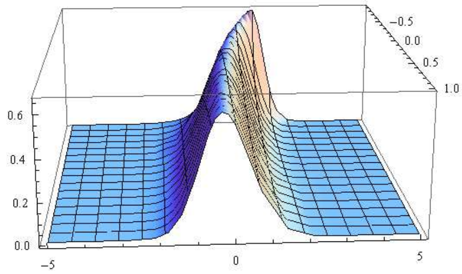

Figure 2. Dependence of $m^+_{+,t}(x,0)$ on x and λ at $z=0$.

From equations (19) follows that at the quantum level the Hamiltonians H^+_- and H^-_+ possesses the same spectrum and wave functions, thus the corresponding to them $K(x,t)$ are the same. At the same time the corresponding to these Hamiltonians stochastic models are described by essentially different potentials, so their $m_t(x,x_0)$ are different. Further, the potential $U^+_-(x)$ has a nontrivial parametric dependence on λ, that corresponds to having the family of stochastic models, the probability densities of which have the same temporal dependence. Having the parametric freedom allows one to change the potential form that is unexpected in the case. In particular, as it has been noticed in literature, physical quantities such as the time of passing a peak of potentials depend essentially on local changes of the potential barrier. Looking at H^+_+, we note that it follows from H^+_- with changing $V^{(+)}_1(x)$ to $-V^{(+)}_1(x)$, as it also takes place in $N=2$ supersymmetry. In its turn the potential of this stochastic system is $U^+_+(x)=-U^+_-(x)$. The wave functions which are used to calculate $K^+_+(x,t)$ have the form of (11) in the case.

Getting back to the parametric dependence of $m^+_{-,t}(x,x_0)$ and $m^+_{+,t}(x,x_0)$, it should be noted that the normalisation condition leads to fixing the λ. The same does not happen in the case of $m^+_{+,t}(x,x_0)$, if instead of $\varphi(x,\varepsilon,c)$ we will use the normed wave function (say, the ground state wave function) of the initial Hamiltonian H^-_-. From definition:

$$m^+_{+,t}(x,x_0)=\frac{\varphi(x,\varepsilon,c)}{1+\lambda\int\limits_{-\infty}^{x}dx'\,[\varphi(x',\varepsilon,c)]^2}\times\frac{1+\lambda\int\limits_{-\infty}^{x_0}dx'\,[\varphi(x',\varepsilon,c)]^2}{\varphi(x,\varepsilon,c)}\sum_{n=0}e^{-\frac{E_n}{D}t}\psi^+_+(x,E_n)\psi^+_+(x_0,E_n) \tag{20}$$

in view of eq. (1.15) it follows that

$$\int\limits_{-\infty}^{\infty}dx m^+_{+,t}(x,x_0)=\int\limits_{-\infty}^{\infty}dx m^+_{+,t=0}(x,x_0)=(\lambda+1)\int\limits_{-\infty}^{\infty}dx\left[\frac{\varphi(x,\varepsilon,c)}{1+\lambda\int\limits_{-\infty}^{x}dx'\,[\varphi(x',\varepsilon,c)]^2}\right]^2=1 \tag{21}$$

It means that the unique restriction to λ is $\lambda\neq-1$, that as it was early noticed corresponds to the absence of singularities at the quantum-mechanical level. It is hard to make an analogous study for $m^+_{-,t}(x,x_0)$ in a general case. However, for the Ornstein-Uhlenbeck process the normalisation condition does not remove the parametric ambiguity at the definite choice of x_0.

3 The Ornstein-Uhlenbeck process

Let us demonstrate the proposed scheme of getting new stochastic models with the well-known Ornstein-Uhlenbeck process. The Fokker-Plank equation which describes the Ornstein-Uhlenbeck leads to a quantum-mechanical potential with the harmonic oscillator potential. The factorization energy coincides with the ground state energy in the case with the harmonic oscillator potential.

$$\left(\frac{p^2}{2}+\frac{\omega^2}{2}x^2\right)\varphi(x,\varepsilon)=\varepsilon\varphi(x,\varepsilon) \tag{22}$$

$$E_n = nD\omega, \psi_-^-(x, E_n) = (\omega/D)^{1/2} H_n(x\sqrt{\omega/D})e^{-\frac{\omega}{D}x^2}, n = 0, 1, ... \tag{23}$$

where $\varepsilon = \frac{D\omega}{2}$ (the energy counts from ε). The potential entering the Langevin equation:

$$U_-^-(x) = \omega x^2/2 = D\xi^2/2,\ \xi = \sqrt{\omega/D}x. \tag{24}$$

For the Ornstein-Uhlenbeck process it is easy to see that, at least for the case of $x_0 = 0$, the normalized condition does also not fix the value of λ. For an arbitrary stochastic process the same is hard to prove. Calculating $m_{+t}^+(\xi, \xi_0)$ we use the wave functions (11) . First of all it has to be pointed out of having the equilibrium value of $m_{+,t\to\infty}^+(\xi, \xi_0)$:

$$m_{+,t\to\infty}^+(\xi, \xi_0) = (\lambda + 1)\left(\frac{\omega}{\pi D}\right)^{1/2} \frac{e^{-\xi^2}}{(1 + \lambda/2 + \lambda/2\Phi(\xi))^2},\ \Phi(\xi) = \frac{2}{\sqrt{\pi}}\int_0^{\xi} dte^{-t^2} \tag{25}$$

As it was mentioned in the above, the normalized condition of the probability density does not remove the λ - parametric freedom. Using the wave functions $\Psi_+^+(x, E_n)$, which are expressed in terms of $\Psi_-^-(x, E_n)$, after simple but tedious calculations we get the expression for the probability density:

$$\begin{array}{l} m_{+t}^+(\xi, \xi_0) = \lambda \left(\frac{\omega}{\pi D}\right)^{1/2} \frac{e^{-\xi^2}}{(1+\lambda/2+\lambda/2\Phi(\xi))^2} + \frac{1}{2}\left(\frac{\omega}{D}\right)^{1/2} \frac{d}{d\xi}\frac{1}{1+\lambda/2+\lambda/2\Phi(\xi)} \times \\ \left[(1 + \lambda/2 + \lambda/2\Phi(\kappa))\left(1 + \Phi\left(\frac{\xi-\kappa z}{\sqrt{1-z^2}}\right)\right) - \frac{\lambda}{\sqrt{\pi}}\int\limits_{-\infty}^{\xi} d\xi' e^{-\xi'^2}\left[1 + \Phi\left(\frac{\kappa-\xi' z}{\sqrt{1-z^2}}\right)\right]\right] \end{array} \tag{26}$$

The form of $m_{+,t}^+(\zeta, \zeta_0)$ can be viewed from the following plots under the following parametrization $\zeta_0 = 0$, $z = e^{-\omega t}$.

Fig.(1,2) shows results of numerical evaluation of the dependence of $m_{+,t}^+(x, 0)$ on x and λ at different z. Thus, when $z = 1$ $m_{+,t}^+(x, 0)$ has well pronounced δ-like shape in concordance with initial conditions. With decreasing of z $m_{+,t}^+(x, 0)$ changes its shape and this changes are especially significant at $\lambda \to -1$. In this case the shift of the maximum of probability density occurs, as well as emergence of substantial assymetry.

4 Conclusions

The described procedure of the obtaining of exactly-solved stochstic models allows to use the results of numerous works concerning exactly-solved as well as quasi-exaxtly-solved quantum mechanical problems. The distinctive feature of this approach is an existence of parametric freedom in potentials, that enter the in the Langevin equation, as well as in transitional probability densities. This situation takes place at any modification in the spectrum of initial Hamiltonian. It's important to mention, that normalization condition for $m_{-,t}^+(x, x_0)$, most probably, could be fulfilled only when certain relation between x_0 and λ exists. This means that stochastic model with $U_-^+(x)$ is "bad". At the same time $m_{+,t}^+(x, x_0)$ is a "good" transitional probability density, which preserve the parametric freedom.

As is well known, [7, 8], local modifications of the shape of the potential in Langevin equation could lead to substantial changes of such quantities as times of the passing through barrier and timeof live in metastable state. Although this quantities are mainly determined by first non-zero energy level in spectrum of $H_{\sigma_1}^{\sigma_2}$, the λ-freedom allows for significant variations of their values. This especially important for potentials with several local minima, which could emerge when constructing isospectral Hamiltonians with factorization energy $\varepsilon < E_0$. In this case potentials $U_{\sigma_1}^{\sigma_2}$ with two wells emerge, symmetric, as well as assymetric and λ-freedom reveals in substantial modification of the shape and height of the barriers, what leads to changes in the rate of the inter-well transitions.

Acknowledgements. Work is supported by INTAS (2006-7928) and NASU-RFFR #38/50-2008 grants.

References

[1] V.P.Berezovoj, A.I.Pashnev, Teor.Mat.Fiz., 74, 392 (1988) (Russian).
[2] V.P.Berezovoj, A.I.Pashnev, Z.Phys. C 51, 525 (1991) 525.
[3] H.Risken, The Fokker-Plank equation, Springer, Berlin, 1989.
[4] G.Junker, Supersymmetric Methods in Quantum and Statistical Physics, Springer, Berlin, 1996.
[5] M.O.Hongler and W.M.Zheng, J.Stat.Phys., 29, 317 (1982).
[6] M.O.Hongler and W.M.Zheng, J.Math.Phys., 24, 336 (1983).
[7] A.M.Berezhkovkii, P.Talkner, J.Emnnerich, V.Yu.Zilserman, J.Chem.Phys., 105, 19890 (1996).
[8] A.N.Malachov, Chaos, 7, 488 (1997).

Proceedings of the International School-seminar
"New Physics and Quantum Chromodynamics at external Conditions", pp. 108 – 110,
3-6 May 2009, Dnipropetrovsk, Ukraine

RENORMALIZATION GROUP APPROACH FOR 2+1D U(1) LATTICE GAUGE THEORY IN FINITE TEMPERATURE LIMIT

O. A. Borisenko[a], V. O. Chelnokov[b]

N.N. Bogolyubov Institute for Theoretical Physics, Kiev, Ukraine

Renormalization group equations describing critical behaviour in the vicinity of the deconfinement phase transition in $3d$ $U(1)$ lattice gauge theory at finite temperature are obtained. These equations are used to check the validity of the Svetitsky-Yaffe conjecture regarding the critical behaviour of lattice $U(1)$ model.

1 Introduction

At high temperatures the partition function of the $3d$ $U(1)$ lattice gauge theory (LGT) coincides in the leading order of the high-temperature expansion with that of $2d$ XY model [1]. The latter is known to possess the Beresinsky-Kosterlitz-Thouless (BKT) phase tranisition of the infinite order. Moreover, at finite temperatures the $3d$ $U(1)$ LGT is invariant under global $U(1)$ rotations acting in a given time-slice of the three-dimensional lattice. These observations led Svetitsky and Yaffe to conjecture that the finite-temperature phase transition in $3d$ $U(1)$ model might belong to the BKT universality class [2]. That means that near the critical point the correlation function between the Polyakov loops should decrease like

$$\Gamma(R) \asymp \frac{1}{R^{\eta(T)}} \ , \tag{1}$$

for $\beta \geq \beta_c$, and

$$\Gamma(R) \asymp \exp\left[-\frac{R}{\xi(t)}\right], \ t = \frac{\beta_c}{\beta} - 1, \ \xi(t) \sim e^{bt^{-\nu}} \ , \tag{2}$$

for $\beta < \beta_c$. The critical indices $\eta(T_c)$ and ν for the XY model are known: $\eta(T_c) = 1/4, \ \nu = 1/2$. Thus, if the Svetitsky-Yaffe conjecture holds for $3d$ U(1) LGT, its critical indices should coincide with those of the XY model.

There seems to be no rigorous analytical proof that those indices do coincide. Recent numerical simulations of Ref.[3] indicate that this is the case, at least at strong coupling region ($\beta_s = 0$). The question remains open if β_s is non-vanishing. Here we attempt to study this problem analytically by constructing renormalization group equations perturbatively in β_s/β_t.

2 Definition of the model

As usually we define compact gauge field variables $\omega_l \in [0; 2\pi]$ on links of an anisotropic $3d$ lattice $\Lambda = L^2 \times N_t$. The anisotropic couplings are defined by

$$\beta_t = \frac{1}{g^2 a_t} \ , \quad \beta_s = \frac{\xi}{g^2 a_s} \ = \ \beta_t \ \xi^2 \ , \tag{3}$$

where a_s, a_t are lattice spacings in the temporal and spatial directions respectively, $\xi = \frac{a_t}{a_s}$, g^2 is a continnum coupling constant. The finite temperature limit is constructed as

$$\xi \to 0, \qquad N_t, L \to 0, \qquad a_t N_t = \beta \ , \tag{4}$$

where β is inverse temperature.

Now we can write down the partition function for the $3d$ $U(1)$ LGT as

$$Z = \int_0^{2\pi} \prod_l \frac{d\omega_l}{2\pi} \ \exp\left[\beta_s \sum_{p_s} \cos\omega(p_s) + \beta_t \sum_{p_t} \cos\omega(p_t)\right] . \tag{5}$$

Here, p_s and p_t are space- and time-oriented plaquettes, $w(p)$ is a plaquette angle defined in a standard way.

Presented by V. O. Chelnokov, e-mail: [a]oleg@bitp.kiev.ua, [b]yyyaduren@rambler.ru

3 An effective $2d$ sine-Gordon model

First, we perform duality transformations which are well-known in the context of the isotropic model. For the anisotropic model we find the dual representation for the partition function of the form

$$Z = \sum_{r(x)=-\infty}^{\infty} \prod_x \prod_{n=0}^{2} I_{r(x)-r(x+e_n)}(\beta_n) \ , \tag{6}$$

where $I_r(x)$ is the modified Bessel function.

Let us now redefine the variables in (6) in the following way

$$r(x,t) = r(x) + \sum_{\tau=1}^{t} \omega(x,\tau) \quad , \quad (\omega(x,\tau) = r(x,\tau) - r(x,\tau-1)) \ . \tag{7}$$

Here and below x contains only spatial coordinates. Temporal coordinate dependence is written explicitly.

Replacing the Bessel functions with their asymptotics at large β_t we obtain after some algebraic manipulations and integration over $\omega(x,\tau)$ the following representation for the partition function

$$Z = \sum_{r(x)=-\infty}^{\infty} Q(r(x)) \exp\left[-\frac{1}{2\beta_t}\sum_{x,n}(r(x)-r(x+n))^2\right] \ , \tag{8}$$

where notations have been used

$$Q(r(x)) = \prod_{K_n=0}^{L-1} \int_{-\infty}^{\infty} \prod_{n,t} dS_n(K,t) \exp\left\{-\frac{1}{2} S_n(K,t) A_{n,n'}(K;t,t') S_{n'}(-K,t') - i h_n(K) \sum_{t=2}^{N_t} S_n(K,t)\right\} \ ,$$

$$A_{n,n'}(K;t,t') = \beta_t \delta_{n,n'} \delta_{t,t'} + \beta_s b_1(\beta_s N_t) \nu(t,t') \left(1-\exp[iK_n]\right)\left(1-\exp[-iK_{n'}]\right) \ ,$$

$$\nu(t,t') = \min(t,t') - 1 - \frac{1}{N_t}(t-1)(t'-1) \ ,$$

$$b_1(x) = \frac{I_1(x)}{I_0(x)}, \ h_n(K) = \frac{1}{L}\sum_x (r(x)-r(x+e_n)) \exp[iKx] \ .$$

Integration over the $S_n(K,t)$ variables leads to the result which we present in the form

$$Z = \sum_{r(x)=-\infty}^{\infty} \exp\left[-\frac{1}{2} r(x) G(x,x')^{-1} r(x')\right] \ . \tag{9}$$

Here we have introduced the Green function $G(x,x')^{-1}$ given by

$$G(x,x')^{-1} = \sum_{n,n'} \left[B_{n,n'}(x,x') - B_{n,n'}(x-e_n,x') - B_{n,n'}(x,x'-e_{n'} + B_{n,n'}(x-e_n,x'-e_{n'}))\right] \ ,$$

$$B_{n,n'}(x,x') = \frac{1}{\beta_t}\delta_{n,n'}\delta_{x,x'} + \frac{1}{L^2}\sum_K \exp[iK(x-x')] \sum_{t,t'=2}^{N_t} A^{-1}_{n,n'}(K;t,t') \ . \tag{10}$$

Expanding the matrix $A^{-1}_{n,n'}$ up to the second order in $\frac{\beta_s}{\beta_t}$ we find

$$G(x,x')^{-1} = 2g^2\beta\left(\Delta - \frac{1}{6}\frac{\beta^3}{g^2 a_s^2}\Delta^2 + \frac{1}{120}\frac{\beta^6}{g^4 a_s^4}\Delta^3\right) \ . \tag{11}$$

with Δ being a two-dimensional Laplace operator.

To compute the partition function in (9) we use the Poisson summation formula. The result is a two-dimensional vortex model with the action

$$S_{vor} = \sum_{x,x'} m_x G(x,x') m'_x \ . \tag{12}$$

As is seen from (11) at large temperatures the interaction betwen vortices is of Coulomb type, i.e. logarithmic, up to corrections. That means in the thermodynamical limit only neutral configurations of vortices contribute to the partition function and, therefore one can apply the methods developed for the XY model to compute sums over vortex configurations. Adding a chemical potential term for the vortices we come finally to

$$Z = \int \prod_x d\phi(x) \exp\left[\frac{1}{2}\sum_{x,x'}\phi(x)G(x,x')^{-1}\phi(x') - 2y\sum_x \cos\left(2\pi\phi(x)\right)\right] \ . \tag{13}$$

The model (13) is of the sine-Gordon type. It follows from (11) that the leading order of the high-temperature expansion coincides exactly with the conventional sine-Gordon model. Corrections produce long-range interactions. This model is starting point for performing renormalization group transformations.

4 The renormalization group equations

To obtain the renormalization group equations we take the continuum limit of the model (13). How to perform the RG transformations for the conventional sine-Gordon model is well-known, see for instance [4]. We follow this strategy and introduce a momentum cutoff λ. Then, integrating out the high-momentum part of the field we get the statistical sum for momentum cutoff $\lambda' = \lambda - d\lambda$. This allows to construct the renormalization group equations in a quite standard way since new partition function turns out to coincide with the original one up to renormalization of all coupling constants and chemical potential. Introducing variables $\beta_{eff} = \frac{1}{2g^2\beta}$, $y = y_0\exp[-\pi^2\beta_{eff}/2]$ and $\gamma = \frac{1}{6}\frac{\beta^3}{g^2}$ we obtain the renormalization group equation in the form

$$\begin{cases} dy &= -y\left(\pi\beta_{eff}(1+\gamma) - 2\right)\dfrac{da}{a} \ , \\ d\beta_{eff} &= -2\pi^4\alpha_2 y^2{\beta_{eff}}^3(1+\gamma)\dfrac{da}{a} \ , \\ d\gamma &= 2\gamma\dfrac{da}{a} + \gamma\dfrac{d\beta_{eff}}{\beta_{eff}} \ . \end{cases} \tag{14}$$

It is convenient to redefine variables according to $X = \pi\beta_{eff}(1+\gamma) - 2, Y = 4\pi\sqrt{\alpha_2}$. Let us recall that the values $X = Y = 0$ are fixed points of the XY model and γ is small by construction. This allows us to rewrite the system of equations near small values of X,Y and γ as

$$\begin{cases} dY &= -YX\dfrac{da}{a} \ , \\ dX &= -Y^2\dfrac{da}{a} + 4\gamma\dfrac{da}{a} \ , \\ d\gamma &= 2\gamma\dfrac{da}{a} \ . \end{cases} \tag{15}$$

This system of RG equations is the same as one for the XY model up to the terms containing γ. Perturbative in γ analysis shows that the renormalization flow of the XY model is not affected when γ is sufficiently small. When γ is growing we run out of the region of the validity of our equations.

5 Summary

RG equations calculated here coincides with the RG equations for the XY model up to a small term which does not affect the universality class. Thus, RG calculations support the Svetitsky-Yaffe conjecture, at least in the region of bare coupling constants where our approximations hold.

Hopefully this result can be extended by going to higher order terms of equations and by solving them to calculate exact values of the critical indices. It is also interesting and important to compute the critical indices from numerical simulations of the $3d$ $U(1)$ LGT. Such computations are now in progress.

References

[1] N. Parga, Phys. Lett. B **107**, 442 (1981)
[2] B. Svetitsky, L. Yaffe, Nucl. Phys. B **210**, 423 (1982)
[3] O. Borisenko, M. Gravina, A. Papa, J.Stat.Mech. (2008) 2008:P08009
[4] J. Kogut, Rev. Mod. Phys. **51**, 659 (1979)

Proceedings of the International School-seminar
"New Physics and Quantum Chromodynamics at external Conditions", pp. 111 − 114,
3-6 May 2009, Dnipropetrovsk, Ukraine

MONOPOLES AND CONFINEMENT IN THE $3D$ $SU(2)$ LATTICE GAUGE THEORY

O. Borisenko[a], S. Voloshin[*,b], J. Boháčik[†,c]

N.N.Bogolyubov Institute for Theoretical Physics, National Academy of Sciences of Ukraine, Kiev, Ukraine,
[†] Institute of Physics, Slovak Academy of Sciences, Bratislava, Slovakia

Using a plaquette formulation for lattice gauge models we describe monopoles of the $3D$ $SU(2)$ theory which appear as configurations in the complete axial gauge and violate the continuum Bianchi identity. Furthermore we derive a dual representation for the Wilson loop in arbitrary representation and calculate the form of the interaction between generated electric flux and monopoles in the region of weak coupling relevant for the continuum limit. The effective theory which controls the interaction is a generalized version of the sine-Gordon model. The string tension is calculated within the semiclassical approximation.

1 Introduction

The problem of the permanent confinement of quarks inside hadrons attracts attention of the theoretical physicists for the last three decades (see [1] and refs. therein for a recent review of the problem). Two of the most popular and the most elaborated mechanisms of confinement are based on the condensation of certain topologically nontrivial configurations - the so-called center vortices or monopoles. In this paper we are interested in the second of these configurations. It was proposed in [2] in the context of continuum compact three dimensional ($3D$) electrodynamics that the string tension is nonvanishing in this theory at any positive coupling constant, and the contribution of monopoles to the Wilson loop was estimated in the semiclassical approximation. Later this consideration was extended to $U(1)$ lattice gauge theory (LGT) in $3D$ [3]. It turns out that these are precisely monopole configurations which make the string tension nonvanishing at all couplings. A rigorous proof of this property was done in [4]. While the monopoles of abelian gauge models can be given by a gauge invariant definition it is not the case for nonabelian models. The most popular approach consists of a partial gauge fixing such that some abelian subgroup of the full nonabelian group remains unbroken. Then, one can define monopoles in a nonabelian theory as monopoles of the unbroken abelian subgroup. Here we propose a different way to define monopoles in nonabelian models. Its main feature is complete gauge fixing. Monopoles appear as defects of smooth gauge fields which violate the Bianchi identity in the continuum limit, in the full analogy with abelian models. Our principal approach is to rewrite the compact LGT in the plaquette (continuum field-strength) representation and to find a dual form of the nonabelian theory. The Bianchi identity appears in such formulation as a condition on the admissible configurations. This allows to reveal the relevant field configurations contributing to the partition function and various observables. Such a program was accomplished for the abelian LGT in [3]. Here we are going to work out the corresponding approach for nonabelian models on the example of $3D$ $SU(2)$ LGT.

2 Plaquette formulation and monopoles

LGT was formulated by K. Wilson in terms of group valued matrices on links of the lattice as fundamental degrees of freedom [5]. The plaquette representation was invented originally in the continuum theory by M. Halpern and extended to lattice models by G. Batrouni [6]. In this representation the plaquette matrices play the role of the dynamical degrees of freedom and satisfy certain constraints expressed by Bianchi identities in every cube of the lattice. In papers [7], [8], [9] we have developed a different plaquette formulation which we outline below.

We start from the partition function that can be written on the dual lattice as [10]

$$Z = \int \prod_{l,k} d\omega_k(l) e^{-\frac{2\beta}{8}\omega_k^2(l)} \prod_x \frac{|W_x|}{\sin W_x} \sum_{m(x)=-\infty}^{\infty} \int \prod_k d\alpha_k(x) \exp\left[-i\sum_k \alpha_k(x)\frac{\omega_k(x)}{2} + 2\pi i m(x)\alpha(x) \right] , \quad (1)$$

where $\alpha(x) = (\sum_k \alpha_k^2(x))^{1/2}$, $W_x = \frac{1}{2}(\sum_k \omega_k^2(x))^{1/2}$ and similarly for W_l. $m(x)$ are arbitrary integers. Auxiliary

[*] Talk presented by S. Voloshin. e-mail: [a]oleg@bitp.kiev.ua,[b]billy.sunburn@gmail.com, [c]Juraj.Bohacik@savba.sk

fields $\alpha_k(x)$ have been introduced for integral representation of the Bianchi identity (see [9] for details)

$$\left[\sum_k \frac{\omega_k(x)}{2}^2\right]^{\frac{1}{2}} = 2\pi m(x)\ ,\ \omega_k(x) = \sum_{n=1}^{3}(\omega_k(x,n) - \omega_k(x-e_n,n)) + \mathcal{O}(\omega_k^2(l))\ .$$

Here, six links $l = (x,n)$ are attached to a site x and $\omega_k(l)$ are link variables dual to original plaquettes. In the continuum limit the last constraint reduces to the familiar Bianchi identity if one takes $m(x) = 0$ for all x. However, when $m(x)$ differs from zero one gets violation of the continuum Bianchi identity at the point x. Clearly, $m(x) \neq 0$ configuration corresponds to the monopole configuration of nonabelian gauge field. Therefore, we may interpret the summation over $m(x)$ as a summation over monopole charges which exist due to the periodicity of $SU(2)$ delta-function (in close analogy with $U(1)$ model).

3 Effective monopole model for $SU(2)$ LGT at large β

Here we would like to calculate the contribution of monopole configurations to the partition function and to the Wilson loop. We make expansion of the action, invariant measure and Jacobian around nontrivial monopole configuration. To do this one should get exact classical equation and find its solution on the nontrivial monopole configuration. We consider that fluctuations around this configuration should be small and restrict ourselves only to the classical solution. We also have to assume that connectors (see its definition in [9]) are not important in generating the string tension and produce only smooth perturbative corrections to the dual gluons.

Starting from (1) we can obtain the following saddle-point equations for fields $\omega_k(l)$ and $\alpha_k(x)$

$$\begin{aligned}&\omega_k(x) = \sum_{l\in x}\omega_k(l) + \epsilon^{kmn}\sum_{l<l'\in x}\omega_m(l)\omega_n(l') + ... = 4\pi m(x)\frac{\alpha_k(x)}{\alpha(x)}\ ,\\ &-\frac{2\beta}{4}\omega_k(l) - i\frac{1}{2}[(\alpha_k(x) - \alpha_k(x+e_n)) + ... = 0\ .\end{aligned} \tag{2}$$

To find the solution of (2) we use an anzatz $\omega_k(l) = \tau_k\omega^s(x)\ ,\ \alpha_k(x) = \tau_k\alpha^s(x)$ where τ_k have properties $\tau_k \cdot \tau_n = 0\ ,\ k \neq n,\ \sum_k \tau_k^2 = 1$. After these substitutions we obtain a solution for functions $\omega^s(l)$ and $\alpha^s(x)$

$$\omega^s(l) = -2\pi D_l(y)m(y)\ ,\ \alpha^s(x) = i\pi\beta G_{xx'}m(x')$$

We use this solution to compute the Wilson loop of the size $R \times T$ in the representation j. Let S be some surface dual to the surface S_{xy} which is bounded by the loop C and consisting of links dual to plaquettes of the original lattice. The expectation value of $W_j(C)$ at $\beta \to \infty$ we present in the form

$$\langle W_j(C)\rangle = \frac{1}{2j+1}\left\langle \chi_j\left(\frac{1}{2}\Omega_C\right)\right\rangle\ ,\ \Omega_C = \left(\sum_k \Omega_k^2(C)\right)^{\frac{1}{2}}\ ,\ \Omega_k(C) = \sum_{l\in S}\omega_k(l) + \mathcal{O}(\omega_k^2(l))\ . \tag{3}$$

Then, by a substitution

$$\omega_k(l) \to\ \tau_k\omega^s(l) + \frac{1}{\sqrt{2\beta}}\omega_k(l)\ ,\ \alpha_k(x) \to\ \tau_k\alpha^s(x) + \sqrt{2\beta}\alpha_k(x)$$

the expectation value of $W(C)$ in (3), averaged by the ensemble in (1), is presented at $\beta \to \infty$ in the form

$$\begin{aligned}\langle W_j(C)\rangle &= \frac{1}{Z}\frac{1}{2j+1}\prod_x\sum_{m(x)\,=\,-\infty}^{\infty} e^{S_{mon}}\int_{-\infty}^{\infty}\prod_{l,k}d\omega_k(l)\int_{-\infty}^{\infty}\prod_{x,k}d\alpha_k(x)\ \chi_j\left(\frac{1}{2}\Omega_C\right)\\ &\times\prod_{l,k}\exp[-\frac{1}{8}\omega_k^2(l) - i\frac{1}{2}\omega_k(l)\left(\alpha_k(x+e_n) - \alpha_k(x)\right)]\ ,\end{aligned} \tag{4}$$

where $\chi_j(x)$ is a $SU(2)$ character and the effective action S_{mon} is of the form

$$S_{mon} = -2\beta\pi^2 m(x)G_{xx'}m(x')\ . \tag{5}$$

To perform the summation over monopole configurations $m_x = 0, \pm 1$ we follow the strategy of Refs.[4], [11]. Using the decomposition $G_{xx'} = B_{xx'} + G_{xx'}(M)$, where $B_{xx'} = G_{xx'} - G_{xx'}(M)$ we rewrite the effective action (5) in the form

$$S_{mon} = -2\beta\pi^2 m(x)B_{xx'}m(x') - 2\beta\pi^2 G_0(M)\sum_x m_x^2 - 2\beta\pi^2\sum_{x\neq x'}m(x)G_{xx'}(M)m(x')\ . \tag{6}$$

The first term in (5) is presented as

$$e^{-2\beta\pi^2 m(x)B_{xx'}m(x')} = (\det B^{-1}_{xx'})^{3/2}\int_{-\infty}^{\infty}\prod_x d\phi_x \exp[-\frac{1}{2\beta}\phi_x B^{-1}_{xx'}\phi_{x'} + i2\pi\phi_x m(x)] \ .$$

The behaviour of $G_{xx'}(M)$ in the thermodynamic and continuum limits is well known

$$G_{xx'}(M) = \frac{2}{\pi R}e^{-\frac{1}{2}MR}, \ R = \left[\sum_k (x_k - x'_k)^2\right]^{\frac{1}{2}} \ .$$

This behaviour allows us to keep only self-energy of the monopoles $S^{SE}_{mon} = -\pi^2 G_0(M)\sum_x m_x^2$ if $MR \gg 1$.

After algebraic manipulations we keep in the sums over monopoles only configurations $m = 0, \pm 1$. This gives the effective model which appears to be of the sine-Gordon type. To write down the final expression we make use of the fact that $B^{-1}_{xx'}(M) \approx G^{-1}_{xx'}$ for M sufficiently large and integrate over fluctuations $\omega_k(x)$ and $\alpha_k(x)$ when $m(x) = 0$. Since we are interested in recovering PT (perturbation theory) result at large β we consider small fluctuations $\omega_k(l) \approx 0$ and use the following asymptotics of $SU(2)$-character uniformly valid in j

$$\langle W_j(C)\rangle \ \simeq \ \int_{S^2} d\sigma_k \left\langle e^{-i\sqrt{j(j+1)}\frac{\Omega_k(C)}{2}\sigma_k}\right\rangle \ \simeq \ \int_{S^2} d\sigma_k \exp[-ij_k(l)\omega_k(l)] \ , \tag{7}$$

where expression for $\frac{\Omega_k(C)}{2}$ is given in (3) and $j_k(l) \ = \ \frac{1}{2}\sqrt{j(j+1)}\sigma_k$ for $l \in S$.

Substituting representation (7) in the expression (4) we integrate out the fluctuations to find

$$\langle W_j(C)\rangle \ = \ \frac{1}{Z}H^{gl}_j H^{mon}_j \ ,$$

where H^{gl}_j is the conventional PT result

$$H^{gl}_j = e^{-\frac{j(j+1)}{2\beta}\sum_{b,b'\in S}G_{bb'}}$$

and for H^{mon}_j one arrives at the following effective model

$$H^{mon}_j = \int_{-\infty}^{\infty}\prod_{x,k} d\phi_x \exp(-S^{mon}_{eff}[\phi_x]),$$

where

$$S^{mon}_{eff}[\phi_x] = \frac{1}{4\beta}\sum_{x,n}(\phi_x - \phi_{x+n})^2 - \gamma\sum_x \frac{1}{2j+1}\chi_j\left(\frac{\Omega_C}{2}\right)\cos 2\pi\phi_x \ .$$

Here $\gamma = 2\exp[-2\pi^2\beta G_0(M)]$ and $\Omega_C = 2\pi\sum_{b\in S} D_b(x)$.

This model possesses an important feature. We see surface independence of the Wilson loop due to the sources which enter through $SU(2)$ group character (see properties of link Green function in our paper [9]).

To perform semiclassical calculations we take the continuum limit. In this limit we get the following saddle-point equation of sine-Gordon type

$$\Delta\alpha(x) = -m^2\frac{1}{2j+1}\chi_j\left(\frac{\Omega_C}{2}\right)\sin\alpha(x) \ . \tag{8}$$

Here we have introduced the Debye mass

$$m^2 = 32\pi^2\beta e^{-2\pi^2\beta G_0(M)} \ . \tag{9}$$

After calculations we find

$$\frac{\Omega_C}{2} \ = \ \pi\varphi(z) + \psi(z, x, y; R, T)$$

where $\varphi(z) \ = \ sign(z)$ and $\psi(x, y; R, T)$ is a correction which decays with R, T growing. If one neglects this correction for large Wilson loop one arrives to

$$\frac{1}{2j+1}\chi_j\left(\frac{\Omega_C}{2}\right) = \frac{1}{2j+1}\frac{\sin(2j+1)\frac{\Omega_C}{2}}{\sin\frac{\Omega_C}{2}} = \cos\left(\pi\varphi(z)\right)$$

for all half-integer j. In this approximation for all half-integer j we write down the saddle-point equation (8) as

$$\Delta\phi(x) \ = \ 2\pi\delta'(x)\theta(x, y; R, T) - m^2\sin\phi(x) \ , \tag{10}$$

where $\theta(x,y;R,T)$ is nonzero only for $x,y \in S$. Far from the boundaries of the contour C the saddle-point equation (10) is essentially one dimensional and has the solution

$$\phi(z) \ = \ 4sign(z) \arctan(e^{-sign(z)mz}) \ . \tag{11}$$

This solution have an essential property

$$\phi(+0) - \phi(-0) \ = \ 2\pi \ . \tag{12}$$

We want to stress that there is no have such a nontrivial solution (with important property (12)) for all integer j. The solution (12) leads to the desirable area law for all half-integer representations

$$\langle W_j(C) \rangle \approx \ e^{-\sigma(j=n+1/2)A_C - \frac{j(j+1)}{2\beta}\sum_{b,b'\in S} G_{bb'}} \ ,$$

where A_C is the area of Wilson loop C and the string tension reads

$$\sigma = \frac{1}{\pi^2\beta} m \ .$$

The second term in the exponent is the leading term of the PT [9]. String rension for all integer j is vanishing. The mass of dual photons is given in (9).

4 Conclusion

In this paper we calculated effective model at large values of β for the expectation value of the Wilson loop in $3D$ $SU(2)$ LGT. This model appears to be a sine-Gordon type and it is valid for all values of representations j of $SU(2)$ group. This model takes into account both the dual photons and the monopole contributions. For all half-integer representation in the semiclassical approximation we have found that the Wilson loop obeys the area law and string tension $\sigma \sim m$. Therefore, proposed mechanism of confinement is able to reproduce this essential feature of the model. It remains unclear if this contribution is also necessary condition of confinement. Our calculations also support the result by Polyakov that the string tension is nonzero only for odd representations j in $U(1)$ LGT [12].

Acknowledgements. Authours thank M. Polykarpov for stimulating discussions. This work was supported by the grant "Vacuum and phase transitions study in SU(N) gauge theories at zero and finite temperatures " between Slovak and Ukrainian Academy of Sciences.

References

[1] J. Greensite, Prog.Part.Nucl.Phys. **51**, 1 (2007) .

[2] A.M. Polyakov, Nucl.Phys. B **120**, 429 (1977).

[3] T. Banks, J. Kogut, R. Myerson, Nucl.Phys. B **121**, 493 (1977).

[4] M. Göpfert, G. Mack, Commun.Math.Phys. **82** 545 (1982) .

[5] K. G. Wilson, Phys.Rev. D **10** 2445 (1974).

[6] M.B. Halpern, Phys.Rev. D **19** 517 (1979); Phys.Lett. B **81** 245 (1979); G. Batrouni, Nucl.Phys. B **208** 467 (1982).

[7] O. Borisenko, S. Voloshin, M. Faber, Analytical study of low temperature phase of $3D$ LGT in the plaquette formulation, Proc. of NATO Workshop "Confinement, Topology and Other Non-perturbative Aspects of QCD", Ed. by J. Greensite, and S. Olejnik, Kluwer Academic Publishers, 33, 2002; [hep-lat/0204028].

[8] O. Borisenko, S. Voloshin, M. Faber, "Perturbation Theory for Non-Abelian Gauge Models in The Plaquette Formulation", Preprint of University of Technology of Vienna, IK-TUW-Preprint 0312401, 2003.

[9] O. Borisenko, S. Voloshin, M. Faber, Field strength formulation, lattice Bianchi identities and perturbation theory for non-Abelian models, Nuclear Physics B **816** [FS], 399 (2009); [hep-lat/0508003].

[10] O. Borisenko, V. Kushnir, A. Velytsky, Phys.Rev. D **62**, 025013 (2000) .

[11] F. Conrady, Analytic derivation of dual gluons and monopoles from $SU(2)$ lattice Yang-Mills theory. III. Plaquette representation, 2006, [hep-th/0610238].

[12] A.M. Polyakov, *Gauge Fields and Strings (Contemporary Concepts of Physics: V.3)*, (Harwood Academic Publishers, Chur and London, 1987).

Proceedings of the International School-seminar
"New Physics and Quantum Chromodynamics at external Conditions", pp. 115 – 118,
3-6 May 2009, Dnipropetrovsk, Ukraine

CENTER VORTICES AND DIRAC EIGENMODES

M. Faber[a], J. Greensite[b], U.M. Heller[c], R. Höllwieser[d], Š. Olejník[e]

[a,d]Atomic Institute, Vienna University of Technology, Wiedner Hauptstr. 8-10, A-1040 Vienna, Austria
[b]Physics and Astronomy Dept., San Francisco State University, San Francisco, CA 94132, USA
[c]American Physical Society, One Research Road, Box 9000, Ridge, NY 11961-9000, USA
[e]Institute of Physics, Slovak Academy of Sciences, SK–845 11 Bratislava, Slovakia

The center vortex model has been proposed as an explanation of confinement in non-Abelian gauge theories. Low-lying Dirac eigenmodes are related to the chiral properties of a gauge configuration. We investigate the correlation of center vortices and Dirac eigenmodes in SU(2) lattice gauge theory.

1 Introduction

Lattice QCD (LQCD) is the main tool for probing QCD in the non-perturbative regime, where QCD predicts quark confinement and chiral symmetry breaking. We work with lattices generated by Monte Carlo simulation of the tadpole improved Lüscher-Weisz pure-gauge action, mainly at coupling $\beta = 3.3$ (lattice spacing $a = 0.15$ fm) for the $SU(2)$ gauge group, which is very appropriate to study the mechanism and relation of these phenomena. Center-Projection is performed by Direct Maximal Center Gauge (adjoint Landau gauge), maximizing the squared trace of link variables $U_\mu(x)$ by the over-relaxation method. The mapping to link variables on the center-projected (or "vortex-only") lattice, for the $SU(2)$ gauge group, is given by $U_\mu(x) \to Z_\mu(x) = \mathrm{signTr}[U_\mu(x)]$ and the link variables on vortex-removed lattices are defined as $U'_\mu(x) = Z_\mu(x)U_\mu(x)$.

2 Center vortex picture of confinement

Center vortices, quantized magnetic flux-lines, compress the gluonic flux into tubes and cause a linearly rising potential at large separations. This confinement mechanism was tested in many ways, for a detailed discussion see Ref. [1]. In Fig. 1 we show vortex limited Wilson loops W_n, with n vortices piercing the Wilson loop. As the loop area increases the Wilson loop approaches the limit $(-1)^n W_0$. Fig. 2 shows the effect of vortex removal on the Creutz ratio, the string tension vanishes whereas for the center-projected ("vortex only") configuration the Creutz ratio approaches the asymptotic string tension. Removing vortices also restores chiral symmetry [2], i.e. the chiral condensate vanishes, which is closely related to low-lying Dirac eigenmodes.

3 Dirac eigenmodes and chiral symmetry breaking

The chiral condensate $\langle\bar\psi\psi\rangle$ is an order parameter for chiral symmetry breaking. According to the Banks-Casher relation [3] $\bar\psi\psi = \pi\rho(0)/V$, the chiral condensate is directly proportional to the density of near zero modes $\rho(0)$. Fig. 3 shows the first twenty eigenvalue pairs of the asqtad staggered Dirac operator [4] on a 20^4 lattice using antiperiodic boundary conditions at $\beta = 3.3$ for full, center-projected and vortex removed configurations. There is a clear gap in the vortex removed spectrum, indicating restored chiral symmetry, whereas in the vortex only case, the chiral condensate seems to be even enhanced in comparison to the original configuration. The vortex excitations of the center-projected lattice carry not only the information about confinement, but are also responsible for chiral symmetry breaking via the Banks-Casher relation. (see also [5, 6, 7])

4 Dirac eigenmode density and vortex correlations

Next we investigate the eigenmode density $\rho_\lambda(x) = \psi^\dagger_\lambda(x)\psi_\lambda(x)$, where $\psi_\lambda(x)$ is the normalized ($\sum_x \rho_\lambda(x) = 1$) eigenvector of the Dirac operator corresponding to the eigenvalue λ. We plot representative maximum density peaks for overlap and asqtad staggered eigenmodes on full configurations in Fig. 4 and for asqtad staggered eigenmodes on center-projected configurations in Fig. 5a. The overlap Dirac operator [8] does not provide reliable results on the singular gauge fields of center-projected configurations. In all other cases the figures show clearly sharp peaks in point-like regions of the lattice volume.

In Fig. 6 we present the vortex density in dependence of the distance (in lattice units a) from these eigenmode density peaks and find strong correlations between the eigenmode density and vortex structures. These dense

e-mail: [a]faber@kph.tuwien.ac.at, [b]jgreensite@gmail.com, [c]heller@ridge.aps.org, [d]hroman@kph.tuwien.ac.at, [e]stefan.olejnik@gmail.com

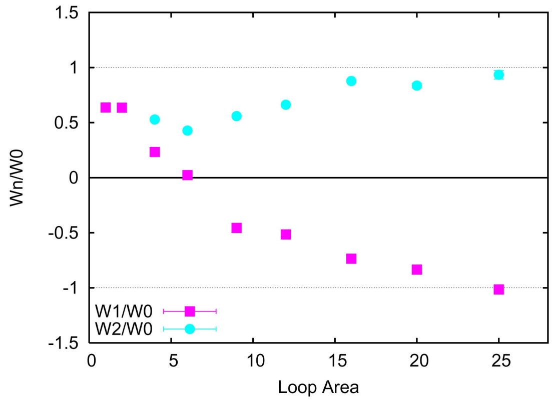

Figure 1. Ratios of vortex limited Wilson loops W_n on 20^4 lattice at $\beta = 3.1$.

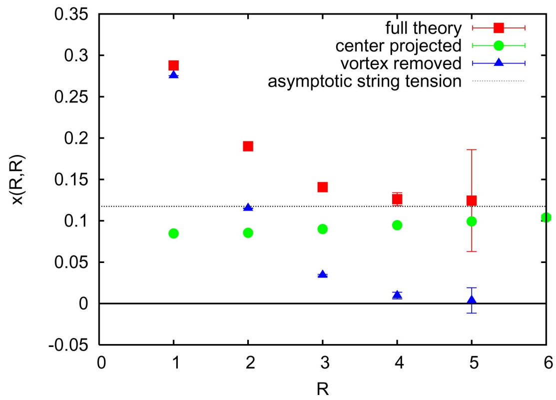

Figure 2. Creutz ratios at $\beta = 3.3$ for full, center-projected and vortex-removed 20^4 lattices.

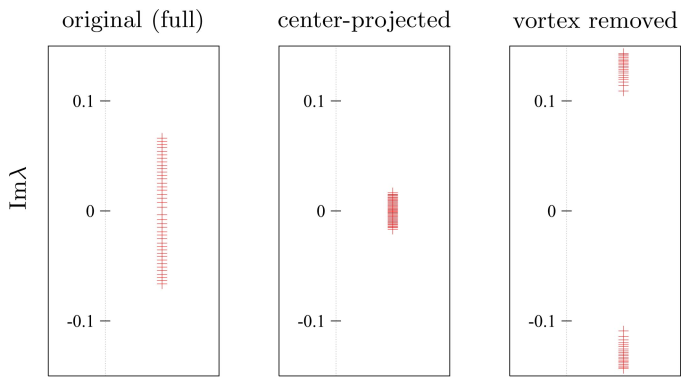

Figure 3. Dirac spectra of asqtad staggered fermions on a 20^4 lattice at $\beta = 3.3$ for full, center-projected and vortex-removed configurations.

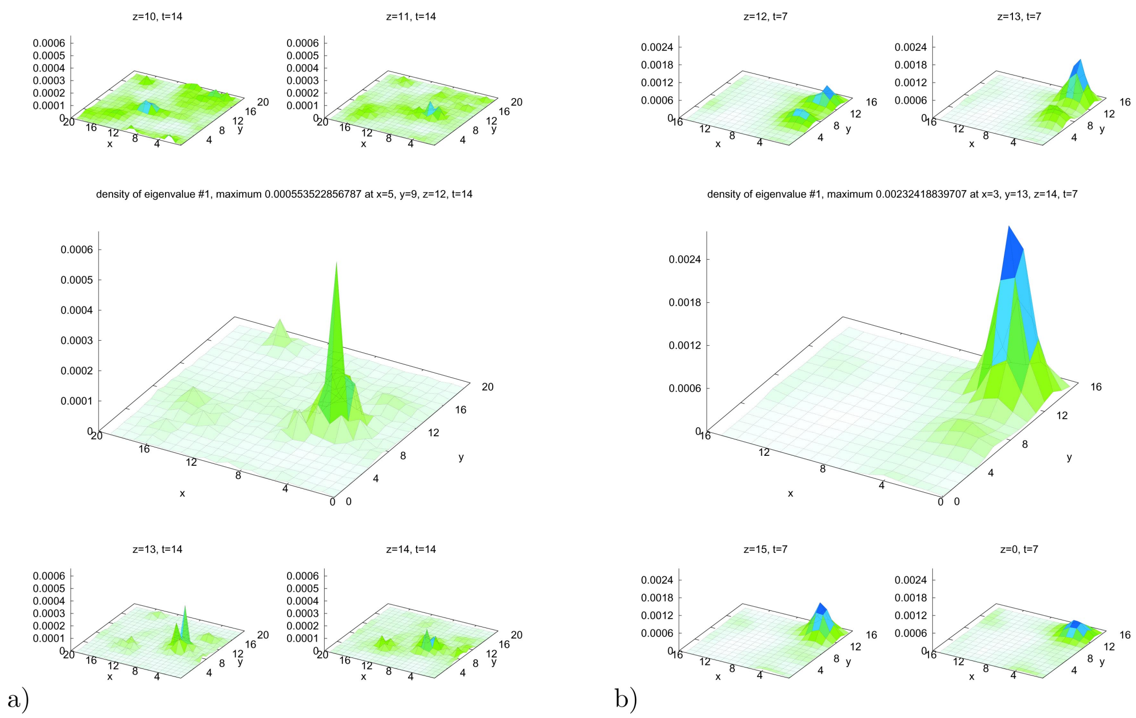

Figure 4. Maximum density peaks (center) of first a) asqtad staggered and b) overlap Dirac eigenmode on a full 20^4- resp. 16^4-lattice configuration, with upper (above) and lower (below) z-slices of the same t-slice.

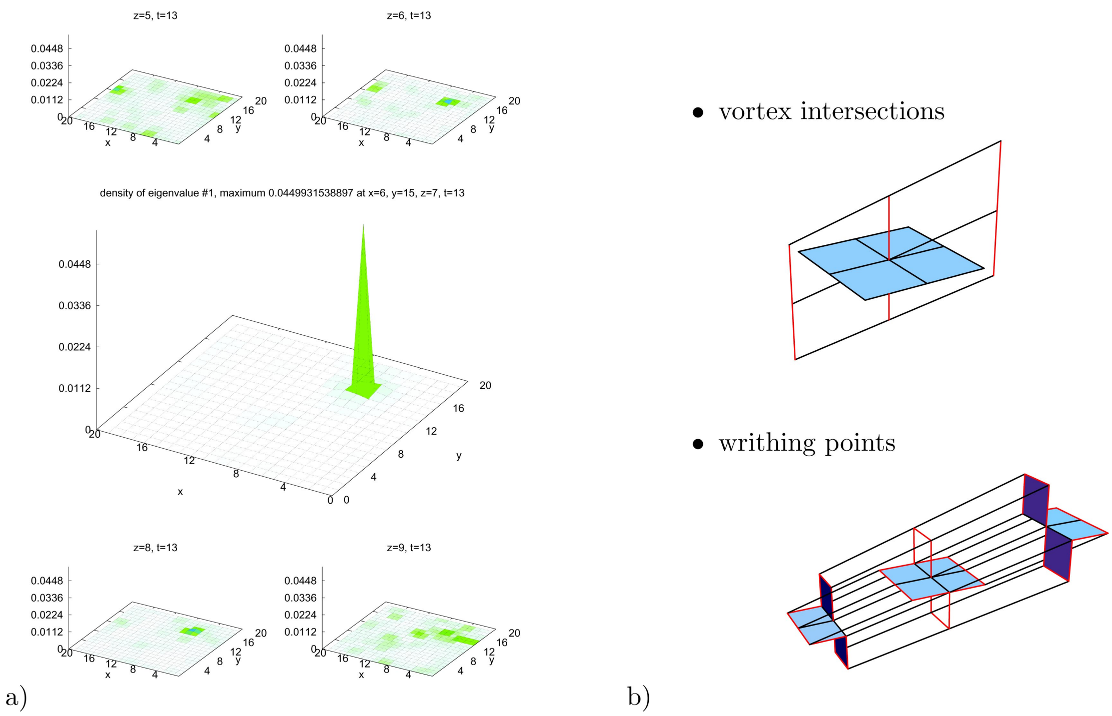

Figure 5. a) Maximum density peaks (center) of first asqtad staggered Dirac eigenmode on a center-projected 20^4-lattice configuration, with upper (above) and lower (below) z-slices of the same t-slice. b) Peaks correlate with topological charge sources, vortex intersection (above) and writhing points (below).

vortex structures at the eigenmode density peaks are known to be sources of topological charge from the picture advocated by Engelhardt and Reinhardt [9], shown in Fig. 5b.

Finally, we directly correlate Dirac eigenmodes of different fermion operators by comparing the position of their eigenmode density peaks. In Fig. 7 we present a representative example of the eigenvalue spectra of overlap and asqtad staggered fermions on a full and the corresponding center-projected 16^4-lattice configuration. We draw a line between two eigenvalues when their eigenmode density peaks match exactly. This is a rather interesting result since we find that the different eigenmode spectra do not provide the same physical contents at comparable energy levels, i.e. the correlations mix between different eigenvalues. The overlap zero mode for example appears as second center-projected and fourteenth full asqtad staggered mode.

5 Conclusions

We presented significant results that the center vortex model not only explains confinement and topological charge, but also the breaking of chiral symmetry. We also find strong correlations between Dirac eigenmode, vortex and topological charge densities. These results were published in [10]. Nevertheless, the final result shows that different fermion realizations on the lattice may lead to slightly different results.

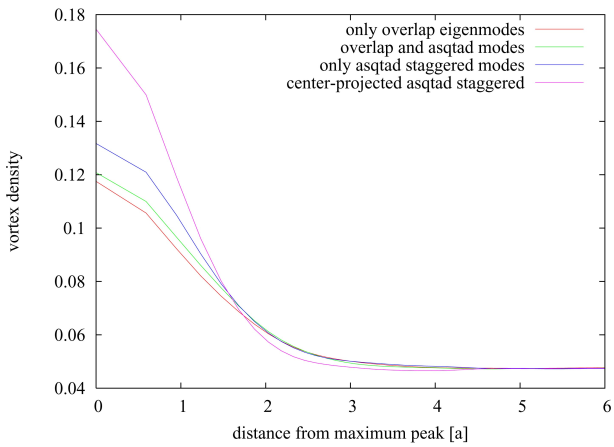

Figure 6. Vortex density in dependence of the distance from maximum Dirac eigenmode density peaks.

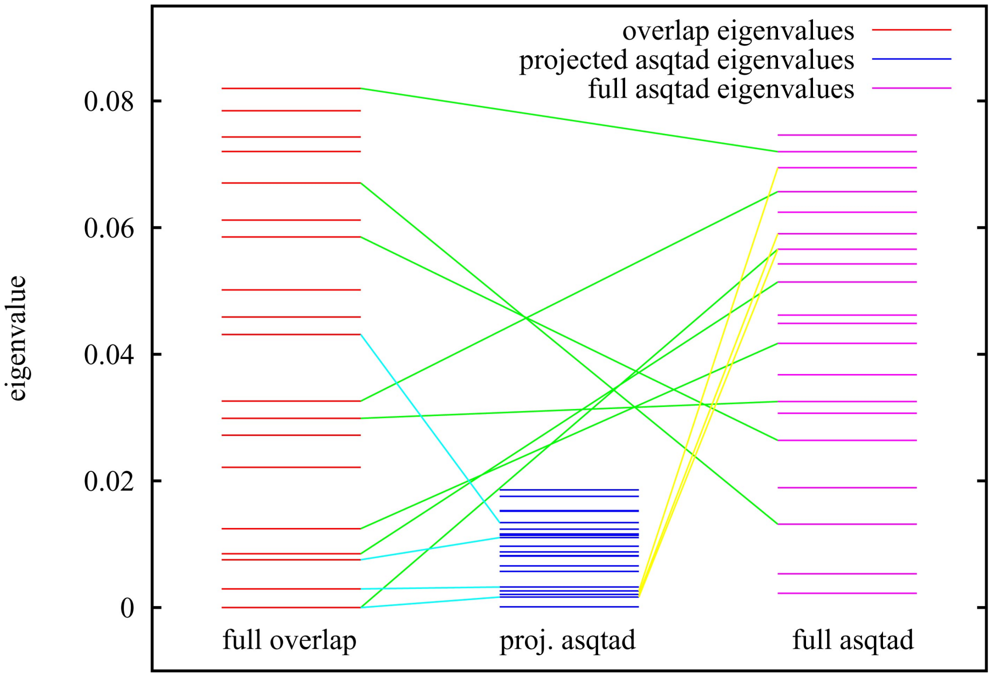

Figure 7. Dirac eigenvalue spectra on a 16^4-lattice configuration with eigenmode correlations (connection lines). For better presentation we just plot the absolute value of the overlap eigenvalues and not the Ginsparg-Wilson circle, which in fact makes no difference for the low-lying modes.

Acknowledgements. This research was supported by "Fonds zur Förderung der Wissenschaften" (FWF) under contract P20016-N16 (R.H.).

References

[1] J. Greensite, Prog. Part. Nucl. Phys. **51**, 1 (2003) [arXiv: hep-lat/0301023].
[2] P. de Forcrand and M. D'Elia, Phys. Rev. Lett. **82**, 4582 (1999) [arXiv:hep-lat/9901020].
[3] T. Banks and A. Casher, Nucl. Phys. **B169**, 103 (1980).
[4] Kostas Orginos, Doug Toussaint and R.L. Sugar, Phys. Rev. **D60**, 054503 (1999) [hep-lat/9903032]; G.P. Lepage, Phys. Rev. **D59**, 074502 (1999) [arXiv:hep-lat/9809157].
[5] C. Alexandrou, P. de Forcrand and M. D'Elia, Nucl. Phys. **A663**, 1031 (2000) [arXiv:hep-lat/9909005].
[6] F. V. Gubarev, S. M. Morozov, M. I. Polikarpov and V. I. Zakharov, [arXiv:hep-lat/0505016].
[7] V. G. Bornyakov, E. M. Ilgenfritz, B. V. Martemyanov, S. M. Morozov, M. Müller-Preussker and A. I. Veselov, Phys. Rev. **D77**, 074507 (2008) [arXiv:hep-lat/0708.3335].
[8] R. Narayanan and H. Neuberger, Nucl. Phys. **B443**, 305 (1995) [hep-th/9411108]; H. Neuberger, Phys. Lett. **B417**, 141 (1998) [hep-lat/9707022].
[9] M. Engelhardt, Nucl. Phys. **B585**, 614 (2000) [arXiv:hep-lat/0004013]; M. Engelhardt and H. Reinhardt, Nucl. Phys. **B567**, 249 (2000) [arXiv:hep-th/9907139].
[10] R. Höllwieser, M. Faber, J. Greensite, U.M. Heller and Š. Olejník, Phys. Rev. **D78**, 54508 (2008) [arXiv:hep-lat/0805.1846].

Proceedings of the International School-seminar
"New Physics and Quantum Chromodynamics at external Conditions", pp. 119 – 121,
3-6 May 2009, Dnipropetrovsk, Ukraine

ON THE LORENTZ STRUCTURE OF THE STRONG INTERACTION POTENTIAL FOR PIONIC HYDROGEN

D. A. Kulikov[a], R. S. Tutik[b]

Dnipropetrovsk National University, Dnipropetrovsk, Ukraine

The new potential model for pionic hydrogen, constructed with the employment of the two-body relativistic equation, is proposed. Within this model, using the experimental data on the strong energy level shift and width of the $1s$ state in pionic hydrogen as input, the pion-nucleon scattering lengths are evaluated. The dependence of the scattering lengths on the Lorentz structure of the strong interaction potential is discussed.

1 Introduction

Experiments performed with hadronic atoms give us an important piece of information on strong interactions at low energy. In particular, the data on the shift in energy and the width in pionic hydrogen [1, 2] allow a precise determination of the pion-nucleon scattering lengths. For this end, the non-relativistic scattering theory, the effective field theory techniques and the potential models are used (see review on this topic in Ref. [3]).

The conventional potential model for pionic hydrogen, the bound $\pi^- p$ system, is the one-particle approximation based on the Klein-Gordon equation with electromagnetic and strong interactions which are included through the Lorentz-vector and Lorentz-scalar potentials, respectively [4]. However, despite the Lorentz structure of the strong interaction potential is still unclarified, the differences appeared when the strong interaction is introduced as the Lorentz-vector potential instead of the Lorentz-scalar one have not been investigated. Such an investigation implies the exact treatment of the relativistic kinematics in the $\pi^- p$ system that forces us to go beyond the one-particle approximation.

Recently, a new wave equation for a relativistic fermion-boson system has been offered [5]. Based on the extension of the $SL(2, C)$ group to the $Sp(4, C)$ one, this equation describes self-consistently the relativistic two-body kinematics as well as the effect of the fermion spin and anomalous magnetic moment and permits us to deal with Lorentz-scalar, Lorentz-vector and Lorentz-tensor potential interactions.

The goal of the present work is to apply the proposed equation [5] to construct a relativistic two-body potential model for pionic hydrogen (more details are given in Ref. [6]) and to investigate the dependence of the pion-nucleon scattering lengths on the Lorentz structure of the strong interaction potential.

2 Model

Let us briefly describe the wave equation for a fermion-boson system derived with the extension of the $SL(2, C)$ group. It is known that the homogeneous Lorentz group $SO(1, 3)$ is covered by the symplectic $SL(2, C) \equiv Sp(2, C)$ group. As a consequence, the wave equation for a relativistic particle can be written within the framework of the $SL(2, C)$ Weyl spinor formalism [7]. It has been shown [5] that the extension of the $SL(2, C)$ group to the $Sp(4, C)$ one enables us to construct relativistic wave equations describing two-body systems.

Consider the system consisted of a spin-1/2 fermion and a spin-0 boson. The wave function of this system is represented by a Dirac spinor or, in our treatment, by two $Sp(4, C)$ Weyl spinors φ and $\bar{\chi}$, whereas the corresponding wave equation has the Dirac-like form

$$\begin{aligned}
[I \otimes \sigma^m (w_m + A_m) + \tau^1 \otimes \sigma^m (p_m + B_m)]\bar{\chi} = {} & [m_+ + S_+ + \tau^1 \otimes I(m_- + S_-) \\
& - \mathrm{i} I \otimes \sigma^m \tilde{\sigma}^n C_{mn} - \mathrm{i}\tau^1 \otimes \sigma^m \tilde{\sigma}^n D_{mn}]\varphi, \\
[I \otimes \tilde{\sigma}^m (w_m + A_m) + \tau^1 \otimes \tilde{\sigma}^m (p_m + B_m)]\varphi = {} & [m_+ + S_+ + \tau^1 \otimes I(m_- + S_-) \\
& - \mathrm{i} I \otimes \tilde{\sigma}^m \sigma^n C_{mn} - \mathrm{i}\tau^1 \otimes \tilde{\sigma}^m \sigma^n D_{mn}]\bar{\chi}.
\end{aligned} \tag{1}$$

Here four-momenta w_m, p_m and mass parameters $m_\pm$ are related to the quantities for the particles of the system by

$$w_m = \frac{1}{2}(p_{1m} + p_{2m}), \qquad p_m = \frac{1}{2}(p_{1m} - p_{2m}), \qquad m_\pm = \frac{1}{2}(m_1 \pm m_2). \tag{2}$$

The Lorentz-scalar ($S_\pm$), Lorentz-vector (A_m, B_m) and Lorentz-tensor (C_{mn}, D_{mn}) potentials in general case are the functions of w_m, p_m and the relative coordinate $x_m = x_{1m} - x_{2m}$. The direct products contain 2×2

e-mail: [a]kulikov_d_a@yahoo.com, [b]tutik@dsu.dp.ua

matrices, namely, σ^m, $\tilde{\sigma}^m$ coming from the one-particle Dirac equation in the Weyl notation [7], the unit matrix I and the Pauli matrices τ^i.

The above equation (1) must be supplemented with the subsidiary condition

$$(w^m p_m - m_+ m_-) \begin{pmatrix} \varphi \\ \bar{\chi} \end{pmatrix} \equiv \frac{1}{4}(p_1^2 - p_2^2 - m_1^2 + m_2^2) \begin{pmatrix} \varphi \\ \bar{\chi} \end{pmatrix} = 0, \tag{3}$$

which guarantees that in the lack of the interaction the constituent particles are on the mass shell, being subjected to the free Dirac and Klein-Gordon equations. Since the developed formalism does not distinguish between the masses of the constituents, in the following we accept, for definiteness, that the Dirac fermion (proton) has the mass m_1 and the Klein-Gordon boson (π^--meson) has the mass m_2.

It is to be pointed that in the presence of the interaction the wave equation (1) and the subsidiary condition (3) must be compatible. The demand of the compatibility imposes the restrictions on the shape of the potentials [5]. Moreover, the potentials must depend on the relative coordinate only through its transverse part $x_{\perp m} = (g_{mn} - w_m w_n/w^2)x^n$ with respect to the total four-momentum w_m, which is conserved and so can be treated as the eigenvalue rather than the operator.

Physically, the shape of the Lorentz-vector and Lorentz-tensor potentials, which are responsible for the electromagnetic interaction between the constituents, is further constrained by the necessity of obtaining the correct values of the relativistic kinetic energy, spin-orbit and Darwin terms in the semirelativistic approximation.

We found that the potentials satisfying all stated conditions can be chosen as

$$\begin{aligned} &A_m = (\mathcal{F} - 1)w_m, \qquad B_m = (\mathcal{F}^{-1} - 1)p_m - \frac{\mathrm{i}}{2\mathcal{F}^2}\frac{\partial \mathcal{F}}{\partial x_\perp^m}\,, \\ &C_{mn} = 0, \qquad D_{mn} = \frac{k_1}{4m_1}\left(\frac{\partial A_n}{\partial x_\perp^m} - \frac{\partial A_m}{\partial x_\perp^n} + \frac{\partial B_n}{\partial x_\perp^m} - \frac{\partial B_m}{\partial x_\perp^n}\right), \end{aligned} \tag{4}$$

where $\mathcal{F} = (1 - 2\mathcal{A}/E)^{1/2}$ with $E = 2\sqrt{w^2}$ denoting the total energy and $\mathcal{A} = \mathcal{A}(x_\perp^2)$ being the scalar function which becomes the Coulomb potential if the point charges are assumed, k_1 is the anomalous magnetic moment of the fermion (for the proton $k_1 = 1.793$).

As regards the Lorentz-scalar potentials $S_\pm$, we demand that they give rise to the conventional scalar potential in the limit when the proton is assumed to be much heavier than the meson and Eq. (1) is reduced to the Klein-Gordon equation. This is achieved with putting

$$S_\pm = \frac{1}{2}\left((m_+ + m_-)^2 + 2m_w\mathcal{S} + \mathcal{S}^2\right)^{1/2} \pm \frac{1}{2}\left((m_+ - m_-)^2 + 2m_w\mathcal{S} + \mathcal{S}^2\right)^{1/2} - m_\pm, \tag{5}$$

where $m_w = m_1 m_2/E$ is the relativistic reduced mass and $\mathcal{S} = \mathcal{S}(x_\perp^2)$ is the scalar potential.

Upon passing to the center-of-mass frame and separating the spatial variables, the wave equation (1) with the introduced interaction is transformed into the set of radial equations

$$\begin{aligned} &\left(\frac{\mathrm{d}}{\mathrm{d}r} + \frac{\kappa}{r} - \frac{k_1(E^2\mathcal{F}^2 - m_1^2 + m_2^2)}{4m_1E^2\mathcal{F}^2}\frac{\mathrm{d}\mathcal{A}}{\mathrm{d}r}\right)G(r) - \left(E_1 - \mathcal{A} + M_1\mathcal{F} + \frac{k_1(\kappa - 1)}{2m_1E\mathcal{F}^2}\frac{1}{r}\frac{\mathrm{d}\mathcal{A}}{\mathrm{d}r}\right)F(r) = 0\,, \\ &\left(\frac{\mathrm{d}}{\mathrm{d}r} - \frac{\kappa}{r} + \frac{k_1(E^2\mathcal{F}^2 - m_1^2 + m_2^2)}{4m_1E^2\mathcal{F}^2}\frac{\mathrm{d}\mathcal{A}}{\mathrm{d}r}\right)F(r) + \left(E_1 - \mathcal{A} - M_1\mathcal{F} + \frac{k_1(\kappa + 1)}{2m_1E\mathcal{F}^2}\frac{1}{r}\frac{\mathrm{d}\mathcal{A}}{\mathrm{d}r}\right)G(r) = 0\,, \end{aligned} \tag{6}$$

where $r = \sqrt{-x_\perp^2}$, $M_1 = (m_1^2 + 2m_w\mathcal{S} + \mathcal{S}^2)^{1/2}$, $E_1 = (E^2 + m_1^2 - m_2^2)/(2E)$ and the quantum number $\kappa = \pm(j + 1/2)$ describes the states with $j = l \mp 1/2$. It is these radial equations that we will use to calculate the pionic hydrogen characteristics.

Now let us specify the explicit form of the potentials needed for the description of the interaction between the proton and the π^--meson. According to Eqs. (4), the electromagnetic interaction is described by the potential function $\mathcal{A}$, which we represent as the sum of three parts

$$\mathcal{A}_{\mathrm{e.m.}} = \mathcal{A}_{\mathrm{pc}} + \mathcal{A}_{\mathrm{ext}} + \mathcal{A}_{\mathrm{vac}}\,, \tag{7}$$

where $\mathcal{A}_{\mathrm{pc}} = -\alpha/r$ with $\alpha = 1/137.036$ is the point Coulomb potential, $\mathcal{A}_{\mathrm{ext}}$ is the addition caused by the finite extension of the charge distributions of the proton and the π^--meson (the Gaussian distributions are accepted), $\mathcal{A}_{\mathrm{vac}}$ is the correction due to the vacuum polarization (the smeared Uehling potential).

We employ the single-channel approximation and account for the pionic hydrogen decay channels by introducing the optical strong interaction potential, for which the square-well form is assumed

$$U_{\mathrm{str}} = \begin{cases} U_0 & \text{for } r \le \sqrt{\frac{5}{3}}\,r_0\,, \\ 0 & \text{otherwise}\,. \end{cases} \tag{8}$$

In order to investigate the influence of the Lorentz structure of the strong interaction potential, we consider two different cases. The first one corresponds to the Lorentz-scalar strong interaction and utilizes the potentials

$$\mathcal{A} = \mathcal{A}_{\rm e.m.}, \qquad \mathcal{S} = U_{\rm str}\,, \tag{9}$$

whereas the second one involves the Lorentz-vector form

$$\mathcal{A} = \mathcal{A}_{\rm e.m.} + U_{\rm str}, \qquad \mathcal{S} = 0. \tag{10}$$

With these two sets of the potentials, we calculated the pion-nucleon scattering lengths. In order to fit the position and width of the quasistationary energy level of the $1s$ state, the radial equations were solved numerically with varying the complex value of the strong interaction potential strength U_0. Under realization of this procedure, the most recent experimental data on the strong energy-level shift, $\epsilon_{1s}^{\rm str} = -7.120 \pm 0.008$ (stat) ± 0.006 (syst) eV, and the width, $\Gamma_{1s} = 0.823 \pm 0.018$ eV, in pionic hydrogen [2] and on the rms charge radii and masses of particles [8] were used. For adapting the experimental data to our single-channel approach, the strong decay channel ($\pi^- p \to \pi^0 n$) was separated out with the replacement of the total decay width, Γ_{1s}, by the partial width, $\Gamma_{1s}^{\pi^0 n} = \Gamma_{1s}/(1 + P^{-1})$, where $P = 1.546(9)$ is the Panofsky ratio.

After the potential strength, U_0, had been adjusted, the electromagnetic interaction was switched off and the radial equations were solved once again to produce the pion-nucleon scattering lengths $a_{\pi^- p}$, $a_{\pi^0 n}$. The whole procedure was repeated with varying the range parameter r_0 between 0.5 fm and 1.5 fm. The calculations with the exponential and Gaussian potentials instead of the square-well potential did not changed the values of $a_{\pi^- p}$, $a_{\pi^0 n}$, as it is expected for the effective-range theory.

3 Results

The final results for pion-nucleon scattering lengths obtained within the proposed relativistic two-body potential model for pionic hydrogen, using the two different Lorentz structure forms (9) and (10), are

$$\begin{array}{lll} \text{Lorentz-scalar strong int.:} & a_{\pi^- p} = 0.0860(6) m_\pi^{-1}\,, & a_{\pi^0 n} = -0.1223(19) m_\pi^{-1}\,, \\ \text{Lorentz-vector strong int.:} & a_{\pi^- p} = 0.0855(6) m_\pi^{-1}\,, & a_{\pi^0 n} = -0.1220(18) m_\pi^{-1}\,, \end{array} \tag{11}$$

where m_π is the π^--meson mass. It is to be pointed that the error in $a_{\pi^- p}$ arises mainly from the range dependence of r_0 and is reduced to $0.0002 m_\pi^{-1}$ if the value $r_0 = 1.0$ fm is fixed, whereas almost all the error in $a_{\pi^0 n}$ comes from the experimental uncertainty in Γ_{1s}.

Thus, we conclude that the difference between the pion-nucleon scattering lengths obtained with the Lorentz-scalar and Lorentz-vector strong interaction is less than or approximately equal to the accuracy with which these scattering lengths can be extracted from the available experimental data.

In addition, we found that the influence of the Lorentz structure of the strong interaction potential varies depending on the type of the wave equation employed. Indeed, it turns out that the difference $a_{\pi^- p}^{\rm scal} - a_{\pi^- p}^{\rm vect} = (0.0860 - 0.0865) m_\pi^{-1} = 0.0005 m_\pi^{-1}$ predicted by our two-body equation is about half of the value $0.0009 m_\pi^{-1}$ obtained within the framework of the Klein-Gordon equation with the same potentials (9) and (10).

Notice that our results on the pion-nucleon scattering lengths are consistent with those recently extracted within the framework of other potential models. In particular, values in Eqs. (11) agree reasonably well with quantities $a_{\pi^- p} = 0.0859(6) m_\pi^{-1}$, $a_{\pi^0 n} = -0.1243(15) m_\pi^{-1}$, calculated using the three-channel relativized potential model [9], and $a_{\pi^- p} = 0.0870(5) m_\pi^{-1}$, $a_{\pi^0 n} = -0.125(4) m_\pi^{-1}$, calculated using the non-relativistic scattering theory [10]. The agreement would be even better if we used, as in Refs. [9, 10], the earlier value for the pionic hydrogen width [1] which is substantially larger than the latest one [2].

References

[1] H.-Ch. Schröder *et al.*, Eur. Phys. J. C **21** 473 (2001).

[2] L.M. Simons, Proc. Int. Workshop on Exotic Hadronic Atoms, Deeply Bound Kaonic Nuclear States and Antihydrogen: Present Results, Future Challenges, Trento, 2006, edited by C. Curceanu, A. Rusetsky and E. Widmann, p.8 [hep-ph/0610201].

[3] J. Gasser, V.E. Lyubovitskij, A. Rusetsky, Phys. Rept. **456**, 167 (2008).

[4] D. Sigg, A. Badertscher, P.F.A. Goudsmit, H.J. Leisi, G.C. Oades, Nucl. Phys. A, **609** 310 (1996).

[5] D.A. Kulikov, R.S. Tutik, Mod. Phys. Lett. A **23**, 1829 (2008).

[6] D.A. Kulikov, R.S. Tutik, *"A new two-body relativistic potential model for pionic hydrogen"* [arXiv:0906.5066].

[7] V.B. Berestetskii, E.M. Lifshitz, L.P. Pitaevskii, *Quantum Electrodynamics* (Pergamon, Oxford 1982).

[8] C. Amsler *et al.*, Phys. Lett. B **667**, 1 (2008).

[9] G.C. Oades, G. Rasche, W.S. Woolcock, E. Matsinos, A. Gashi, Nucl. Phys. A **794**, 73 (2007).

[10] T.E.O. Ericson, B. Loiseau, S. Wycech, Phys. Lett. B **594**, 76 (2004).

Proceedings of the International School-seminar
"New Physics and Quantum Chromodynamics at external Conditions", pp. 122 – 126,
3-6 May 2009, Dnipropetrovsk, Ukraine

JUST ONE MORE APPROACH TO CALCULATING THE QCD GROUND STATE

S. V. Molodtsov[1,2, a], G. M. Zinovjev[3, b]

[1]Joint Institute for Nuclear Research, RU-141980, Dubna, Moscow region, RUSSIA.
[2]Institute of Theoretical and Experimental Physics, RU-117259, Moscow, RUSSIA.
[3]Bogolyubov Institute for Theoretical Physics, UA-03143, Kiev, UKRAINE.

The quark behaviour in the background of intensive stochastic gluon field is studied. An approximate procedure for calculating the effective Hamiltonian is developed and the corresponding ground state within the Hartree-Fock-Bogolyubov approach is found. The comparative analysis of various model Hamiltonian is given and transition to the chiral limit in the Keldysh model is discused in detail. We study response to the process of filling up the Fermi sphere with quarks, calculate the vacuum pressure and demonstrate the existence of filled-in state degenerate with the vacuum one.

We study the quark (anti-quark) behaviour while being influenced by intensive stochastic gluon field and work in the context of the Euclidean field theory. The corresponding Lagrangian density is the following

$$\mathcal{L}_E = \bar{q}\ (i\gamma_\mu D_\mu + im)\ q\ , \tag{1}$$

here q ($\bar{q}$) — are the quark (anti-quarks) fields with covariant derivative $D_\mu = \partial_\mu - igA^a_\mu t^a$ where A^a_μ is the gluon field, $t^a = \lambda^a/2$ are the generators of colour gauge group $SU(N_c)$ and m is the current quark mass. As the model of stochastic gluon field we refer to the example of (anti-)instantons considering an ensemble of these quasi-classical configurations. On the way to construct an effective theory we consider the quenched approximation and neglect all the contributions coming from gluon fields A_{ex} generated by the (anti-)quarks $A_{ex} \ll A$. Then the corresponding Hamiltonian description results from

$$\mathcal{H} = \pi\dot{q} - \mathcal{L}_E\ ,\quad \pi = \frac{\partial \mathcal{L}_E}{\partial \dot{q}} = iq^+\ , \tag{2}$$

and $\mathcal{H}_0 = -\bar{q}\ (i\gamma\nabla + im)q$, for noninteracting quarks. In Schrödinger representation the quark field evolution is determined by the equation for the quark probability amplitude Ψ as

$$\dot{\Psi} = -H\Psi\ , \tag{3}$$

with the density of interaction Hamiltonian $\mathcal{V}_S = \bar{q}(\mathbf{x})\ t^a\gamma_\mu A^a_\mu(t,\mathbf{x})\ q(\mathbf{x})$. The explicit dependence on "time" is present at the gluon field only. The creation and annihilation operators of quarks and anti-quarks $a^+, a,\ b^+, b$ have no "time" dependence and consequently

$$q_{\alpha i}(\mathbf{x}) = \int \frac{d\mathbf{p}}{(2\pi)^3}\frac{1}{(2|p_4|)^{1/2}}\ \left[\ a(\mathbf{p},s,c)\ u_{\alpha i}(\mathbf{p},s,c)\ e^{i\mathbf{px}} + b^+(\mathbf{p},s,c)\ v_{\alpha i}(\mathbf{p},s,c)\ e^{-i\mathbf{px}}\right]\ . \tag{4}$$

The stochastic character of gluon field (which we supposed) allows us to develop the approximate description of the state Ψ if the following procedure of averaging $\Psi \to \langle\Psi\rangle = \int_0^t\ d\tau\ \Psi(\tau)/\ t$ is intoduced. With this procedure taken the futher step is to turn to the approach of constructing a density matrix $\langle\overset{*}{\Psi}\Psi\rangle$. However, here we believe that at calculating the ground state (or more generally with quasi-stationary state) it might be sufficiently informative to operate with the averaged amplitude directly. Then in the interaction representation $\Psi = e^{H_0 t}\Phi$ we have the equation for state Φ as $\dot{\Phi} = -V\Phi$, $V = e^{H_0 t}V_S e^{-H_0 t}$. Now the "time" dependence appears in quark operators as well and after averaging over the short-wavelength component one may obtain the following equation

$$\langle\dot{\Phi}(t)\rangle = +\int_0^\infty d\tau\ \langle V(t)V(t-\tau)\rangle\ \langle\Phi(t)\rangle\ . \tag{5}$$

The limitations to have such a factorization validated are well known in the theory of stochastic differential equations (see, for example, [1]). The integration interval in Eq.(5) may be extended to the infinite "time" because of the rapid decrease (supposed) of the corresponding correlation function. Now we are allowed to

e-mail: [a]molodtsov@itep.ru, [b]Gennady.Zinovjev@cern.ch

deal with amplitude $\langle\Phi(t)\rangle$ in the right hand side of Eq.(5) instead the amplitude with the shifted arguments in order to get an ordinary integro-differential equation. In the quantum field theory applications it is usually difficult to construct the correlation function in the most general form. However, if we are going to limit our interest by describing the long-wavelength quark component only then gluon field correlator $\langle A^a_\mu(x)A^b_\nu(y)\rangle$ may be factorized and as a result we have

$$\langle\dot{\Phi}(t)\rangle = \int d\mathbf{x}\ \bar{q}(\mathbf{x},t)\ t^a\gamma_\mu\ q(\mathbf{x},t)\ \int_0^\infty d\tau \int d\mathbf{y}\ \bar{q}(\mathbf{y},t-\tau)\ t^b\gamma_\nu\ q(\mathbf{y},t-\tau)\ g^2\langle A^a_\mu(t,\mathbf{x})A^b_\nu(t-\tau,\mathbf{y})\rangle\ \langle\Phi(t)\rangle\ .$$

Having assumed the correlation function rapidly decreasing in "time" we could ignore all the retarding effects in the quark operators. Turning back to the Schrödinger representation we have for the state amplitude $\chi = e^{-H_0 t}\langle\Phi\rangle$ the following equation

$$\dot{\chi} = -H_{ind}\ \chi\ , \quad \mathcal{H}_{ind} = -\bar{q}\ (i\gamma\nabla + im)\ q - \bar{q}\ t^a\gamma_\mu\ q\ \int d\mathbf{y}\ \bar{q}'\ t^b\gamma_\nu\ q'\ \int_0^\infty d\tau\ g^2\langle A^a_\mu A'^b_\nu\rangle\ , \tag{6}$$

with $q = q(\mathbf{x})$, $\bar{q} = \bar{q}(\mathbf{x})$, $q' = q(\mathbf{y})$, $\bar{q}' = \bar{q}(\mathbf{y})$ and $A^a_\mu = A^a_\mu(t,\mathbf{x})$, $A'^b_\nu = A^b_\nu(t-\tau,\mathbf{y})$. Now the correlation function might be presented as $\int_0^\infty d\tau\ g^2\langle A^a_\mu A'^b_\nu\rangle = \delta^{ab}\ \delta_{\mu\nu}\ I(\mathbf{x}-\mathbf{y}) + J_{\mu\nu}(\mathbf{x}-\mathbf{y})$. In our consideration we ignore the contribution of the second formfactor spanning on the components of the vector $\mathbf{x}-\mathbf{y}$. Thus, on output we receive the Hamiltonian of four-fermion interaction with the formfactor rooted in the presence of two quark currents in the points $\mathbf{x}$ and $\mathbf{y}$. With this form of the effective Hamiltonian we could apply the Hartree–Fock–Bogolyubov method to find its ground state as one constructed by the quark–anti-quark pairs with the oppositely directed momenta

$$|\sigma\rangle = T\ |0\rangle\ , \quad T = \Pi_{p,s,c}\ \exp\left\{\ \frac{\theta}{2}\ \left[\ a^+(\mathbf{p},s,c)\ b^+(-\mathbf{p},s,c) + a(\mathbf{p},s,c)\ b(-\mathbf{p},s,c)\ \right]\ \right\}\ , \tag{7}$$

where the parameter $\theta(\mathbf{p})$ characterizes the pairing strength. Minimizing the mean energy functional one is able to determine the angle θ magnitude $\frac{d\langle\sigma|H_{ind}|\sigma\rangle}{d\theta} = 0$. By the help of dressing tranformation T we introduce the creation and annihilation operators of quasi-particles $A = T\ a\ T^{-1}$, $B = T\ b\ T^{-1}$. Dropping the calculation details out (see Ref. [2]) we present here the following result for the mean energy as a function of the θ angle

$$\begin{aligned}
&\langle\sigma|H_{ind}|\sigma\rangle = -\int \frac{d\mathbf{p}}{(2\pi)^3}\ \frac{2N_c\ p_4^2}{|p_4|}\,(1-\cos\theta) - \\
&-\widetilde{G}\int \frac{d\mathbf{p}d\mathbf{q}}{(2\pi)^6}\left\{-(3\widetilde{I}-\widetilde{J})\frac{p_4\ q_4}{|p_4||q_4|} + (4\widetilde{I}-\widetilde{J})\frac{p\ q}{|p_4||q_4|}\left(\sin\theta - \frac{m}{p}\cos\theta\right)\left(\sin\theta' - \frac{m}{q}\cos\theta'\right) + \right.\\
&\left. +(-2\widetilde{I}\delta_{ij} - 2\widetilde{J}_{ij} + \widetilde{J}\delta_{ij})\ \frac{p_i\ q_j}{|p_4||q_4|}\ \left(\cos\theta + \frac{m}{p}\sin\theta\right)\left(\cos\theta' + \frac{m}{q}\sin\theta'\right)\ \right\}\ ,
\end{aligned} \tag{8}$$

here the following designations are used $p = |\mathbf{p}|$, $q = |\mathbf{q}|$, $\widetilde{I} = \widetilde{I}(\mathbf{p}+\mathbf{q})$, $\widetilde{J}_{ij} = \widetilde{J}_{ij}(\mathbf{p}+\mathbf{q})$, $\widetilde{J} = \sum_{i=1}^3 \widetilde{J}_{ii}$, $p^2 = q^2 = -m^2$, $\theta' = \theta(q)$ where $\widetilde{G}$ is the constant of corresponding four-fermion interaction (the relevant details can be found in [2]). The first integral in Eq. (8) comes from free Hamiltonian, and we make a natural subtraction (adding the unit) in order to have zero mean free energy when the angle of pairing is trivial. **Nambu–Jona-Lasinio model**. In order to get an idea of the parameter scales we continue with handling the model in which the formfactor behaves in the coordinate space as $I(\mathbf{x}-\mathbf{y}) = \delta(\mathbf{x}-\mathbf{y})$, $J_{\mu\nu} = 0$, dropping contribution spanned on the $p_i q_j$ tensor also. Actually, it corresponds to the Nambu–Jona-Lasinio model [3]. As well known the model with such a formfactor requires the regularization and, hence, the cutoff parameter Λ comes to the play

$$W = \int^\Lambda \frac{d\mathbf{p}}{(2\pi)^3}\ \left[|p_4|\,(1-\cos\theta) - G\frac{p}{|p_4|}\left(\sin\theta - \frac{m}{p}\cos\theta\right)\int^\Lambda \frac{d\mathbf{q}}{(2\pi)^3}\,\frac{q}{|q_4|}\left(\sin\theta' - \frac{m}{q}\cos\theta'\right)\right]\ . \tag{9}$$

We adjust the NJL model with the parameter set given by Hatsuda and Kunihiro [3] in which $\Lambda = 631$MeV, $m = 5.5$MeV. One curious point of this model is that the solution for optimal angle θ in the whole interval $p \in [0,\Lambda]$ can be found by solving the simple trigonometrical equation $(p^2+m^2)\ \sin\theta - M_q\,(p\cos\theta + m\sin\theta) = 0$, with the dynamical quark mass $M_q = 2G\ \int^\Lambda \frac{d\mathbf{p}}{(2\pi)^3}\,\frac{p}{|p_4|}\ \left(\sin\theta - \frac{m}{p}\cos\theta\right)$. Eventually the results obtained look like $M_q = -335$ MeV for dynamical quark mass and $\langle\sigma|\bar{q}q|\sigma\rangle = -i\ (245\text{ MeV})^3$ for the quark condensate with the following definition of the quark condensate $\langle\sigma|\bar{q}q|\sigma\rangle = \frac{i\ N_c}{\pi^2}\ \int_0^\infty dp\ \frac{p^2}{|p_4|}\ (p\sin\theta - m\cos\theta)$. **The Keldysh model**. Now we are going to analyse the limit, in some extent, opposite to the NJL model, i.e. we are dealing with the formfactor behaving as a delta function but in the momentum space (analogously the Keldysh model,

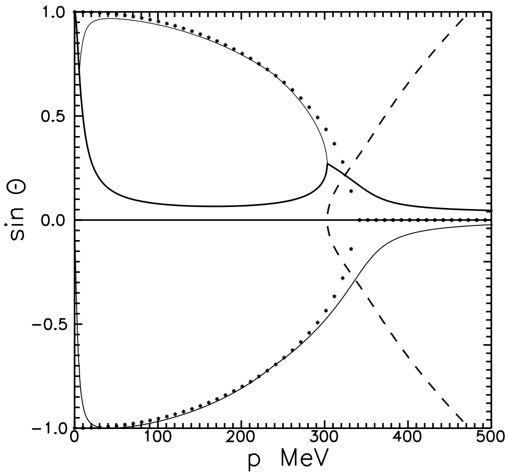

Figure 1. Phase portrait of the Keldysh model, $\sin\theta$ as a function of momentum p(MeV). The dotted curve corresponds to the solution with the negative values of angle in the chiral limit $m = 0$. Dashed line for imaginary values.

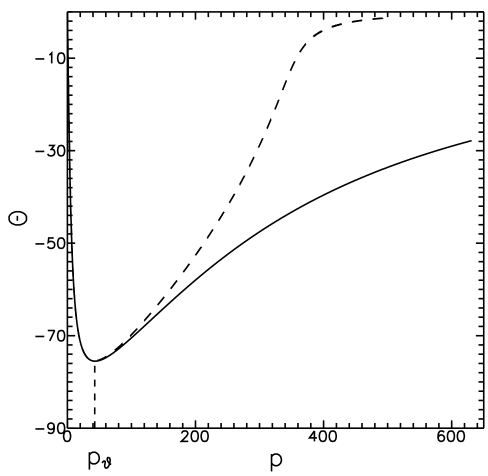

Figure 2. The optimal angle θ as a function of momentum p(MeV). The solid line corresponds to the NJL model and the dashed one to the Keldysh model. The current quark mass is $m = 5.5$ MeV and $p_\theta \sim 40$ MeV.

well known in the physics of condensed matter [4]), $I(\mathbf{p}) = (2\pi)^3\ \delta(\mathbf{p})$. Here the mean energy functional has the following form

$$W(m) = \int \frac{d\mathbf{p}}{(2\pi)^3}\ \left[|p_4|\ \ (1-\cos\theta) - G\ \frac{p^2}{|p_4|^2}\left(\sin\theta - \frac{m}{p}\cos\theta\right)^2\right]\ . \tag{10}$$

contrary to the NJL model there is no need to introduce any cut off. The equation for calculating the optimal angle θ becomes the transcendental one $|p_4|^3\ \sin\theta - 2G\ \ (p\cos\theta + m\sin\theta)\,(p\sin\theta - m\cos\theta) = 0$, and, clearly, it is rather difficult to get its solution in a general form. Fortunately, it is much easier and quite informative to analyse the model in the chiral limit $m = 0$. There exist one trivial solution $\theta = 0$ and two nontrivial ones (for the positive and negative angles) which obey the equation $\cos\theta = \frac{p}{2G}$. Obviously, these solutions are reasonable if the momentum is limited by $p < 2G$. Then for the mean energy (for real solution) we have: $W_\pm(0) = -\frac{G^4}{15\pi^2}$, and for the quark condensate: $\langle\sigma|\bar{q}q|\sigma\rangle(0) = \frac{i\ N_c\ G^3}{2\pi}$. For the trivial solution the mean energy equals to zero together with the quark condensate $W_0(0) = 0$, $\langle\sigma|\bar{q}q|\sigma\rangle_0(0) = 0$. Introducing the practical designation $\sin\theta = \frac{M_\theta}{(p^2+M_\theta^2)^{1/2}}$ which characterizes the pairing strength by the parameter M_θ we have, for example, for the nontrivial solution $M_\theta = \left(4G^2 - p^2\right)^{1/2}$. In order to compare the results with the NJL model we fixed the value of four-fermion interaction constant as $M_\theta(0) = 2G = 335$ MeV. It is interesting to notice that the respective energy becomes constant $E(p) = \sqrt{p^2 + M_\theta^2}$, $E(p) = 2G$.

After having done the analysis in the chiral limit which is shown by the dotted line in Fig.1 we would like to comment the situation beyond this limit. The evolution of corresponding branches is available on the same plot 1. The minimum of mean energy functional can be realized with the piecewise continuous functions. At the local vicinity of coordinate origin we start with some branch of the solution, then relevant solution passes from one possible branch to another one at any subinterval. But in any case there is only one way to continue the real solution at streaming to the infinite limit. As to the functional (10) the contribution of the term proportional to the cosine in the second parenthesis is divergent even if the angle θ is zero. It means the mean energy out of chiral limit goes to an infinity at any nonzero value of quark mass. The same conclusion is valid for the chiral condensate. In principle this functional could be regularized and corresponding continuation might be done but it is out of this presentation scope (see Ref. [2]). It is not difficult to demonstrate the similar discontinuities of functional are present, for example, for Gaussian $I(\mathbf{x}) = G\ \exp\left(-a^2\ \mathbf{x}^2\right)$, and exponential $I(\mathbf{x}) = G\ \exp\left(-a\ |\mathbf{x}|\right)$, formfactors and they are present even in the NJL model but this fact is masked by the cut off parameter. Comparing the optimal angles in the NJL and Keldysh models (see Fig. 2) it is interesting to notice that the formation of quasiparticles becomes significant at some momentum value close to the origin $p_\theta \sim 40$ MeV (for the Gaussian and exponentional formfactors it is around $p_\theta \sim 150$ MeV) but not directly at the zero value. It is clear the inverse value of this parameter determines the characteristic size of quasiparticle.

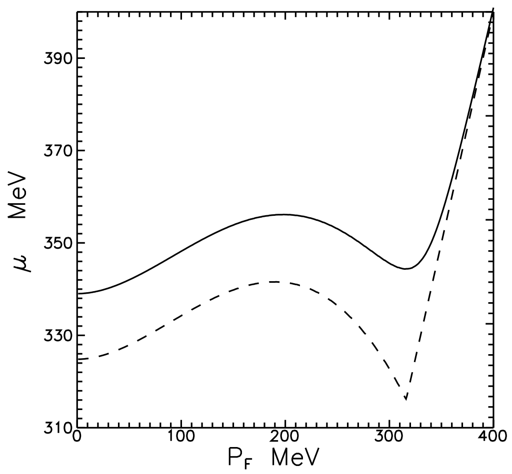

Figure 3. The quark chemical potential as a function of the Fermi momentum for the NJL model. The solid line corresponds to the current quark mass $m = 5.5$ MeV and the dashed one shows the behaviour in the chiral limit.

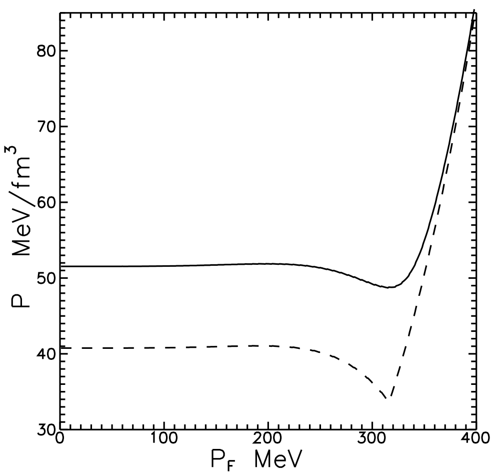

Figure 4. The pressure of the quark ensemble as function of the Fermi momentum. The solid line for the current quark mass $m = 5.5$ MeV. The dashed one—in chiral limit.

Analysing the discontinuity of mean energy functional and quark condensate we face some troubles at fitting the quark condensate, for example. However, the dynamical quark mass and quark condensate are nonobservable quantities and it is curious to remark here that although the mean energy of the quark system is minus infinity the meson observables are finite and even in Keldysh model the mesons are recognizable with reasonable scale and we can in principle make a fit for this observables [5].

Now our central issue could be formulated in the following way — to construct the state filled in by quasi-particles (the Sletter determinant) $|N\rangle = \prod_{|\mathbf{p}|<P_F;s} A^+(\mathbf{P};s)\ |\sigma\rangle$, which possesses the minimal mean energy $\langle N|H|N\rangle$ (surely, we assume the quasi-particles are stable). Here P_F stands for the Fermi momentum and the polarization runs over all possible values. It allows us to optimize the dressing transformation and, as the consequence, to follow up the modifications of quasiparticles being influenced by the process of filling in the Fermi sphere. Eventualy it fixes the form of charge operator (particle number operator) $|\langle N|\bar{q}i\gamma_4 q|N\rangle|$. Let us define the partial energy density per one quark degree of freedom, as $w = \frac{\mathcal{E}}{2N_c}$, $\mathcal{E} = E/V$ where E is the total energy of ensemble. For the ensemble of quasi-particles we obtain the following expression for the partial energy

$$\begin{aligned}\langle N|w|N\rangle = \int^{P_F} \frac{d\mathbf{p}}{(2\pi)^3}|p_4| + \int_{P_F} \frac{d\mathbf{p}}{(2\pi)^3}|p_4|(1-\cos\theta) - \\ - G\int_{P_F} \frac{d\mathbf{p}}{(2\pi)^3}\ \frac{p}{|p_4|}\ \left(\sin\theta - \frac{m}{p}\cos\theta\right)\int_{P_F} \frac{d\mathbf{q}}{(2\pi)^3}\ \frac{q}{|q_4|}\ \left(\sin\theta' - \frac{m}{q}\cos\theta'\right)\ \widetilde{I}\ .\end{aligned} \tag{11}$$

It could have ruther interesting interpretation if compared to the vacuum mean energy Eq.(8). It is easy to see that for the state with the filled-in Fermi sphere the angles of pairing could be defined by the condition of functional minimum (11) only for the momenta larger than Fermi momentum P_F. Then the quarks composing the Fermi sphere look like the free (non-interacting) ones, as seen from the first term of Eq. (11). Now let us calculate the quark chemical potential which, by definition, is an energy necessary for adding (removing) one quasi-particle to (from) a system $\mu = \frac{\partial E}{\partial N}$, where $N = 2N_c\ V\ \int^{P_F} \frac{d\mathbf{p}}{(2\pi)^3} = \frac{N_c}{3\pi^2}\ V\ P_F^3$ is the total number of particles in the volume V. Redefining the chemical potential as $\mu = \frac{2\pi^2}{P_F^2}\ \frac{\partial w}{\partial P_F}$ we consider the model with correlation function behaving as the δ-function in the coordinate space, which corresponds to NJL model. The following relation could be obtained in this case (see Ref. [6])

$$\mu = [P_F^2 + M_q^2]^{1/2}\ .$$

Let us remind that for the free fermion gas the chemical potential increases monotonically with the Fermi momentum growing. The curious feature of the NJL model is the appearance of state almost degenerate with the vacuum state while the process of filling up the Fermi sphere reaches to the momenta close to the dynamical quark mass value (the similar value is peculiar to the momentum of quark inside a baryon), see Fig. 3. This state density with the factor 3 (which expresses the relation between baryonic and quark degrees of freedom) absorbed corresponds to a normal nuclear density ($n \sim 0.12/\mathrm{fm}^3$), and chiral condensate could be estimated as $| < \bar{q}q >^{1/3} | \sim 100$ MeV. In the chiral limit the chemical potential is close to the discussed point and is even smaller than the vacuum one. The full coincidence of the chemical potentials occurs at the values of current quark mass around 2 MeV. In fact, Fig. 3 shows that the u quark bond looks stronger than one of the d quark. The pressure of the quark ensemble $P = -\frac{dE}{dV} = -\frac{\partial E}{\partial V} + \frac{P_F}{3V} \frac{\partial E}{\partial P_F} = -\mathcal{E} + \mu\ n$, is depicted in Fig. 4 as a function of the Fermi momentum where $n = N/V$ is the quark density. The quark pressure at the values of the Fermi momentum close to the quantity of dynamical quark mass is approximately degenerate with the vacuum pressure (slightly lower than the vacuum one). The vacuum density is of order 40—50 MeV/fm^3 and corresponds well to the value extracted from the bag models. Apparently our estimate of the effects responding to the process of filling up the Fermi sphere entails a hope to understand a routine feature of hadron world, namely, the fact of quark equilibrium in the vacuum and inside the proton. The chemical potential degeneracy and specific behaviour of the quark pressure (with one new essential element which is just the presence of instability region $dP/dP_F < 0$) justify, in principle, the conventional bag model. It urges to consider the filled states $|N\rangle$ as natural 'building' material for baryon octet (on the strong interaction scale only).

Acknowledgements. We are grateful to the Organizers and personally professor V. Skalozub for a nice meeting and kind invitation to present our results. This work was supported by the INTAS Grant 04-84-398 and the Grant of National Academy of Sciences of Ukraine.

References

[1] N. G. Van Kampen, Phys. Rep. **24**, 171 (1976).
[2] S. V. Molodtsov, G. M. Zinovjev, Teor. Mat. Fiz., **160** (2009) 444, ArXiv:0811.4405.
[3] M. K. Volkov, A. E. Radzhabov, Phys. Usp. **176**, 569 (2006);
T. Hatsuda and T. Kunihiro, Phys. Rep. **247**, 221 (1994).
[4] L. V. Keldysh, Doctor. Thesis (FIAN, 1965);
E. V. Kane, Phys. Rev. **131**, 79 (1963);
V. L. Bonch-Bruevich, in *Physics of solid states*, M., VINITI, 1965.
[5] S. V. Molodtsov, M. K. Volkov, G. M. Zinovjev, Teor. Mat. Fiz., in print, ArXiv:0812.2666.
[6] S. V. Molodtsov, G. M. Zinovjev, ArXiv:0812.4122.

Proceedings of the International School-seminar
"New Physics and Quantum Chromodynamics at external Conditions", pp. 127 – 131,
3-6 May 2009, Dnipropetrovsk, Ukraine

SPIN IDENTIFICATION OF THE HEAVY RESONANCES IN ATLAS EXPERIMENT AT THE CERN LHC

I. A. Serenkova [a], A. V. Tsytrinov[b], A. A. Pankov [c]

The Abdus Salam ICTP Affiliated Centre, Technical University of Gomel, 246746 Gomel, Belarus

Once a new heavy resonance is observed as a peak in the cross section, one should distinguish among the different underlying non-standard interactions that may in principle produce a similar effect. The spin of the objects exchanged in the various novel interactions is a relevant aspect in this regard. We here discuss the expectations on the identification reach on the spin-2 Randall-Sundrum resonances, characterizing gravity with one warped extra dimension, against spin-1 and spin-0 non-standard exchanges with the same mass. We focus on the electron pair production process at the LHC with ATLAS using fast detector simulation . We find the discovery(identification) reaches of the gravitons at the 5σ level (95% C.L.) at the LHC for a time-integrated luminosity of $100\,\mathrm{fb}^{-1}$ in the ATLAS experiment that are 2.1 TeV (1.2 TeV) and 3.9 TeV (2.9 TeV) for k/M_{Pl}=0.01 and 0.1, respectively.

1 Introduction

Heavy quantum states, with masses $M \gg M_{W,Z}$, are generally predicted by new physics (NP) models. If the masses are in the TeV range, such non-standard objects could be directly revealed as peaks, or resonances, in the cross sections for reactions among standard model (SM) particles at supercolliders.

The *discovery reach* represents the upper limit of the mass range where a peak can be observed experimentally. It depends, among other things, on the collider energy and the expected statistics, and determines an accessible region for the NP model parameters. However, once a peak is observed, the determination of the underlying model against others, potentially giving the same mass and number of events, is needed. Accordingly, for any model, the *identification reach* defines the upper limit of the mass range where the source of the peak can be determined or, equivalently, the competitor models can be excluded for all values of their parameters. Clearly, the identification reach is expected to select a subdomain of the model parameters accessible to discovery.

The resonance spin represents a powerful discriminating observable in this regard. Popular examples of NP scenarios that can produce (narrow) peaks in cross sections with the same mass and number of events, and can be discriminated by a spin analysis are: *i)* Models of gravity in extra spatial dimensions (spin-2); *ii)* Models with heavy neutral gauge bosons Z' (spin-1); and *iii)* SUSY models with R-parity breaking sneutrino couplings (spin-0). Here, we discuss the identification reach on the lowest-lying, spin-2, Randall-Sundrum (RS) graviton resonance [1], against *both* the spin-1 and spin-0 hypotheses, that can be obtained from the experimental study of the inclusive dielectron production process at LHC:

$$p + p \to e^+e^- + X. \tag{1}$$

While the total resonant cross section, integrated over the dilepton invariant mass under the peak at $M = M_G$, determines the number of events, hence the discovery reach

2 New physics models

RS model of gravity in extra dimensions. This scenario is a candidate solution to the gauge hierarchy problem, and its simplest version is based on one compactified 'warped' spatial extra dimension and a two-brane setup. The SM particles are localized to the TeV brane, gravity can propagate in the full 5-dimensional bulk and in particular, on the Planck brane, has an effective scale determined by $\overline{M}_{\rm Pl} = 1/\sqrt{8\pi G_{\rm N}} = 2.44 \times 10^{18}$ TeV. On the TeV brane the gravity scale Λ_π is suppressed by the exponential 'warp' factor, $\Lambda_\pi = \overline{M}_{\rm Pl}\exp(-\pi k R_c)$, with $k \sim \overline{M}_{\rm Pl}$ the 5-dimensional curvature and R_c the compactification radius. Boundary conditions at the branes determine a tower of spin-2 graviton resonances $G^{(n)}$ $(n \geq 1)$. Their predicted mass spectrum is $M_n = M_1 x_n/x_1$ with M_1 the lowest resonance mass and x_n the roots of the Bessel function $J_1(x_n) = 0$. Their

e-mail: [a]inna.serenkova@cern.ch, [b]tsytrin@rambler.ru, [c]pankov@ictp.it

TeV brane couplings to the SM particles are given by

$$-\mathcal{L}_{\mathrm{TeV}} = \left[\frac{1}{\overline{M}_{\mathrm{Pl}}} G^{(0)}_{\mu\nu}(x) + \frac{1}{\Lambda_\pi}\sum_{n=1}^{\infty} G^{(n)}_{\mu\nu}(x)\right] T^{\mu\nu}(x), \tag{2}$$

where $T^{\mu\nu}$ is the energy-momentum tensor and $G^{(0)}$ denotes the zero-mode, ordinary, graviton. For $kR_c \simeq 12$, Λ_π as well as the masses M_n (through the relation $M_1 = \Lambda_\pi k x_1/\overline{M}_{\mathrm{Pl}}$) are $\mathcal{O}(\mathrm{TeV})$. This opens up the interesting possibility of observing gravity effects at colliders, in particular to reveal the graviton excitation exchange in the process 1. The contributing, tree level, partonic processes

$$q\bar{q} \to G \to e^+e^- \qquad \text{and} \qquad gg \to G \to e^+e^- \tag{3}$$

should yield cross-section peaks at the invariant dilepton mass $M = M_n$, with characteristic angular distributions [2].

The RS model thus depends on two independent parameters, that can be chosen as $M_G \equiv M_1$ and the universal 'coupling' $c = k/\overline{M}_{\mathrm{Pl}}$ (in which case Λ_π is a derived parameter). Theoretically 'natural' limits are $0.01 \le c \le 0.1$ and $\Lambda_\pi < 10$ TeV [3]. Current 95% C.L. experimental lower limits on M_G, from the Tevatron collider, range from 300 GeV ($c = 0.01$) to 900 GeV ($c = 0.1$) [4]. One should notice that the unevenly spaced spectrum could be distinctive of the model by itself. However, in practice, due to the large masses involved, only the first RS resonance might be accessible at LHC, so that the spin-2 determination should be a necessary test of the RS model.

Heavy neutral gauge bosons. Turning to spin-1 exchanges in the process 1, Z's generally occur in electroweak models based on extended gauge symmetries. The leading-order partonic process, $q\bar{q} \to Z' \to e^+e^-$, should show up as a peak in the dilepton invariant mass distribution at $M = M_{Z'}$ with, in this case, the *same* angular distribution as the SM γ and Z exchanges. Besides the mass $M_{Z'}$, the model parameters are the vector and axial-vector Z' couplings to quarks and leptons. Popular scenarios are the cases where such couplings are specified theoretically: the list includes Z'_χ, Z'_ψ, Z'_η, Z'_{LR}, Z'_{ALR} models, and the 'sequential' Z'_{SSM} model with the same couplings as the SM. Details can be found, *e.g.*, in the recent Ref. [5]. It turns out that, at the assumed LHC luminosity, the spin-2 RS resonance can be distinguished from the ALR and SSM spin-1 scenarios already at the level of signal events [6]. For the other Z' models, there are 'confusion regions' in the parameter spaces where spin-2 and spin-1 exchanges give rise to the same peaks and number of events, and therefore can be distinguished by a spin analysis only. Current experimental, model-dependent, lower limits on $M_{Z'}$, from the Tevatron collider, are in the range 500-900 GeV [7].

Sneutrino exchange. In SUSY theories with R-parity breaking, sparticles can be exchanged in the process 1 and appear as peaks in the dilepton invariant mass. This is the case of the spin-0 sneutrino formation by quark-antiquark annihilation, followed by leptonic decay [8]: $q\bar{q} \to \tilde{\nu} \to e^+e^-$. At the peak in the dilepton invariant mass, $M = M_{\tilde{\nu}}$, the spin-0 character implies a flat angular distribution. Basically, the cross section in this model depends on $M_{\tilde{\nu}}$ and on the product $X = (\lambda')^2 B_l$, where λ' is the R-parity breaking sneutrino coupling to $d\bar{d}$ and B_l the sneutrino leptonic branching ratio. Current constraints on X are very loose, and there exists an extended domain where $\tilde{\nu}$ production can mimic RS resonance formation (same mass and number of events under the peak), for details see [6].

3 Discovery and identification of Randall-Sundrum graviton resonance

Simulations were done with ATLFAST (ATHENA 12.0.6) to produce gravitons in proton-proton collisions at 14 TeV centre-of-mass energy. This version PYTHIA [9] uses the CTEQ6L parton distribution function. For illustrative purposes Fig.1 shows the invariant mass distribution of lepton pairs from a 1.5 TeV graviton simulation (with c=0.01) obtained with ATHENA(PYTHIA). The number of events shown correspond to one year of the LHC running at the design luminosity of 10^{34} cm^{-2}s^{-1} giving an integrated luminosity of 100 fb^{-1}. Also, in numerical computation we have assumed a uniform efficiency of reconstruction of lepton pairs of order 0.9. Graviton can be seen as a peak in the invariant mass distribution of leptons.

The process 3 must be detected above the background from the SM processes $pp \to \gamma, Z \to e^+e^- + X$. The dielectron channel will be analyzed at the LHC in the ATLAS and CMS detectors, and as is discussed below, both detectors have the ability to probe the narrow graviton resonance [10]. Experimentally, the discovery of a narrow resonance depends to a significant degree on the bin size for data collection with the chance of detection increasing with a decreasing bin size. This is so because the integral over the bin is effectively independent of the bin size for the signal (assuming the narrow resonance falls within the bin). However, this integral is essentially linearly dependent on the bin size for the SM background. In the analysis of the SM background we have included the Z, γ, and $\gamma - Z$ interference terms in the Drell-Yan analysis, but have not included the backgrounds from other sources such as from $t\bar{t}, b\bar{b}, WW, WZ, ZZ$ etc. However, these backgrounds are

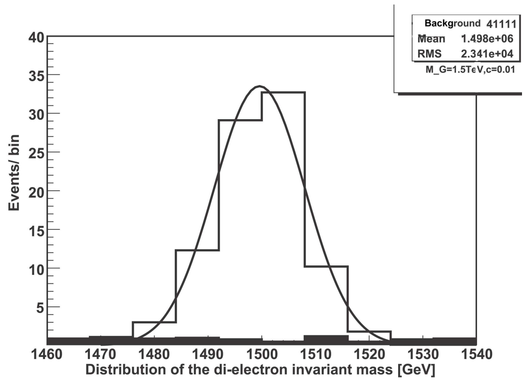

Figure 1. Distribution of the di-electron invariant mass for resonant graviton production with $M_G = 1.5$ TeV, $k/\bar{M}_{Pl} = 0.01$ ($c = k/\bar{M}_{Pl}$) and Drell-Yan background at the LHC.

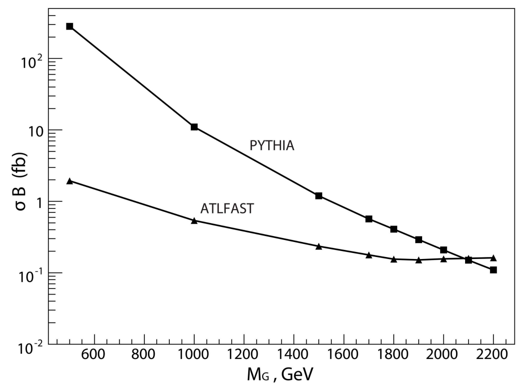

Figure 2. The cross section times leptonic branching fraction, $\sigma \cdot B$, for $G \to l^+l^-$ in the RS model cross-section with $c = 0.01$ and the smallest detectable cross section times branching ratio $(\sigma \cdot B)_{min}$.

known to be at best a few percent of the Drell-Yan background [11]. Regarding the bin size, it depends on the energy resolution σ_E/E of the calorimeter. For an electromagnetic calorimeter the energy resolution is typically parameterized by $\sigma_E/E = a/\sqrt{E} \oplus b \oplus c/E$ where addition in quadrature is implied [12]. The term proportional to $1/\sqrt{E}$ is the so called stochastic term and arises from statistic related fluctuations. The term b is due to detector non-uniformity and calibration errors, and the term c is due mostly to noise. For the ATLAS detector (liquid Ar/Pb) the energy resolution is parameterized by [12] $\sigma_E = 10\%/\sqrt{E} \oplus .4\% \oplus .3/E$, where E is in units of GeV. From the above we find the following relations for the bin size B (taken to be $6\sigma_E$) at the mass scale M (M is measured in units of TeV)

$$\mathrm{B}_{\mathrm{ATLAS}} = 24(0.625M + M^2 + 0.0056)^{1/2}\mathrm{GeV}. \tag{4}$$

For $M > 3$ TeV, the M^2 term dominates in Eq. (4) and the bin size goes linearly in M, so $\mathrm{B}_{\mathrm{ATLAS}} \sim 24M$ GeV for large M.

The sensitivity for graviton G detection was studied in several of the possible decay channels. The decay to two electrons is considered the most promising discovery channel. It has a low branching ratio of about 2%, but a very clear signature of two back-to-back high p_T electrons with an invariant mass equal to the mass of the G. The background from SM processes is small, mostly originating from the high-mass tail of the Drell-Yan spectrum.

In Fig.2 we give the discovery reach for finding graviton resonance G with $c = 0.01$ as a function of M_G for integrated luminosity of 100 fb^{-1}. The criterion used for the discovery limit in the analysis given here is an assumption that $5\sqrt{N_B}$ events or 10 events, whichever is larger, constitutes a signal where N_B is the SM background, and we have scaled the bin size with M_G appropriate for the ATLAS detector. With an assumption of efficiencies as stated above, one finds that with 100 fb^{-1} of integrated luminosity, one can explore G up to about 2.1 TeV with $c = 0.01$.

Angular distributions in the C-M frame of the final dilepton state give clear signatures of the spin of the produced particle in the Drell-Yan process. Thus angular distributions are a powerful tool in distinguishing the spin-2 particle G from Z' spin-1 and spin-0 (sneutrino). The CDF group has already carried out angular distribution analyses [13] using the cumulative data at the Tevatron and more detailed analyses are likely to follow. Similar analyses at the LHC would allow one to investigate the spin of an observed resonance with much more data. In the following we give a relative comparison of the angular distributions arising from the Z' and from scalar sneutrino and also from the massive gravtion of warped geometry. The angular distributions for spin-2 G, spin-1 Z' and spin-0 $\tilde{\nu}$ are shown in Fig.3.

To quantify the distinction between spin-2 , spin-1 and spin-0 resonances it is conveniently to use an integrated asymmetry, center-edge asymmetry [14, 15, 16] which can be written in parton level as follows:

$$\hat{\sigma}_{\mathrm{CE}} \equiv \left[\int_{-z^*}^{z^*} - \left(\int_{-1}^{-z^*} + \int_{z^*}^{1} \right) \right] \frac{d\hat{\sigma}}{dz}\, dz, \quad \hat{\sigma} \equiv \int_{-1}^{1} \frac{d\hat{\sigma}}{dz}\, dz, \tag{5}$$

where $z = \cos\theta_{\mathrm{cm}}$, with θ_{cm} the angle, in the c.m. frame of the two leptons, between the lepton and the proton. Here, $0 < z^* < 1$ is a parameter which defines the border between the "center" and the "edge" regions. The

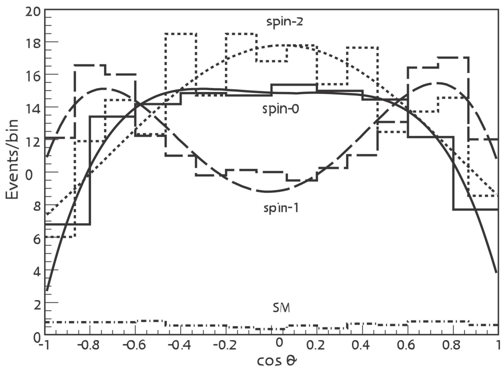

Figure 3. Angular distribution of leptons in the dilepton center-of-mass system for spin-2 graviton resonant production in the RS model with ; spin-0 (sneutrino) resonant production and spin-1 (Z') resonant production with same number of events at $M_G = M_{Z'} = M_{\tilde{\nu}} = 1.5$ TeV

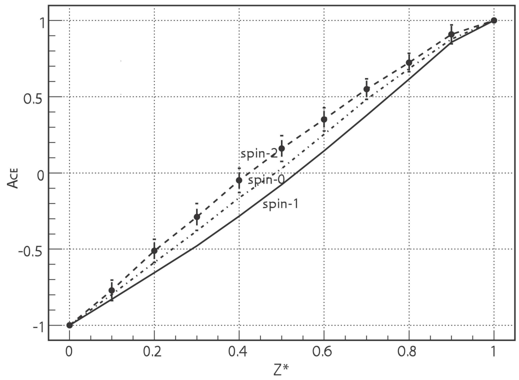

Figure 4. Center-egde asymmetry A_{CE} as a function of kinematical parameters z^* for spin-1 Z', spin-2 G at $c = 0.01$ and spin-0 $\tilde{\nu}$ and $M_{Z'} = M_G = M_{\tilde{\nu}} = 1.5$ TeV.

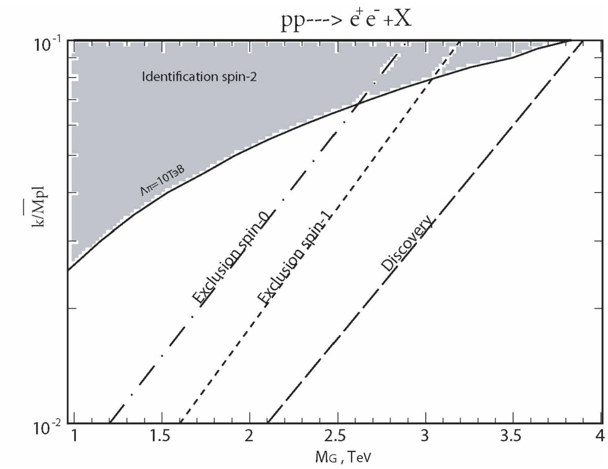

Figure 5. Discovery limits and identification reaches (95% C.L.) on the spin-2 graviton parameters in the plane (M_G, c) , using center-edge asymmetry at the LHC with integrated luminosity of $100 fb^{-1}$.

center–edge asymmetry can then for a given dilepton invariant mass M be defined as

$$A_{\rm CE}(M) = \frac{d\sigma_{\rm CE}/dM}{d\sigma/dM}, \tag{6}$$

where a convolution over parton momenta is performed, and we obtain $d\sigma_{\rm CE}/dM$ and $d\sigma/dM$ from the inclusive differential cross sections $d\sigma_{\rm CE}/dM\,dy\,dz$ and $d\sigma/dM\,dy\,dz$, respectively, by integrating over z and over rapidity y between $-Y$ and Y, with $Y = \log(\sqrt{s}/M)$ [15]. The center-egde asymmetry A_{CE} as a function of kinematical parameters z^* for spin-1 Z', spin-2 G at $c = 0.01$ and spin-0 $\tilde{\nu}$ and $M_{Z'} = M_G = M_{\tilde{\nu}} = 1.5$ TeV are shown on Fig.4. In Fig. 5 shows identification reaches (95% C.L.) on the spin-2 graviton parameters in the plane (M_G, c) , using center-edge asymmetry at the LHC with integrated luminosity of $100 fb^{-1}$ obtained from the conventional χ^2 - analysis and discovery criterion is an assumption that $5\sqrt{N_B}$ events or 10 events, whichever is larger, constitutes a signal where N_B is the SM background.

In conclusion, we have considered the RS scenario parametrized by M_G and $k/\bar{M}_{\rm Pl}$.We find the discovery (identification) reaches of the gravitons at the 5σ level (95% C.L.) at the LHC in the ATLAS experiment that are 2.1 TeV (1.2 TeV) and 3.9 TeV (2.9 TeV) for $k/\bar{M}_{Pl}$ and 0.1, respectively.

Acknowledgements. This work is partially supported by the ICTP through the OEA-Affiliated Centre-AC88 and also the Belarusian Republican Foundation for Fundamental Research .

References

[1] L. Randall and R. Sundrum, *Phys. Rev. Lett.* **83**, 3370 (1999); **83**, 4690 (1999).

[2] T. Han, J. D. Lykken and R. J. Zhang, *Phys. Rev. D* **59**, 105006 (1999); G. F. Giudice, R. Rattazzi and J. D. Wells, *Nucl. Phys. B* **544**, 3 (1999).

[3] H. Davoudiasl, J. L. Hewett and T. G. Rizzo, *Phys. Rev. Lett.* **84**, 2080 (2000); *Phys. Rev. D* **63**, 075004 (2001);

[4] V. M. Abazov *et al.* [D0 Collaboration], *Phys. Rev. Lett.* **100**, 091802 (2008).

[5] P. Langacker, arXiv:0801.1345 [hep-ph].

[6] P. Osland, A. A. Pankov, N. Paver and A. V. Tsytrinov, *Phys. Rev. D* **78**, 035008 (2008).

[7] T. Aaltonen *et al.* [CDF Collaboration], *Phys. Rev. Lett.* **99**, 171802 (2007).

[8] J. Kalinowski, R. Ruckl, H. Spiesberger and P. M. Zerwas, *Phys. Lett. B* **406**, 314 (1997); **414**, 297 (1997); T. G. Rizzo, *Phys. Rev. D* **59**, 113004 (1999).

[9] T. Sjostrand *et al.*, Comput. Phys. Commun. **135**, 238 (2001), LU TP 00-30.

[10] ATLAS Collaboration, Reports No. CERN-LHCC-99-14, CERN-LHCC-99-15.

[11] R. Cousins, J. Mumford, V. Valuev, "Detection of Z' gauge bosons in the dimuon decay mode" in CMS, CMS Note 2005/002.

[12] The Review of Particle Physics, W.-M. Yao et al., Journal of Physics, G 33, 1 (2006).

[13] A. Abulencia *et al.* [CDF Collaboration], Phys. Rev. Lett. **96**, 211801 (2006) [arXiv:hep-ex/0602045].

[14] P. Osland, A. A. Pankov and N. Paver, Phys. Rev. D **68**, 015007 (2003) [arXiv:hep-ph/0304123].

[15] E. W. Dvergsnes, P. Osland, A. A. Pankov and N. Paver, *Phys. Rev.* D **69**, 115001 (2004).

[16] E. W. Dvergsnes, P. Osland, A. A. Pankov and N. Paver, *Int. J. Mod. Phys.* A **20** 2232 (2005).

Proceedings of the International School-seminar
"New Physics and Quantum Chromodynamics at external Conditions", pp. 132 – 136,
3-6 May 2009, Dnipropetrovsk, Ukraine

RELATIVISTIC GENERALIZATION OF THE THRESHOLD S-FACTOR

O. P. Solovtsova[a]

Gomel State Technical University, Belarus

The new relativistic Coulomb-like threshold resummation S-factor in quantum chromodynamics is presented. The consideration is given within the framework of quasipotential approach in quantum field theory which is formulated in relativistic configuration representation for two particles of unequal masses.

1 Introduction

As is well known, a description of quark-antiquark systems close to threshold does not permit us to cut off the perturbative series even if the expansion parameter, the QCD coupling constant α_s, is small [1, 2]. The reason consist in that the real expansion parameter in the threshold region is α_s/v, where $v = \sqrt{1-4m^2/s}$ is a quark velocity and m is a quark mass. To obtain a meaningful result, these threshold singularities of the form $(\alpha_s/v)^n$ have to be summarized. In the nonrelativistic case, for the Coulomb interaction

$$V(r) = -\frac{\alpha}{r} \tag{1}$$

this resummation is realized by the known Gamov–Sommerfeld–Sakharov S-factor [3, 4, 5]

$$S_{\rm nr} = \frac{X_{\rm nr}}{1-\exp(-X_{\rm nr})}\,, \qquad X_{\rm nr} = \frac{\pi\,\alpha}{v_{\rm nr}}\,, \tag{2}$$

which is related to the wave function of the continuous spectrum at the origin by $|\psi(0)|^2$. Here $2\,v_{\rm nr}$ is the relative velocity of two nonrelativistic particles.

In the relativistic theory the nonrelativistic approximation needs to be modified. The relativistic modification of the S-factor (2) in QCD in the case of two particles of equal masses ($m_1 = m_2 = m$) was executed in Ref. [6] and it consisted in the change $v_{\rm nr} \to v$. This factor was used for the description of effects close to the threshold of pair production in the processes $e^+e^- \to t\bar{t}$ and $e^+e^- \to W^+W^-$ [7]. Just the same form of the S-factor for the interaction of two particles of equal masses was later suggested in Ref. [8]. The relativistic S-factor for two particles of arbitrary masses ($m_1 \neq m_2$) we are interested in was presented in Ref. [9]. This factor was derived within the framework of relativistic quantum mechanics on the basis of the Schrödinger equation.

The new step to relativistic generalization of the S-factor in the case of two particles of equal masses was made by Milton and Solovtsov in Ref. [10]. For this purpose, the relativistic quasipotential (RQP) approach proposed by Logunov and Tavkhelidze [11] in the form suggested by Kadyshevsky [12] turned out to be convenient. This approach gives the following expression for the relativistic S-factor:

$$S(\chi) = \frac{X(\chi)}{1-\exp\left[-X(\chi)\right]}\,, \qquad X(\chi) = \frac{\pi\,\alpha}{\sinh\chi}\,, \tag{3}$$

where χ is the rapidity related to the total c. m. energy of interacting particles $\sqrt{s}$ by $2m\cosh\chi = \sqrt{s}$. The function $X(\chi)$ in Eq. (3) can be expressed in terms of v as $X(\chi) = \pi\,\alpha\sqrt{1-v^2}/v$.

The resummation factor appears in the parametrization of the imaginary part of the quark current correlator, the Drell ratio $R(s)$, which can be approximated in terms of the Bethe-Salpeter (BS) amplitude of two charged particles $\chi_{\rm BS}(x)$ at $x = 0$. The nonrelativistic replacement of this amplitude by the wave function, which obeys the Schrödinger equation with the Coulomb potential (1), leads to formula (2) with a substitution $\alpha \to 4\,\alpha_s/3$ for the QCD case. The possibility of using the QP approach for our task is based on the fact that the BS amplitude, which parameterizes the physical quantity $R(s)$, is taken at $x = 0$; therefore, in particular, at the relative time $\tau = 0$.

Applications of the Eq. (3) for describing some hadronic processes can be found in Refs. [13, 14]. Recently, the relativistic S-factor (3) has been applied to reanalyze the mass limits obtained for magnetic monopoles which might have been produced at the Fermilab Tevatron [15].

The purpose of this work is to generalize the previous study started in Ref. [10] to the case of the interaction of two particles of unequal masses ($m_1 \neq m_2$) and compare to other known forms [6, 7, 8, 9, 16].

We dedicate this paper to the memory of our scientific leader I. L. Solovtsov.

e-mail: [a]solovtsov@gstu.gomel.by

2 The integral form of the quasipotential equation: the case of two particles of unequal masses

A starting point is the QP equation in the momentum space constructed in Ref. [17] for the RQP wave function $\Psi_{q'}(\mathbf{p}')$ of two relativistic particles of unequal masses:

$$(2E_{q'}\,-\,2E_{p'})\,\Psi_{q'}(\mathbf{p}')=\frac{2\,\mu}{m'\,(2\pi)^3}\int d\Omega_{k'}\,\widetilde{V}\,(\mathbf{p}'\,,\mathbf{k}';\,E_{q'})\,\Psi_{q'}(\mathbf{k}')\,, \tag{4}$$

where $d\Omega_{k'}=m'\,d\mathbf{k}'/E_{k'}$ is the relativistic three-dimensional volume element in the Lobachevsky space, $E_{k'}=\sqrt{m'^{\,2}+\mathbf{k}'^{\,2}}$, $m'=\sqrt{m_1\,m_2}$, and $\mu=m_1\,m_2/(m_1+m_2)$ is the usual reduced mass. Equation (4) represents a relativistic generalization of the Lippmann-Schwinger equation in the spirit of the Lobachevsky geometry which is realized on the upper half of the mass hyperboloid $E_{k'}^2-\mathbf{k}'^{\,2}=m'^{\,2}$. This equation describes the scattering over the quasipotential $\widetilde{V}\,(\mathbf{p}',\,\mathbf{k}';\,E_{q'})$ of an effective relativistic particle having mass m' and a relative 3-momentum $\mathbf{k}'$, emerging instead of the system of two particles and carrying the total c. m. energy of the interacting particles, $\sqrt{s}$, proportional to the energy $E_{k'}$ of one effective relativistic particle of mass m':

$$\sqrt{s}=\sqrt{{m_1}^2+\mathbf{k}^2}+\sqrt{{m_2}^2+\mathbf{k}^2}=\frac{m'}{\mu}E_{k'},\qquad E_{k'}=\sqrt{m'^{\,2}+\mathbf{k}'^{\,2}}. \tag{5}$$

The proper Lorentz transformations mean a translation in the Lobachevsky space. The role of the plane waves corresponding to these translations are played by the following functions:

$$\xi(\mathbf{p}'\,,\mathbf{r})=\left(\frac{E_{p'}-\mathbf{p}'\cdot\mathbf{n}}{m'}\right)^{-1-ir\,m'}\,, \tag{6}$$

where the module of the radius-vector, $\mathbf{r}$, $(\mathbf{r}=r\,\mathbf{n}\,,|\mathbf{n}|=\mathbf{1})$ is a relativistic invariant [18].

The application of Shapiro transformations (or ξ-transformations) to Eq. (4) leads to the equation which is the integral form of the relativistic Schrödinger equation in the configuration representation:

$$\frac{1}{(2\pi)^3}\int d\Omega_{p'}\,\left(2E_{q'}-2E_{p'}\right)\,\xi(\mathbf{p}'\,,\mathbf{r})\int d\mathbf{r}'\,\xi^*(\mathbf{p}'\,,\mathbf{r}')\,\psi_{q'}(\mathbf{r}')=\frac{2\mu}{m'}\,V(r)\,\psi_{q'}(\mathbf{r})\,, \tag{7}$$

where the right-hand side is already local in the configuration representation and the transform of the potential, $V(r)$, is given in terms of the same relativistic plane waves.

The integral equation (7) can be reduced to the form

$$\frac{1}{(2\pi)^3}\int d\Omega_p\,\left(2E_q-2E_p\right)\,\xi(\mathbf{p}\,,\boldsymbol{\rho})\int d\boldsymbol{\rho}'\,\xi^*(\mathbf{p}\,,\boldsymbol{\rho}')\,\psi_q(\boldsymbol{\rho}')=\frac{2\,\mu}{m'}\,V(\rho)\,\psi_q(\boldsymbol{\rho})\,, \tag{8}$$

where we introduced the following notation:

$$\begin{gathered}
\mathbf{q}'=m'\,\mathbf{q}\,,\mathbf{p}'=m'\,\mathbf{p}\,,\mathbf{q}=\sinh(\chi_q)\,\mathbf{n}_q\,,\mathbf{p}=\sinh(\chi_p)\,\mathbf{n}_p\,,|\mathbf{n}_q|=|\mathbf{n}_p|=1\,,\\
\boldsymbol{\rho}=m'\,\mathbf{r}\,,\boldsymbol{\rho}'=m'\,\mathbf{r}'\,,\,\rho=m'\,r\,,\,\rho'=m'\,r'\,,\\
d\mathbf{r}'=m'^{-3}\,d\boldsymbol{\rho}'\,,d\Omega_{p'}=m'^3\,d\Omega_p\,,d\Omega_p=\frac{d\mathbf{p}}{E_p}\,,E_{q'}=m'\,E_q\,,E_{p'}=m'\,E_p\,,\\
E_q=\sqrt{1+\mathbf{q}^2}\,,E_p=\sqrt{1+\mathbf{p}^2}\,,\,\xi(\mathbf{p}'\,,\mathbf{r})=\left(E_p-\mathbf{p}\cdot\mathbf{n}\right)^{-1-i\rho}\equiv\xi(\mathbf{p}\,,\boldsymbol{\rho})\,,\\
V(r)=V(\rho/m')\equiv m'\,V(\rho)\,,\psi_{q'}(\mathbf{r})=\psi_{m'\,q}(\boldsymbol{\rho}/m')\equiv\psi_q(\boldsymbol{\rho})\,,\Psi_{q'}(\mathbf{p}')\equiv m'^{-3}\,\Psi_q(\mathbf{p})\,.
\end{gathered} \tag{9}$$

Equation (8) is transformed to

$$\begin{aligned}
&\frac{2}{\pi}\int\limits_0^\infty d\chi'\frac{(\sinh\chi')^{2\ell+2}\,(-1)^{\ell+1}}{\rho^{(\ell+1)}}\,(2\cosh\chi-2\cosh\chi')\left(\frac{d}{d\cosh\chi'}\right)^{\ell}\left(\frac{\sin\rho\chi'}{\sinh\chi'}\right)\times\\
&\times\left(\frac{d}{d\cosh\chi'}\right)^{\ell}\frac{1}{\sinh\chi'}\int\limits_0^\infty d\rho'\frac{\rho'\,\sin\rho'\chi'}{(-\rho')^{(\ell+1)}}\,\varphi_\ell(\rho'\,,\chi)=\frac{2\,\mu}{m'}\,\frac{V(\rho)\,\varphi_\ell(\rho\,,\chi)}{\rho}\,.
\end{aligned} \tag{10}$$

Here χ' and χ are the rapidities which are related to $E_p\,,E_q$ as $E_p=\cosh\chi'\,,E_q=\cosh\chi$,

$$p_\ell(\rho\,,\cosh\chi)=\frac{(-1)^{\ell+1}}{\rho}\sqrt{\frac{\pi}{2\sinh\chi}}\,(-\rho)^{(\ell+1)}\,P^{-1/2-\ell}_{-1/2+i\rho}(\cosh\chi),\quad(-\rho)^{(\ell+1)}=i^{\ell+1}\frac{\Gamma(\ell+1+i\rho)}{\Gamma(i\rho)},$$

$P^{\nu}_{\mu}(z)$ is a Legendre function of the first kind, $\Gamma(z)$ is the gamma-function.

Thus, Eq. (10) differs from the corresponding equation in the case of two particles of equal masses only by the factor $2\mu/m'$ turning into 1 at $m_1=m_2$.

3 Relativistic S-factor

The solution of Eq. (10) with the potential (1) in the case of the interaction of two relativistic particles of equal masses was obtained in Ref. [10]. It leads to expression (3) for the relativistic S-factor. We use the method developed in Ref. [10] and seek a solution in the form

$$\varphi_\ell(\rho\,,\chi) = \frac{(-\rho)^{(\ell+1)}}{\rho}\int\limits_\alpha^\beta d\zeta\, e^{i\rho\zeta}\, R_\ell(\zeta\,,\chi)\,, \tag{11}$$

where the ζ-integration is performed in the complex plane over a contour with end points α and β: $\alpha = -R - i\varepsilon\,, \beta = -R + i\varepsilon\,, R \to +\infty\,, \varepsilon \to +0$. Substituting (11) into (10), we obtain the equation

$$\begin{gathered}(-1)^\ell \int\limits_\alpha^\beta d\zeta\, R_\ell(\zeta\,,\chi)\left(\frac{d}{d\cosh\zeta}\right)^\ell \Big[(\sinh\zeta)^{2\ell+1}\ (2\cosh\chi - 2\cosh\zeta)\times \\ \left(\frac{d}{d\cosh\zeta}\right)^\ell\left(\frac{e^{i\rho\zeta}}{\sinh\zeta}\right)\Big] = -\frac{2\,\alpha\,\mu}{m'\,\rho}\prod_{n=1}^{\ell}(\rho^2+n^2)\int\limits_\alpha^\beta d\zeta\, e^{i\rho\zeta}\, R_\ell(\zeta\,,\chi)\,.\end{gathered} \tag{12}$$

It should be noted that solutions of this equation, and hence Eq. (10), do not contain any more the i-periodic constants. For $\ell = 0$ the solution of Eq. (12) leads to the following expression for the RQP partial wave function:

$$\varphi_0(\rho\,,\chi) = C_0(\chi)\frac{\rho}{\rho^{(1)}}\int\limits_\alpha^\beta d\zeta \frac{e^{(i\rho+1)\zeta}}{(e^\zeta - e^\chi)^2}\left[\frac{e^\zeta - e^{-\chi}}{e^\zeta - e^\chi}\right]^{-1+iA}\,, \quad A = \frac{\alpha\,\mu}{m'\,\sinh\chi}\,. \tag{13}$$

Performing in Eq. (13) ζ-integration in the complex plane along a contour with end points α and β (in the same way as in Ref. [10]) we obtain the resulting solution in the form

$$\varphi_0(\rho\,,\chi) = C_0(\chi)\frac{2\,\rho\,\sinh(\pi\,\rho)}{\rho^{(1)}}\int\limits_{-\infty}^{\infty} dx \frac{e^{(i\rho+1)x}}{(e^x + e^\chi)^2}\left[\frac{e^x + e^{-\chi}}{e^x + e^\chi}\right]^{-1+iA}\,. \tag{14}$$

This solution can also be represented in terms of hypergeometric function as

$$\varphi_0(\rho\,,\chi) = -N_0(\chi)(-\rho)^{(1)}\, e^{i\rho\chi + iA\chi}\, F\left(1 - iA, 1 - i\rho; 2; 1 - e^{-2\chi}\right)\,. \tag{15}$$

The normalization constant $N_0(\chi)$ in Eq. (15) can be obtained (see Ref. [10] for details) from the condition

$$\lim_{\alpha\to 0}\varphi_0(\rho\,,\chi) = \rho\, p_0(\rho\,,\cosh\chi) \xrightarrow[\rho\to\infty]{} \frac{\sin(\rho\chi)}{\sinh\chi}\,. \tag{16}$$

By using relations (15) and (16), taking into account that $\chi_{\mathrm{BS}}(x=0) = \psi_q(\boldsymbol{\rho})|_{\rho=i}$ and the wave function $\psi_q(\boldsymbol{\rho})$ at $\rho = i$ contains only s-waves ($\ell = 0$), we can calculate $|\psi_q(i)|^2$. This leads to the following expression for the relativistic S-factor in the case of two particles of unequal masses:

$$S_{\,\mathrm{uneq}}(\chi) = \lim_{\rho\to i}\left|\frac{\varphi_0(\rho\,,\chi)}{\rho}\right|^2 = \frac{X_{\,\mathrm{uneq}}(\chi)}{1 - \exp\left[-X_{\,\mathrm{uneq}}(\chi)\right]}\,, \qquad X_{\,\mathrm{uneq}}(\chi) = \frac{2\,\pi\,\alpha\,\mu}{m'\,\sinh\chi}\,, \tag{17}$$

where χ is the rapidity which is related to the total c. m. energy, $\sqrt{s}$, as $({m'}^2/\mu)\cosh\chi = \sqrt{s}$.

The function $X_{\,\mathrm{uneq}}(\chi)$ in Eq. (17) can be expressed in terms of the 'velocity' u in the form

$$X_{\,\mathrm{uneq}}(\chi) = \frac{\pi\,\alpha\,\sqrt{1-u^2}}{u}\,, \qquad u = \sqrt{1 - \frac{4\,{m'}^2}{\bar{s}}}\,, \quad \bar{s} = s - (m_1 - m_2)^2\,. \tag{18}$$

Note that the relativistic relative velocity v, which can be expressed through the total energy $\sqrt{s}$:

$$\mathrm{v} = 2\sqrt{\frac{s - (m_1+m_2)^2}{s - (m_1-m_2)^2}}\,\left[1 + \frac{s - (m_1+m_2)^2}{s - (m_1-m_2)^2}\right]^{-1}\,, \tag{19}$$

connects with the velocity u as

$$\mathrm{v} = \frac{2\,u}{1+u^2}\,. \tag{20}$$

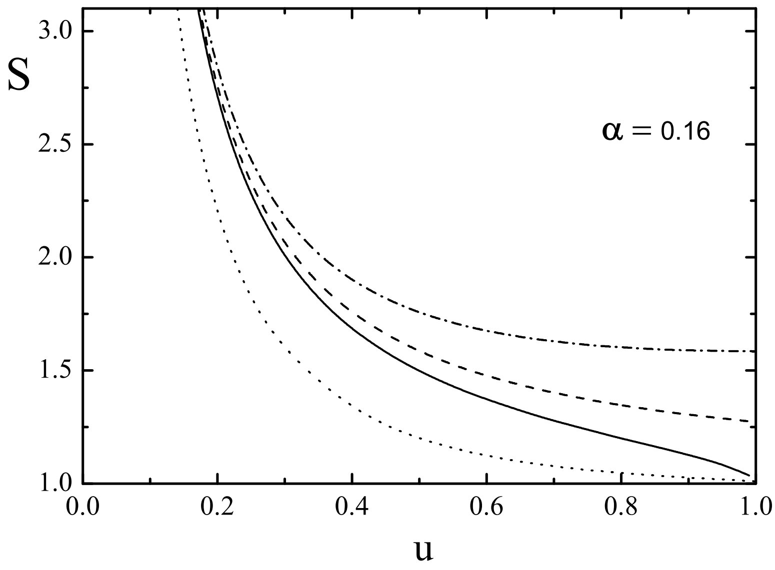

Figure 1. The solid line represents the relativistic S-factor (17); the dashed line the nonrelativistic S-factor (2); the dotted line taken from Ref. [16] the factor defined by formula (23); the dash-dotted the factor (21).

The S-factor (17) differs from the S-factor for the interaction of two relativistic particles of unequal masses

$$S_{\rm A}(\,{\rm v}) = \frac{X_{\rm A}(\,{\rm v})}{1 - \exp\left[-X_{\rm A}(\,{\rm v})\right]}\,, \qquad X_{\rm A}(\,{\rm v}) = \frac{2\,\pi\,\alpha}{\rm v}\,, \tag{21}$$

which was obtained in Ref. [9], by the meaning of the relativistic relative velocity, v, which here is given by expression (19). Besides, in the case of equal masses ($m_1 = m_2 = m$), the new S-factor (17) differs also from the factor

$$S_{\rm H}(\,{\rm v_H}) = \frac{X_{\rm H}(\,{\rm v_H})}{1 - \exp\left[-X_{\rm H}(\,{\rm v_H})\right]}\,,\; X_{\rm H}(\,{\rm v_H}) = \frac{2\,\pi\,\alpha}{\rm v_H}\,,\; {\rm v_H} = \frac{2\,\beta}{1+\beta^2}\,,\; \beta = \sqrt{1 - \frac{4\,m^2}{s}}\,, \tag{22}$$

which was presented in Ref. [8].[1] Indeed, the factors (21) and (22) in the form and in the nonrelativistic limit $(\,{\rm v}\,,\,{\rm v_H}\,, u \to 0)$ coincide with the factor (17). However, the relativistic limits $(\,{\rm v}\,,\,{\rm v_H} \to 1)$ of the factors (21) and (22) differ essentially from the relativistic limit of the factor (17) equal to unity as $u \to 1$. Furthermore, in the case of the interaction of two relativistic particles of equal masses the S-factor (17) differs from the factor

$$K = G(\eta)\,\kappa\,, \qquad G(\eta) = \frac{2\pi\eta}{1 - \exp(-2\pi\eta)}\,, \tag{23}$$

which was obtained in Ref. [16], not only in form but also in a different behavior in the nonrelativistic $(\,{\rm v}\,, u \to 0)$ and the relativistic $(\,{\rm v}\,, u \to 1)$ limits.

To illustrate the difference between the above factors, we show in Fig. 1 the behavior of the S-factors (2), (17), (21) and (23) as functions of u for a fixed value of $\alpha = 0.16$. This figure demonstrates that the relativistic S-factors considered have an essentially different behavior as $u \to 1$.

4 Conclusion

The new relativistic threshold resummation S-factor (17) for the interaction of two relativistic particles of unequal masses was obtained. For this aim the relativistic quasipotential equation in relativistic configuration representation [17] with the Coulomb potential for the interaction of two relativistic particles of unequal masses was used. The Coulomb potential only formally has the same form as the nonrelativistic potential but differs in the relativistic configuration representation since its behavior corresponds to the quark-antiquark potential $V_{q\bar{q}} \sim \bar{\alpha}_s(Q^2)/Q^2$ with the invariant charge $\bar{\alpha}_s(Q^2) \sim 1/\ln Q^2$. So, the principal effect coming from the running of the QCD coupling is accumulated.

The new relativistic S-factor (17) obtained reproduces both the known nonrelativistic behavior and the expected ultrarelativistic limit (see Refs. [19, 20]). The S-factor (17) coincides in form with the nonrelativistic S-factor (2); however, the role of the parameter of velocity is played not by the relative velocity of interacting particles, v but by the relative velocity of an effective relativistic particle emerging instead of the system of two

[1] The same expression can be found in earlier paper [6].

particles. It was shown that there is a difference between the expression (17) obtained here and other known forms.

It should be noted that the S-factor may be significant in interpreting strong-interaction physics. In some physically interesting cases the function $R(s)$ occurs as a factor in an integrand, as, for example, in the case of inclusive τ decay or in the Adler D-function, and the behavior of the S-factor at intermediate values of u becomes important.

Acknowledgements. I would like to thank the Organizing Committee for the support and the excellent organization of the NPQCD-2009. Useful conversations with E. A. Kuraev, R. N. Faustov and N. B. Skachkov are gratefully acknowledged.

This work was supported in part by BelRFBR-JINR grant No. F08D-001 and RFBR grant No. 08-01-00686.

References

[1] T. Appelquist and H.D. Politzer, Phys. Rev. Lett. **34**, 43 (1975); Phys. Rev. D **12**, 1404 (1975).

[2] E.C. Poggio, H.R. Quinn, and S. Weinberg, Phys. Rev. D **13**, 1958 (1976).

[3] G. Gamov, Zeit. Phys. **51**, 204 (1928).

[4] A. Sommerfeld, Atombau und Spektrallinien, vol. II (Vieweg, Braunschweig, 1939).

[5] A.D. Sakharov, Sov. Phys. JETP **18**, 631 (1948).

[6] V.S. Fadin and V.A. Khoze, Sov. J. Nucl.Phys. **48**, 309 (1988); V.S. Fadin, V.A. Khoze, and T. Sjostrand, in Proc. of the 24-th Rencontre de Moriond: New results in hadronic interactions (Gif-sur-Yvette, Frontieres, 1989), p. 19; Z. Phys. C **48**, 613 (1990).

[7] V.S. Fadin, V.A. Khoze, A.D. Martin, and A. Chapovsky, Phys. Rev. D **52**, 1377 (1995).

[8] A. H. Hoang, Phys. Rev. D **56**, 7276 (1997).

[9] A. B. Arbuzov, Nuov. Cim. A **107**, 1263 (1994).

[10] K.A. Milton and I.L. Solovtsov, Mod. Phys. Lett. A **16**, 2213 (2001).

[11] A.A. Logunov and A.N. Tavkhelidze, Nuov. Cim. **29**, 380 (1963).

[12] V.G. Kadyshevsky, Nucl. Phys. B **6**, 125 (1968).

[13] K.A. Milton, I.L. Solovtsov, and O.P. Solovtsova, Phys. Rev. D **64**, 016005 (2001).

[14] K.A. Milton, I.L. Solovtsov, and O.P. Solovtsova, Mod. Phys. Lett. A **21**, 1355 (2006).

[15] K.A. Milton, Proc. of the Int. Seminar Denoted to the Memory of I. L. Solovtsov, Dubna, 15-18 Jan. 2008, JINR, Dubna, D4-2008-65, 2008, p. 82.

[16] J.H. Yoon and C.Y. Wong, Phys. Rev. C **61**, 044905 (2000); J. Phys. G: Nucl. Part. Phys. **31**, 149 (2005).

[17] V.G. Kadyshevsky, M.D. Mateev, and R M. Mir-Kasimov, Sov. J. Nucl. Phys. **11**, 388 (1970).

[18] V.G. Kadyshevsky, R.M. Mir-Kasimov, and N.B. Skachkov, Sov. J. Part. Nucl. **2**, 69 (1972).

[19] W. Lucha and F.F. Schöberl, Phys. Rev. Lett. **64**, 2733 (1990).

[20] W. Lucha and F.F. Schöberl, Phys. Lett. B **387**, 573 (1996).